DEVELOPMENT DESIGN METHODS FOR PREDICTING HYPERSONIC AERODYNAMIC CONTROL CHARACTERISTICS

Z. POPINSKI and C. F. EHRLICH

FOREWORD

This is the final report of work accomplished by the Lockheed-California Company, a division of the Lockheed Aircraft Corporation, under Contract No. AF 33(615)-2512. The contract was initiated under Project No. 8219, Task No. 821902.

This report provides the results of work performed during the period from June 2, 1965 to April 15, 1966. The work was administered under the direction of the Flight Control Division, Air Force Flight Dynamics Laboratory located at Wright-Patterson Air Force Base, Ohio, by Mr. Eugene Fleeman, Project Engineer. The manuscript was released by the authors in July 1966 for publication as an RTD technical report.

At the Lockheed-California Company, this program was conducted under the direction of Mr. C. F. Ehrlich as Principal Investigator, assisted by Mr. Z. Popinski. In addition to the authors, Messrs. H. H. W. Drosdat, F. X. Hurley, and J. J. Rising contributed to the correlation and prediction sections and Mr. R. B. Salido assisted in heat transfer correlations.

Special appreciation is given to Mr. T. R. Sieron of the Air Force Flight Dynamics Laboratory for his guidance and assistance.

This technical report has been reviewed and is approved.

C.B. Westbrook
Chief, Control Criteria Branch
Flight Control Division
Air Force Flight Dynamics Laboratory

ABSTRACT

Design methods are developed for determining aerodynamic control effectiveness at hypersonic speeds along body surface. Pressure and heat transfer distributions in separated regions due to aerodynamic control deflection are described in terms of characteristic magnitudes and distance parameters by semi-empirical correlations. The forms of these correlations are inferred from theory and experimental data. Using these correlations, pressure distribution in the separated region over a deflected flap is approximated and expressions for force and moment coefficients are determined. General charts are developed which present separation and flow parameters over a range of flight conditions for a typical hypersonic vehicle.

Flow separation over a fin-plate configuration is presented using experimental measurements. Also, characteristics of flow over a flat plate, flat delta wing, and delta with dihedral are analyzed using visual flow records and pressure measurements from the point of view of two-dimensional flow. Applicability of the correlation expressions to separated flow on various configurations is discussed and calculated aerodynamic coefficients are compared with measured values. The experimental programs, test results, test model geometry, correlation expressions and prediction methods are reviewed critically, and the applicability of prediction methods discussed.

TABLE OF CONTENTS

TABLE OF CONTENTS (Continued)

TABLE OF CONTENTS (Continued)

TABLE OF CONTENTS (Concluded)

LIST OF ILLUSTRATIONS

LIST OF ILLUSTRATIONS (Continued)

LIST OF ILLUSTRATIONS (Continued)

LIST OF ILLUSTRATIONS (Continued)

LIST OF ILLUSTRATIONS (Continued)

LIST OF ILLUSTRATIONS (Continued)

LIST OF ILLUSTRATIONS (Concluded)

SYMBOLS

A	axial force
a	speed of sound
AR	aspect ratio
b	span
C	finite flap effectiveness factor
C	viscosity-temperature constant
c	chord
C_A	axial force coefficient
C_D	drag coefficient
C_f	local skin friction coefficient
C_p	pressure coefficient
C_P	specific heat at constant pressure
C_L	lift coefficient
C_m	pitching moment coefficient
C_N	normal force coefficient
C_γ	constant in the blast-wave expression
c_{flap}	flap chord
D	drag
d_{LE}	diameter of leading edge
d_1	upstream interaction length
d_2	downstream interaction length to peak pressure

d_3	downstream interaction length to pressure rise
G	parameter required to describe boundary-layer growth
h	heat transfer coefficient
HL	hinge line
HM	hinge moment
K	hypersonic similarity parameter
K	general constant
k	thermal conductivity
L	lift
L	reference length for moment coefficients
L	length associated with deflected flap geometry
ℓ_s	separation length
ℓ_{fi}	free interaction length
ℓ_2	downstream heat transfer interaction length
M	Mach number
M	moment
N	normal force
n	coordinate normal to streamline
n	coordinate normal to shock sheet
n	parameter required to describe boundary layer growth
Nu	Nusselt number
P	pressure
P_{t2}	total pressure behind the shock
P_3	pressure behind a reflected shock

Pr	Prandtl number
q	dynamic pressure
q	heat flux
r	recovery factor
Re	Reynolds number
S	reference area
s	coordinate along streamline
s	coordinate along shock sheet
St	Stanton number
T	temperature
U	velocity of outer flow
u	velocity in viscous region
x	longitudinal coordinate
X_s	coordinate of shock locus
x_t	distance to transition point
y	lateral coordinate
z	vertical coordinate
α	angle of attack or flow deflection angle
Δ	incremental change
Γ	a function of relative flap chord length
γ	ratio of specific heats
δ_f	flap deflection angle
δ	boundary layer thickness
δ_{o_B}	incompressible boundary layer thickness (no reference temperature conditions used)

δ	wedge angle
δ^*	displacement thickness of boundary layer
Λ	sweep angle
μ	viscosity
ρ	density
θ	shock-wave angle measured from upstream flow direction
θ	inclination of surface to flow
ϕ	angle associated with geometry of separation
$\bar{\chi}$	hypersonic interaction parameter
ω	exponent in viscosity-temperature relation

Subscripts and Superscripts

AV	average
asymp	asymptotic
aw	adiabatic wall
b	body
b	blast wave
$\mathbb{C}$	center line
CP	center of pressure
e	outer flow
fp	flat plate
HL	hinge line
INV	inviscid
INC	incipient
LE	leading edge

SYMBOLS (Concluded)

MRP	moment reference point
OS	oblique shock
P	plateau
pk	peak
ref	reference
S	separation
SL	shock loss
t	total or reservoir conditions
w	condition at wall
w	windward side
α	local condition upstream of interaction due to angle of attack
δ	due to boundary layer displacement
0	upstream of interaction
∞	free stream
*	reference temperature

SECTION I

INTRODUCTION

The development of efficient hypersonic vehicles involves solution of problems associated with lower-speed aircraft together with additional complexities introduced by the more severe environment of hypersonic flight. Spatial arrangement of the vehicle elements and configuration optimization for performance and stability may lead to shapes which create complex flow fields, resulting in interference flow and flow separation.

Flow separation is a common and important phenomenon in the aerodynamics of aircraft and aerospace vehicles. It can occur in several ways, such as ahead of deflected flaps, on the leeward side of a surface inclined at large angles of attack, near the impingement of a shock wave upon the boundary layer of a body, and on a curved surface. Separation often limits the usefulness of aerodynamic devices; for example, separation limits the maximum lift of an airfoil.

Separation may be referred to as any reverse flow which increases drag or decreases lift in external flow. In low-speed flight, the principal effect of flow separation is to cause drastic modification of the pressure distribution.

In supersonic and hypersonic flow, the presence of shock waves is associated with strong pressure gradients which gives rise to interactions between boundary layers and shock waves. These interactions often lead to flow separation. The occurrence of shock-induced separation may influence heat transfer, pressure distribution, and the aerodynamic characteristics of a vehicle. From a thermodynamic point of view, the interaction region is characterized by a reduction of local heating rates in the separated region and a substantial heating rate increase at the reattachment point. Flow separation in the vicinty of trailing-edge flaps and around fins will result in changes in pressure distribution and will influence the control characteristics of a vehicle. It is, therefore, essential, from a practical point of view, to understand the flow-separation phenomena and to describe the flow conditions in the separated region.

This study is primarily concerned with the development of semi-empirical correlations for characteristic parameters of a separated flow at hypersonic speeds. The correlation equations developed describe the pressure and heat-transfer distributions in terms of local flow properties by defining characteristic magnitudes and distance parameters. Knowing these quantities, relations for incremental aerodynamic force and moment coefficients are developed. Thus, methods are obtained for predicting the effectiveness of aerodynamic controls, as influenced by separation phenomena, over a wide range of flight conditions.

Section II

FLOW SEPARATION PHENOMENA

The fluid near the body surface in a viscous flow is retarded by the skin friction forces. The velocity of the fluid in the boundary layer varies from zero at the wall to approximately the inviscid value at the outer edge. In the absence of other forces acting to further retard this flow, the slope of the velocity profile, $\frac{\partial u}{\partial y}$, is positive at the wall and gradually approaches zero at the edge of the boundary layer (Figure 1). If, in addition to wall shear, the flow encounters a pressure increase in the streamwise direction, deceleration of the flow takes place. Due to the work done against this pressure force, the energy of the fluid is reduced and the fluid may be brought to rest. This condition will be experienced first by the very low momentum fluid within the boundary layer and nearest the wall. Downstream of this region the acting force will cause the fluid near the wall to flow in the upstream direction, creating a backflow. The normal velocity gradient at the wall, $\left.\frac{\partial u}{\partial y}\right)_w$ must be positive when the fluid next to the wall moves with the stream and negative when the fluid in this region flows against the stream. It follows that where the two flows meet, $\left.\frac{\partial u}{\partial y}\right)_w = 0$. This point on the wall which divides these two regions of flow is defined as the separation point.

In most fluid dynamic situations, the force giving rise to separation is an adverse pressure gradient, i.e., the pressure increasing in the downstream direction. In order for the separation to occur the pressure rise must be large enough and the gradient must be sufficiently severe. In a supersonic flow, an adverse pressure gradient may be generated by the aerodynamic shape of the body (for example, a compression corner) or by an external source such as an impinging shock wave. In each case, the supersonic flow experiences a pressure rise across a shock wave. Ideally the shock wave represents a discontinuous rise in pressure. Actually the pressure rise takes place over a finite distance. There is a region in the part of the boundary layer nearest the wall where the flow is subsonic. In this region, pressure waves will propagate upstream of the disturbance. Experiments have shown that such disturbances may be propagated a significant distance upstream. The process by which this pressure field spreads through the subsonic portion of the boundary layer is referred to as "pressure diffusion."

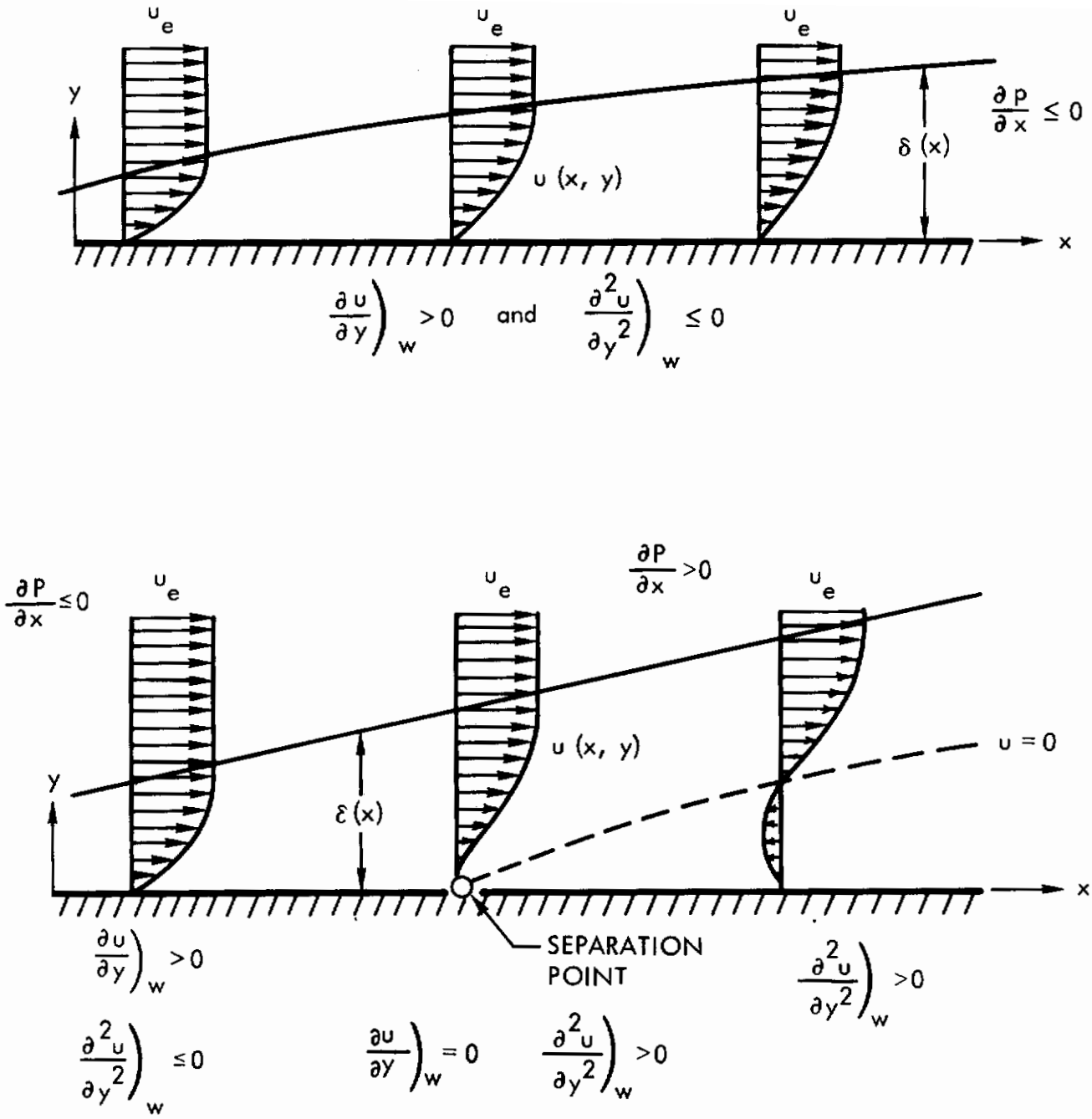

Figure 1. Boundary Layer Velocity Profiles

INCIDENT SHOCK

An illustrative case of the separated flow is an oblique shock incident on a boundary layer along a flat plate.

An oblique shock impinging on a flat plate in an inviscid flow generates a step increase in pressure and causes a flow deflection as shown in Figure 2. When an oblique shock impinges on a flat plate with a boundary layer, a quite different flow pattern results (Figure 3). The viscous flow cannot negotiate an abrupt pressure rise, and therefore the pressure rise must be spread over a finite distance. A strong adverse pressure gradient generated by the incident shock causes the boundary layer to thicken; if the incident shock is strong enough, the flow separates from the wall and a bubble of dead air is created. Due to the deflection of the external flow, caused by the growth of the boundary layer ahead of the shock impingement, a family of compression wavelets upstream of the impingement fans out. The slowly moving air in the separated region is essentially at constant pressure, and the incident shock is reflected from it in the form of a fan of expansion waves. The streamlines are deflected toward the plate and then turned parallel to the wall, which causes a flow compression and generates another family of compression wavelets.

The pressure distribution in viscous flow deviates markedly from that of an inviscid flow; it shows a pressure rise ahead of the shock impingement, reaches a plateau value in the separated region, rises to a peak value, and drops to the final inviscid pressure downstream of the reattachment. If the shock is not strong enough to cause separation, the pressure pattern resembles that for a regular reflection except that the rise is spread over a small length, of the order of the boundary layer thickness, ahead of the shock impingement point. If the shock strength is increased and exceeds that needed for incipient separation, the separation point moves upstream of the shock impingement point since the boundary layer can withstand only a weak pressure gradient in the separated region.

The pressure rise at separation seems to be fixed by the characteristics of the boundary layer, and to be free from any downstream influence, e.g., the method of inducing the separation ("free interaction"). If the final pressure is substantially higher than the pressure rise to separation, a considerable pressure rise must occur after separation over a certain length. Hence, once the shock strength exceeds the magnitude required to provoke separation, the length of the interaction region increases rapidly.

CORNER FLOW

For the case of a compression corner, illustrated in Figure 4, the effect of separation is to alter the flow geometry such that the supersonic flow will be compressed in two stages, by a compression shock at separation and by a reattachment shock.

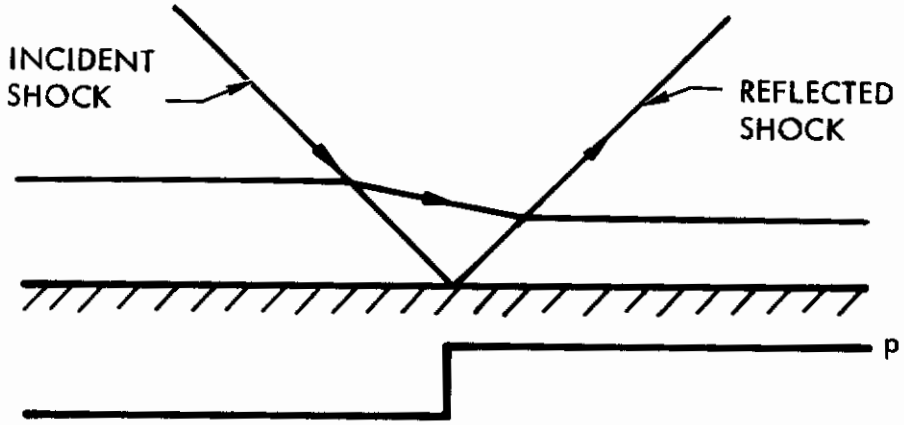

Figure 2. Regular Shock Reflection in Inviscid Flow

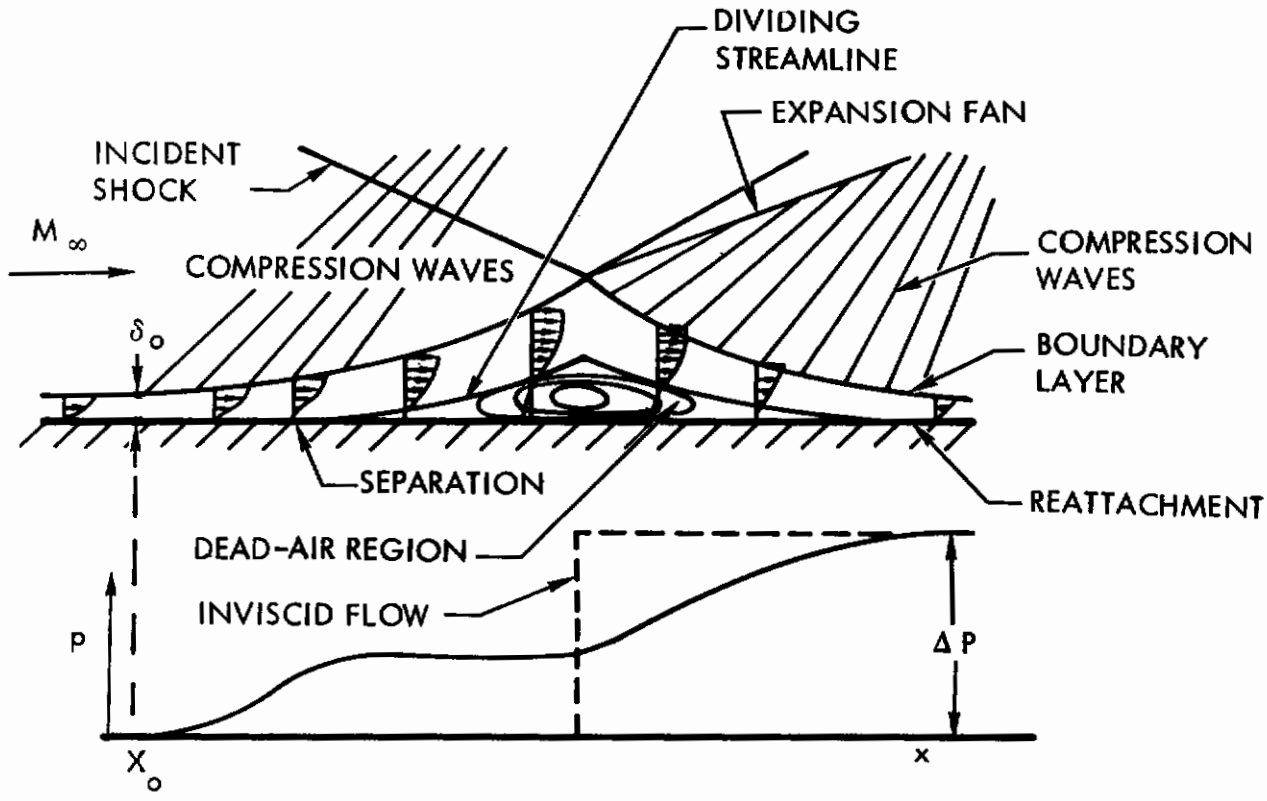

Figure 3. Shock Wave - Boundary Layer Interaction (Reference 24)

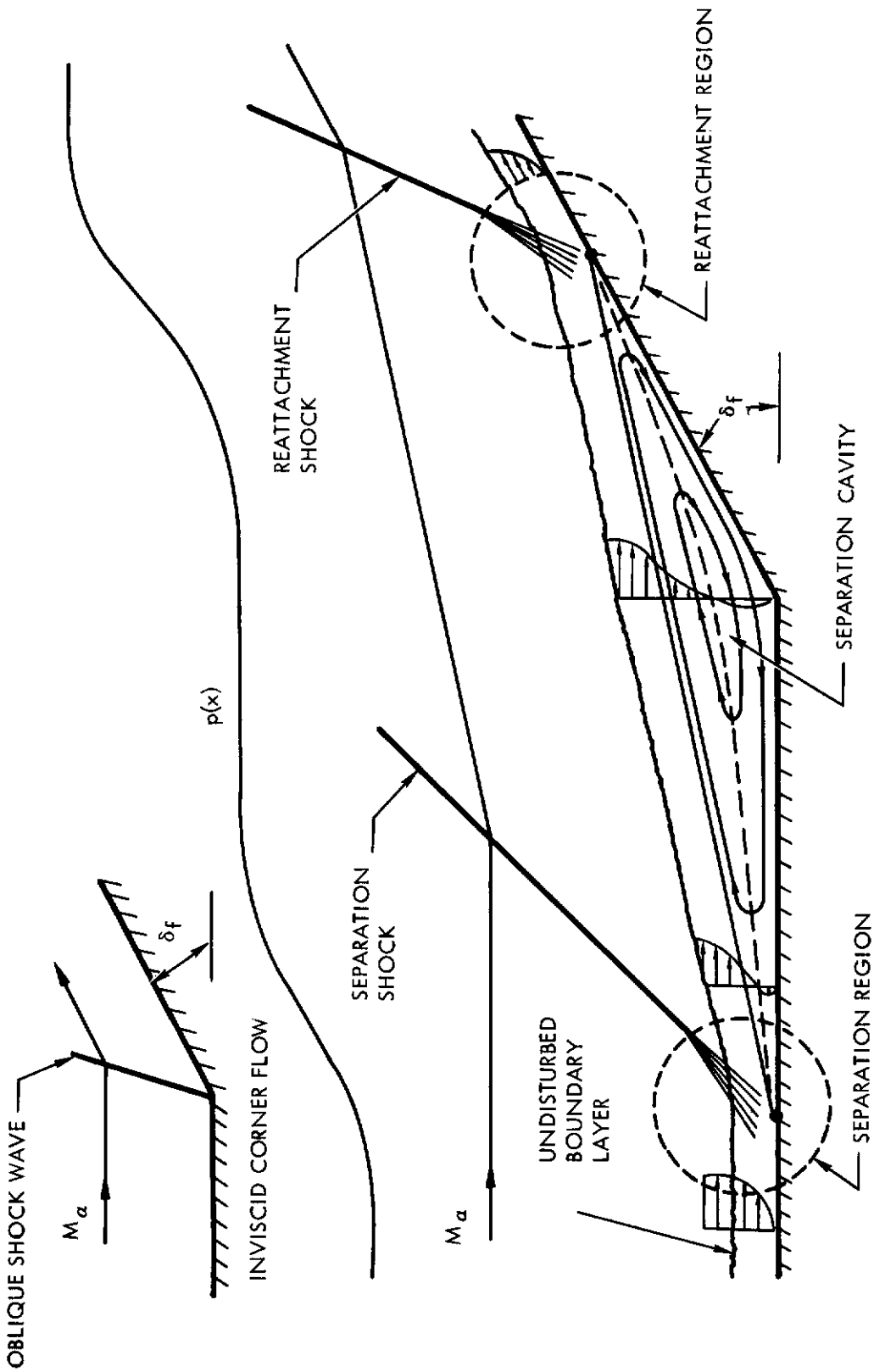

Figure 4. Flow Separation in Viscous Corner Flow

At reattachment, the supersonic flow is compressed to its final value, i.e., that value corresponding to the local slope of the body at that point. The fluid with sufficient momentum to proceed against the reattachment pressure rise continues downstream after reattachment, while that having insufficient momentum is reversed back into the separated region.

EFFECT OF STATE OF THE BOUNDARY LAYER ON PRESSURE PROFILE

Flow separations of initially laminar and turbulent boundary layers have basically similar behavior, but the streamwise scale of the interaction over which the pressure rise is spread is much longer for laminar than for turbulent boundary **layers** (Figure 5). Therefore it is necessary to distinguish between wholly laminar boundary layers and wholly turbulent boundary layers.

TRANSITIONAL SEPARATION REGION

It has been noted that the location of transition relative to the separation and reattachment points is an important variable influencing the pressure distribution. Consequently it is of interest to examine the effect of transition in this region.

It has been observed that the transition point can traverse the separation region at almost constant Reynolds number. (See Figures 8 and 10, Reference 1.) Analytical or empirical formulations for the determination of the position of transition in the separated region are therefore not available. One can only discuss the effects of transition on the pressure profile as shown by experimental pressure distribution.

The transitional separation region is characterized by large pressure gradients near transition. This region has been noted to be unsteady (Reference 2). An abrupt pressure rise before the hinge line is observed when transition is near reattachment (References 1 to 3). This may be observed in Figure 6. The plateau pressure level and the general shape of the pressure distribution upstream of transition is similar to those of the laminar case.

SOME THEORETICAL CONSIDERATIONS

The separated flow field can be analyzed by assuming a flow model consisting of a thin, constant-pressure viscous mixing layer separated from a solid surface by an enclosed region of low-velocity air (dead air) (Reference 4). The flow model under consideration is represented essentially by the mixing of a high-velocity stream with a low-velocity stream, along the dividing streamline between the separation and reattachment points (Figure 7). The dividing streamline divides the dead air from the separated flow proper, and no fluid enters or leaves the dead-air region (mass must be conserved). The uniform stream of velocity u_e mixes with the dead air and the mixing layer thickens and grows parabolically, beginning at the origin of mixing. The air scavenged from the dead-air region is balanced by that reversed back into the dead-air region by the pressure rise in the reattachment zone.

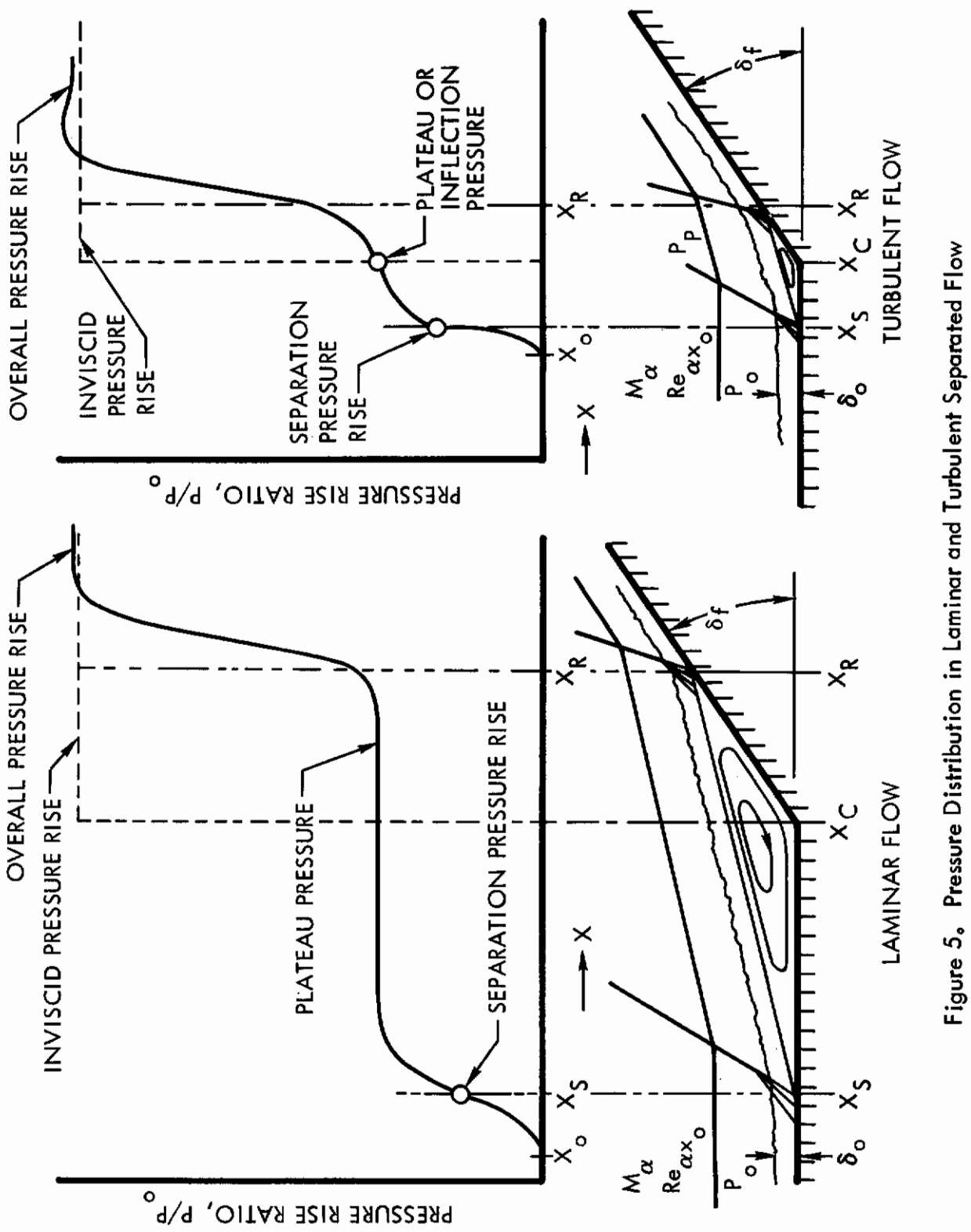

Figure 5. Pressure Distribution in Laminar and Turbulent Separated Flow

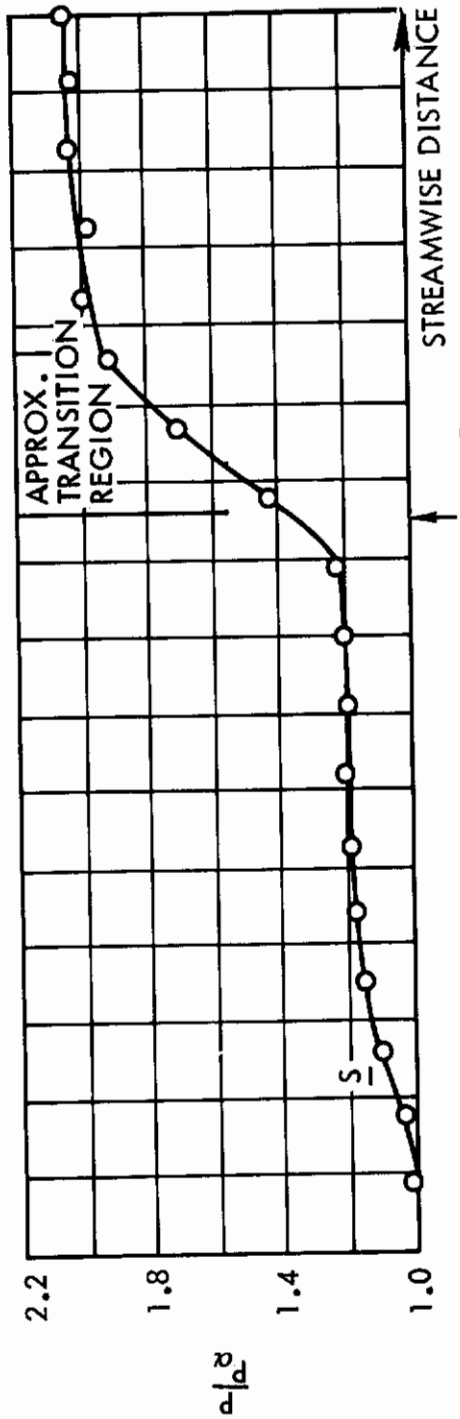

Figure 6. Effect of Transition Location on Pressure Distribution in a Corner Flow (Reference 2)

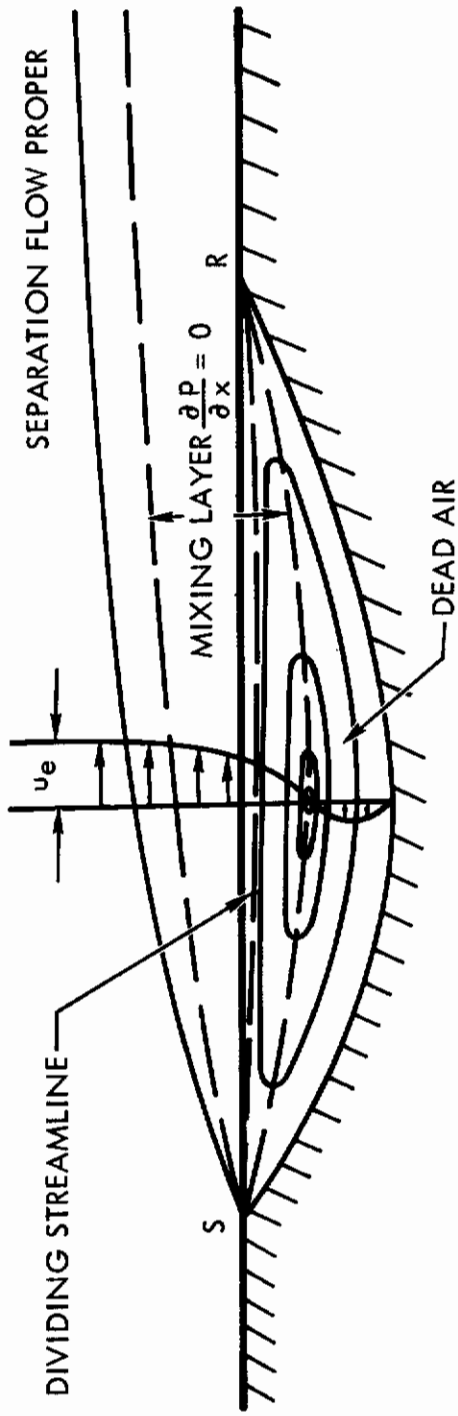

Figure 7. Mixing Layer Model (Reference 4)

In order for a particle along a streamline within the mixing layer to be able to overcome the pressure rise through the reattachment zone and pass downstream, its total pressure P_t must be larger than the static pressure P' at the end of the reattachment zone (Figure 8, particle (a)). A particle such as (b), however, has a low velocity with a correspondingly low $P_t < P'$. Assuming that the boundary-layer thickness at separation is zero, the asymptotic velocity along the dividing streamline has been calculated for two-dimensional laminar flow to be equal to $u = 0.587\ u_e$.

IMPORTANT FLOW SEPARATION PARAMETERS

The main factors affecting the interaction between a shock wave and a boundary layer are:

- Mach number
- Reynolds number
- Shock strength
- State of boundary layer (laminar, turbulent transitional)
- Location of transition

For example, an increase of Mach number increases the magnitude of the plateau pressure and an increase of Reynolds number reduces the plateau pressure. This can be shown using the equation for plateau pressure for laminar flow

$$(C_p)_P = \frac{\frac{P_P}{P_{ref}} - 1}{\frac{1}{2}\gamma M^2} \cong \frac{C}{R_e^{\frac{1}{4}} (M^2-1)^{\frac{1}{4}}}$$

which can be rearranged for large Mach number to the form

$$\frac{P_p}{P_{ref}} \simeq 1 + \frac{C\, M^{1.5}}{R_e^{\frac{1}{4}}}$$

An increase of the shock strength has only slight effect on plateau pressure and increases the upstream interaction length (References 5 and 6).

The state of the boundary layer influences the physical scale of the interaction. Laminar separation extends over a larger distance than turbulent separated flow, and the laminar pressure rise is more gradual as compared with the abrupt pressure rise in turbulent flow. It has been recognized that location of transition relative to separation and reattachment points is an important variable.

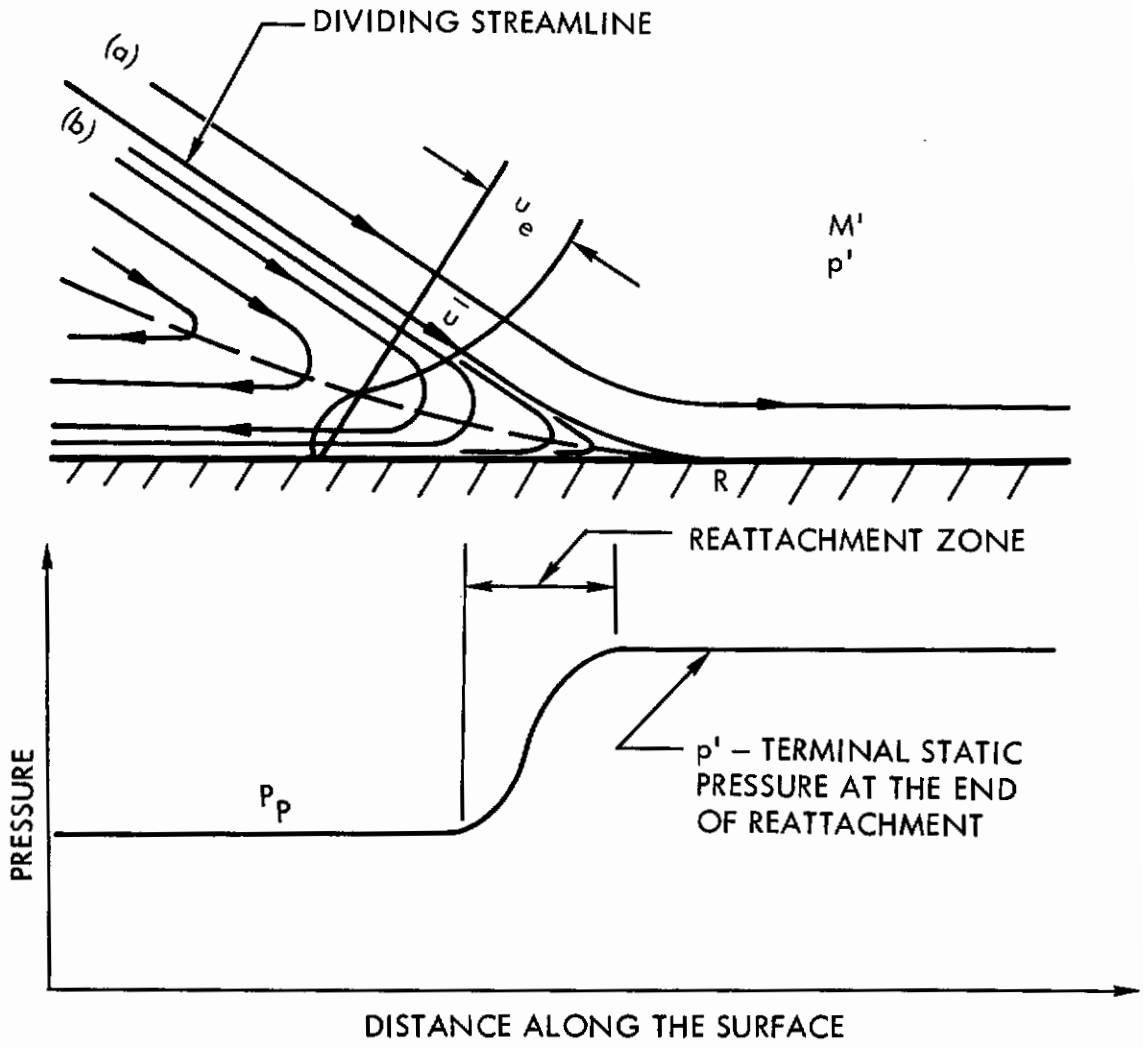

Figure 8. Separation Flow at Reattachment (Reference 4)

When transition is close to the separation point, the flow lacks two-dimensionality and is relatively unsteady. Pressure in the transition region frequently reaches a peak value which is higher than in turbulent flow. (Incidentally, the stability of a separated boundary layer increases markedly with an increase in Mach number.)

Another important parameter is the temperature of the wall. Wall cooling has only a slight effect on the magnitude of plateau pressure but reduces the interaction length (Figure 9).

The effect of wall temperature on location of separation point is shown in Figure 10 (Reference 7). The distance between the beginning of interaction and the separation point is shown as a function of the position of the beginning of interaction, with wall temperature as a parameter. It is noted that as the wall is cooled, the distance (X_S-X_O) decreases and becomes zero at some critical temperature ratio. Simultaneously the pressure at separation becomes equal to the pressure at the beginning of interaction, and no separation occurs. The limiting line on the left indicates tangency of the dividing streamline to the edge. Also the inclination of the dividing streamline in the reattachment region is reduced by wall cooling, and as a consequence the over-all distance of separated flow is decreased.

THEORETICAL ANALYSES OF SEPARATED FLOW

The complex and challenging problem of interaction between a shock wave and a boundary layer has occupied many investigators since 1939, when the interaction phenomena were first observed by Ferri (Reference 8) during tests on an airfoil in a supersonic tunnel where a favorable pressure gradient was expected. Since that time, numerous workers have investigated various facets of the interference flow. Although our knowledge is still far from complete, a considerable understanding of the interaction phenomena has been gained over the last two decades. However, in spite of the persistent and long-time effort on this subject, a satisfactory and simple theoretical analysis adequate for engineering applications does not exist. The interaction involves the separation point, the separation region, and re-attachment; and each of these might be considered to be one of the unsolved problems of fluid dynamics.

An introductory discussion and a historical review of the developments in the field of separated flow phenomena can be found in References 9, 10 and 11.

The simple case of an oblique shock wave impinging on a flat plate has been the subject of numerous theoretical and experimental investigations. The flat plate model has the advantage of being able to separate the effects of the interaction from those arising from the pressure gradient associated with a curved surface. The theoretical study of even such simple types of interaction presents many difficulties. Some early investigations treating the problems are described in References 12, 13 and 14.

One feature which has received much attention in theoretical considerations is the effect of the shock wave on the upstream flow. It was thought that these effects could be explained in terms of the propagation of disturbances

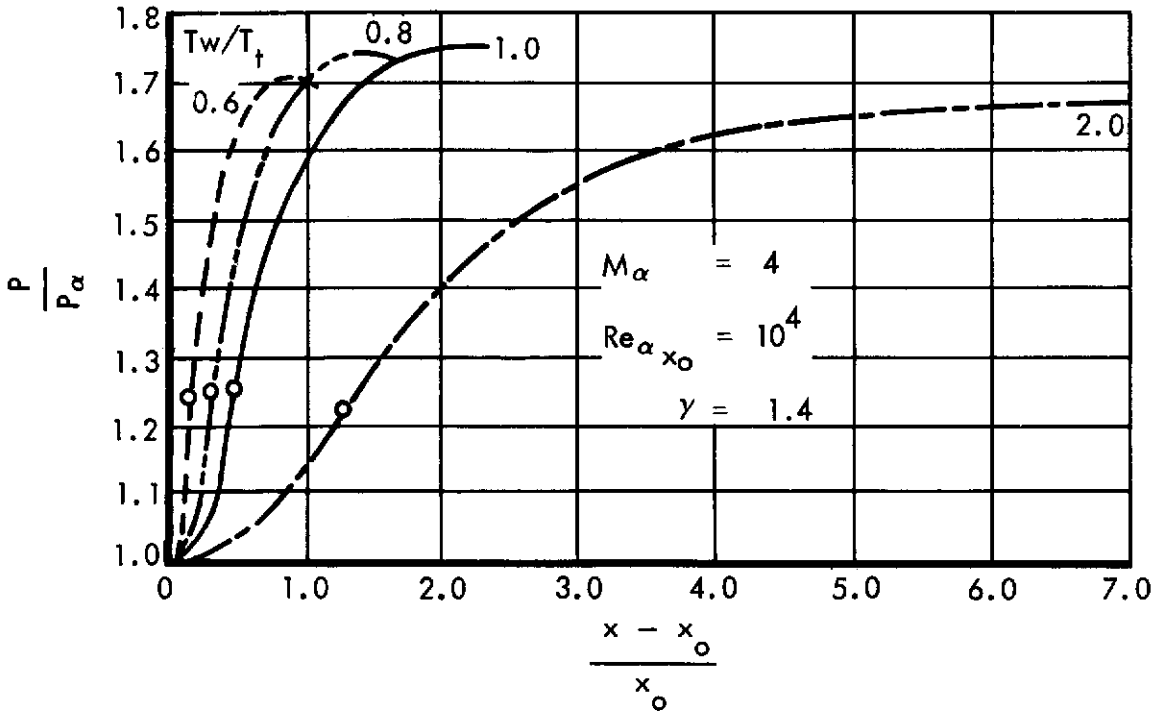

Figure 9. Wall Temperature Effect on Pressure Distribution in Separated Flow over a Curved Surface (Reference 28)

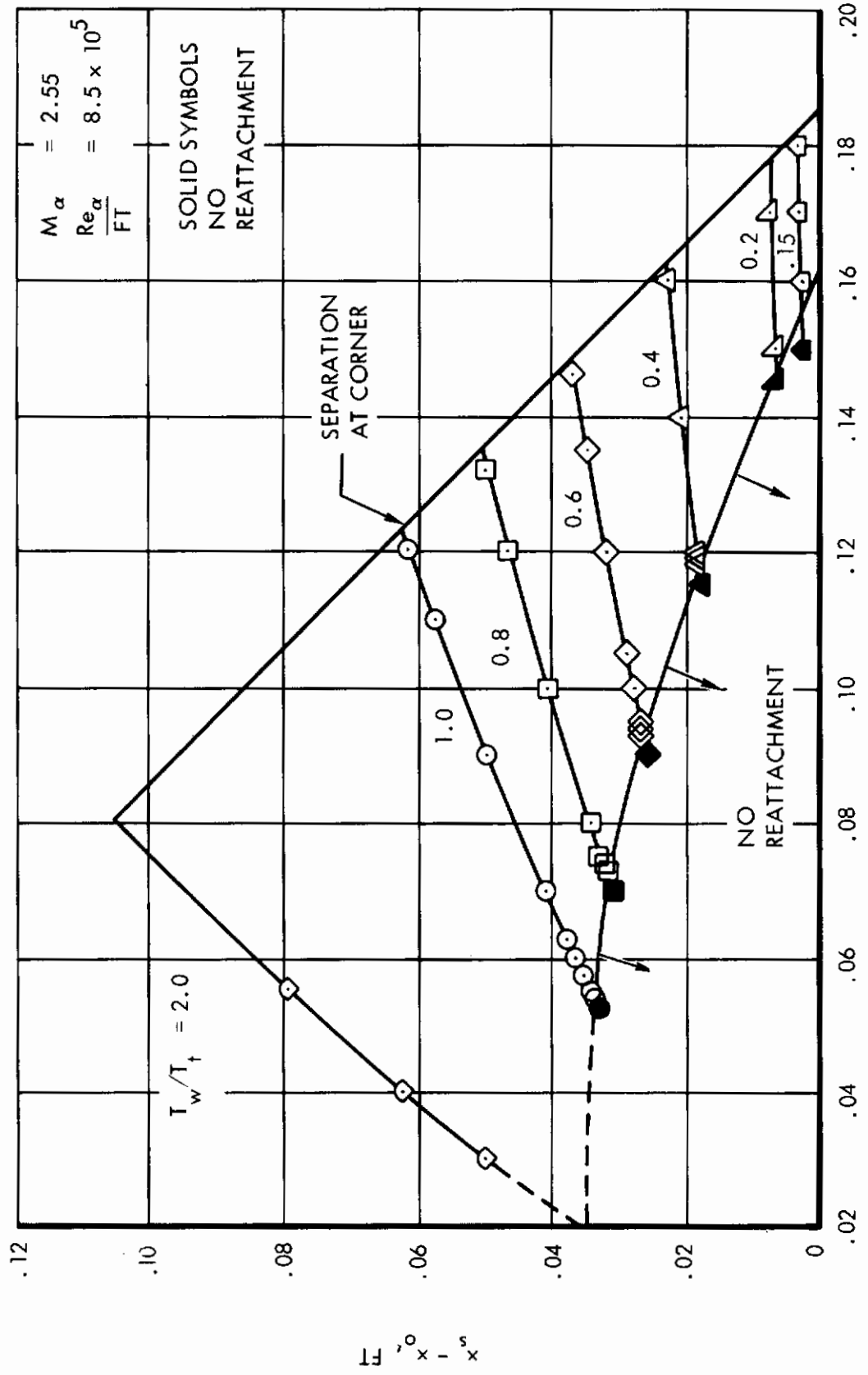

Figure 10. Distance Between Beginning of Interaction and Location of Separation as Influenced by Cooling (Reference 7)

upstream through the subsonic flow within the boundary layer near the wall. A simple theory which neglected viscosity effects other than those producing velocity profiles in the boundary layer was proposed. It was found, however, that the predicted upstream effects were much smaller than those observed, and the differences between the upstream effects in laminar and turbulent flow could not be accounted for (References 15, 16 and 17).

Another approach to account for the effects upstream of the interaction was to consider the mechanism of the interaction between the changes in thickness of the boundary layer and the pressure changes which they produce. The theories developed along this line (References 18 and 19) seem to be in reasonable agreement with experiments for weak shock waves.

In strong shock waves, which generate pressure gradients in excess of those required to produce separation, the separation point moves upstream until the pressure gradient drops to the separation value. The problem of boundary-layer separation ahead of the impingement point is dealt with in References 20, 21, and 22.

The mixing layer theory has been applied to the interaction problem by Crocco (Reference 23). This theory recognizes a mixing between the high-velocity external flow and the slower-moving air in the boundary layer, or the transport of momentum from the outer stream to the dissipative stream as a fundamental process that determines the pressure rise that can be supported by the flow. Since the external flow cannot be regarded as a known datum for the calculation of the dissipative flow, it is necessary to relate the thickening of the boundary layer and the consequent deflection of the external flow to the pressure distribution by simple-wave flow relations. This method uses a generalization of the von Karman momentum integral and treats the flow as quasi-one-dimensional with properly defined mean velocity and temperature; it is based on certain parameters characteristic of the boundary-layer profile. Interrelationships among these parameters are obtained from similar solutions of the boundary layer equations. The flux details are lost by this method, but it is believed that this simplified model preserves the main features of the interactions with the external flow.

Quantitative disagreement between experiments and the theoretical results obtained by the Crocco-Lees method for the region upstream of separation prompted Glick (Reference 24) to re-examine this method. As a result, an improved correlation function based on low-speed theoretical and experimental data was developed. The separated and re-attached regions were reviewed and a physical model incorporating the concept of the dividing streamline **was assumed.** Using the Crocco-Lees approach and the estimated correlation functions for the separated and re-attachment regions, the problem of the shock-wave and laminar boundary layer interaction was analyzed. The calculated pressure distribution showed a satisfactory agreement with experiments.

A simple new method was developed along the lines of the well-known Pohlhausen method, which is applicable to problems with extensive separation (Reference 25). A sample calculation of pressure for the laminar foot of the interaction compared favorably with results obtained by the Crocco-Lees method.

A more conventional integral method following Karman-Pohlhausen for the study of the interaction problem resulting from a swept planar shock wave and a laminar boundary layer on a normal plane is described in Reference 26. The three-dimensional effects due to sweep are resolved by considering the problem in a plane normal to the shock plane and by considering the effect of the cross-flow velocity component separately. The method is based on a fourth-degree or higher polynomial for velocity and enthalpy profiles.

Another method based on a modified Pohlhausen approach with the velocity distribution represented by a fifth-degree polynomial with two undetermined parameters is presented in Reference 27. The concept of a dividing streamline is used. This method represents an improvement in pressure and shear values over those obtained by the one-parameter method.

Abbott et al.(Reference 28) describe a method which is based on solution of the boundary layer equations by the usual integral method with the Prandtl-Meyer equation for the pressure rise at the edge of the boundary layer. Pre-separation and post-separation regions are studied. Pressure distribution is calculated, and the effect of Mach number, Reynolds number, and wall temperature are established. However, the calculated temperature profiles in the separation region are unrealistic: the calculated flow temperature decreases as one moves away from a cooled wall, thus the cool wall is in the unlikely situation of heating the separated region. This trend can be ascribed to the use of similar velocity and temperature profiles in both the boundary layer and the dead-air region.

One of the more recent methods is due to Lees and Reeves (Reference 29). This paper presents a theory which is capable of including the entire separated flow without introducing semi-empirical features. It is based on the assumption that the boundary layer approximations are valid over the entire viscous flow region. The integral method with the first moment of momentum in addition to the momentum integral is employed. The successful application of this method to separated and re-attaching flows is attributed to the proper choice of the one-parameter family of velocity profiles.

A numerical method of treating laminar separated flow was reported recently by Nielsen et al. This method of solution is based on integral relations due to Dorodnitsyn. The boundary layer equations are transformed by the Stewartson and then by the Dorodnitsyn transformation such as in Reference 30. For axisymmetric flow, a Mangler transformation is applied. The success of this method is believed to depend primarily on the form of the equation for velocity profiles. The advantage of this method over those using a one-parameter family of profiles is that it is possible to obtain higher approximations to the solution and thus permit assessment of how closely the assumed velocity profiles approximate the actual non-similar family of profiles. The solution of the simultaneous differential equations is obtained by an IBM 7094 digital computer. This program which gives the velocity and pressure distribution throughout the boundary layer for either two-dimensional or axisymmetric configurations for adiabatic and non-adiabatic cases is described in detail in References 31 and 7.

Section III

FLOW PROPERTIES ALONG THE BODY SURFACE

LOCAL PRESSURE DISTRIBUTION

The pressure distribution over the surface of a vehicle flying at high Mach number and low Reynolds number consists of inviscid and viscous contributions and is established as a result of the so-called viscous-inviscid interactions.

Viscous-Inviscid Interactions

A thick boundary layer at hypersonic velocity changes the effective shape of the body and affects the inviscid external pressure which, in turn, influences the development of the boundary layer. The resulting pressure is higher than the inviscid pressure in the absence of viscous interactions. A measure of the effect of the interaction on the pressure is the interaction parameter

$$\bar{\chi} = \frac{M_\alpha^3 \sqrt{C}}{\sqrt{Re_{\alpha x}}}$$

The viscous interaction parameter $\bar{\chi}$ is used for delineating the viscous interaction phenomena into weak and strong interactions (Ref. 32).

The weak interactions occur when the deflection resulting from the growth of the boundary layer is sufficiently small. This is usually expressed by the relation

$$K = M_\alpha \theta_b \cong O(1) \text{ or less}$$

and

$$\frac{d\delta^*}{dx} < \theta_b$$

In terms of the viscous interaction parameter $\bar{\chi}$, for $\bar{\chi} \leq 1$, the effect of the interaction is small; for $\bar{\chi} \approx (1)$ or greater, the effect of the interaction might be significant. Thus, weak interactions appear at low angles of attack if the Reynolds number is high at high Mach number, or if the Mach number is moderately supersonic at low Reynolds number. They might also occur on a compression surface at sufficiently high angles of attack.

Strong interactions occur when $K^2 \gg 1$ and $\frac{d\delta^*}{dx} > \theta_b$ or if $\bar{X} \gg 1$. A strong pressure interaction region exists in the flow over a flat surface at low angles of attack when the local Mach number is sufficiently large and the Reynolds number is sufficiently small. The high Mach numbers and low Reynolds numbers which make viscous interaction important generally preclude turbulence in the boundary layer. The effects of viscosity on a flat plate cause the boundary layer to displace the inviscid flow from the plate by a distance equal to the boundary layer displacement thickness, δ^*. Since the streamwise pressure variation is dependent upon the local flow deflection, the change of displacement thickness with distance along the plate should be found in order to determine the effective body shape. This new body shape determines a new pressure distribution.

It is apparent that the influence of any pressure gradient on the growth of the boundary layer will in turn influence the pressure distribution. Therefore, a certain interdependence between the viscous and inviscid flow exists that affects the establishment of an equilibrium condition between these two flow regimes.

Pressure Distribution From Theory

The pressure distribution of a complex body flying at hypersonic velocity is obtained by numerical calculations which are rather lengthy and complex. Some approximate theories for determining the flow field include:

- Newtonian Impact Theory
- Constant Energy Solutions

The Newtonian theory predicts distribution for cases in which the flow is assumed to deflect parallel to the body. Constant energy solutions are based upon the analogy of the flow field generated by a slender or blunted body and a blast wave generated by exploding a line charge along the axis of symmetry. The blast wave solution is accurate far downstream and invalid locally near the nose. It is basically valid for a body with zero thickness.

A number of expressions for the pressure distribution were obtained from theory. One of the methods, as presented in Reference 33, is the basic tangent wedge solution which leads to the following expression for pressure distribution on a compression surface:

$$\frac{P}{P_\infty} = 1 + \left[\frac{\gamma(\gamma+1)}{4}\right] K^2 + \gamma K \sqrt{1 + \left[\frac{\gamma+1}{4}\right]^2 K^2} \qquad (1)$$

where

$$K = M_\infty \theta$$

This formula may be reduced for weak interactions and $K < 1$ to an approximate form

$$\frac{P}{P_\infty} = 1 + \gamma K$$

and for strong interactions where $K \gg 1$

$$\frac{P}{P_\infty} = \frac{\gamma(\gamma+1)}{2} K^2$$

The above formula is restricted to freestream Mach number M_∞ greater than 3, and to a local flow inclination, $\theta = \theta_b + \frac{d\delta^*}{dx}$, of less than 20 degrees (Ref. 33)

Bluntness Effects

The solution for P/P_∞ as described above should be increased linearly by a bluntness increment in case the leading edge is not sharp. The results of blast wave analyses are utilized to calculate this contribution. An expression for pressure distribution due to blast wave effects is given in Ref. 34 as

$$\frac{P_b}{P_\infty} = \left(\frac{1}{2}\right)^{\frac{2}{3}} C_\gamma (C_D)^{\frac{2}{3}} \frac{M_\infty^2 \cos^2 \Lambda_e}{\left(\frac{x}{d}\right)^{\frac{2}{3}}} \qquad (2)$$

$$\Lambda_e = \arcsin(\cos \alpha \sin \Lambda)$$

where $C_\gamma = 0.112$ for air, Λ_e is the effective sweep angle, and C_D is the drag coefficient of the leading edge.

Equation (1), in conjunction with the bluntness expression (2) was used for the predictions presented on Figures 11, 12, and 13 (for $C_D = 1.2$ and $\Lambda = 90°$). For the particular experimental conditions the bluntness contribution is negligible for $\alpha > 10$ deg and $x/d > 16$ at $M_\infty < 10$.

Boundary Layer Displacement Contribution

In the weak interaction regime, the boundary layer displacement contribution to K can be found from the classical compressible displacement-layer expression presented in Reference 35. For zero angle of attack:

$$\frac{d\delta^*}{dx} = \left[\frac{0.865}{M_\infty^2} \frac{T_w}{T_\infty} + 0.166 (\gamma-1)\right] \sqrt{C} \frac{M_\infty^2}{\sqrt{Re_{\infty_x}}} \qquad (3)$$

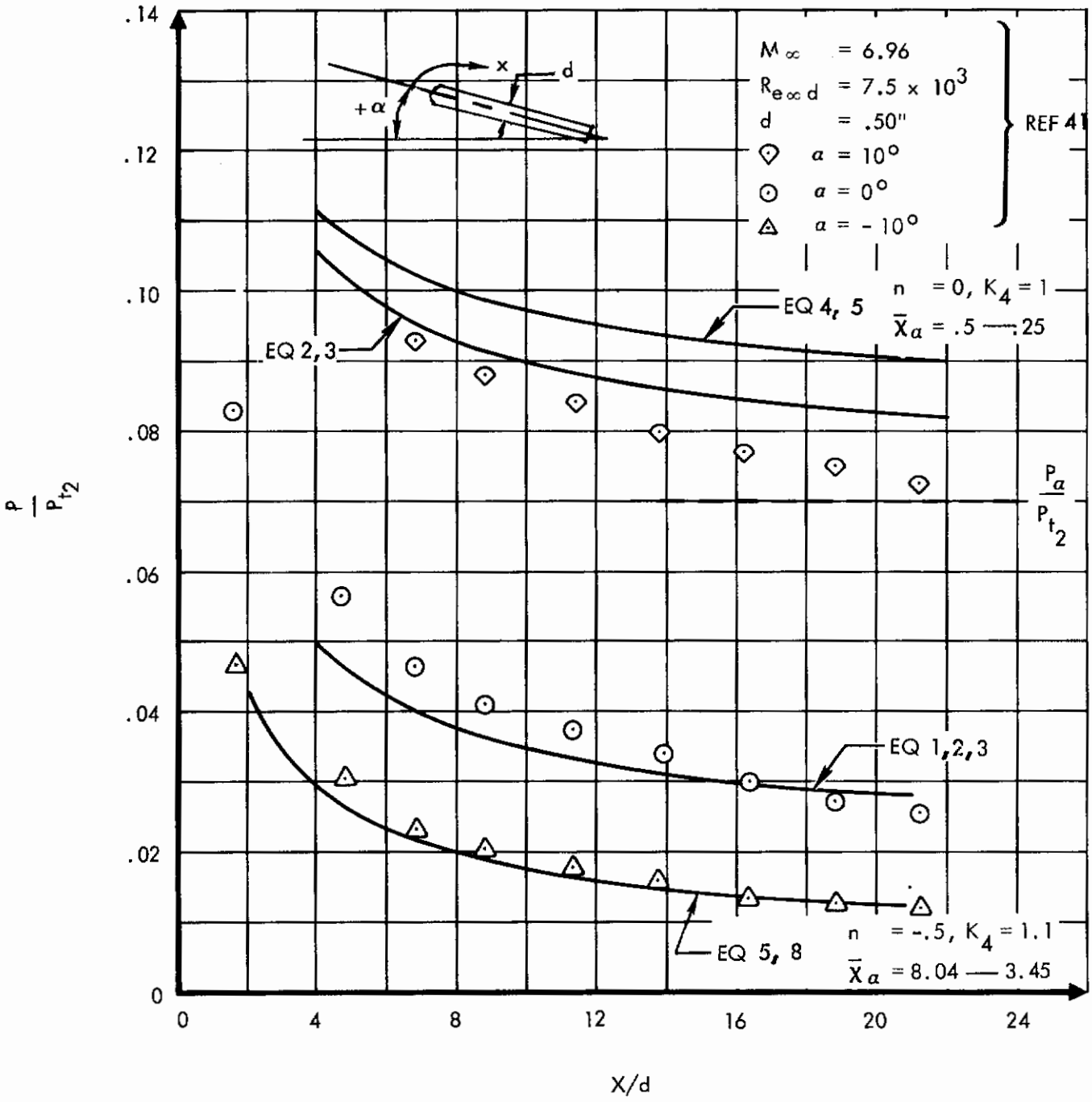

Figure 11. Pressure Distribution Along Blunted Flat Plate, M_∞ = 6.96

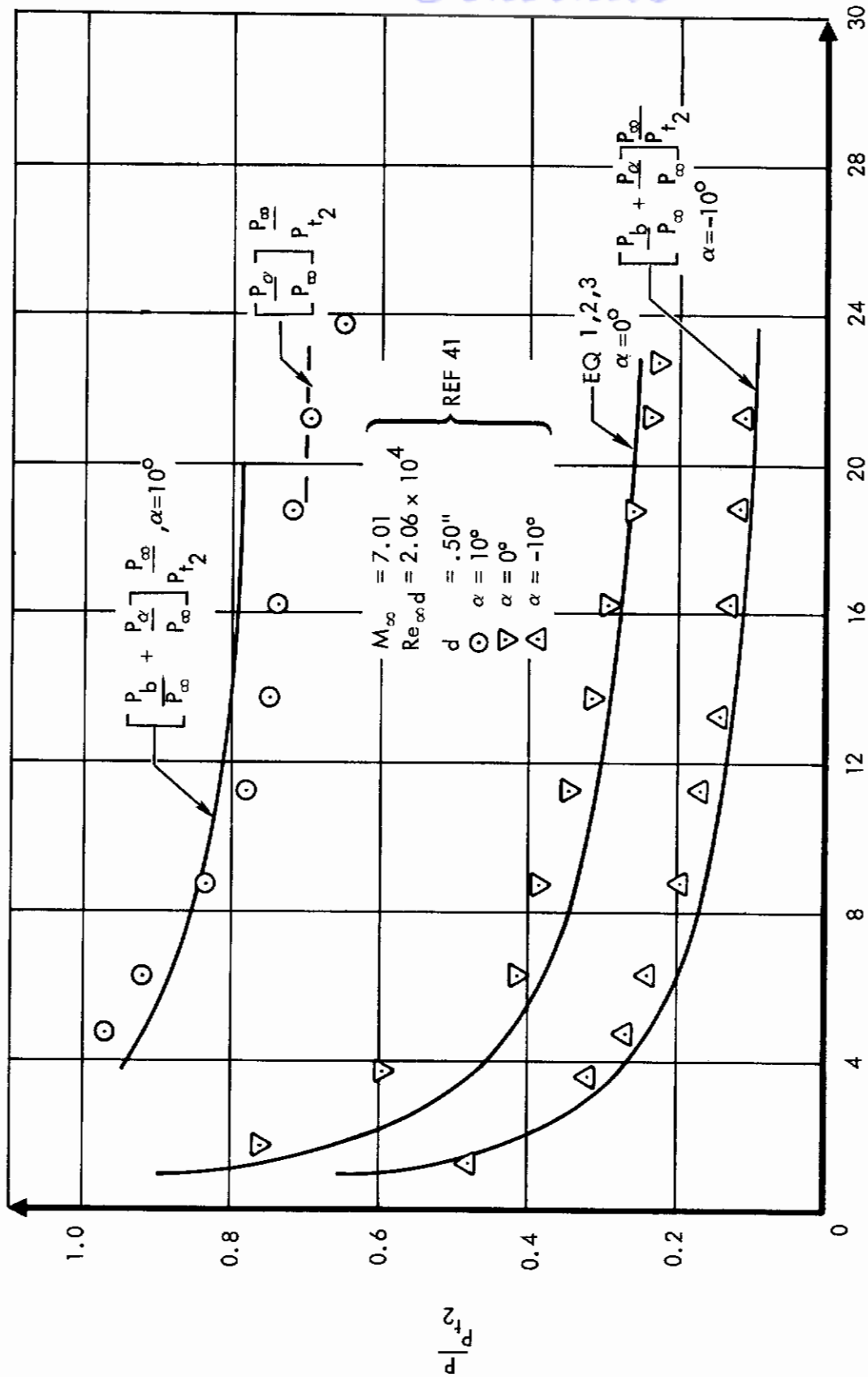

Figure 12. Pressure Distribution Along Blunted Flat Plate, $M_\infty = 7.01$

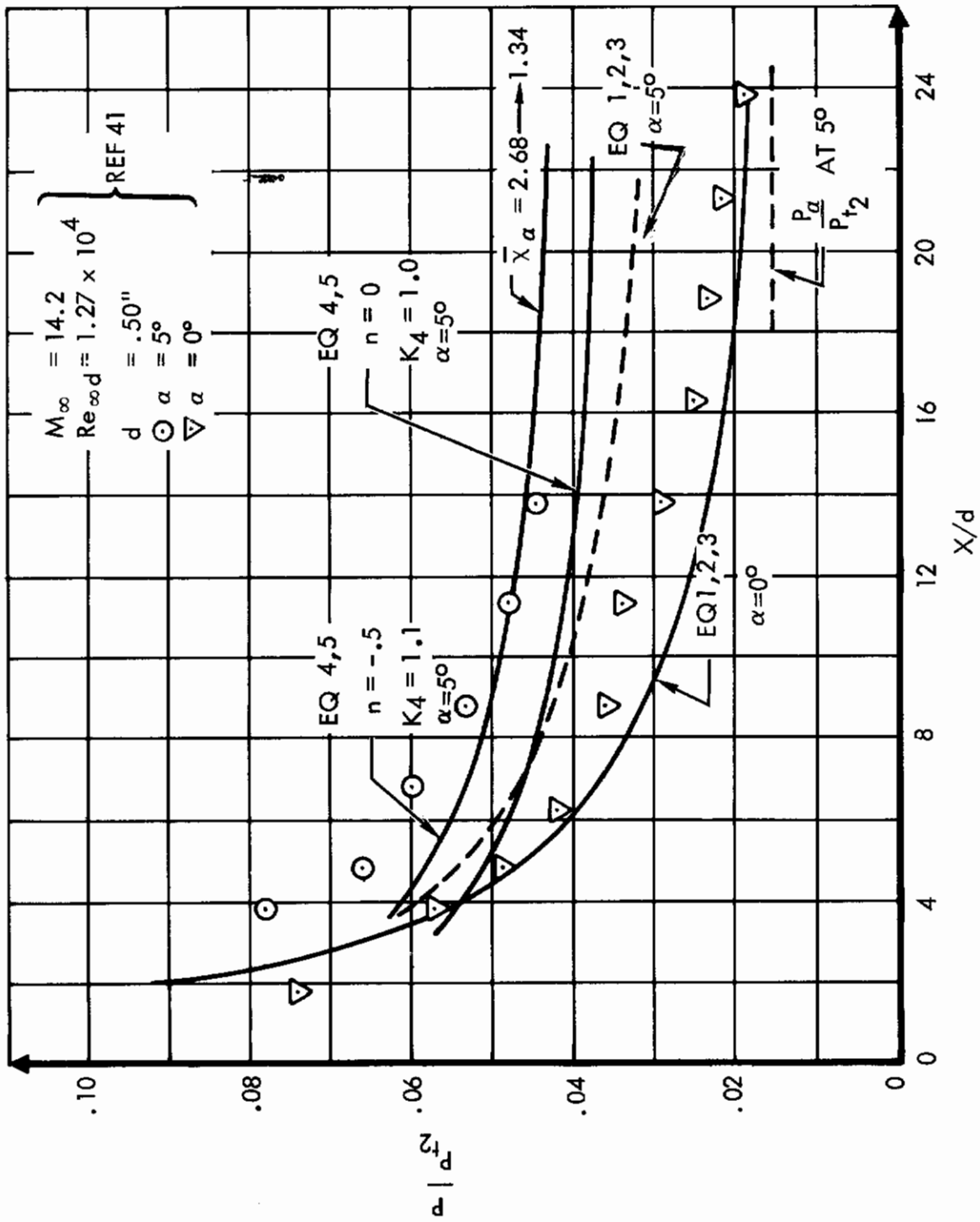

Figure 13. Pressure Distribution Along Blunted Flat Plate, M_∞ = 14.2

If $\alpha \neq 0$, free stream quantities must be replaced by the first estimate of inviscid local quantities, using for example $K = M_\infty \theta_{body}$ and the tangent wedge solution, Equation 1, or employing the oblique shock tables (Reference 36). A more complete treatment of this procedure is included in subsequent discussions.

Another way of treating the case for $\alpha \neq 0$ is to regard the viscous-induced pressure distribution as a perturbation on the inviscid distribution as follows. Once again, the flow properties encountered by the boundary layer are approximated by the inviscid flow properties. The tangent wedge approximation is then used to calculate the viscous contribution, that is:

$$\frac{P}{P_\infty} = \left\{ 1 + \left[\frac{\gamma(\gamma+1)}{4}\right] K_\delta^2 + \gamma K_\delta \sqrt{1 + \left[\frac{\gamma+1}{4}\right]^2 K_\delta^2} \right\} \frac{P_\alpha}{P_\infty} \qquad (4)$$

where

$$K_\delta = M_\alpha \frac{d\delta^*}{dx}$$

For a more general case, the viscous interaction contribution as modified by the bluntness included pressure gradient must be considered. The interaction regimes are classified in accordance with previous definitions of weak and strong interaction. An expression for K_δ is obtained following the approach in Reference 37. This relation accounts for the boundary layer growth as influenced by the local pressure distribution proportional to a power of distance, $P_{LOCAL} \sim x^n$. The following expression for K_δ was obtained

$$K_\delta^2 = \frac{1}{\gamma(\gamma+1)} \left\{ \sqrt{\left(\frac{P_b}{P_\infty}\frac{P_\infty}{P_\alpha}\right)^2 + \frac{\gamma(\gamma+1)}{2}\left[(1-n)\,K_4\right]^2\left[(G\,\bar{X}_\alpha)\right]^2} - \frac{P_b}{P_\infty}\frac{P_\infty}{P_\alpha} \right\} \qquad (5)$$

where

$$K_\delta = M_\alpha \frac{d\delta^*}{dx} \cong M_\alpha \frac{d\delta}{dx}$$

K_4 is determined from Figure 14 or 15, using the appropriate value for n.
n = 0 (weak interaction)
n = -1/2 (strong interaction)

If the inviscid pressure gradient due to nose blunting is much greater than the viscous induced pressure gradient, the applicable equation is (Ref. 37):

$$K_\delta = \frac{5}{6} \frac{K_4\, G\, \bar{X}_\alpha}{\sqrt{\frac{P_b}{P_\alpha}}} \quad \left(\text{For } \frac{P_b}{P_\alpha} > 1\right)$$

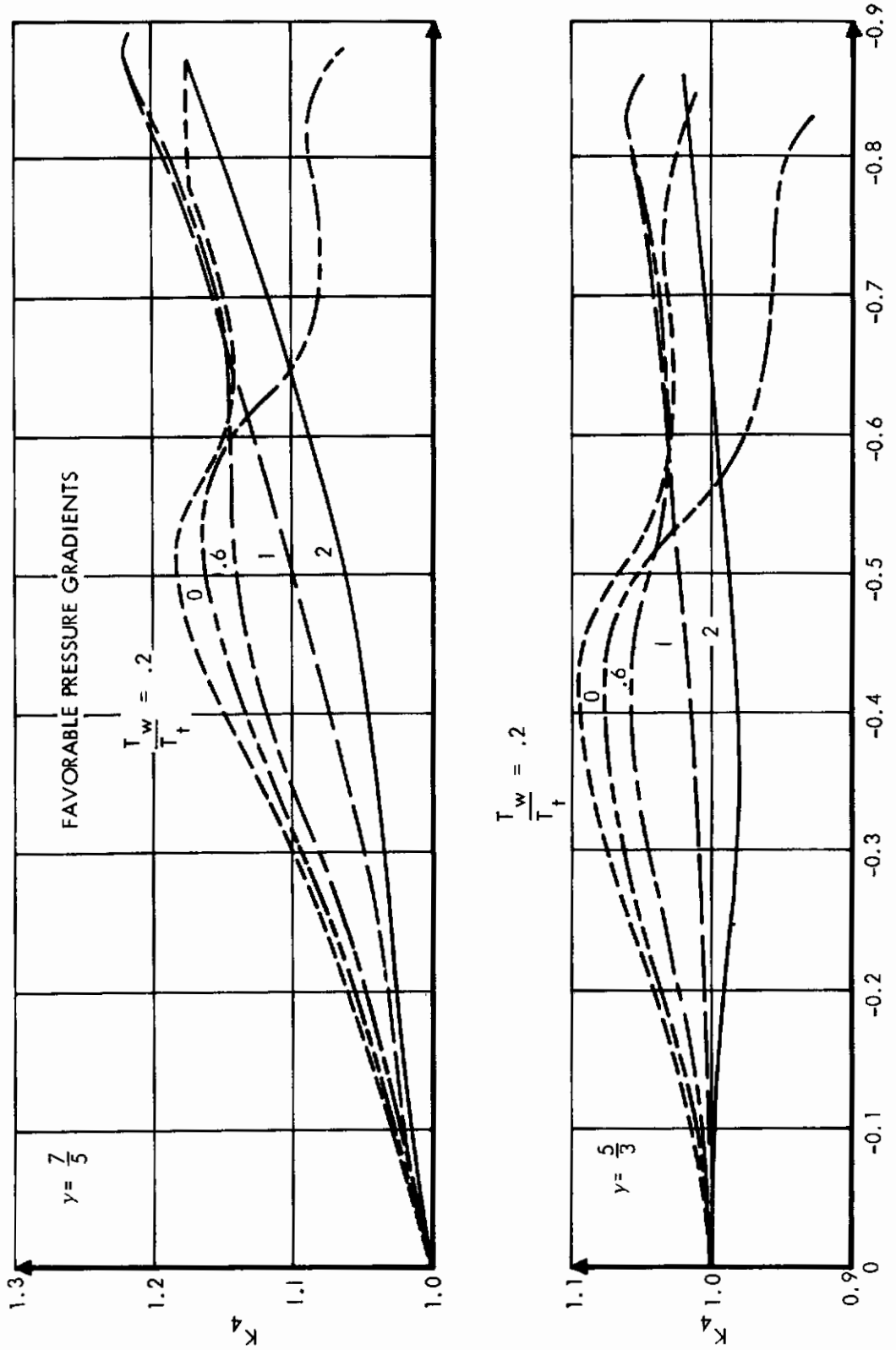

Figure 14. Variation of Coefficient K_4 in Boundary-Layer-Thickness Law with Pressure Gradient

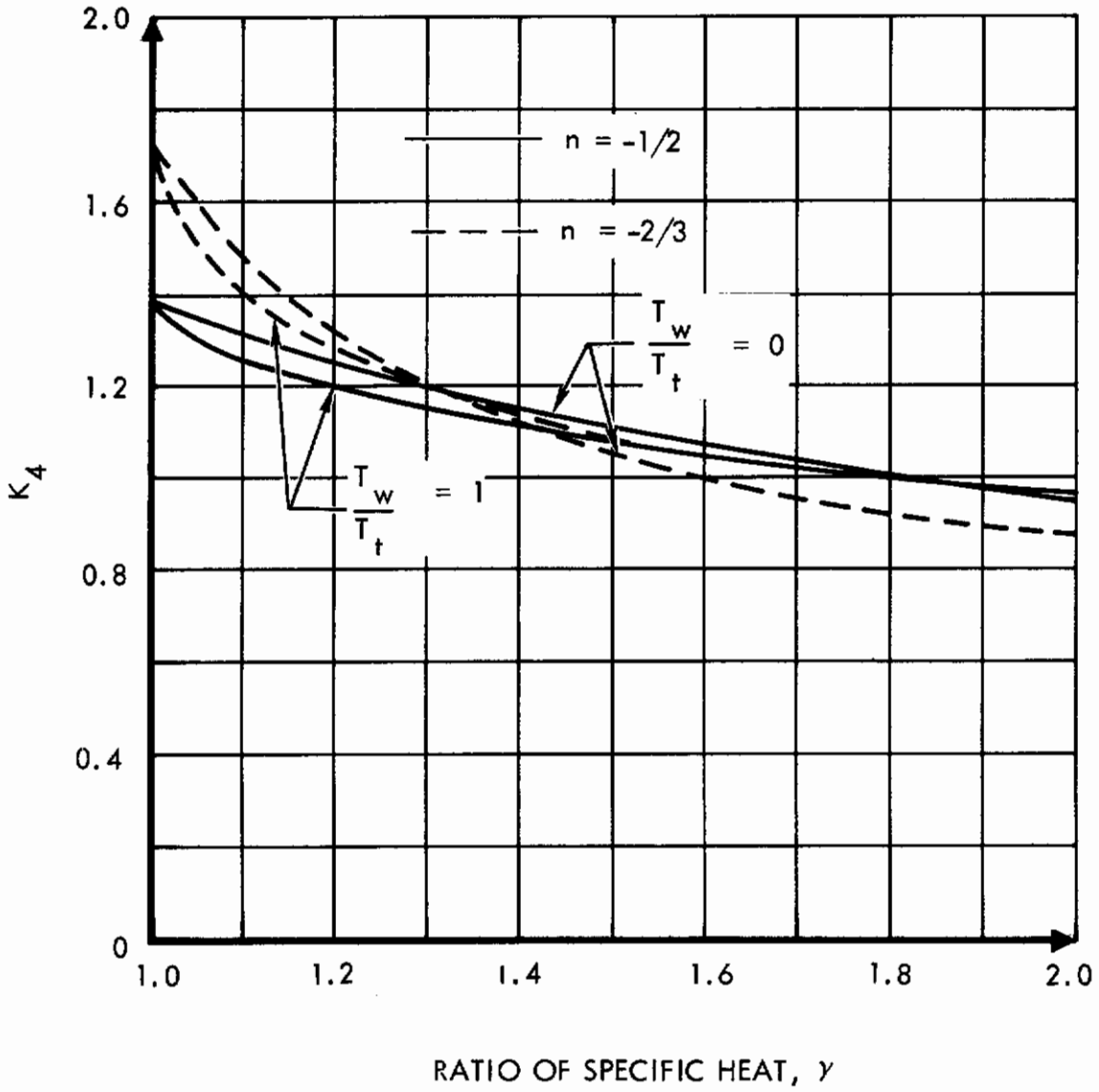

Figure 15. Effect of γ on the Coefficient K_4 (Reference 43)

where K_4 corresponds to n = -2/3 for blunt nose.

Further investigation has resulted in the following equation for the sharp leading edge case

$$\frac{P}{P_\infty} = \left\{ 1 + \frac{\frac{\gamma}{2} G \bar{X}_\alpha}{\sqrt{1 + \frac{\gamma}{2} G \bar{X}_\alpha}} \left[1 + \frac{\frac{\gamma G}{2} \bar{X}_\alpha}{2\left(1 + \frac{\gamma}{2} G \bar{X}_\alpha\right)} \right] + \frac{\gamma + 1}{4\gamma} \frac{\left(\frac{\gamma G}{2} \bar{X}_\alpha\right)^2}{\left(1 + \frac{\gamma G}{2} \bar{X}_\alpha\right)} \left[1 + \frac{\frac{\gamma G}{2} \bar{X}_\alpha}{2\left(1 + \frac{\gamma G}{2} \bar{X}_\alpha\right)} \right]^2 \right\} \frac{P_\alpha}{P_\infty} \tag{6}$$

which is valid for weak interaction with $\bar{X}_\alpha < 1$.

For strong interactions with $\bar{X}_\alpha \gg 1$, the following equation presented in Ref. 37 is valid

$$\frac{P}{P_\infty} \cong \left[0.83 + \frac{3}{4} \sqrt{\frac{\gamma(\gamma + 1)}{2}} G \bar{X}_\alpha \right] \frac{P_\alpha}{P_\infty} \tag{7}$$

where the bracketed expression

$$\left[\quad \right] \geq 1$$

If α = 0, freestream conditions are to be used. Expressions for the "G" parameter are:

$$G = 1.7208 \frac{\gamma - 1}{2} \left(\frac{Tw}{Tt} + 0.3859 \right), \text{for Pr} = 1$$

$$G = 1.648 \frac{\gamma - 1}{2} \left(\frac{Tw}{Ta\ w} + 0.352 \right), \text{for Pr} = 0.725$$

These equations are compared with experimental data in Figure 16, taken from Reference 37, showing the appropriate regions of applicability.

Combined Effects of Incidence and Displacement

An alternate procedure is to define a total similarity parameter K_t which combines the angle of attack effect and the flow displacement effect of the boundary layer. This method is valid if the total deflection angle is less than 20 degrees.

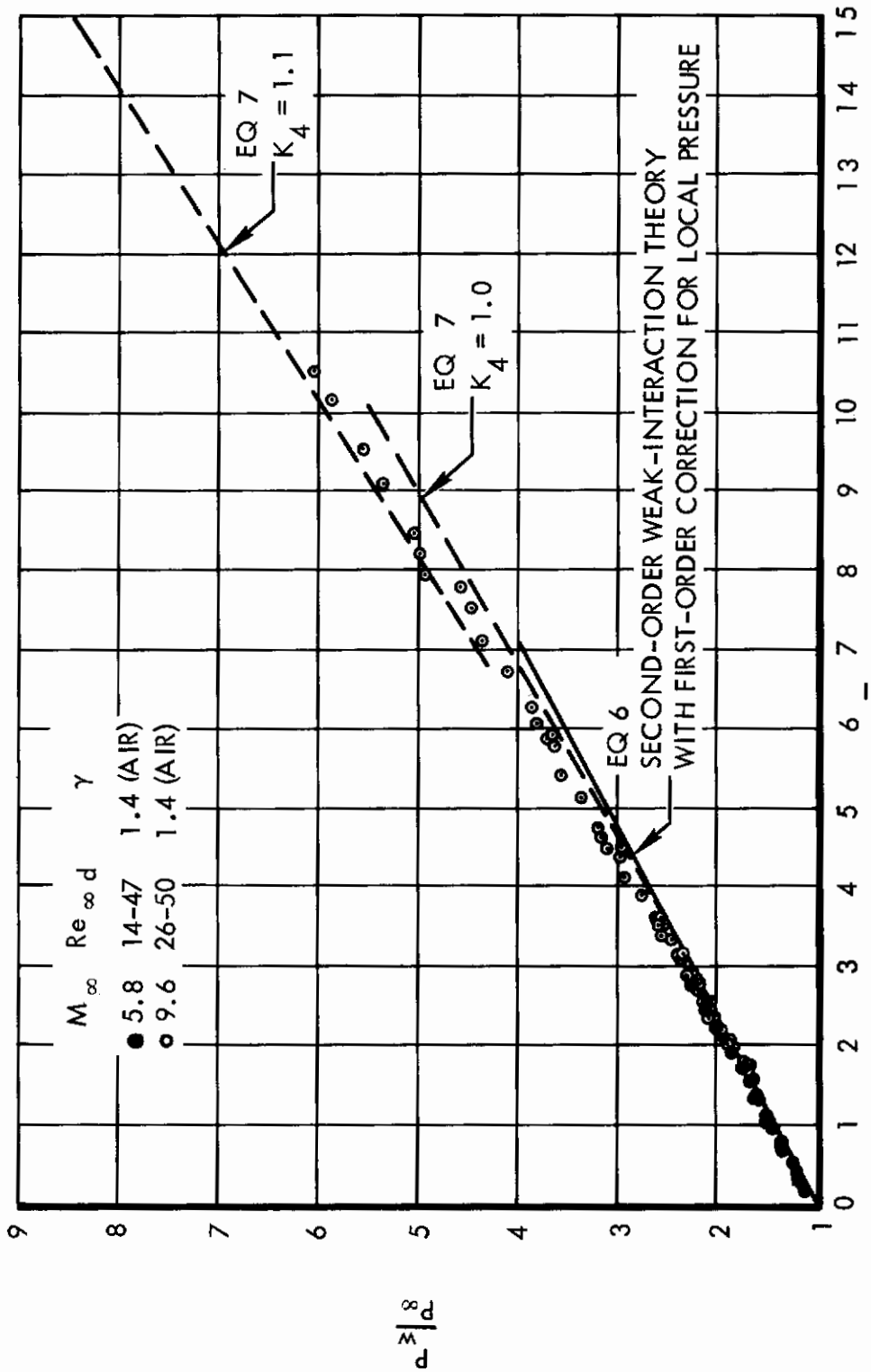

Figure 16. Various Theories for Predicting Boundary-Layer Displacement Effects on a Flat Plate in Air and Comparison with Experiment (Reference 37)

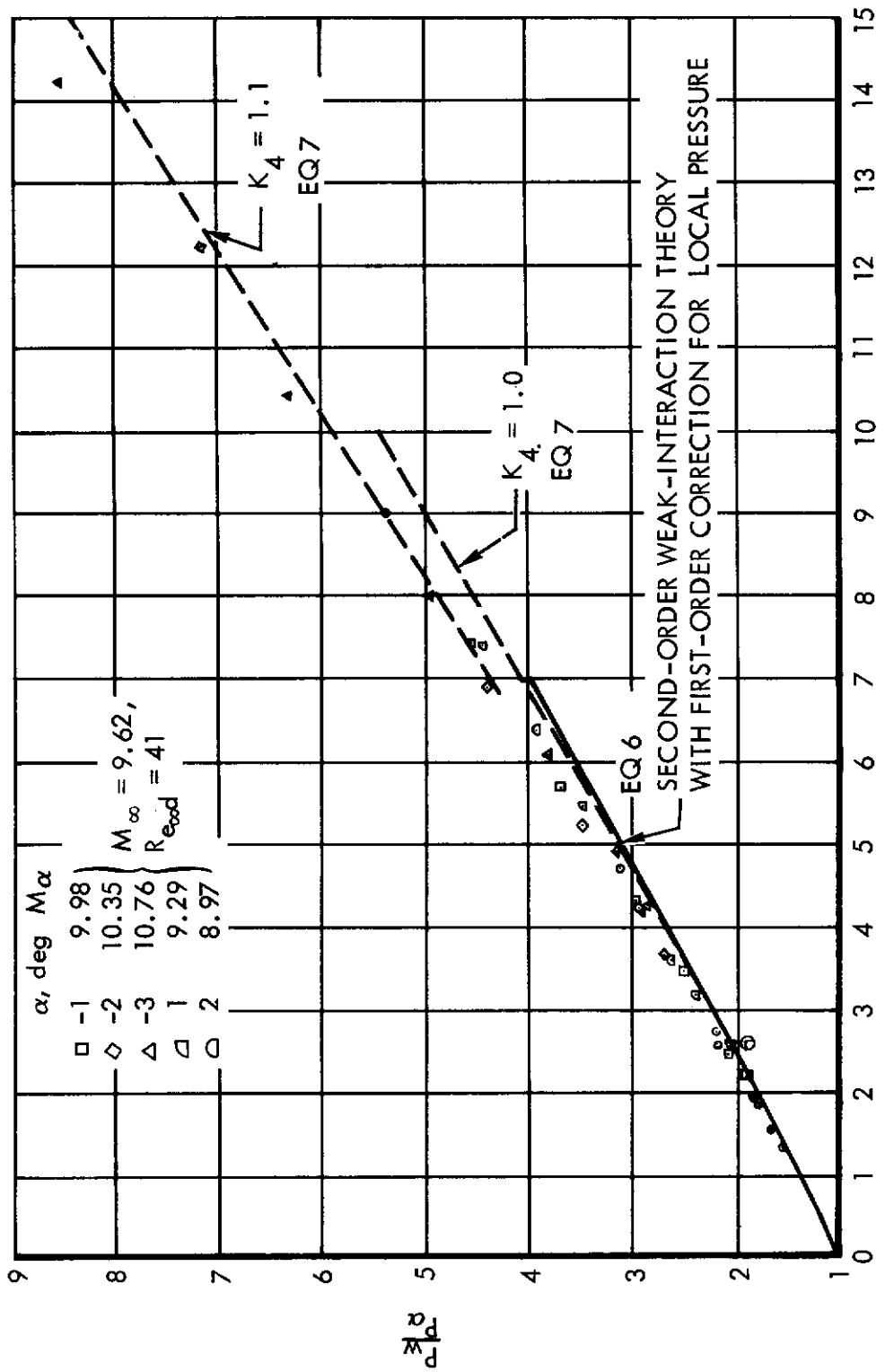

(b) $\alpha \neq 0$.

Figure 16. Various Theories for Predicting Boundary-Layer Displacement Effects on a Flat Plate in Air and Comparison with Experiment (Reference 37) (Concluded)

Thus:

$$K_t = K_{\theta_B} + (K_\infty)_\delta = M_\infty \theta_B + M_\infty \left(\frac{d\delta^*}{dx}\right)$$

$$K_{\infty_\delta} = K_\delta \frac{M_\infty}{M_\alpha}$$

where K_δ is determined as before. For $K_t > 0$, the tangent wedge formula may be used. Flat plates at small negative angles of attack may still show positive pressure coefficients on the expansion surface because the viscous effects may be such as to give net positive flow deflections. This effect accounts for positive pressure coefficients noted in recent test data on surfaces which would normally be considered to be in expansion flow (Ref. 38).

For such surfaces, Newtonian Theory would predict $C_p = 0$ and a Prandtl-Meyer expansion would indicate $C_p < 0$.

When the expansion angle is greater than the displacement effect, $K_t < 0$, the applicable expression for the hypersonic similarity pressure distribution is (Ref. 39):

$$\frac{P}{P_\infty} = \left[1 + \frac{(\gamma - 1)}{2} K_t\right]^{\frac{2}{\gamma-1}} \qquad (8)$$

$$\text{For } -\frac{2}{\gamma-1} \leq K_t \leq 0$$

The blast wave effect from leading edge bluntness is assumed to be additive (Figure 11).

From the form of the above equation, note that as long as K_t is negative, the viscous effect does not dominate. In this case one has a number less than one, raised to a large power. The result is a pressure ratio $\frac{P}{P_\infty}$ which is less than unity.

Actually these results for expansion surfaces are less reliable than the results for compression surfaces. No satisfactory results are available for cases in which $K_t \leq -\frac{2}{\gamma-1}$.

Viscous effects were found to be negligible on compression surfaces at large angles of attack, especially at large downstream distances. That is, the previous expressions for pressure distribution reduce to:

$$\frac{P}{P_\infty} = \frac{P_\alpha}{P_\infty} + \frac{P_b}{P_\infty}$$

For large x/d, the blast wave effects diminish and P/P_∞ approaches $\frac{P_\alpha}{P_\infty}$, the oblique-shock pressure ratio. The oblique shock pressure ratio may be determined from Reference 36.

Relative Magnitude of Bluntness Effects and Viscous Effects

Most theoretical investigations of the interaction between the boundary layer and the external flow are based on the assumption that the leading edge or the nose is infinitely sharp. Actual vehicles, however, cannot tolerate sharp edges since some blunting must be provided in order to control the heating rates. The relative magnitude of the inviscid pressure generated by a blunt forward part as compared with the self-induced pressure due to viscous interaction is discussed in the following paragraphs.

Viscous effects will outweigh any inviscid effects in the blunt region when the Reynolds number based on a dimension indicating the bluntness of a body is of the order of 100. When the Reynolds number is not too small, the inviscid pressure field will dominate the forward part of the body and control the growth of the boundary layer, and the viscous effects will be negligible. Nevertheless, far downstream where the inviscid overpressure is small, viscous interaction might show up.

The distance at which the relative magnitude of the inviscid pressure is comparable with the pressure due to the interaction for a body of revolution with nose diameter d **is given by (Reference 32):**

$$Re_{\infty_d} \sim \frac{M_\infty^4 C_\infty}{\bar{X}_{\infty_d}}$$

With an interaction parameter for strong interaction assumed to be $\bar{X} \geq 4$ and with $C_\infty = O(1)$, the self-induced pressure becomes significant when

$$Re_{\infty_d} \sim \frac{M_\infty^4}{4}$$

For $Re_{\infty_d} \ll M_\infty^4$, one can expect a strong interaction region fully developed at the nose, and an insignificant effect of the blunt nose. If $Re_{\infty_d} \sim M_\infty^4$ no strong interactions are noticeable at the nose. As Re_{∞_d} increases, the inviscid effects spread downstream away from the blunt region, but the interaction might still be important on the slender part of the body if the inviscid overpressure $(P-P_\infty)$ is small, particularly because of a rapid inviscid pressure decay on axi-symmetric bodies. Eventually, at high angles of attack, the inviscid overpressure is so large that viscous-induced pressure is negligible.

Table 1 (Reference 40) shows test flow conditions for blunted elliptical cones for a Mach number range from 5 to 36. Calculations show that for $M_\infty < 10$, no strong interaction can exist at the nose. Since $\bar{X} < 1$, only weak interaction might be effective on the slender part of the body, and at $M_\infty = 5$ these effects are probably negligible.

For $M > 14$, where $\bar{X} >> 4$, one probably has strong interaction at the nose.

The expression to be used in a practical application for the pressure distribution calculation will depend on the prevalent flow conditions. Another parameter for estimating the relative magnitude of bluntness viscous effects has been established in Reference 37. If

$$\Gamma = \frac{G}{\sqrt{\frac{C_D \, Re_{\infty_d}}{M_\infty^3 \, C}}} > \frac{2}{3},$$

the leading edge bluntness effects are negligible.

In the case of $\Gamma < 1/10$ the viscous contribution is small to negligible compared with the blunt, leading edge effects on pressure. For $\Gamma < 1/2$ both the bluntness effects and the viscous effects should be considered. To compare the different formulations, a number of experimental distributions from Reference 41 were used(Figures 11 to 13). The solution containing self-induced effects should be used only at $\bar{X}_\alpha \gg 1$. It is primarily useful on leeward surfaces, where extensive viscous interaction may be expected, and for high Mach numbers ($M_\infty > 14$). In general the test Reynolds number was too high to induce substantial viscous pressures. The inviscid solution should suffice under most conditions for calculating P_o/P_∞. The viscous pressure increment is most noticeable near the nose where $\bar{X}$ is larger and the boundary-layer slope is steeper. A calculation at the hingeline should be undertaken to determine the significance of the viscous pressure contribution. Figures 11, 12, and 13 show the decreasing importance of leading-edge and viscous effects at large downstream distances ($x/d > 16$). At these downstream positions the inviscid sharp wedge solution is the most accurate for $\alpha > 0$.. Figure 12 shows that the inviscid solution, $P/P_\infty = P_\alpha/P_\infty + P_b/P_\infty$, is sufficient for $\alpha = +10^\circ$ and -10° for all $x/d > 1$.

TABLE I

LOCAL FLOW PROPERTIES

Actual vehicle configurations can be represented in many cases by simple elements like wedges or cones.

Briefly, it can be said that for two-dimensional bodies with small bluntness and negligible viscous effects, the local pressure can be expressed as a first approximation by the pressure behind an oblique shock wave (Reference 36). On bodies with blunted leading edge, pressure near the leading edge will be higher than that predicted by the oblique shock theory and may asymptotically approach the oblique shock value far downstream from the nose.

For a point relatively near a blunt leading edge, the shock loss theory of Moeckel (Reference 42) may be used to describe the properties of the outer flow. The static pressure ratio P_α/P_∞ must be known beforehand, whether from tangent wedge calculations, or blast wave theory, etc. It is assumed that the streamlines of interest pass through the leading-edge bow shock, and then expand isentropically to the known P_α/P_∞. The leading-edge shock plane has its normal inclined to the flow at an angle which is approximately equal to the sweep angle Λ. To find the Mach number $M_{\alpha_{SL}}$ corresponding to P_α, one first notes the expression for the ratio of total to local pressure for isentropic expansion behind the shock ($\gamma=1.4$):

$$\frac{P_{t_2}}{P_\alpha} = \left(1 + \frac{M^2_{\alpha_{SL}}}{5}\right)^{\frac{7}{2}}$$

The total pressure behind the shock and the static pressure ahead of the shock are related by:

$$\frac{P_{t_2}}{P_\infty} = \left[\frac{6\, M^2_\infty \cos^2\Lambda\,(M^2_\infty + 5)}{5\,(M^2_\infty \cos^2\Lambda + 5)}\right]^{\frac{7}{2}} \left(\frac{6}{7\, M^2_\infty \cos^2\Lambda - 1}\right)^{\frac{5}{2}}$$

Solving these equations for $M_{\alpha_{SL}}$, one obtains:

$$M_{\alpha_{SL}} = \left[\left(\frac{P_\infty}{P_\alpha}\right)^{\frac{2}{7}} \left(\frac{6}{7\, M^2_\infty \cos^2\Lambda - 1}\right)^{\frac{5}{7}} \frac{6\, M^2_\infty \cos^2\Lambda\,(M^2_\infty + 5)}{M^2_\infty \cos^2\Lambda + 5} - 5\right]^{\frac{1}{2}} \qquad (9)$$

T_t for isentropic flow is

$$\frac{T_t}{T_\alpha} = 1 + 0.2\, M^2_{\alpha_{SL}}$$

Since T_t is constant for an ideal gas in adiabatic flow, one can calculate the local (α) quantities.

Specifically, the Reynolds number ratio becomes:

$$\frac{\frac{\rho_\alpha U_\alpha}{\mu_\alpha}}{\frac{\rho_\infty U_\infty}{\mu_\infty}} = \frac{(Re/in)_\alpha}{(Re/in)_\infty} = \left(\frac{P_\alpha}{P_\infty}\frac{T_\infty}{T_\alpha}\right) \cdot \left(\frac{M_\alpha}{M_\infty}\frac{\sqrt{T_\alpha}}{\sqrt{T_\infty}}\right) \cdot \left(\left(\frac{T_\infty}{T_\alpha}\right)^{\frac{3}{2}} \frac{T_\infty + 198.6}{T_\alpha + 198.6}\right)$$

$$\frac{(Re/in)_\alpha}{(Re/in)_\infty} = \frac{P_\alpha}{P_\infty}\left[\frac{1 + 0.2\,M_\alpha^2}{1 + 0.2\,M_\infty^2}\right]^2 \frac{M_\alpha}{M_\infty}\left[\frac{\frac{T_\infty\,(1 + 0.2\,M_\infty^2)}{1 + 0.2\,M_\alpha^2} + 198.6}{T_\infty + 198.6}\right] \qquad (10)$$

In this expression the perfect gas equation, the relationship between local and total temperatures, the proportionality of sound speed to square root of static temperature, and the Sutherland viscosity law have been employed.

For a point considered to be relatively far from leading edge bluntness, oblique shock theory can be used to obtain the properties of the outer flow when P_α/P_∞ is known beforehand. It is implied that any contributions to static pressure on the body, such as from viscous interaction or even bluntness effects, can be represented as an effective thickening of the body. Then, the solution for Mach number behind the corresponding oblique shock is:

$$M_{\alpha_{OS}} = \left[\frac{M_\infty^2\left(6\frac{P_\alpha}{P_\infty} + 1\right) - 5\left(\left(\frac{P_\alpha}{P_\infty}\right)^2 - 1\right)}{\frac{P_\alpha}{P_\infty}\left(\frac{P_\alpha}{P_\infty} + 6\right)}\right]^{\frac{1}{2}} \qquad (11)$$

As with the shock-loss method, all local properties are now known. Reynolds number ratio may be calculated either by equation 10 or by

$$(Re/in)_\alpha = (Re/in)_\infty \frac{M_\alpha}{M_\infty}\frac{P_\alpha}{P_\infty}\left(\frac{T_\infty}{T_\alpha}\right)^{\frac{1}{2}}\frac{\mu_\infty}{\mu_\alpha} \qquad (12)$$

where any appropriate expression for the viscosity ratio may be inserted (for instance the Sutherland law).

When bluntness is not zero, the actual M_α will generally turn out to be somewhere between $M_{\alpha_{SL}}$ and $M_{\alpha_{OS}}$. From the pressure distributions that were examined in deriving the correlations given in this report, it was possible to obtain good estimates for M_α values on surfaces with leading edges of various bluntness dimensions. The following formula for local Mach number is suggested (Figure 17.)

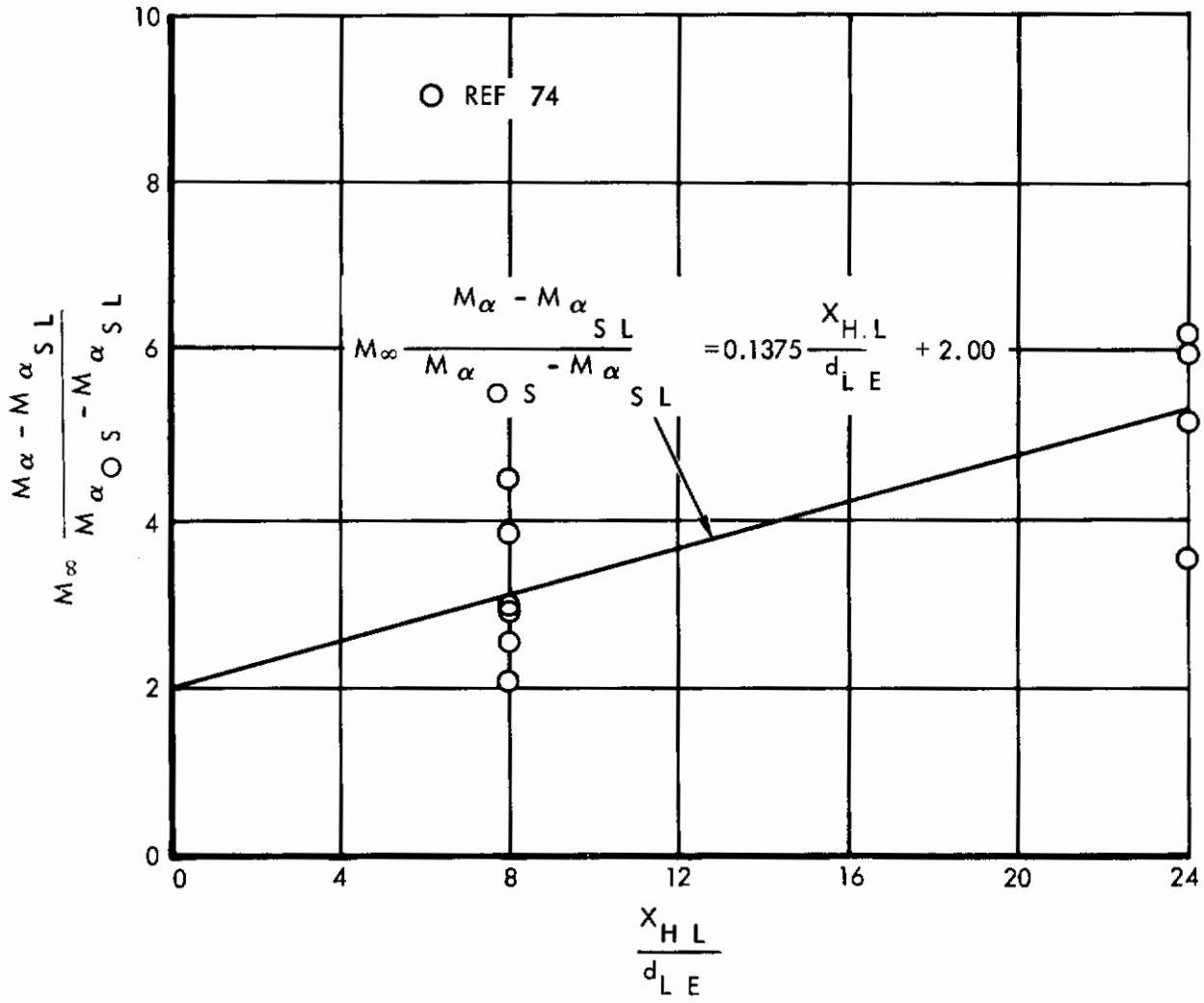

Figure 17. Bluntness Effect on Local Mach Number, M_α

$$M_{\alpha} = \frac{1}{M_{\infty}} \left[M_{\alpha_{OS}} - M_{\alpha_{SL}} \right] \left[.1375 \frac{X_{HL}}{d_{LE}} + 2.00 \right] + M_{\alpha_{SL}}, \text{ for } \frac{.1375 \frac{X_{HL}}{d_{LE}} + 2.00}{M_{\infty}} \leq 1. \quad (13)$$

And $M_{\alpha} = M_{\alpha_{OS}}$ for $\dfrac{.1375 \frac{X_{HL}}{d_{LE}} + 2.00}{M_{\infty}} > 1.$

BOUNDARY LAYER THICKNESS

The thickness of a boundary layer is an important viscous flow parameter frequently used as a physical scale in investigating viscous flow phenomena.

The correlations of distance parameters describing the pressure distribution in separated flow developed in the following sections are expressed in terms of the boundary layer thickness. A simple expression for boundary layer thickness was developed by modifying the classical Blasius laminar formula: the fluid properties used in calculating the Reynolds number are based on the reference temperature, T*. For the blunt leading edge case, of if large viscous-induced pressure gradients are present, the boundary layer thickness is reduced by the factor $\left(\frac{P_w}{P_{\alpha}}\right)^{-\frac{1}{2}}$ (Reference 43).

The following equations for the boundary layer are suggested:

$$\delta = \frac{5.2}{\sqrt{\frac{P_w}{P_{\alpha}}}} \sqrt{\frac{x\,d}{Re^{*}_{\alpha d}}}, \quad \text{for blunt leading edge} \quad (14)$$

and

$$\delta = \frac{5.2\,x}{\sqrt{\frac{P_w}{P_{\alpha}} Re^{*}_{\alpha x}}}, \quad \text{for sharp leading edge} \quad (15)$$

where

$$\frac{Re^{*}_{\alpha}}{x} = \frac{Re_{\alpha}}{x} \left(\frac{T_{\alpha}}{T^{*}}\right) \left(\frac{\mu_{\alpha}}{\mu^{*}}\right) \approx \frac{Re_{\alpha}}{x} \left(\frac{T_{\alpha}}{T^{*}}\right)^{1.76}$$

and

$$\frac{T^{*}}{T_{\alpha}} = .28 + .5 \frac{T_w}{T_{\alpha}} + .22 \frac{T_{aw}}{T_{\alpha}} \quad \text{(Ref 44)}$$

with

$$\frac{T_{aw}}{T_\alpha} = 1 + \frac{\gamma - 1}{2} M_\alpha^2 \, Pr^{\frac{1}{2}}$$

The predicted values of boundary layer thickness are compared in Figure 18 with available experimental measurements from References 34, 45, and 46, assuming $T_{aw} = T_w$ for tests. It was found that for $M_\infty < 6$ the pressure ratio factor usually can be neglected. The boundary layer thickness for turbulent flow was expressed by a modification of the classical formula from Reference 47

$$\delta = \frac{0.154\ x}{\left[(Re_{\alpha x})\left(\frac{T_\alpha}{T^*}\right)\left(\frac{\mu_\alpha}{\mu^*}\right)\right]^{1/7}} = \frac{0.154\ x}{\left[(Re_{\alpha x})\left(\frac{T_\alpha}{T^*}\right)^{1.67}\right]^{1/7}} \qquad (16)$$

where, for turbulent flow, in the expression for $\frac{T^*}{T_\alpha}$,

$$\frac{T_{aw}}{T_\alpha} = 1 + \frac{(\gamma - 1)}{2} M_\alpha^2 \, Pr^{\frac{1}{3}}$$

and

$$\mu \sim T^{0.76}$$

Figure 19 presents a comparison of equation 16 with test data from Reference 48. Due to the lack of experimental data no effects of pressure gradients for turbulent flow were determined.

REAL GAS EFFECTS

A blunt object flying through the atmosphere at hypersonic speeds experiences severe heating from the air which passes through the standing bow shock. Part of the kinetic energy of the flowing gas is transformed into thermal energy. This alters the behavior of the air, which can no longer be considered a perfect medium. At high enough velocities, higher degrees-of-freedom of gas species are excited. Vibration, dissociation, and ionization of gas particles may become important. The usual flow processes, coupled with the rate processes, are responsible for these real gas effects.

For increasing temperature, significant quantities of energy are absorbed by the vibrational mode. A molecule can absorb only a certain maximum of energy in this form before its bond is broken altogether (dissociation). Another real gas phenomenon is the absorption of energy by electrons. Complete detachment of an electron is called ionization.

From the explanation above, it is seen that "real gas effects" cause reductions in kinetic temperatures by diverting energy into other energy modes. This is very important in reducing recovery temperatures for high speed vehicles to tolerable levels.

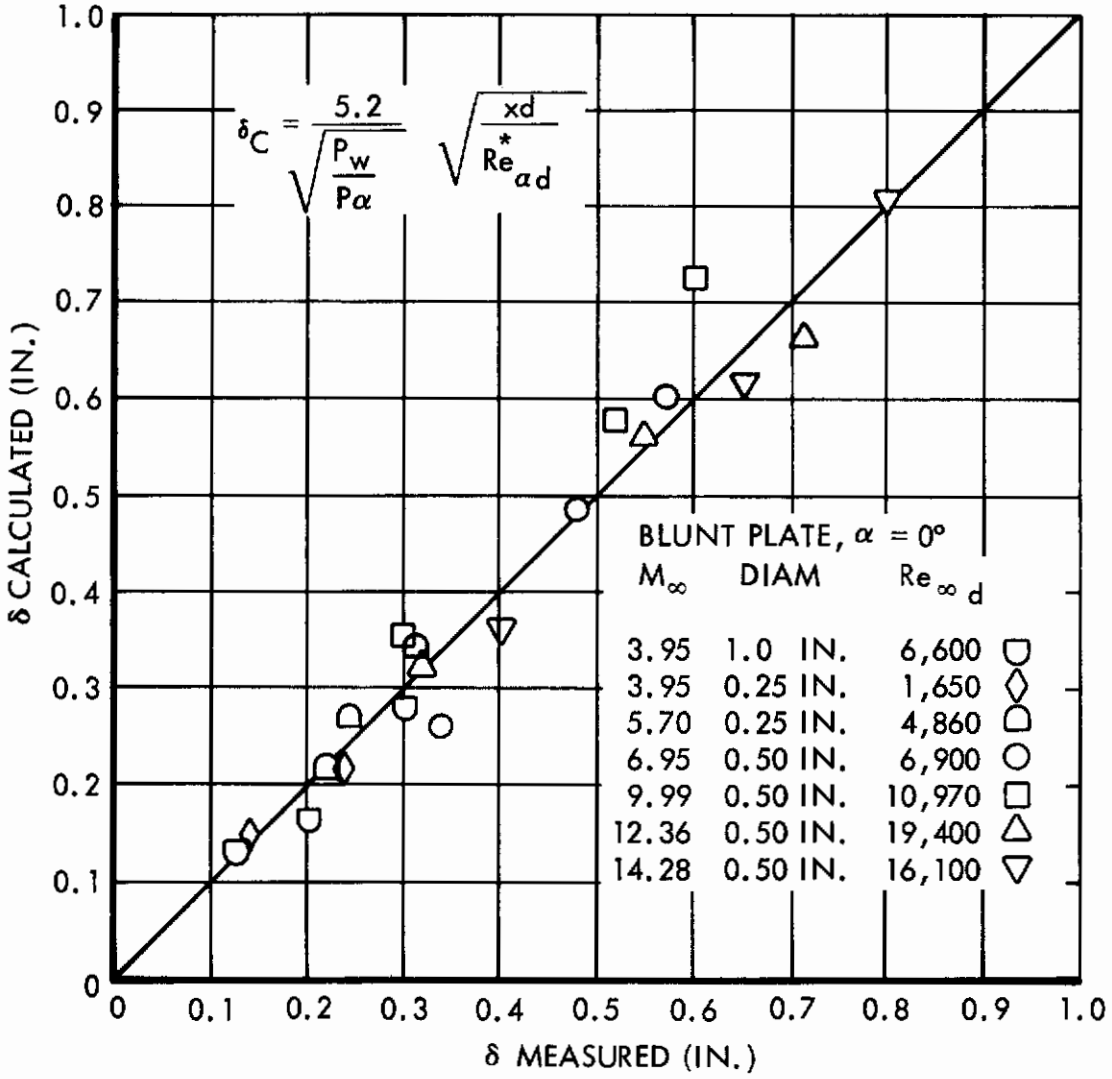

Figure 18. Correlation of Boundary Layer Thickness for Laminar Flow

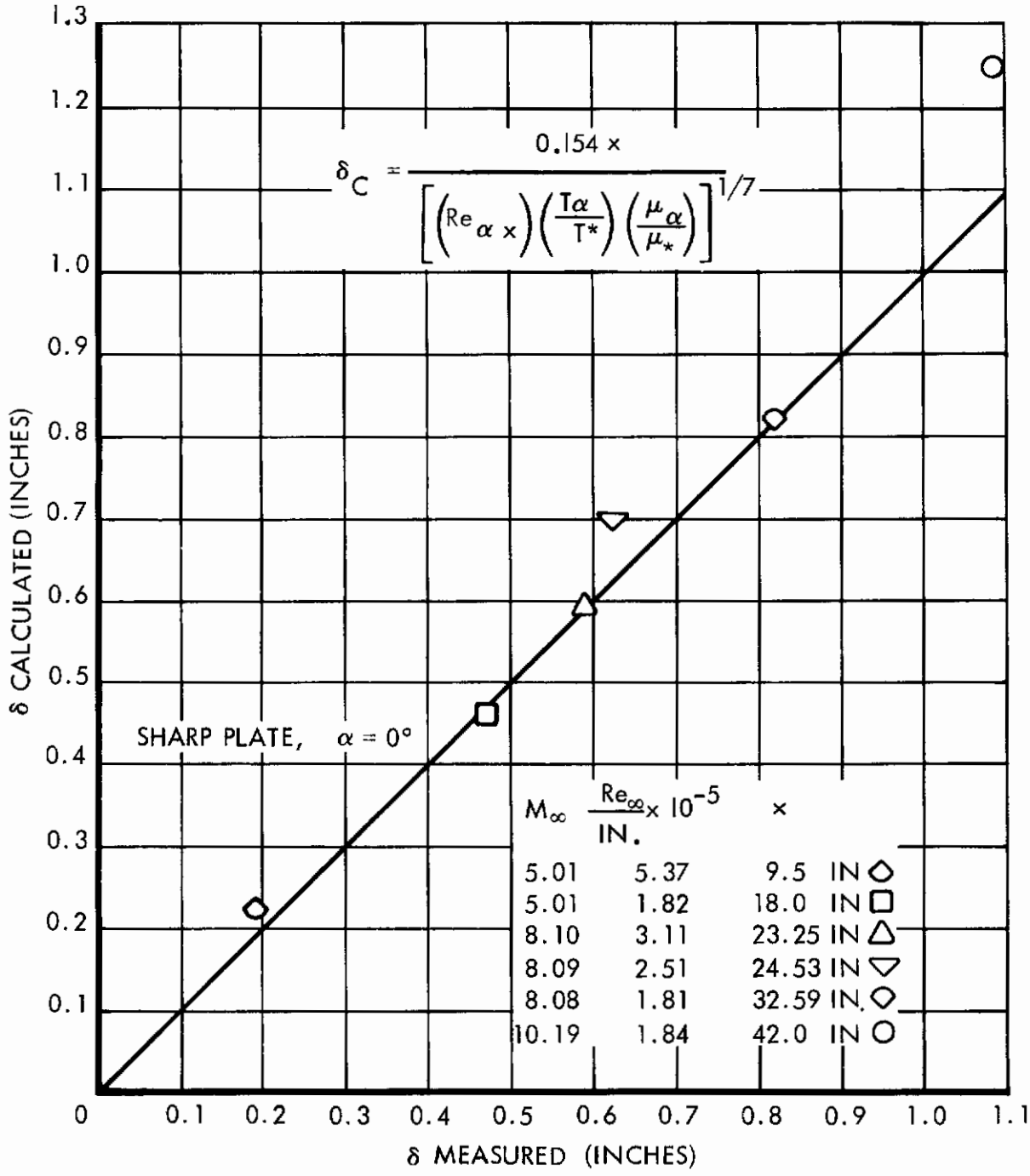

Figure 19. Correlation of Boundary Layer Thickness for Turbulent Flow

The adjustment from one equilibrium state to another does not occur instantaneously. An average required number of molecular collisions can be identified for each energy mode. Therefore, adjustment times or relaxation times vary in an inverse manner with static pressure. A high-speed vehicle in the upper atmosphere may have relaxation times which are considerably greater than the time required for a typical particle to traverse the body. In this case, the flow is nearly "frozen" rather than in equilibrium, and very little energy exchange exists. This may be treated as a perfect gas flow with a constant isentropic exponent corresponding to the frozen condition.

When the ratio of the relaxation time to flow time is of the order of unity, non-equilibrium conditions might exist. If this ratio is small, equilibrium flow prevails.

Considering compression by a wedge, frozen (or non-equilibrium) flow involves higher temperature, higher sound speed, higher pressure, and lower Mach number than equilibrium flow. Figures 20 and 21 compare frozen, equilibrium, and perfect gas pressures resulting from wedge shocks for various typical flight conditions.

It should be noted that the perfect gas and frozen gas assumptions give approximately the same results, namely higher pressures and temperatures than for equilibrium flow. The difference between frozen flow and equilibrium flow conditions increases with velocity and wedge angle. At an altitude of 200,000 ft and a wedge angle δ = 25 deg, the real gas effects are noticeable at velocity $u_\infty \geq 8000$ ft/sec. Figure 22 shows the altitude effects on oblique shock pressure ratio for a wedge angle of 25 degrees. It can be seen that real gas effects become important above 100,000 ft for velocities above 11,000 ft/sec. The equilibrium values are based on results from Reference 49.

For a long enough vehicle, one would observe a streamwise decay of pressure from the frozen to the equilibrium value. Such a pressure distribution is similar to the pattern that would occur in the flow of a perfect gas over a slightly blunted wedge. Therefore, it is not surprising that the shock shapes for the two problems are also similar, i.e., curved.

For a blunt body, frozen or non-equilibrium flow results in higher temperatures. The shock standoff distance is increased. Static pressure, however, is a little below the equilibrium value. Figure 23 indicates the real gas flow regimes on a velocity-altitude plot, for blunted surfaces one and ten feet in length. It can be seen that flow conditions and corresponding reaction rates for the assumed gas model depend on flight path and body size. For a one-foot body, non-equilibrium conditions may exist at a velocity of 10,000 ft/sec above an altitude of 170,000 ft, while for a ten-foot body, this altitude increases to about 210,000 ft. This is because the flow time on a larger body is increased and the gas particles have more time for adjustment.

It would be consistent with the work so far on pre-separation flow properties to advise the use of either perfect gas or equilibrium relations for each problem, depending on whether perfect or equilibrium flow is a closer

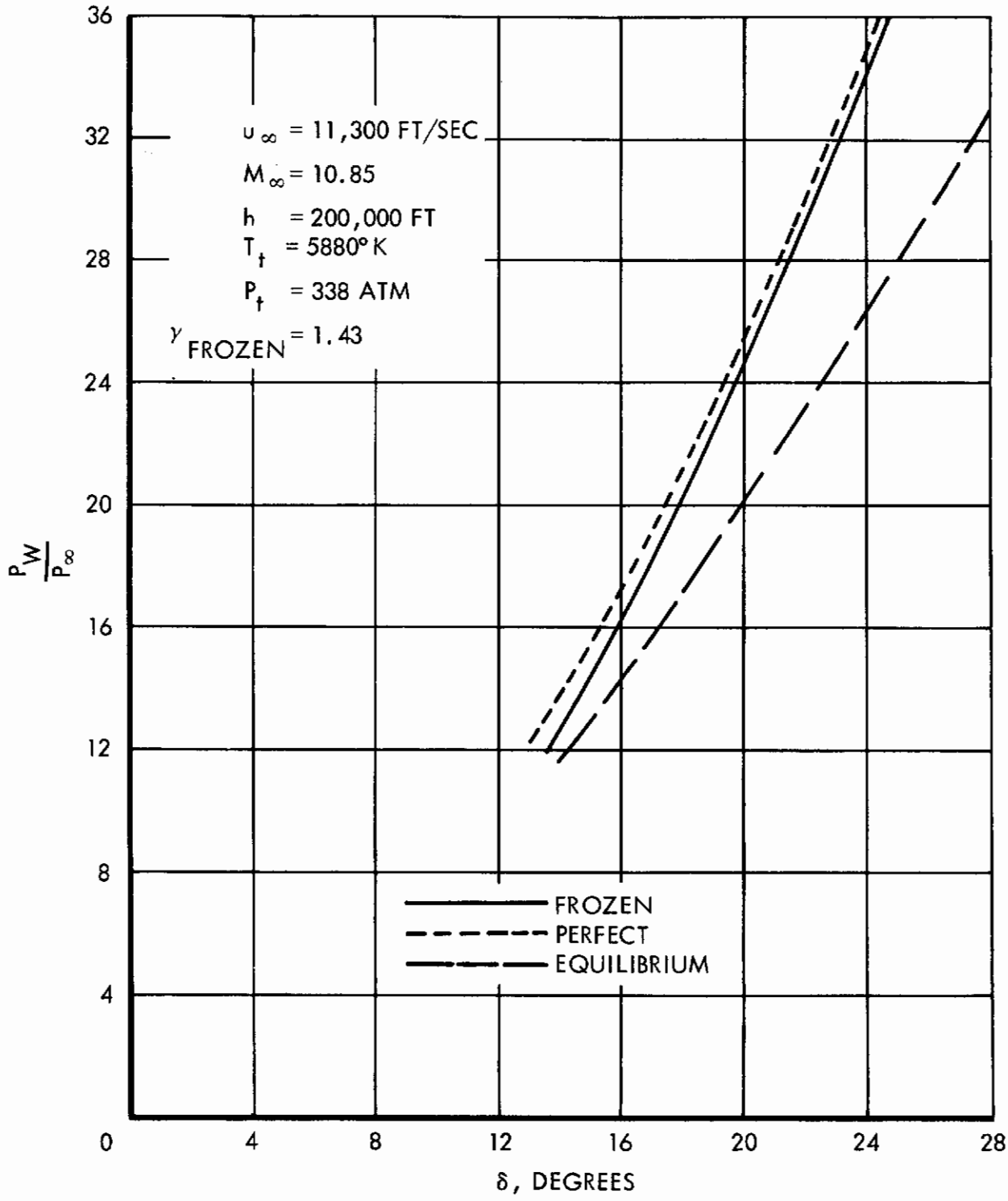

Figure 20. Oblique Shock Pressure Ratio P_W/P_∞ vs δ for Equilibrium, Perfect, and Frozen Gas Flow

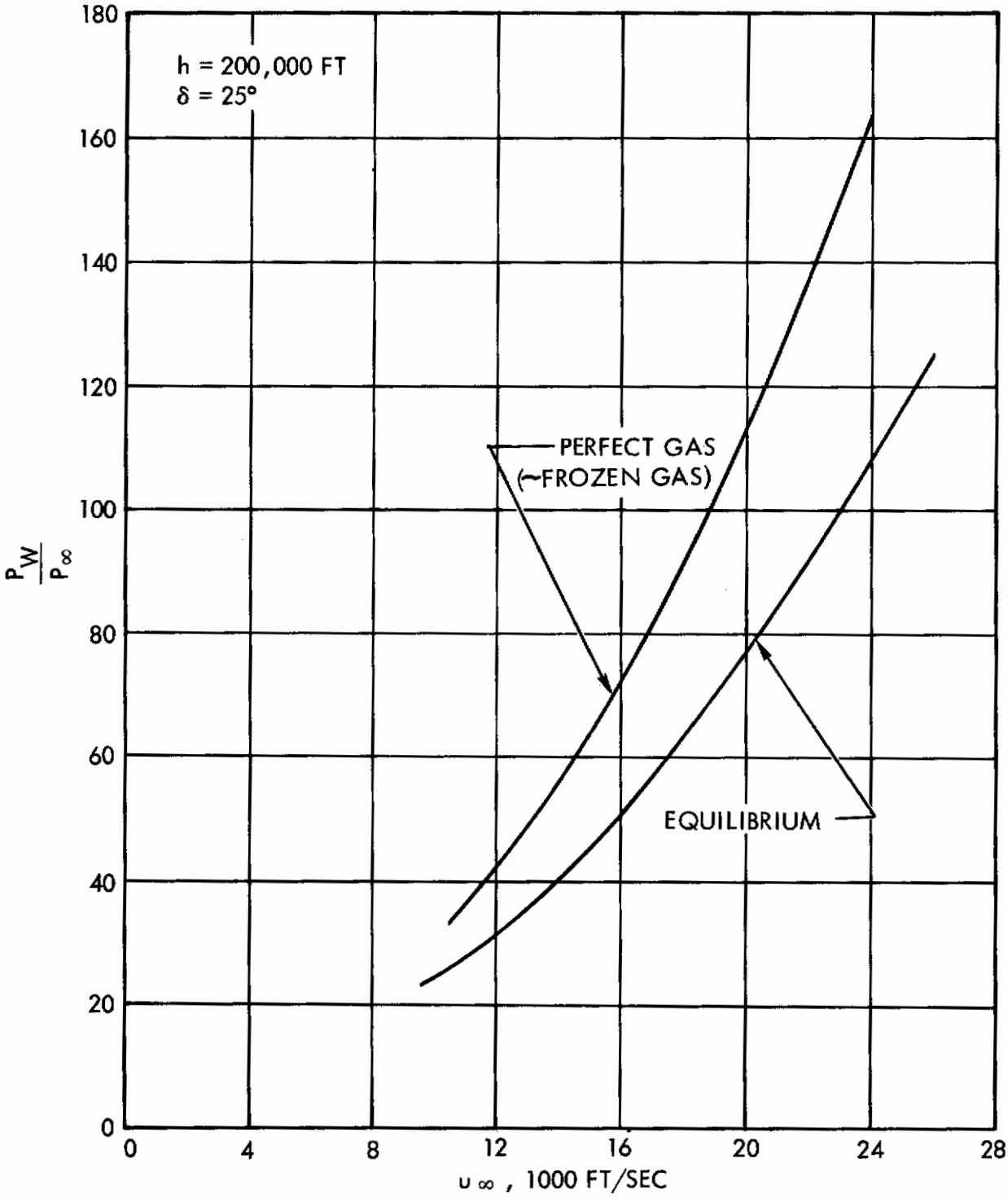

Figure 21. Oblique Shock Pressure Ratio vs Flight Velocity

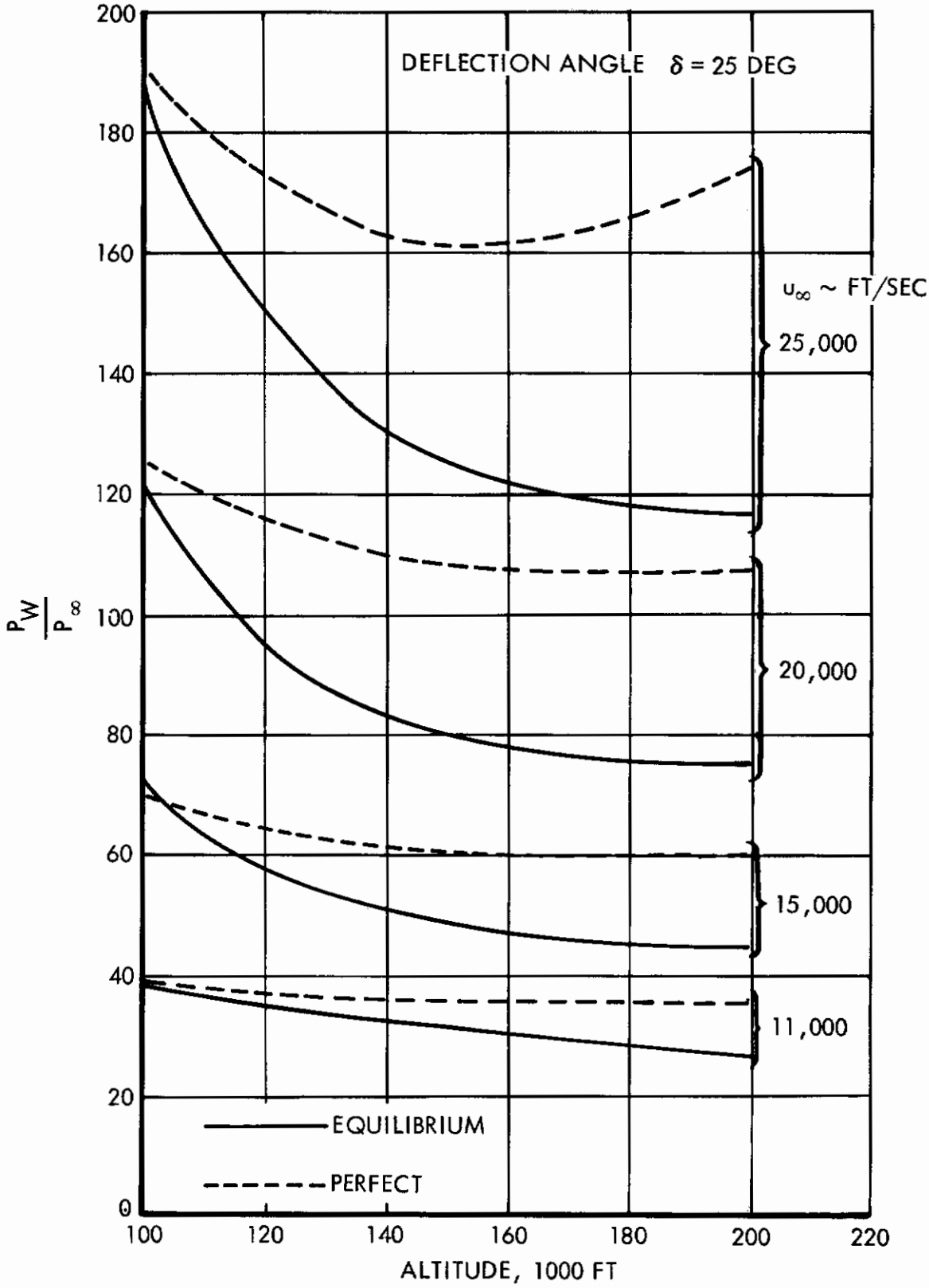

Figure 22. Oblique Shock Pressure Ratio for Equilibrium Flow and Perfect Gas Flow

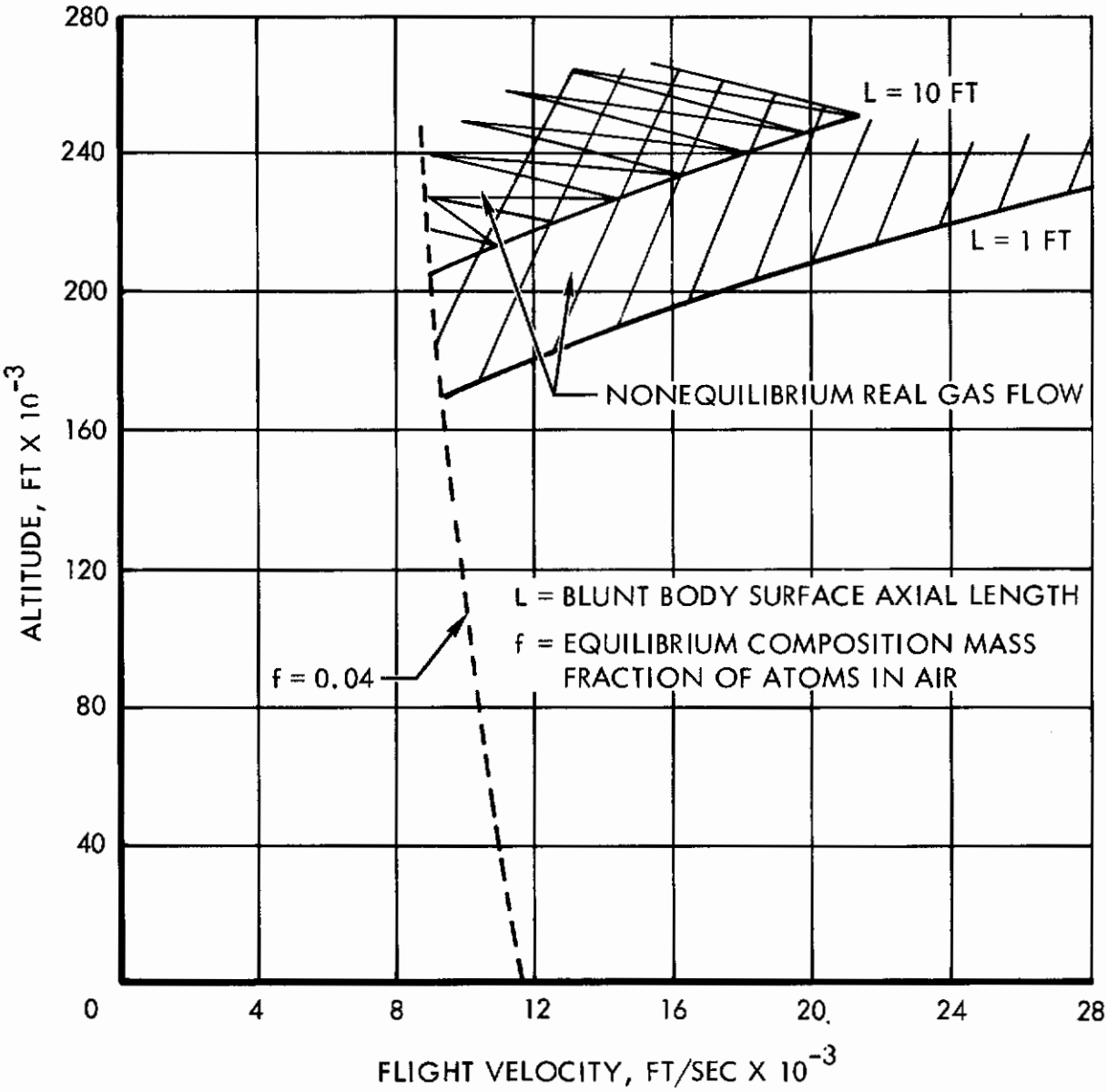

Figure 23. Spectrum of Flight Conditions Including Nonequilibrium Real Gas Regime (Reference 49)

approximation. It should be remembered that the differences between perfect and equilibrium flow values decrease as deflection angles decrease and as the altitude decreases.

An accounting of real gas effects is given in Reference 50. Included therein are some aspects of hypersonic flow and associated real gas effects, test facilities, some discussion of relaxation times, some results for real gas wedge flows in the atmosphere, a description of blunt body flow, and a relatively up-to-date bibliography.

Section IV

SEMI-EMPIRICAL CORRELATIONS FOR SEPARATED FLOW

In this section, the equations to be used for the prediction of separated flow pressure distributions are developed. The behavior of the separated flow depends strongly on whether the boundary layer is laminar or turbulent; therefore, the discussion begins with an examination of the transition phenomenon. A criterion for establishing the location of transition is presented. The next step is to determine the minimum pressure rise required to cause flow separation, and incipient separation criteria for both the laminar and turbulent cases are given. Finally, correlation expressions are presented for the parameters necessary for the construction of the complete pressure distributions for both laminar and turbulent separation.

TRANSITION FROM LAMINAR TO TURBULENT FLOW

An investigation of transition phenomena was presented by Deem and Murphy in Reference 51. They collected large quantities of experimental data concerning transition of boundary layers in high speed flows, and derived an empirical expression for the prediction of transition distance. The higher Mach number data were taken mainly from the experiments of that paper, and from the measurements of References 52, 53, and 54. The scatter of the collected data is significant; nevertheless, there is reason to believe that the resulting expression is useful for prediction of transition. The complexity of the phenomenon is shown by the fact that the Deem-Murphy equation involves unit Reynolds number to a fractional power. There is a strong Mach number effect, with increasing Mach number tending to increase stability of the boundary layer for $M > 3$. A crossflow factor must be included when there is sweep. Any effects of wall temperature were noted to be surprisingly slight.

Certain comments concerning the final results of Deem and Murphy in Reference 51 are in order. That paper is particularly concerned with the effect of leading edge bluntness. Regimes of bluntness are defined and, in fact, iteration is required to get answers. Furthermore, the expression for very large bluntness includes a combination of free-stream and local quantities. It is believed, however, that the transition distance of the boundary layer should depend only upon the flow properties which it senses during its development.

Therefore, the following equation for transition distance is recommended:

$$X_t(\text{feet}) = \frac{5.38\times10^{2}+1.94\times10^{2}\left|M_{\alpha}-3\right|^{\frac{3}{2}}(\cos\Lambda)^{\frac{1}{2}}}{\left[(\text{Re}/\text{in.})_{\alpha}\right]^{.6}} \qquad (17)$$

In this expression α - subscript properties are the local quantities. These local quantities are to be calculated as well as possible through the use of any available methods, such as tangent wedge, blast wave, or the Moeckel shock loss theory (Reference 42) when leading edge bluntness is comparatively large. (A more detailed discussion of local flow properties is presented in Section III.) The Deem-Murphy result and the above result become identical when there is no bluntness and angle of attack is zero.

The coordinate X_o which identifies the beginning of the interaction is not known a priori. However, for vehicles of practical dimensions, the percentage difference between X_o and X_{HL} will usually be rather small. Therefore, it can be assumed that Equation (17) predicts a turbulent boundary layer if $X_t < X_{HL}$ or $\text{Re}_{\alpha X_t} < \text{Re}_{\alpha X_{HL}}$.

To indicate the validity of Equation (17) for prediction of the state of the boundary layer at the hinge line (or shock impingement point), Figure 24 has been constructed. In this plot, the spectra of data employed in devising the interaction length and pressure level correlations for both the laminar and turbulent cases have been collected and compared with Equation (17). The Reynolds number versus Mach number plot seems to be appropriate for delineating the laminar and turbulent regimes, but in this case there is no single dividing line between laminar and turbulent; an X_{HL} (or alternatively, an $\text{Re}_{\alpha}/\text{in.}$) must be specified because Equation (17) contains unit Reynolds number. The procedure for constructing the X_{HL} isolines in Figure 24 was to select X_{HL} and $\text{Re}_{\alpha X_{HL}}$ (and therefore $\text{Re}_{\alpha}/\text{in.}$), and solve for M_{α} from Equation (17) for $\Lambda = 0$ and $M_{\alpha} > 3$. In this work most interest is in $M_{\alpha} > 3$. It is seen from the plot that the Deem-Murphy formula as suggested here separates the believed laminar data from the believed turbulent data very well.

The results presented in Figure 25 indicate that for a typical equilibrium reentry glide trajectory, executed by a blunted vehicle, e.g. 30 feet in length, control surfaces are likely to encounter both the laminar and the turbulent boundary layer. Very large bluntness was assumed, and the shock loss theory was employed. Computations also show that sweep has a significant effect on transition distances. The very high sweep of 70° tended to cause a decrease in X_t roughly 25 - 45%.

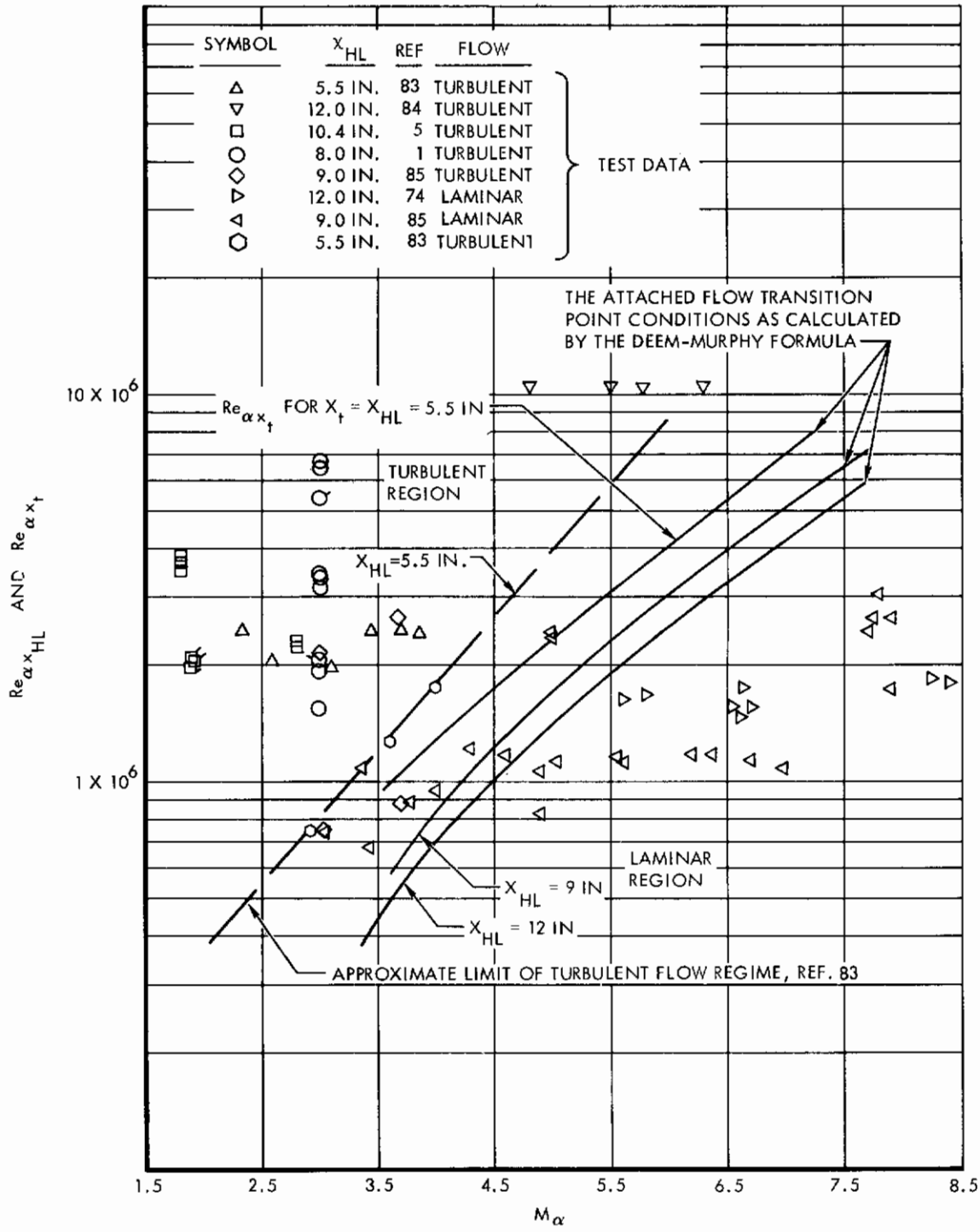

Figure 24. Regions for Existence of the Laminar and Turbulent Boundary Layers

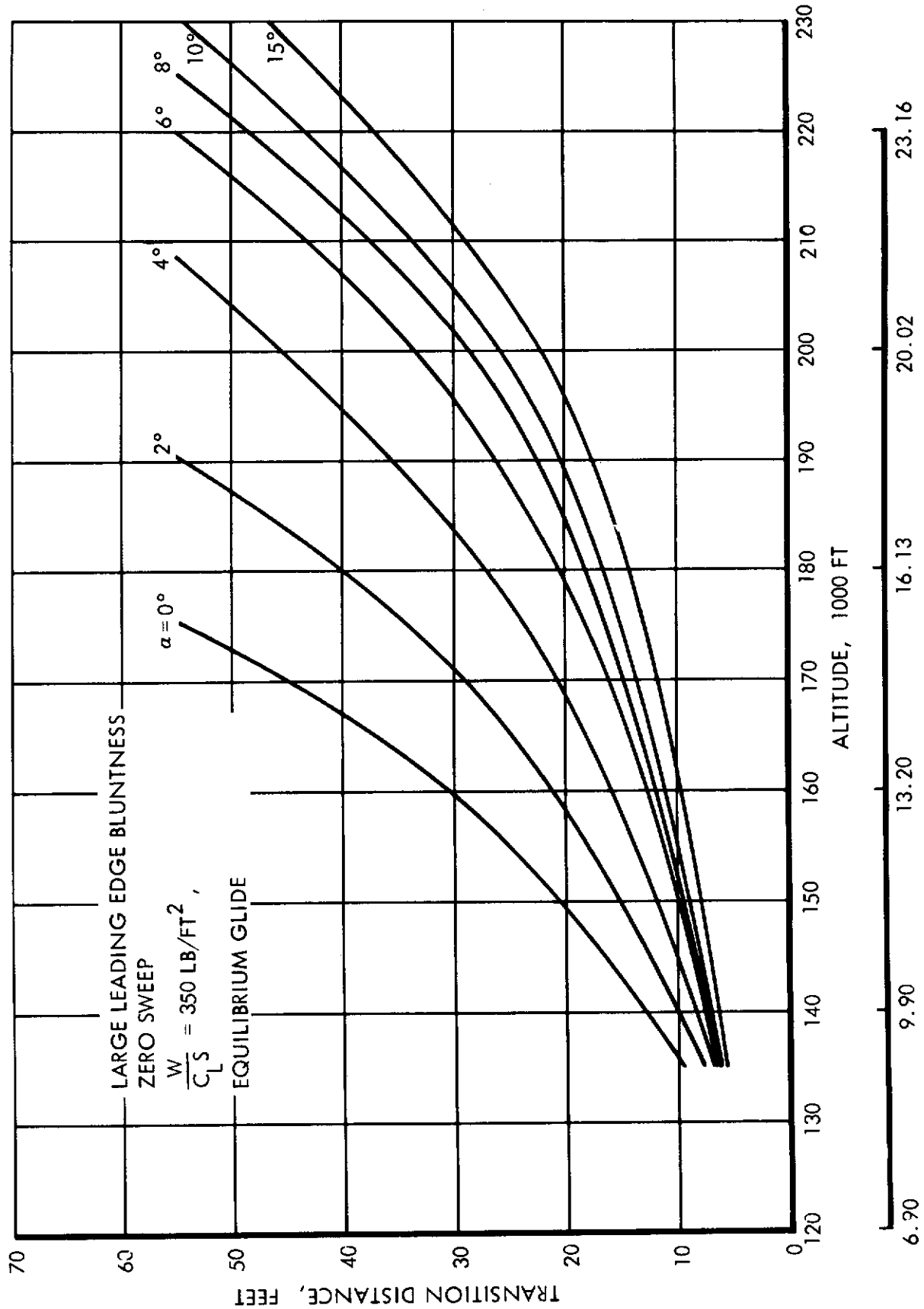

Figure 25. Transition Distance as a Function of Altitude and Angle of Attack

It should be mentioned that the correlation formula presented here does not take account of many factors which should affect transition distance in some manner. In particular, the flight of a real vehicle through the atmosphere will involve some conditions which are not simulated in wind tunnel tests. The following factors should be mentioned relative to the X_t correlation given above.

- Higher Mach number data is still required.
- Free stream turbulence level is known to have an effect on transition distance.
- Actual vehicle configurations are more complex than the wind tunnel flat plate models.
- It is believed that there is a stabilizing effect of cooling (Reference 55), and a real vehicle may have a protective cooling system.
- Surface roughness or protrusions contribute to instability.
- Real gas effects, relaxation time, and flow time influence the gas composition and local flow properties.

CONDITIONS AT INCIPIENT SEPARATION

It is well established that the existence of a sudden pressure rise, as at a compression corner or across an impinging shock, does not always lead to flow separation. Some minimum overall pressure ratio for incipient separation is required. The first step in the examination of the interaction region is the determination or correlation of the quantity:

$$(C_p)_{INC} = \left(\frac{P_2 - P_c}{q_o}\right)_{INC}$$

There exists a simple theory for the form of the relation between the pressure parameters and the other flow properties in the separated region (Reference 56). For this reason the correlations for these pressure parameters are semi-empirical rather than empirical. Dynamically, the situation is that of a pressure rise overcoming the shear force between the attached boundary layer and the surface. Since the vertical height over which the pressure differential acts is itself related to the pressure increase through the Prandtl-Meyer relation

$$C_p = \frac{2}{\sqrt{M^2-1}}\Delta\theta \sim \frac{2}{\sqrt{M^2-1}}\frac{\Delta n}{\Delta s}$$

the force balance is of the form

$$C_P \Delta n \sim C_P \left[\sqrt{M^2-1}\ C_P \Delta s\right] \sim C_f \Delta s$$

$$C_P \sim \frac{\sqrt{C_f}}{\sqrt[4]{M^2-1}}$$

For the laminar boundary layer $C_f \sim \sqrt{Re_{\alpha X_{HL}}}$, and for the turbulent boundary layer a common assumption is $C_f \sim \sqrt[5]{Re_{\alpha X_{HL}}}$ (it is considered that transition has occurred relatively nearer X = 0 than $X = X_{HL}$). Therefore the data for the incipient separation pressure are plotted as

$$C_{P_{\alpha_{INC}}} \left(Re_{\alpha X_{HL}}\right)^{\frac{1}{4}} \text{ vs } (M_\alpha{}^2-1) \text{ for laminar cases, and}$$

$$C_{P_{\alpha_{INC}}} \left(Re_{\alpha X_{HL}}\right)^{\frac{1}{10}} \text{ vs } (M_\alpha{}^2-1) \text{ for turbulent cases,}$$

in Figures 26 and 27. By establishing a straight-line curve fit through the data in each case, the following expressions result:

For laminar flow:

$$C_{P_{\alpha_{INC}}} \left(Re_{\alpha X_{HL}}\right)^{\frac{1}{4}} = 2.03\ (M^2-1)^{-0.306} \tag{18}$$

and for turbulent flow:

$$C_{P_{\alpha_{INC}}} \left(Re_{\alpha X_{HL}}\right)^{\frac{1}{10}} = 2.20 \text{ (constant)} \tag{19}$$

Some experimental data shown in Figure 26 were reducted from values for separation point pressure, using a theoretical relation from Reference 56:

$$C_{P_{INC}} = 2C_{P_s}$$

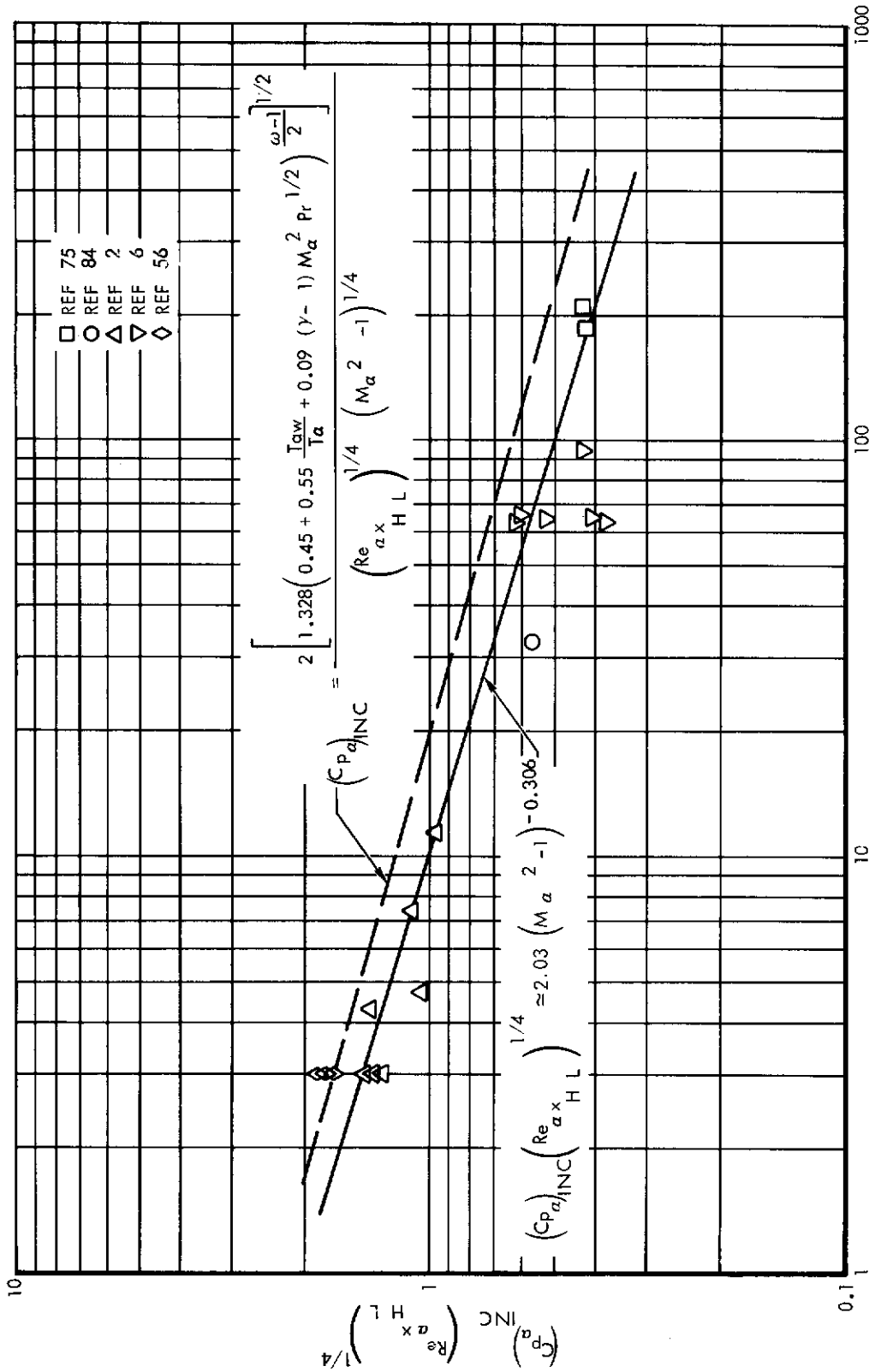

Figure 26. Laminar Incipient Separation

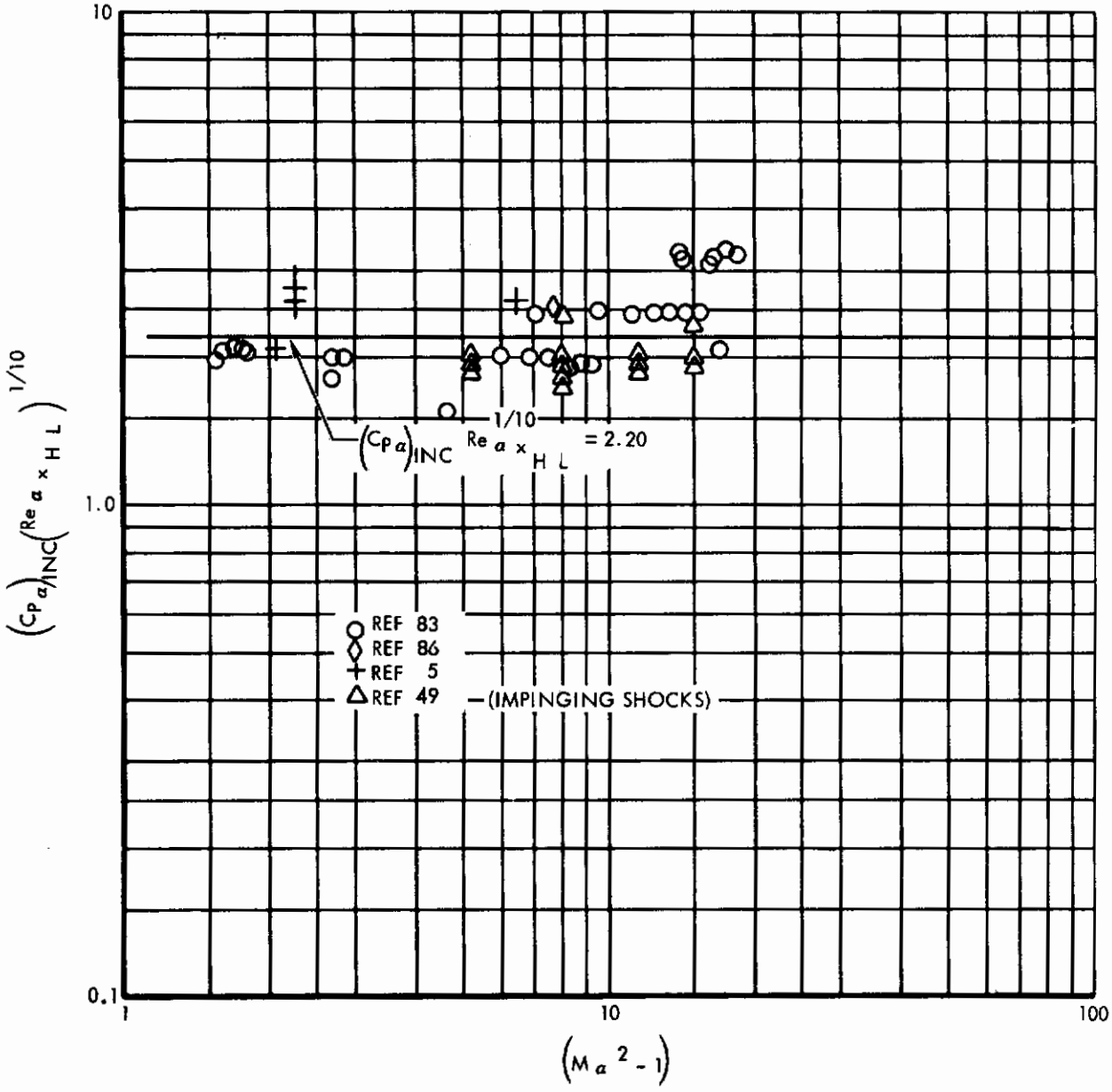

Figure 27. Turbulent Incipient Separation

The theory in Reference 56 shows good agreement with the experimental data. The theoretically derived expression

$$C_{P_{\alpha_{INC}}} = 2\sqrt{\frac{2C_{fo}}{(M_\alpha - 1)^{\frac{1}{2}}}}, \qquad (20)$$

where the undisturbed-flow skin friction coefficient is (Reference 57)

$$C_{fo} = .664\left[.45+.55\frac{T_{aw}}{T_\alpha} + .09\,(\gamma-1)M_\alpha^2 Pr^{\frac{1}{2}}\right]^{\frac{\omega-1}{2}},$$

is represented by a straight line of nearly the same slope as the correlation line, and with only a slight displacement from it.

It could not be established that the turbulent flow follows a similar trend. Also, the range of Reynolds numbers in the available data is too small to determine whether the tenth root relation really is representative of the turbulent data. Each expression does, however, correlate the available data over the ranges of test conditions.

DEFINITION OF THE INTERACTION PARAMETERS

To describe the characteristics of the separated flow region completely and without ambiguity, some definitions of the interaction parameters have to be formulated.

Figure 28 presents a typical pressure profile within the interaction region. The distance parameters are based on a common reference line which is defined for various model configurations as a geometrical shock impingement point, hinge line (for corner flow), or forward face of a step.

The beginning of the pressure interaction, x_o, is defined as the point where pressure just begins to rise. The upstream spread of the pressure is expressed by the upstream pressure interaction length, d_1, defined as the distance from the beginning of the interaction to the reference line. The free interaction length, ℓ_{fi}, is defined as the distance from the beginning of the interaction to the point where the pressure distribution reaches the straight section of the pressure plateau. The downstream interaction length, d_2, is the distance from the reference line to the point of intersection of

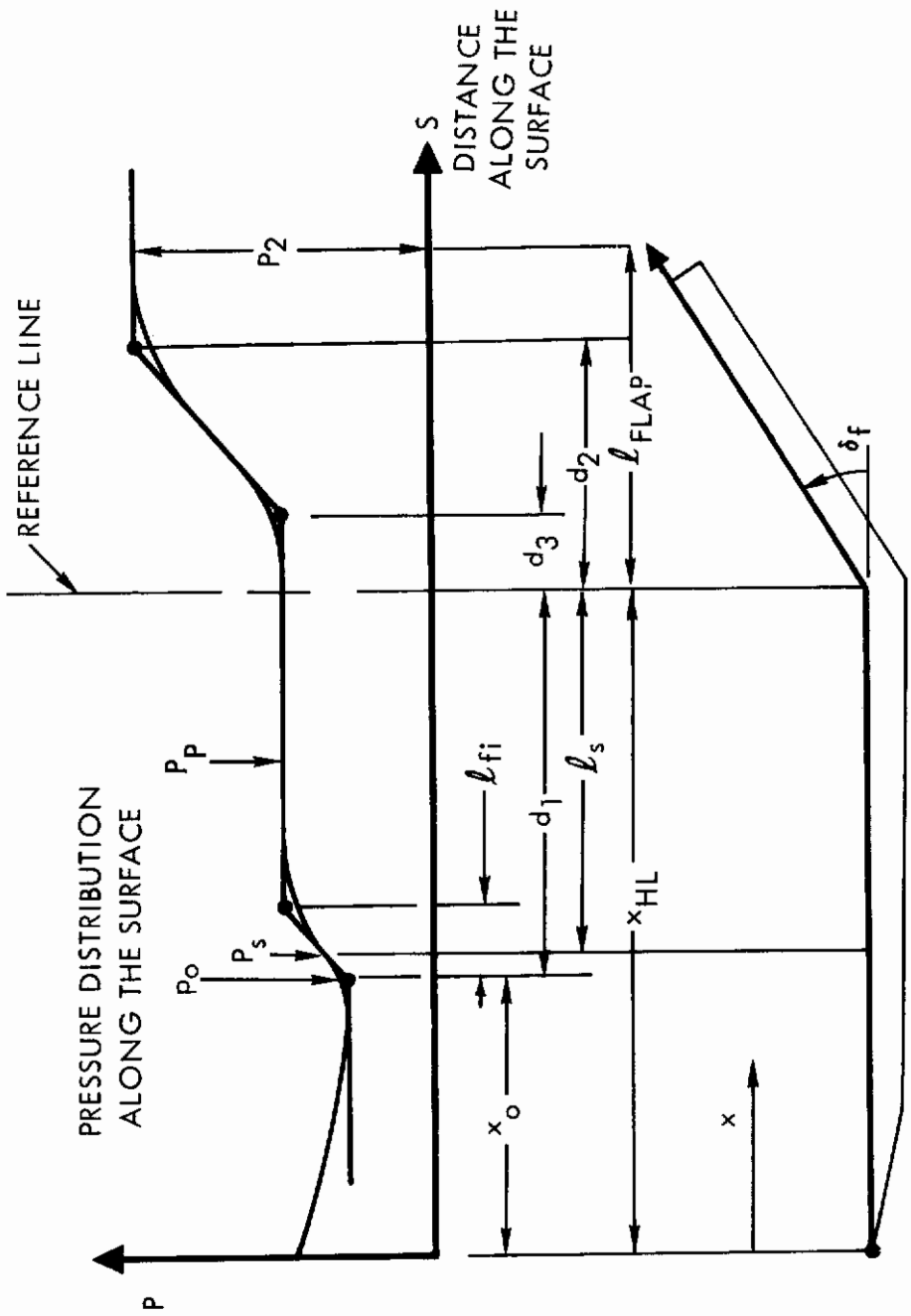

Figure 28. Definition of Interaction Parameters for Laminar and Turbulent Separated Flow

two lines tangent to the pressure curve, as shown, in the downstream region. The parameter d_3 is the distance from the reference line to the point of intersection of two lines tangent to the pressure curve as indicated in Figure 28. The separation length, ℓ_s, is the distance from the separation point to the reference line (the separation point is obtained from Schlieren photographs as the point of deflection of the boundary layer). Pressure levels are defined corresponding to the previously mentioned characteristic regions and positions. Therefore, P_o and P_s correspond to pressures at x_o and to ℓ_s respectively. Pressure over the separated region is established at a level defined by P_P. The final downstream pressure is designated by P_2.

SEMI-EMPIRICAL CORRELATIONS FOR LAMINAR SEPARATED FLOW

Flow separation occurs if the applied pressure rise is sufficiently large, i.e. is equal to or exceeds the pressure rise for incipient separation. Once this condition is reached a characteristic pressure distribution within the separated region is developed.

In order to approximate this pressure profile, the interaction parameters must be known. The purpose of this section is to present methods of correlating the interaction parameters Q_i into general expressions in the form

$$Q_i = f_i \left(M_{\alpha}, Re, \frac{P}{P_{\alpha}}\right)$$

These correlations are expressed in terms of local properties as defined in Section III, assuming that incipient separation conditions have been reached or exceeded. The evaluated experimental data cover a range of $M_{\alpha} = 1.9$ to 8.4 with some data at $M_{\alpha} \approx 14$ and $Re_{\alpha X_o} = 1.2 \times 10^5$ to 1.4×10^6.

Plateau Pressure, P_P

One of the most important features of the shock wave boundary layer interaction is the plateau pressure which extends over the separated region. This plateau pressure corresponds to a region of relatively constant slope of the separated boundary layer. It has been established from a simple momentum equation argument (Reference 56) or by using an order of magnitude analysis (Reference 2), that the plateau pressure can be expressed by the following functional relation:

$$(C_{P_{\alpha}})_P = \frac{P_P - P_o}{\frac{\gamma}{2} M_{\alpha}^2 P_o} = f\left(M_{\alpha}, Re_{\alpha X_o}\right)$$

or more specifically

$$(C_{P_\alpha})_P = \frac{K(M_\alpha^2-1)^n}{\left(Re_{\alpha x_o}\right)^{\frac{1}{4}}}$$

To obtain K and n, the experimental values of $(C_{P_\alpha})_P \left(Re_{\alpha x_o}\right)^{\frac{1}{4}}$ were plotted versus (M_α^2-1) on log-log paper (Figure 29). The equation of the linear curve fit through the data is:

$$(C_{P_\alpha})_P = \frac{1.56(M_\alpha^2-1)^{-0.262}}{\left(Re_{\alpha x_o}\right)^{\frac{1}{4}}} \qquad (21)$$

Upstream Interaction Length, d_1

Knowing the magnitude of the plateau pressure, it is still necessary to find the streamwise spread of the pressure interaction region. The concept of the free interaction states that separated flow can be subdivided into a region upstream of separation (which is independent of the method of inducing separation), and a reattachment region. One can treat these regions separately. This was the basis for suggesting separate distance parameters for upstream and downstream interaction lengths. The upstream spread of the pressure interaction is expressed by the length d_1.

It has been observed that the upstream spread of the separated flow increases with the magnitude of the adverse pressure gradient as expressed by the pressure ratio across the shock wave or by the magnitude of the flap angle. This trend was indicated by experimental data for both laminar flow (Reference 81) and turbulent flow (Reference 5). On the other hand the plateau pressure increases slightly with the increasing flap angle. Thus, the magnitude of the adverse pressure gradient which has to be negotiated by the boundary layer can be expressed by non-dimensionalized pressure difference $(P_2 - P_p)/P_o$, $(P_2 - P_o)/P_o$, $(P_p - P_o)/P_o$ or by the parameter $M_\alpha\delta$. An attempt to correlate d_1/δ_o as a function of $(P_2 - P_p)/P_p\gamma M_\alpha^2$, which was suggested in literature (Reference 89), did not lead to a successful and conclusive correlation. A correlation of d_1/δ_o versus $(P_2 - P_o)/P_o$ resulted in the expression

$$\frac{d_1}{\delta_o} = 570\, M_\alpha^{-2.92}\left(\frac{P_2}{P_o} - 1\right)^{1.056}$$

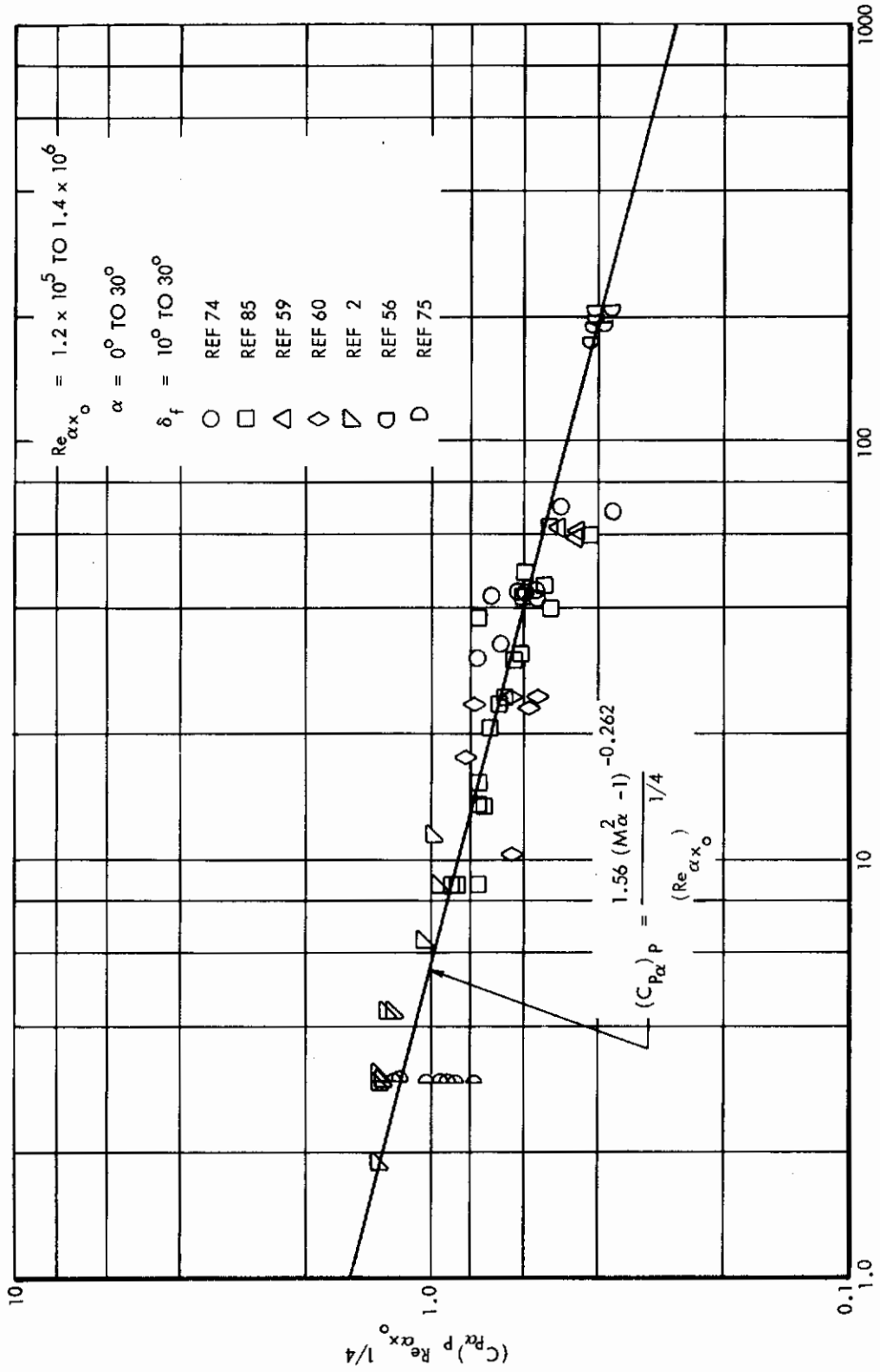

Figure 29. Plateau Pressure Correlation for Laminar Corner Flow (for Sharp Leading Edge Base Plate)

Figure 30 shows a plot of experimental data in relation to the line represented by the above correlation equation. A correlation of d_1/δ_o as a function of $M_\alpha\delta$ has led to the following equation (Figure 31).

$$\frac{d_1}{\delta_o} = \frac{1030}{M^{1.75}} (2.65)^{M_\alpha\delta}$$

The scatter of the test points is comparable to that of Figure 30. Although the experimental data inferred that the upstream interaction length is influenced by the deflection angle or pressure difference, the evaluated test data did not result in an acceptable correlation of d_1/δ_o as a function of these parameters. The reason for this might be the incompleteness of test data and insufficient variation of evaluated test data.

A functional relation of the form

$$\frac{d_1}{\delta_o} = F\left(\frac{P_p}{P_o}, M_\alpha\right)$$

was therefore used to correlate the experimental data.

To obtain a specific relation, d_1/δ_o was plotted versus $\left(\frac{P_p}{P_o} - 1\right)$ (Figure 32). Mach number M_α was noted for each point and the systematic variation of this parameter across the plot suggested the relation:

$$\frac{d_1}{\delta_o} = F\left(M_\alpha\right)\left(\frac{P_p}{P_o} - 1\right)^n .$$

where n is the slope of the data for each constant M_α.

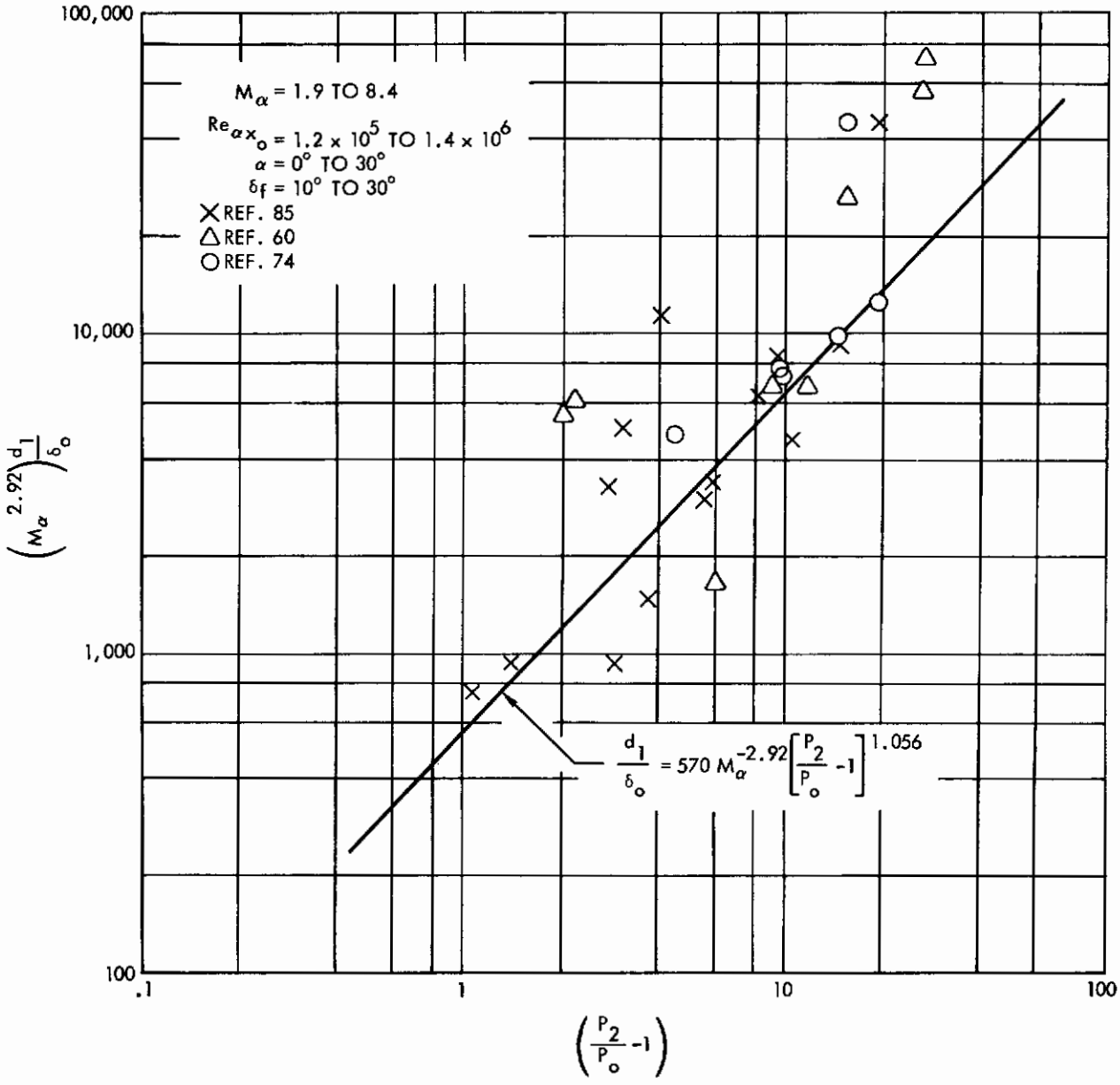

Figure 30. Alternate Upstream Interaction Length Correlation for Laminar Corner Flow (with Sharp Leading Edge Base Plate)

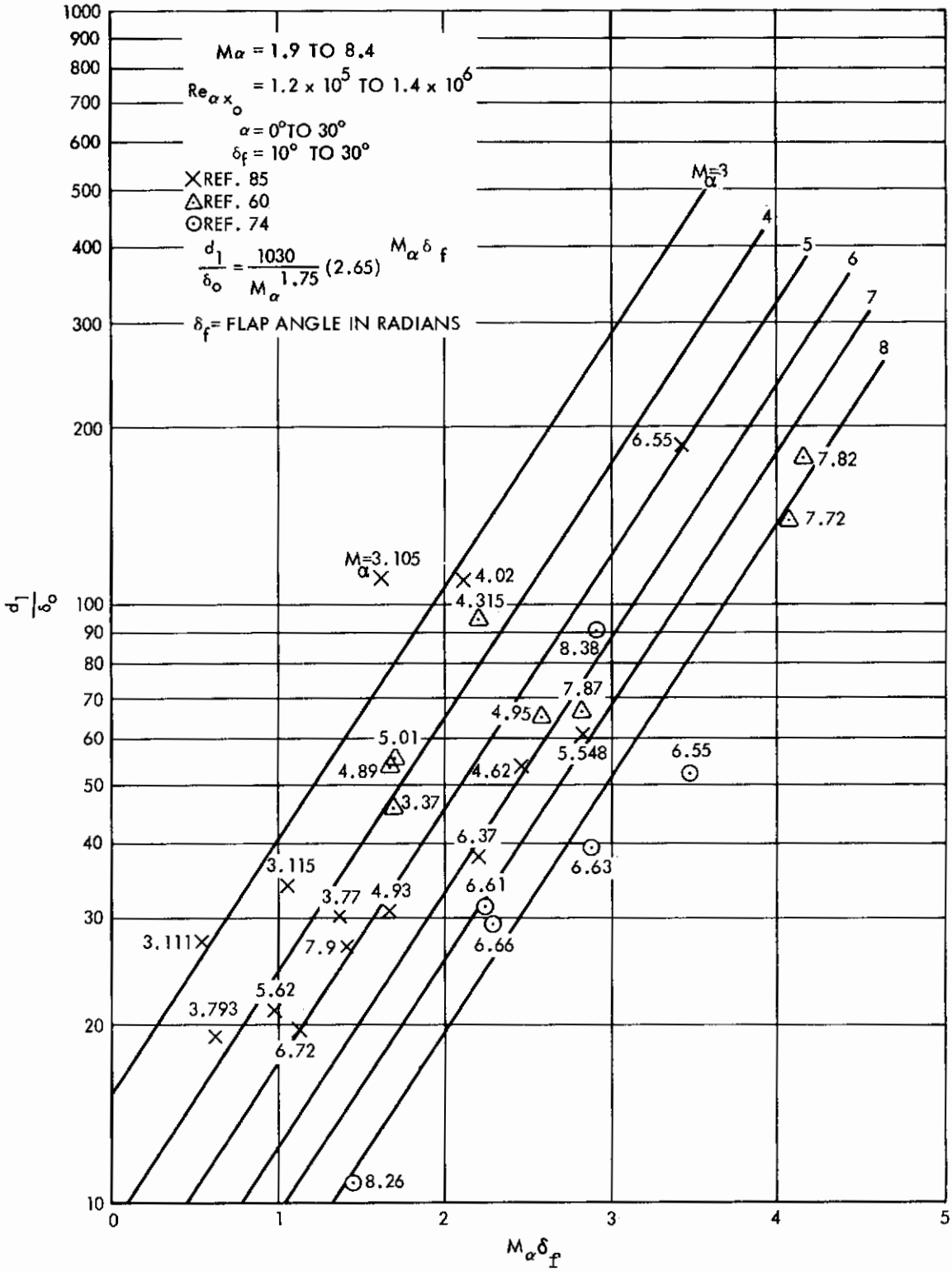

Figure 31. Parametric Plot for Alternate Upstream Interaction Length for Laminar Corner Flow (with Sharp Leading Edge Base Plate)

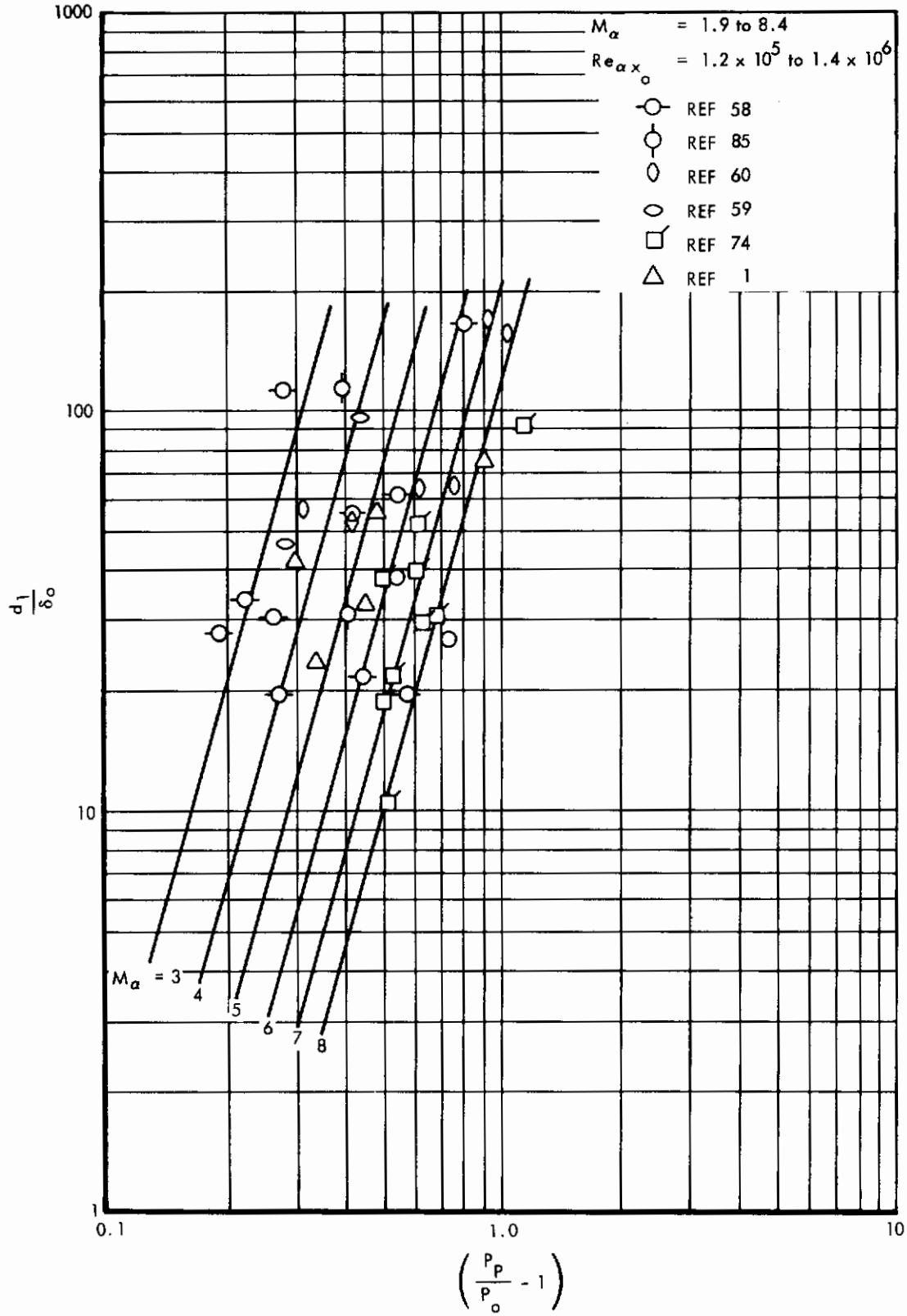

Figure 32. Parametric Plot for Upstream Interaction Length for Laminar Corner Flow (with Sharp Leading Edge Base Plate)

The equation for $F(M_\alpha)$ was obtained by approximating straight lines through the points of constant Mach number. When the values of $F(M_\alpha)$ were obtained from the preceding equation and plotted versus M_α on log-log paper it was found that $F(M_\alpha)$ has the form $K(M_\alpha)^m$ (Figure 33). From this plot K and m were obtained. Therefore

$$\frac{d_1}{\delta_o} = K \left(M_\alpha \right)^m \left(\frac{P_p}{P_o} - 1 \right)^n \qquad \text{(Figure 34)}$$

The resulting equation for d_1 which appears to give best results, is

$$\frac{d_1}{\delta_o} = 5.69 \times 10^5 \; M_\alpha^{-4.3} \left(\frac{P_p}{P_o} - 1 \right)^{3.5} \qquad (22)$$

Free Interaction Length, ℓ_{fi}

The first part of the pressure profile, from the beginning of the interaction to the plateau pressure, is called "free interaction"; its length is defined by the free interaction length, ℓ_{fi}. For the correlation of the free interaction length, the same procedure as for the correlation of d_1 was followed (Figures 35 and 36). The resulting expression for the free interaction length is

$$\frac{\ell_{fi}}{\delta_o} = 2.47 \times 10^5 \; M_\alpha^{-4.2} \left(\frac{P_p}{P_o} - 1 \right)^{3.45} \qquad \text{(Figure 37)} \quad (23)$$

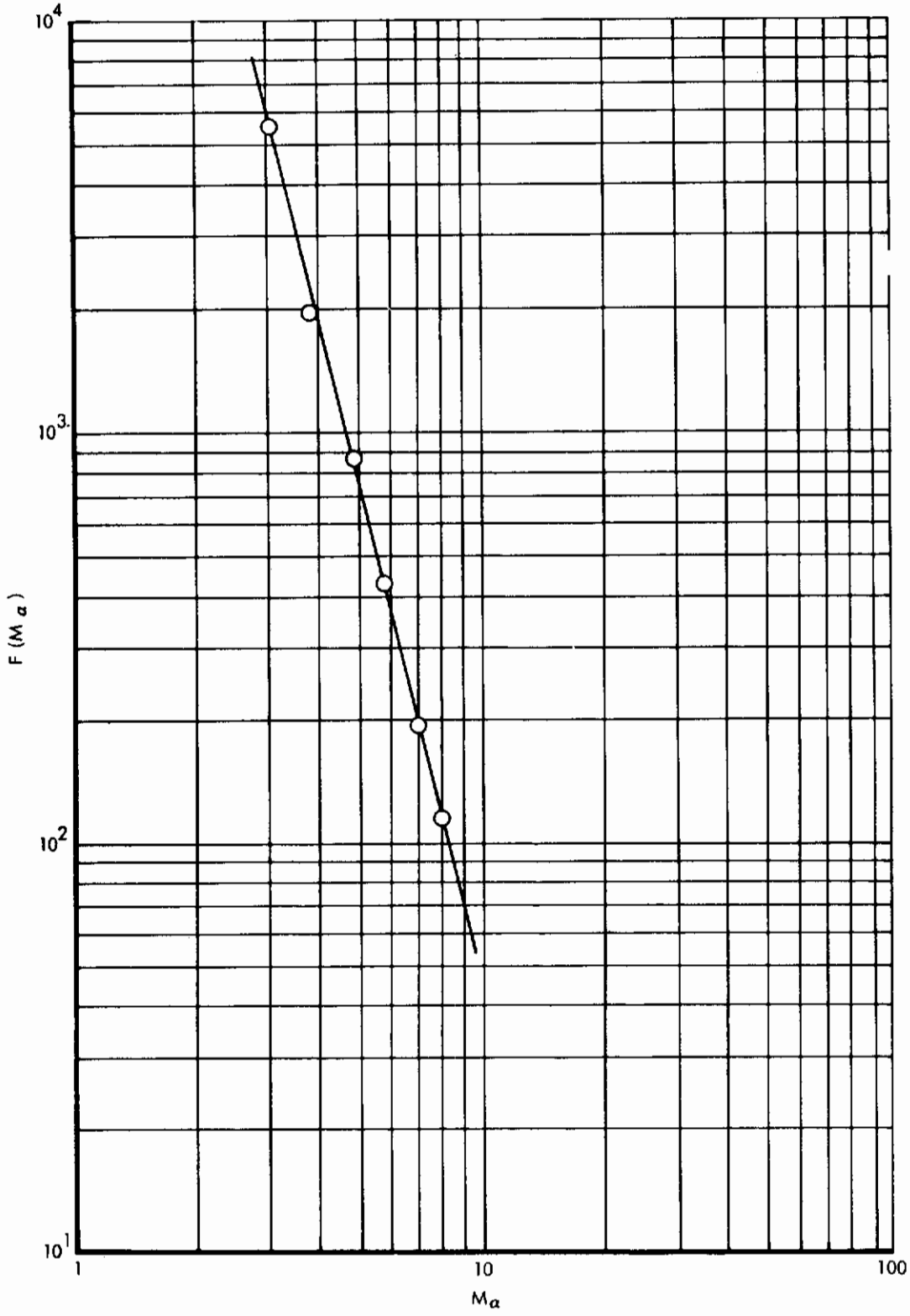

Figure 33. Parametric Plot for Upstream Interaction Length Correlation for Laminar Comer Flow - Auxiliary Plot

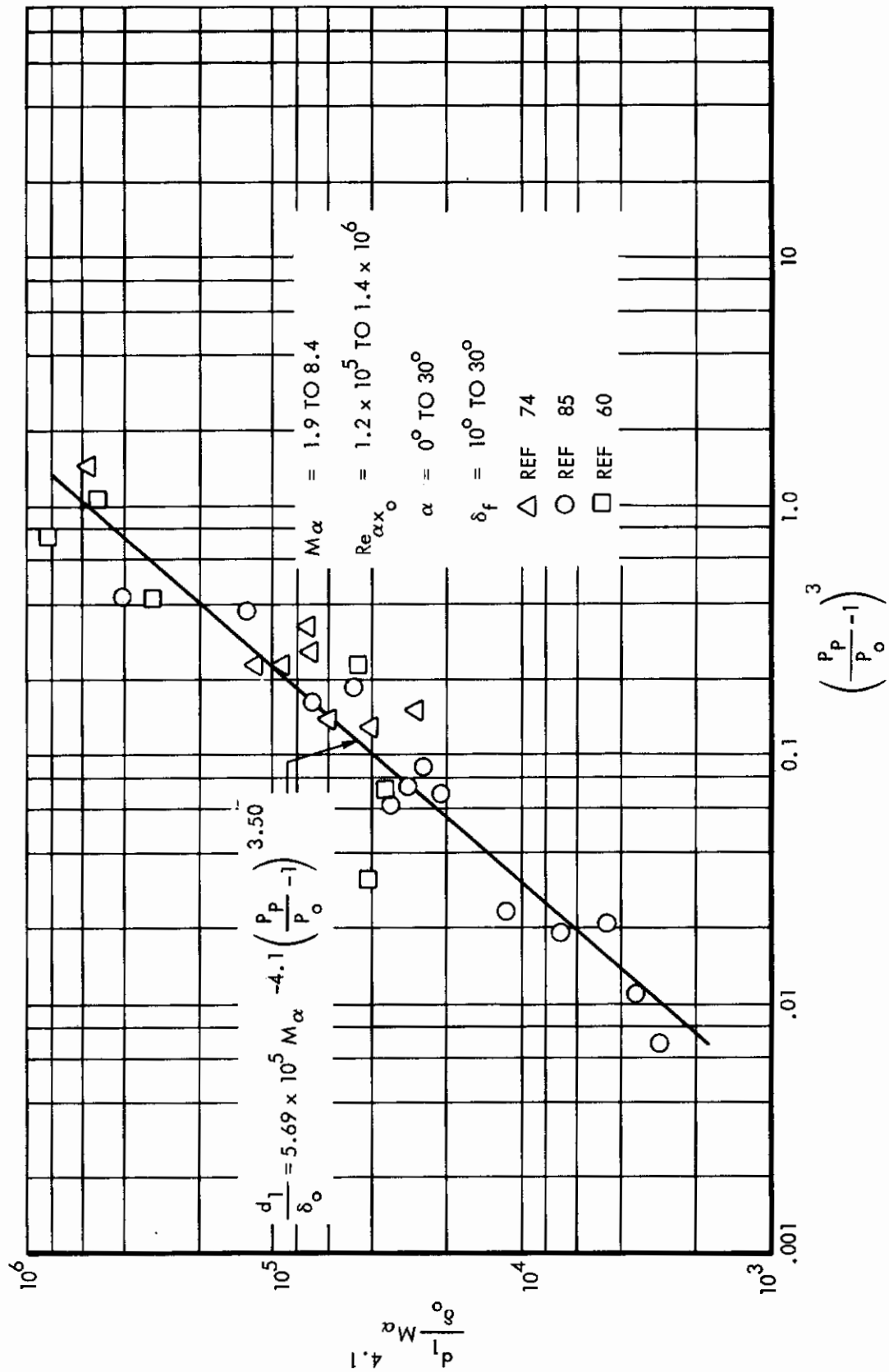

Figure 34. Upstream Interaction Length Correlation for Laminar Corner Flow (with Sharp Leading Edge Base Plate)

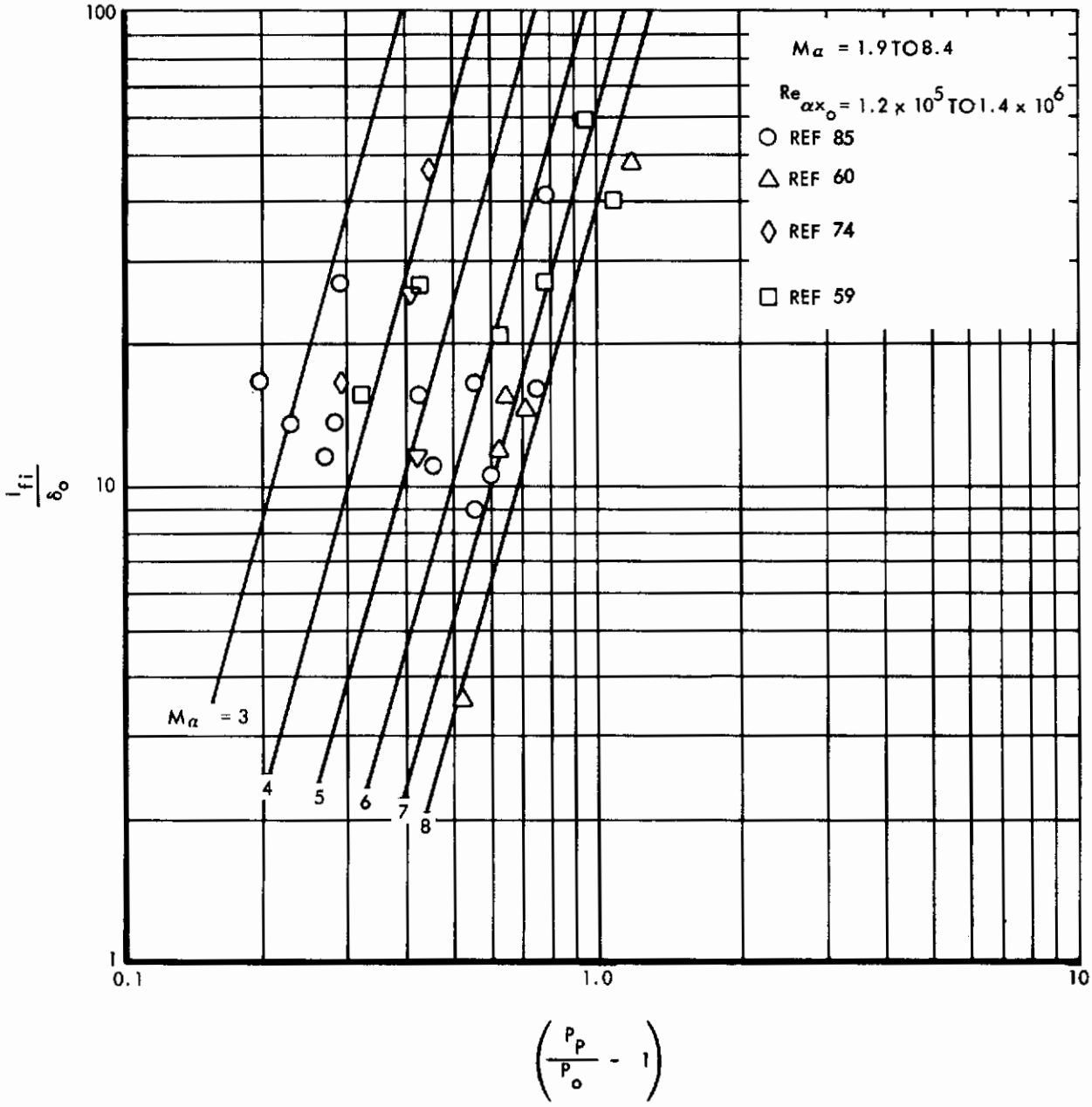

Figure 35. Parametric Plot for Free Interaction Length for Laminar Corner Flow (with Sharp Leading Edge Base Plate)

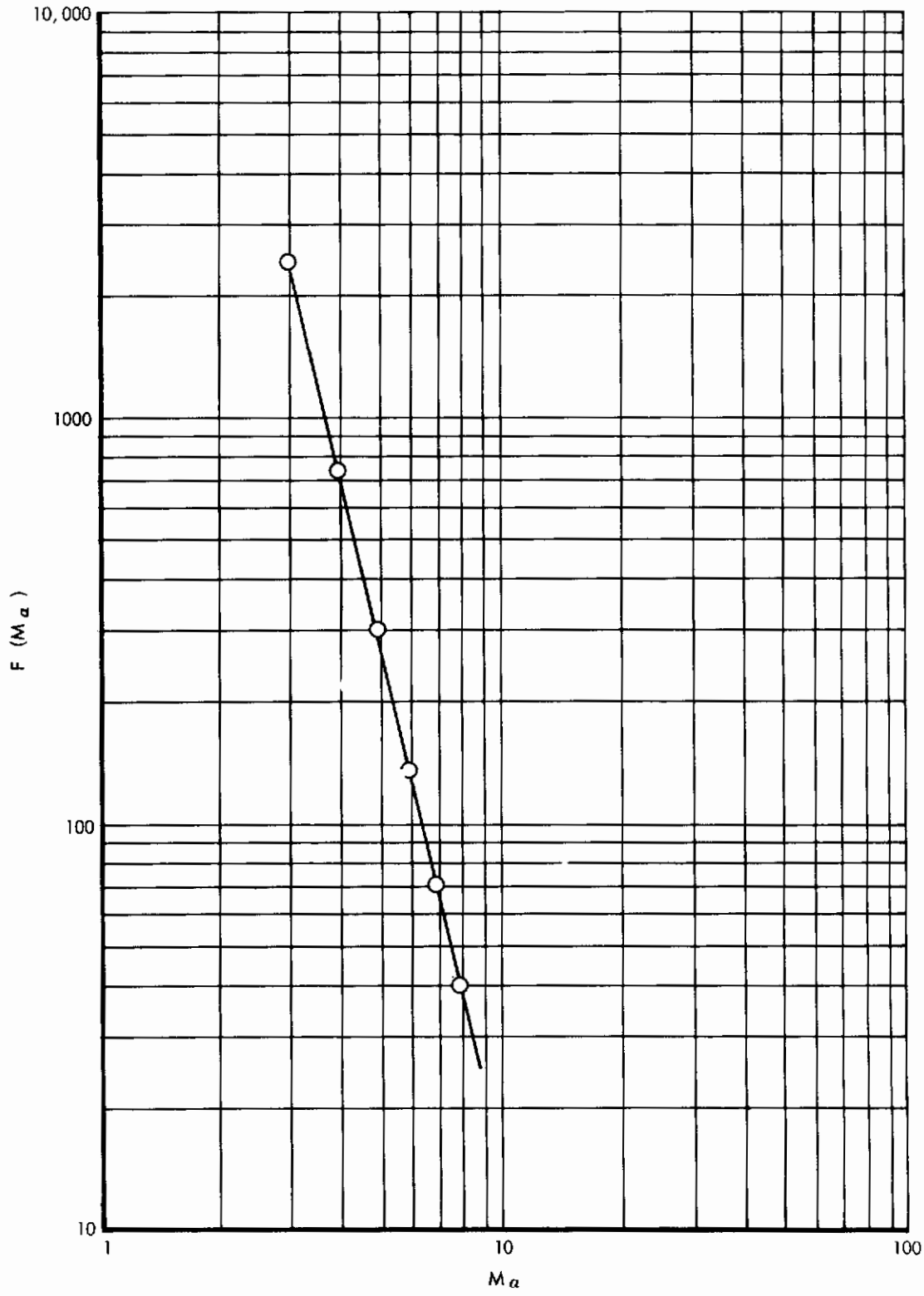

Figure 36. Free Interaction Length Correlation for Laminar Corner Flow – Auxiliary Plot

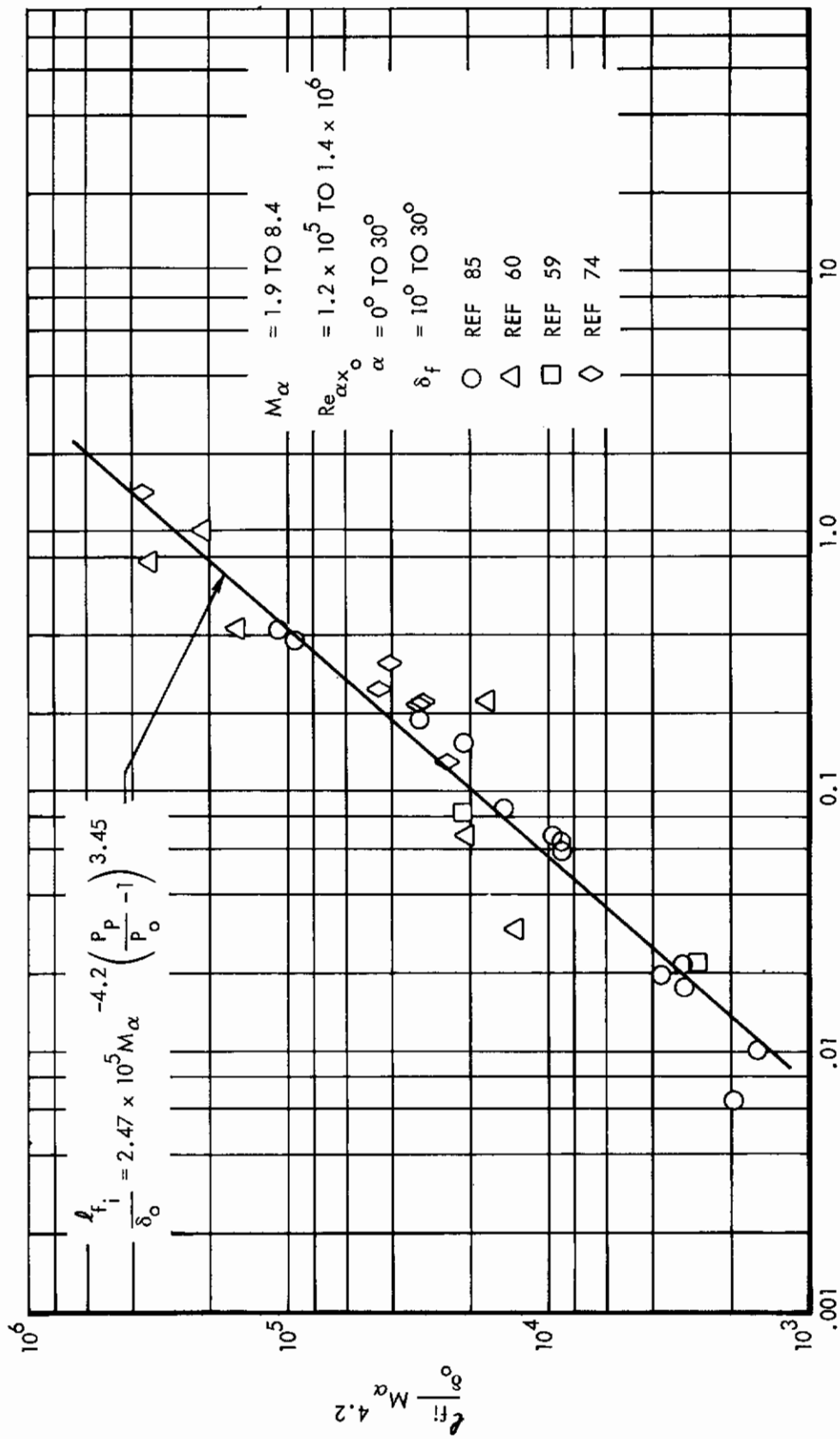

Figure 37. Free Interaction Length Correlation for Laminar Corner Flow (with Sharp Leading Edge Base Plate)

Downstream Interaction Length to Pressure Rise, d_3

The distance d_3 corresponds to the beginning of flow reattachment as defined in Figure 28. Figure 38 is a detail sketch of this region.

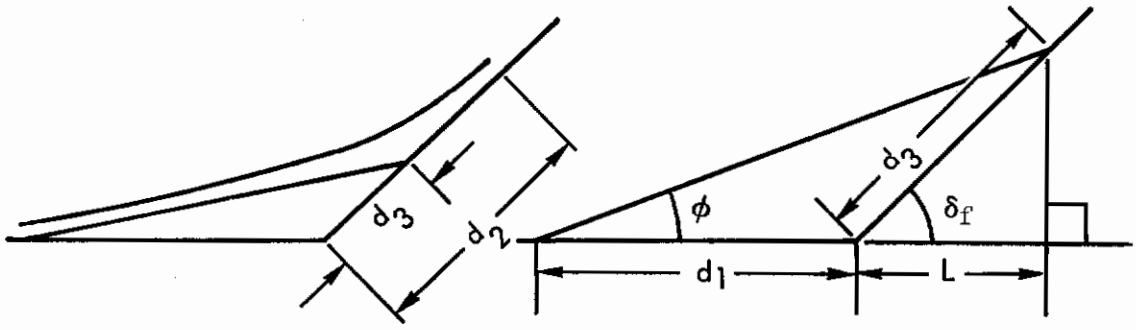

Figure 38. Definition of Downstream Interaction Parameters

To determine d_3, the angle ϕ is first obtained from $\phi = \nu_p - \nu_o$, where ν is the Prandtl-Meyer Function. Table II of Reference 36 yields ν as a function of either M or P/P_t. The value of ν_o follows from M_α and the value of ν_P follows from $P_P/P_t = P_P/P_o \times P_o/P_t$. Once ϕ is known, the quantity d_3 is obtained from the simple geometrical relation

$$\frac{\tan \phi}{\tan \delta_f} = \frac{L}{d_1 + L}$$

Therefore:

$$L = \frac{d_1 \tan \phi}{\tan \delta_f - \tan \phi}, \quad d_3 = \frac{L}{\cos \delta_f} = \frac{d_1 \tan \phi}{\sin \delta_f - \cos \delta_f \tan \phi} \qquad (24)$$

Downstream Interaction Length to Peak Pressure, d_2

The location of the final rise to the pressure P_2 behind an oblique shock is defined by the downstream interaction length d_2 (Section IV). Two methods have been used to determine this parameter.

Method 1. The following correlation, together with its stated modifications, gives satisfactory answers for any input parameters. Since d_1 is a dimension of the same order as d_2, and since $M_\alpha \delta_f$ indicates the strength of the disturbance cause by the flap deflection, plots of d_2/d_1 versus $M_\alpha \delta_f$ were

constructed. The available data had been obtained for different flap lengths, and the parameter C_{flap}/d_1 was introduced in order to account for the effect of finite flap length. Expressing the parameter $d_2/d_1 \sqrt{C_{flap}/d_1}$ as a function of $(M_\alpha \delta_f)$, the following correlation expression for average values is obtained:

$$\frac{d_2}{d_1} \frac{1}{\sqrt{\frac{C_{flap}}{d_1}}} = 0.545 - 0.0403 (M_\alpha \delta_f) \qquad (25)$$

The possibility of obtaining unreasonable answers for d_2/d_1 is eliminated by imposing certain cutoff points for the above expression. These are expressed mathematically by:

For $\frac{C_{flap}}{d_1} \geq 1$: $\frac{d_2}{d_1} = .545 - .04 (M_\alpha \delta_f)$

For $\frac{C_{flap}}{d_1} \leq 0.25$: $\frac{d_2}{d_1} = .273 - .02 (M_\alpha \delta_f)$

For $M_\alpha \delta_f \geq 5$: $\frac{d_2/d_1}{\sqrt{\Gamma}} = .344$

where

$$\Gamma = \begin{cases} \frac{C_{flap}}{d_1}, & \text{if } .25 \leq \frac{C_{flap}}{d_1} \leq 1 \\ 1, & \text{if } \frac{C_{flap}}{d_1} \geq 1 \\ .25, & \text{if } \frac{C_{flap}}{d_1} \leq .25 \end{cases}$$

Method 2. The correlation expression for d_2 given below is applicable for small flap deflection angles ($\delta_f \leq 15$), and flow conditions in the Mach number and Reynolds number region M_α = 1.9 to 8.4 and $Re_{\alpha x_o}$ = 1.2 x 10^5 to 1.4 x 10^6,

respectively. It is again recognized that the pressure rise as characterized by $M_\alpha \delta_f$ should be a significant factor. However δ_f itself is carried as a separate parameter. To obtain a correlation, d_2/d_1 was plotted versus $(M_\alpha \delta_f)$. From this a parametric dependence on δ_f was observed (Figure 39). A function of the form

$$\frac{d_2}{d_1} = F(\delta_f)\ (M_\alpha \delta_f)^m$$

was selected to fit the data. The exponent m is the slope of the parametric lines. The function $F(\delta_f)$ could then be calculated and plotted versus δ_f. This resulted in $F(\delta_f) = K\ \delta_f^n$ (Figure 40), where n and K are determined from the graph. The final equation for d_2 is

$$\frac{d_2}{d_1} = 8.4 \times 10^{-3}\ \delta_f^{-2.875}\ (M_\alpha \delta_f)^{1.59} \quad \text{(Figure 41)} \qquad (26)$$

where δ_f is expressed in radians.

Peak Flap Pressure, P_2

Because the flow is turned more gradually when a separated region exists, than it would be through a single oblique shock, the final pressure reached on the flap generally will be between the isentropic value and the single shock value (maximum entropy rise). Therefore, it is suggested that for laminar cases the average of these two values be used, with the following exceptions (Figure 42): For $M_\alpha > 6$, the single shock value appears to be better than the average value for the final pressure. For $M_\alpha < 6$ and $\delta_f \leq 10°$, it is immaterial which of the methods of pressure ratio calculation is employed.

Separation Distance, ℓ_s

Some iterative numerical methods of analyzing the separated flow (Reference 7) require the conditions at the separation point, to start the procedure.

The actual separation point of the boundary layer is defined by the occurrence of zero velocity gradient at the wall in the direction normal to the wall,

$$\left.\frac{\partial u}{\partial y}\right|_w = 0 ,$$

and is correlated by the equation

$$\frac{\ell_s}{\delta_B} = \left(\frac{P_2}{P_0} - 1\right)^{2.8} \left(R_{e_{\alpha_{\infty}}}\right)^{\frac{1}{2}} M_\alpha^{-3.28} \quad \text{(Figure 43)} \qquad (27)$$

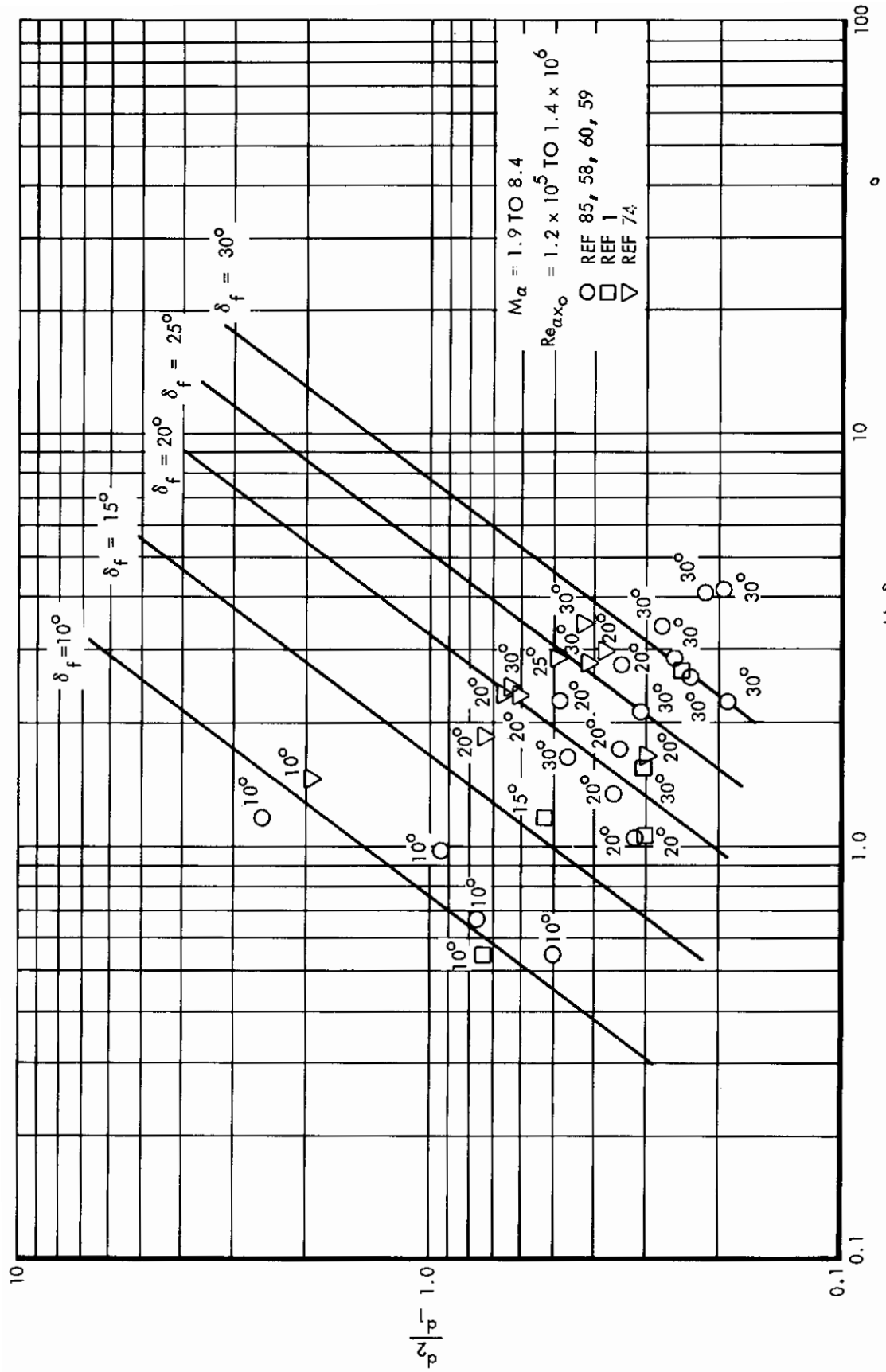

Figure 39. Parametric Plot for Downstream Interaction Length for Laminar Corner Flow (with Sharp Leading Edge Base Plate)

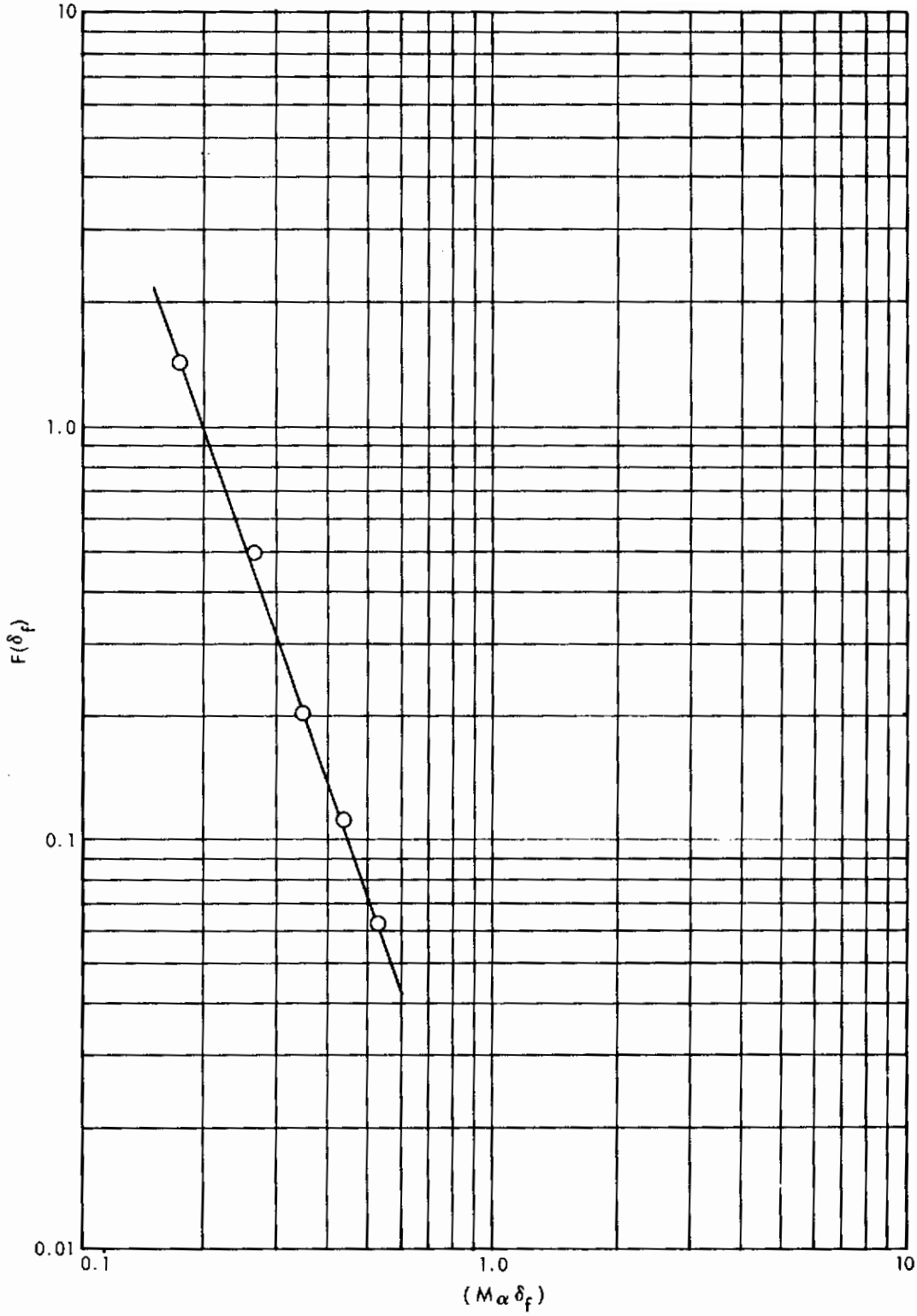

Figure 40. Downstream Interaction Length Correlation for Laminar Corner Flow - Auxiliary Plot

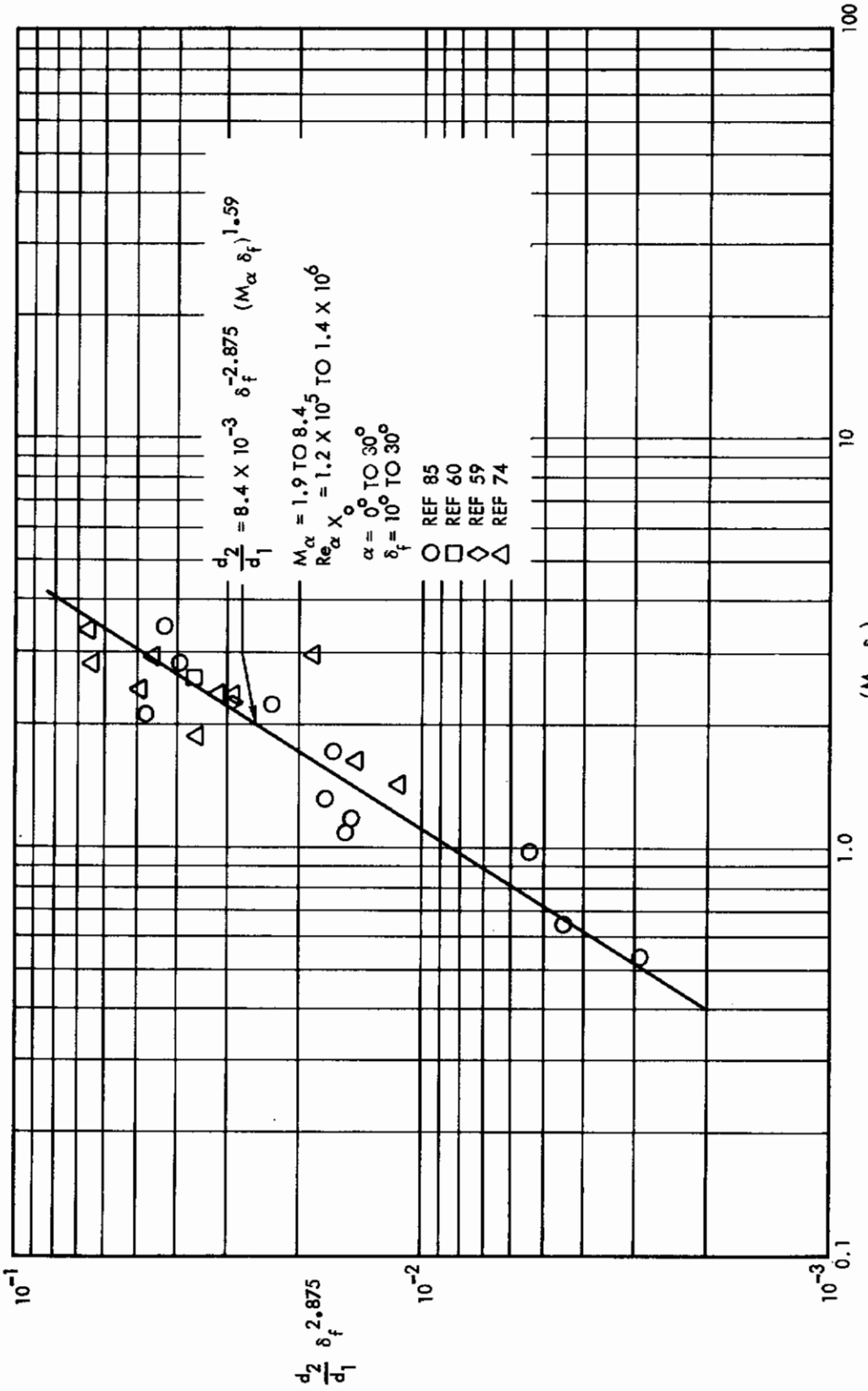

Figure 41. Downstream Interaction Length Correlation for Laminar Corner Flow (with Sharp Leading Edge Base Plate)

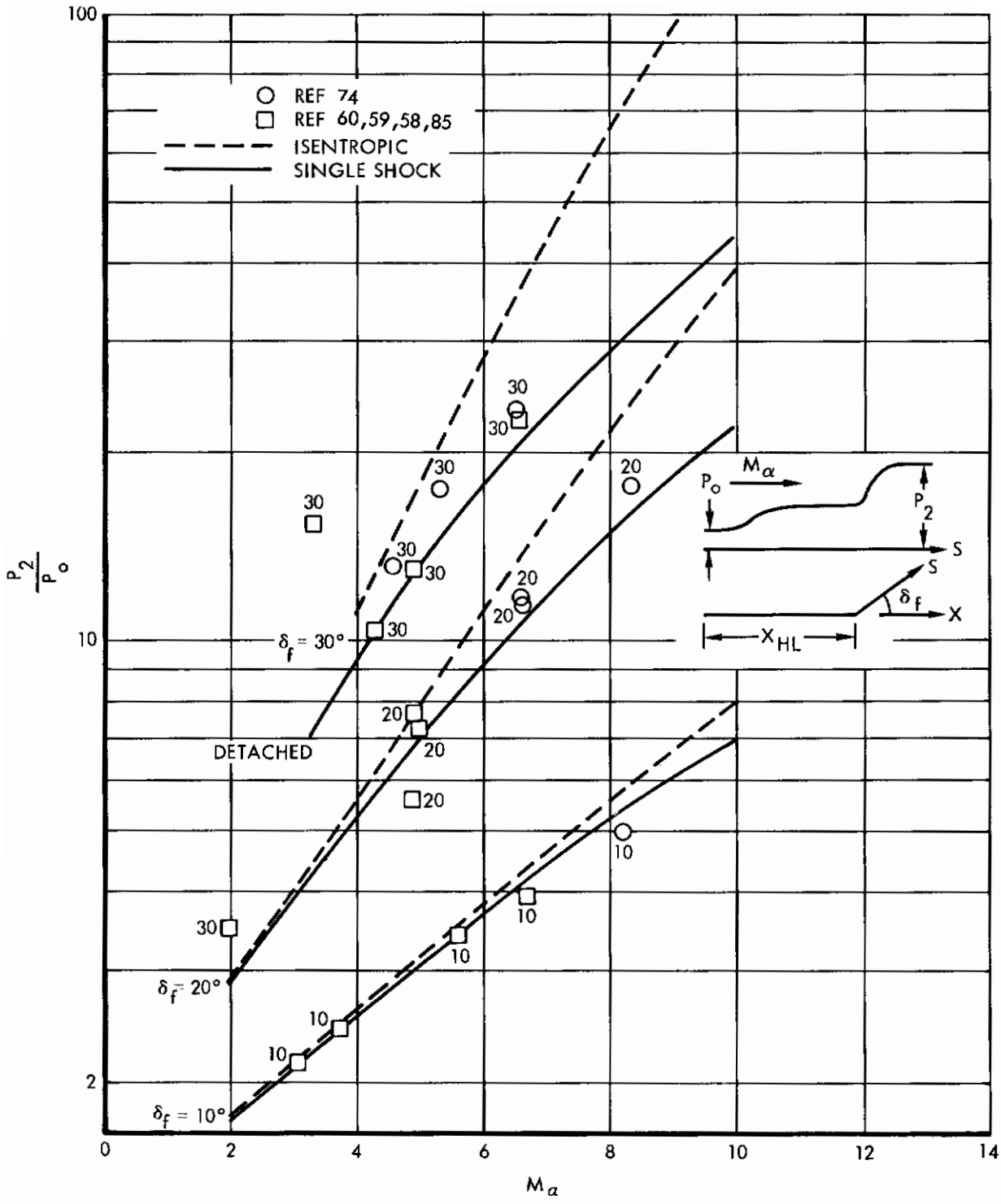

Figure 42. Peak Flap Pressure for Isentropic and Single Shock Compression

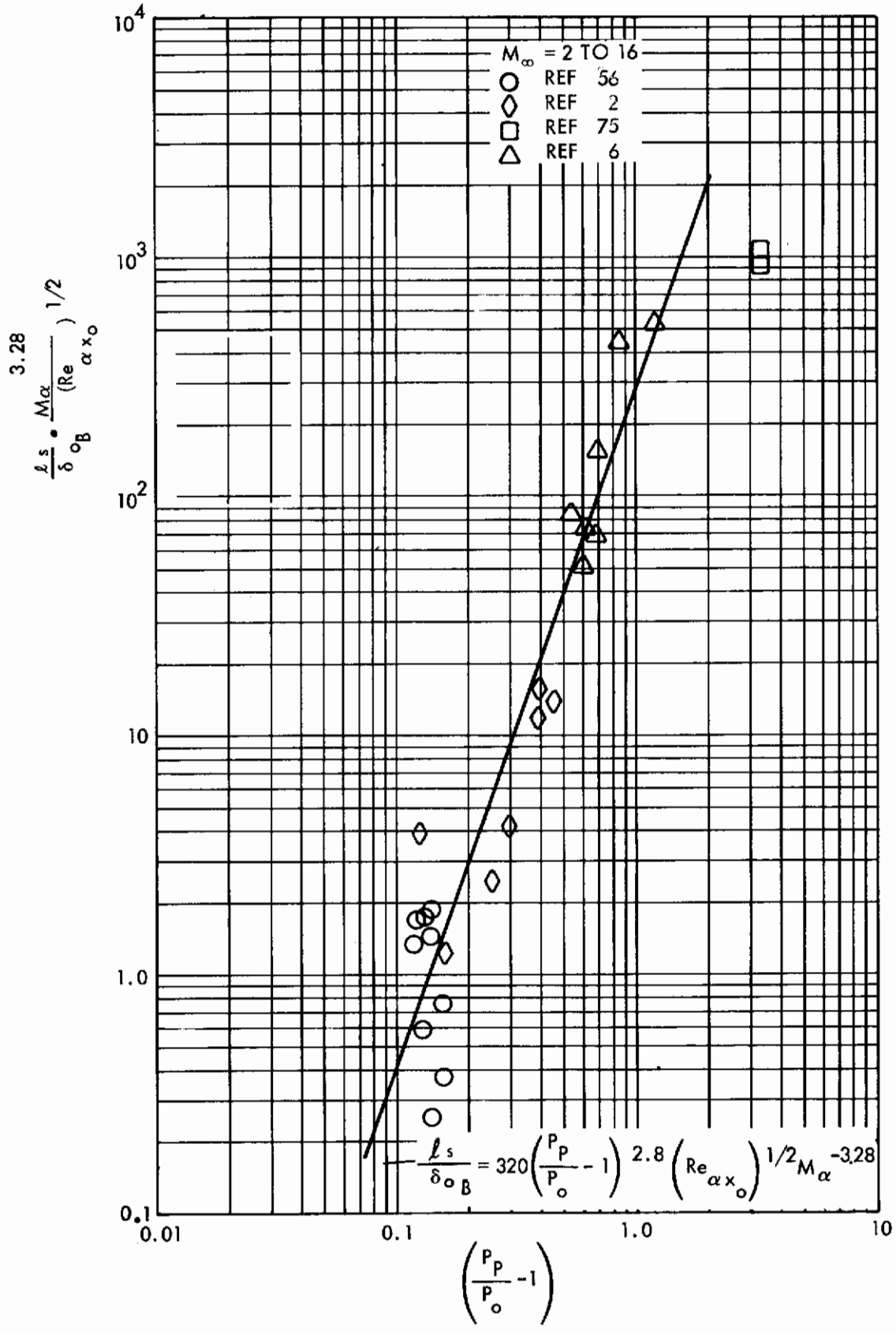

Figure 43. Separation Length for Laminar Flow

where

$$\delta_{o_B} = \frac{5.2\, x_o}{\sqrt{Re_{\alpha x_o}}}$$

Separation Pressure, P_s

The pressure level associated with the separation position has been derived theoretically (Reference 56). It has been found that the pressure coefficient at separation can be approximated by

$$\left(C_{p_\alpha}\right)_s = \sqrt{\frac{2\, C_{f_o}}{(M_\alpha^2 - 1)^{1/2}}}$$

where C_{f_o} is the skin friction coefficient for the undisturbed region. Using the expression for C_{f_o} from Reference 30, the following relation was obtained.

$$\left(C_{p_\alpha}\right)_s = \sqrt{\frac{1.328\left[0.45 + 0.55\frac{T_w}{T_\alpha} + 0.09(\gamma-1)M_\alpha^2 \Pr^{\frac{1}{2}}\right]^{\frac{\omega-1}{2}}}{R_{e_{\alpha x_o}}^{\frac{1}{2}} (M_\alpha^2 - 1)^{\frac{1}{2}}}} \qquad (28)$$

The pressure at the separation point for laminar flow has been correlated for various configurations in Reference 6, resulting in a second expression for $(C_{p_\alpha})_s$:

$$(C_{p_\alpha})_s = \frac{0.91\,(M_\alpha^2 - 1)^{-0.287}}{\left(Re_{\alpha x_o}\right)^{\frac{1}{4}}} \qquad (29)$$

A comparison between the two expressions may be seen in Figure 44. The good agreement between these two expressions tends to indicate the validity of the theoretical relation.

The Effect of Finite Flap Span

Pressure distribution in the separated region over the flap is influenced by finite flap span. Some data for partial span flap pressure distributions are presented in References 58, 59 and 60. Figure 45 shows the configuration considered.

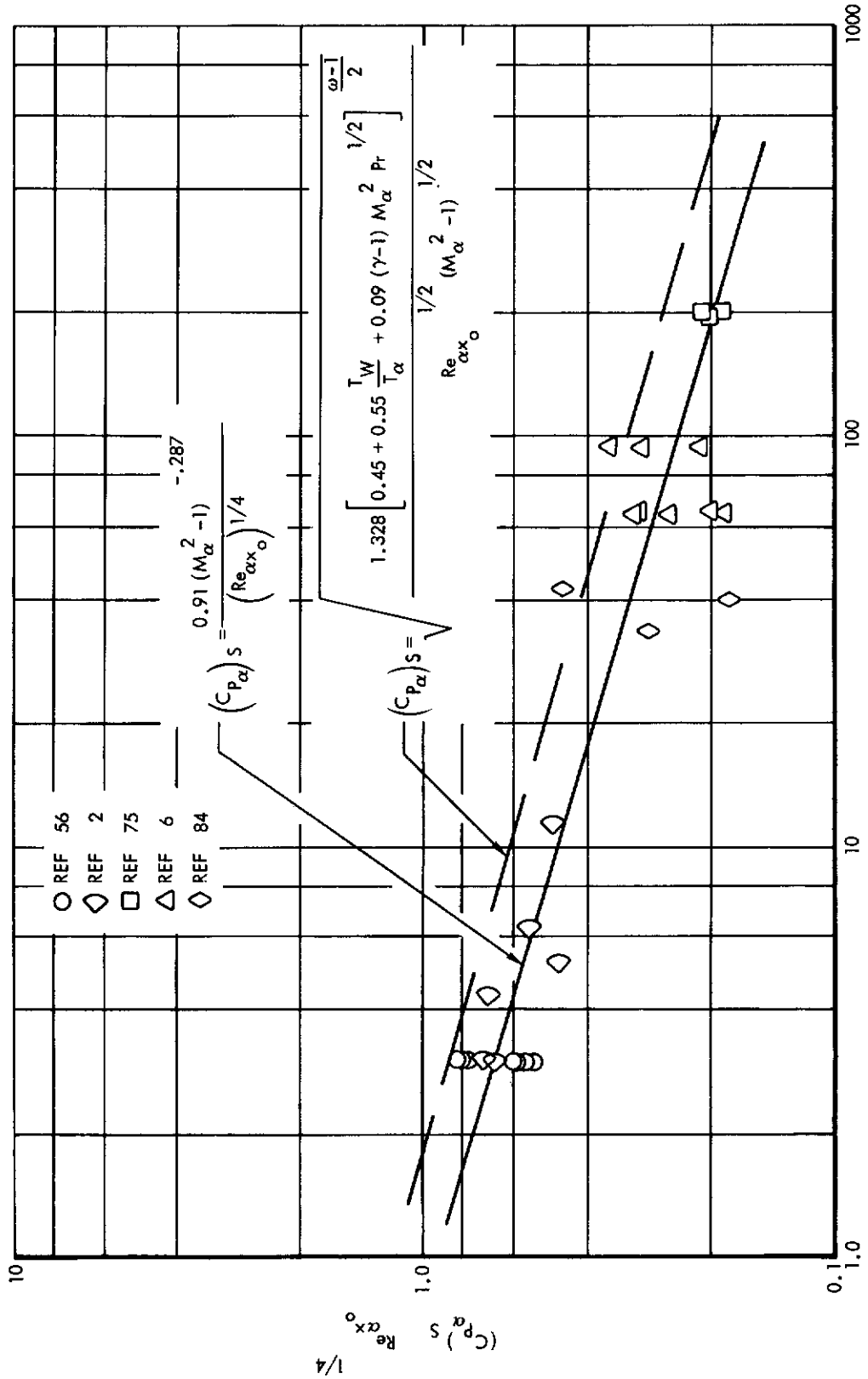

Figure 44. Pressure at Separation for Laminar Flow

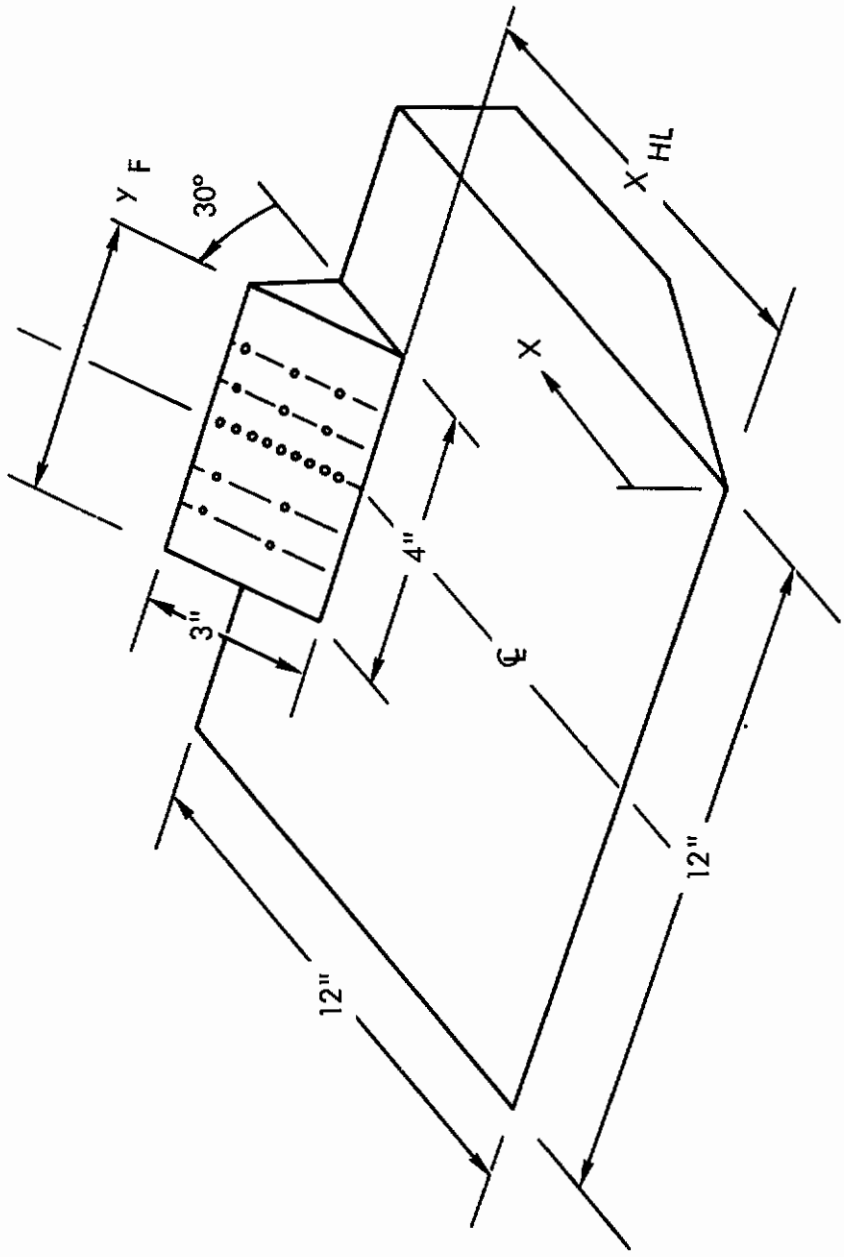

Figure 45. Model Used in Finite Flap Span Tests

It is desired to construct some empirical correlation for an average flap pressure defined by the equation:

$$\int_0^{y_f} (P_{\mathfrak{L}} - P)\, dy = CP_{\mathfrak{L}}\, y_f = (P_{\mathfrak{L}} - P_{av})y_f$$

$$P_{av} = P_{\mathfrak{L}} (1 - C)$$

The pertinent span parameter was not varied in the available data. The average value of C, which indicates average percentage loss in flap force for the evaluated tests, was 14%. Attempts to identify Mach number, Reynolds number, or position effects on C values were unsuccessful. The flap aspect ratio of the test model was

$$AR = \frac{y_f^2}{y_f C_{flap}} = 1.33$$

Presumably, $C \longrightarrow 0$ as $AR \longrightarrow \infty$, and percentage flap force loss C should increase monotonically to unity as AR decreases, i.e., as the deviation from two-dimensionality increases. In the absence of more information for partial span flap effect, an approximation for (1-C) for design purposes is indicated by the broken line on Figure 46.

SEMI-EMPIRICAL CORRELATIONS FOR TURBULENT SEPARATED FLOW

The distance and pressure parameters as shown on Figure 28 are again used to describe the pressure profile. The methods used to obtain the correlations for turbulent flow are virtually identical to those used in the laminar problem. The correlations cover a Mach number and Reynolds number range of M_α = 1.5 to 6.2 and $Re_{\alpha x_o}$ = 7 x 10^5 to 6 x 10^6, respectively.

Plateau Pressure, P_P

The plateau pressure is defined as the approximately constant pressure reached in the separated flow region. Using the parameters suggested by theory and by previous correlations, $(C_{P_\alpha})_P$ was taken to be a function of $Re_{\alpha x_o}$ and M_α. The correlation was obtained by plotting $(C_{P_\alpha})_P\ Re_{\alpha x_o}^{1/10}$ versus $(M_\alpha^2 - 1)$. This led to an expression for $(C_{P_\alpha})_P$ of the form

$$(C_{P\alpha})_P = \frac{K(M^2\alpha - 1)^n}{\left(Re_{\alpha x_o}\right)^{1/10}}$$

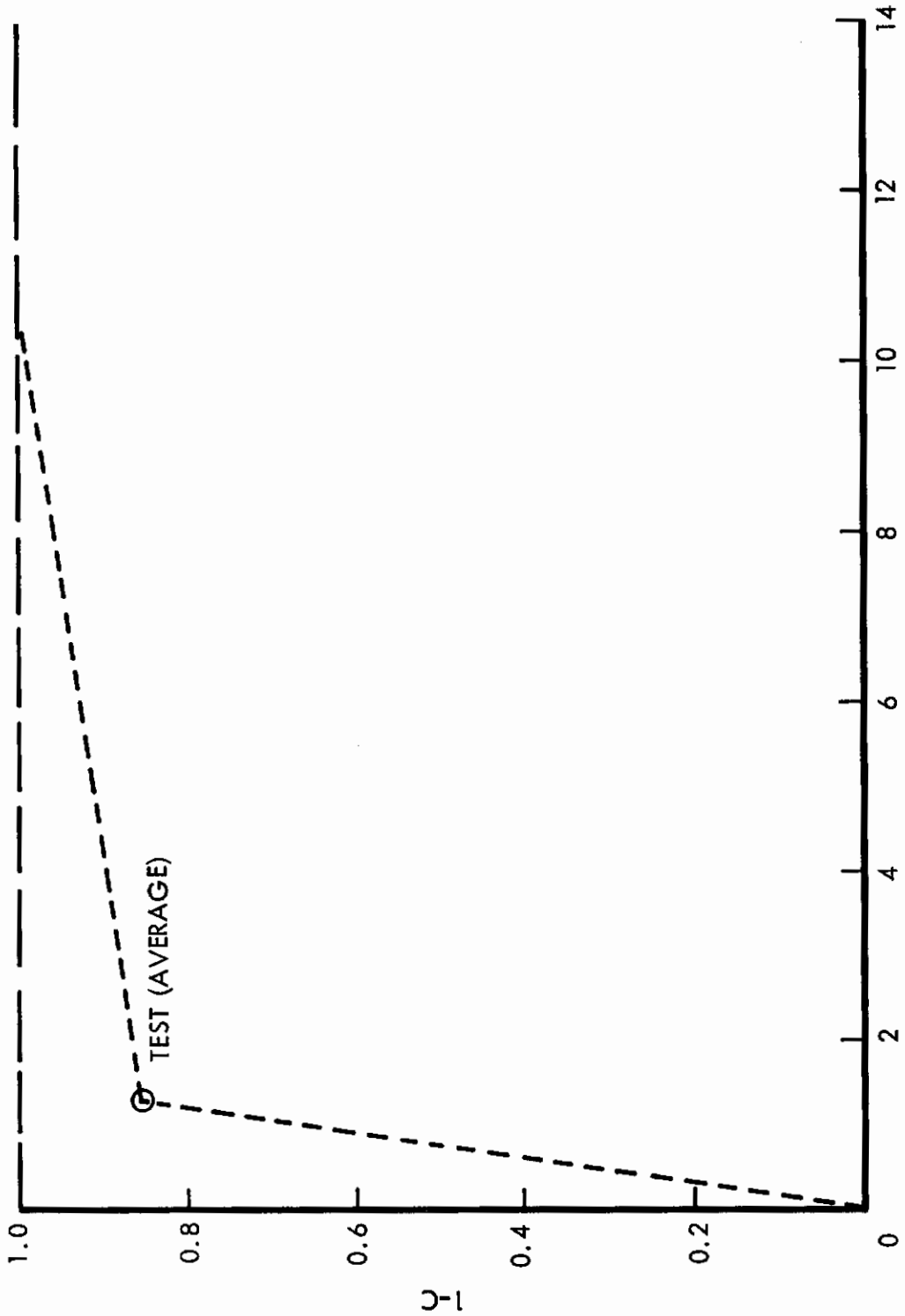

Figure 46. Finite Span Flap Force Expressed as a Fraction of the Two-Dimensional Result

where K and n were determined from the plot in Figure 47 by finding an equation for a straight line drawn through the data. The following expression for $(C_P)_P$ was obtained.

$$(C_{P\alpha})_P = \frac{\left(\frac{P_p}{P_o} - 1\right)}{\frac{\gamma}{2} M_\alpha^2} = \frac{1.91 \ (M_\alpha^2 - 1)^{-.309}}{(Re_{\alpha x_o})^{1/10}} \qquad (30)$$

Upstream Distance Parameter, d_1

The quantity d_1 was correlated by assuming the functional relation:

$$d_1 = f\left(M_\alpha, \ Re_{\alpha x_o}, \ \frac{P_p - P_o}{P_o}\right)$$

The distance d_1 was non-dimensionalized by the boundary layer thickness, δ_o, where:

$$\delta_o = \frac{.154 x_o}{\left[Re^*_{\alpha x_o}\right]^{1/7}}$$

From a plot of (d_1/δ_o) versus $(P_P/P_o - 1)$ a function of the form

$$\frac{d_1}{\delta_o} = F(M_\alpha)\left(\frac{P_p}{P_o} - 1\right)^n$$

was inferred, and both n and $F(M_\alpha)$ were obtained. The reduced test results are shown in Figure 48. The resulting final equation for d_1 has the form

$$\frac{d_1}{\delta_o} = 1.1 \times 10^6 \left[M_\alpha^{-1.67}\left(\frac{P_p}{P_o} - 1\right)\right]^{8.55} \qquad (31)$$

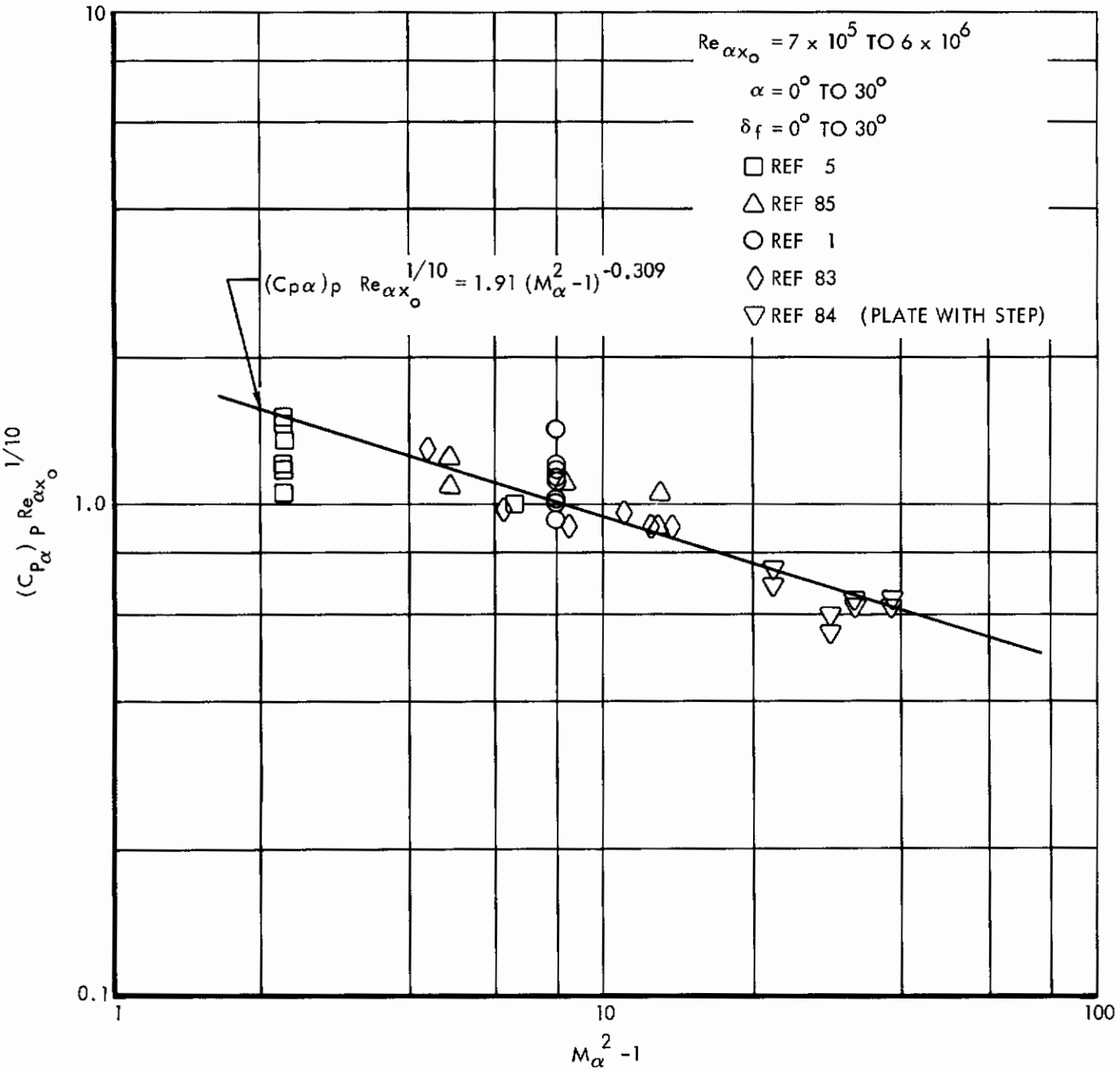

Figure 47. Plateau Pressure Correlation for Turbulent Corner Flow and Plate with Step (with Sharp Leading Edge Base Plate)

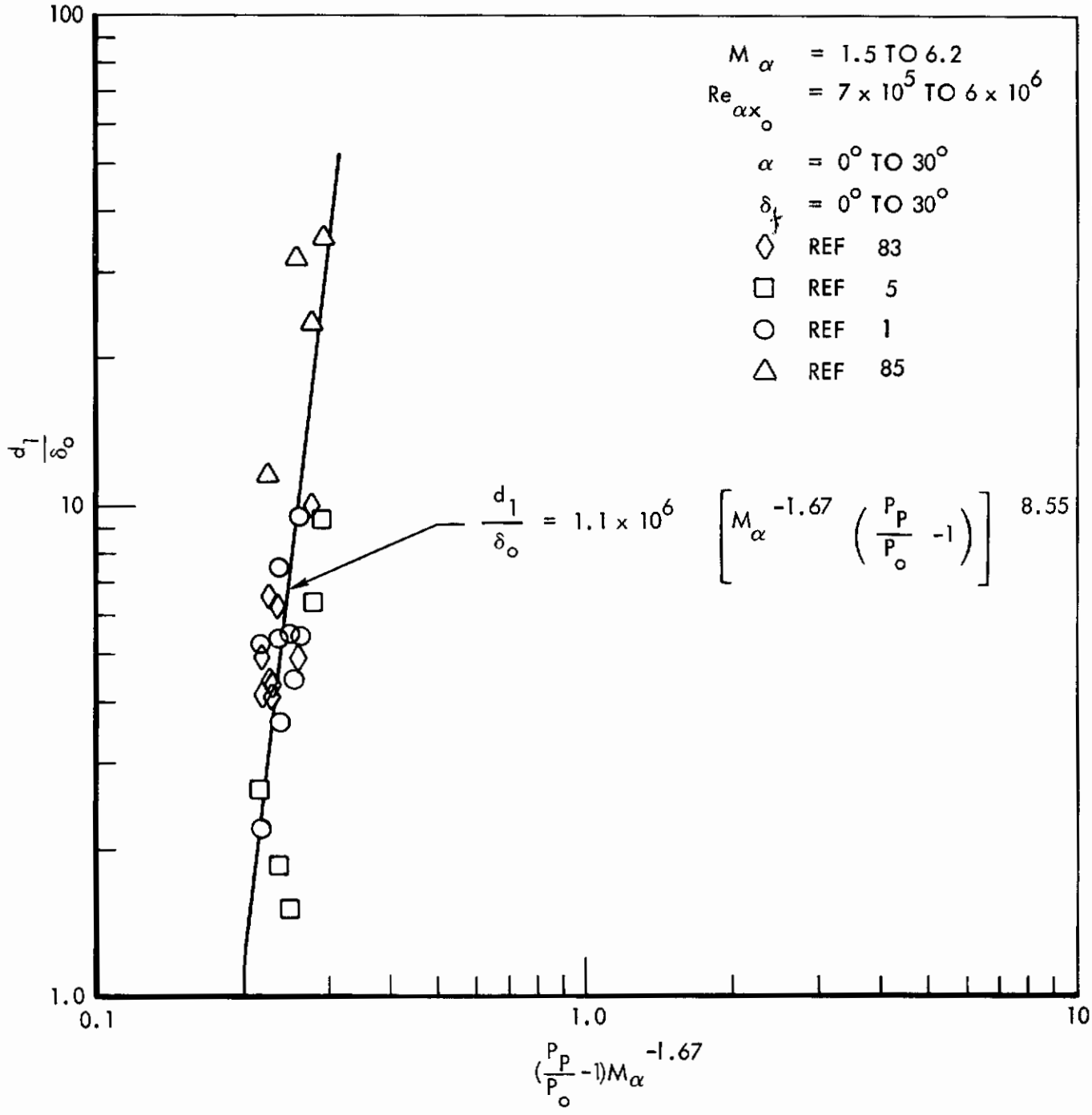

Figure 48. Upstream Interaction Length Correlation for Turbulent Corner Flow (with Sharp Leading Edge Base Plate)

Free Interaction Length, ℓ_{fi}

The determination of ℓ_{fi}, the free interaction length, followed a procedure identical with the determination of d_1. A functional relation of the form

$$\frac{\ell_{fi}}{\delta_o} = F(M_\alpha)\left(\frac{P_p}{P_o} - 1\right)^n$$

where $F(M_\alpha) = KM_\alpha^m$, was found. The exponent and constants were obtained from Figure 49.

The resulting equation for ℓ_{fi} is

$$\frac{\ell_{fi}}{\delta_o} = 1.84 \times 10^4 \left[\frac{\frac{P_p}{P_o} - 1}{M_\alpha^{1.325}}\right]^{8.40} \qquad (32)$$

Downstream Interaction Length to Peak Pressure, d_2

The downstream distance parameter d_2 indicates the location where pressure reaches the final peak flap value, as indicated in Figure 28.

Method 1. A functional relationship in the form

$$\frac{d_2}{d_1} = F(\delta_f)\ (M_\alpha \delta_f)^m$$

was used for correlation. A plot of d_2/d_1 versus $M_\alpha \delta_f$ led to a dependence on flap angle

$$F(\delta_f) = K(\delta_f)^n$$

The final relation was therefore of the form

$$\frac{d_2}{d_1} = K(\delta_f)^n\ (M_\alpha \delta_f)^m$$

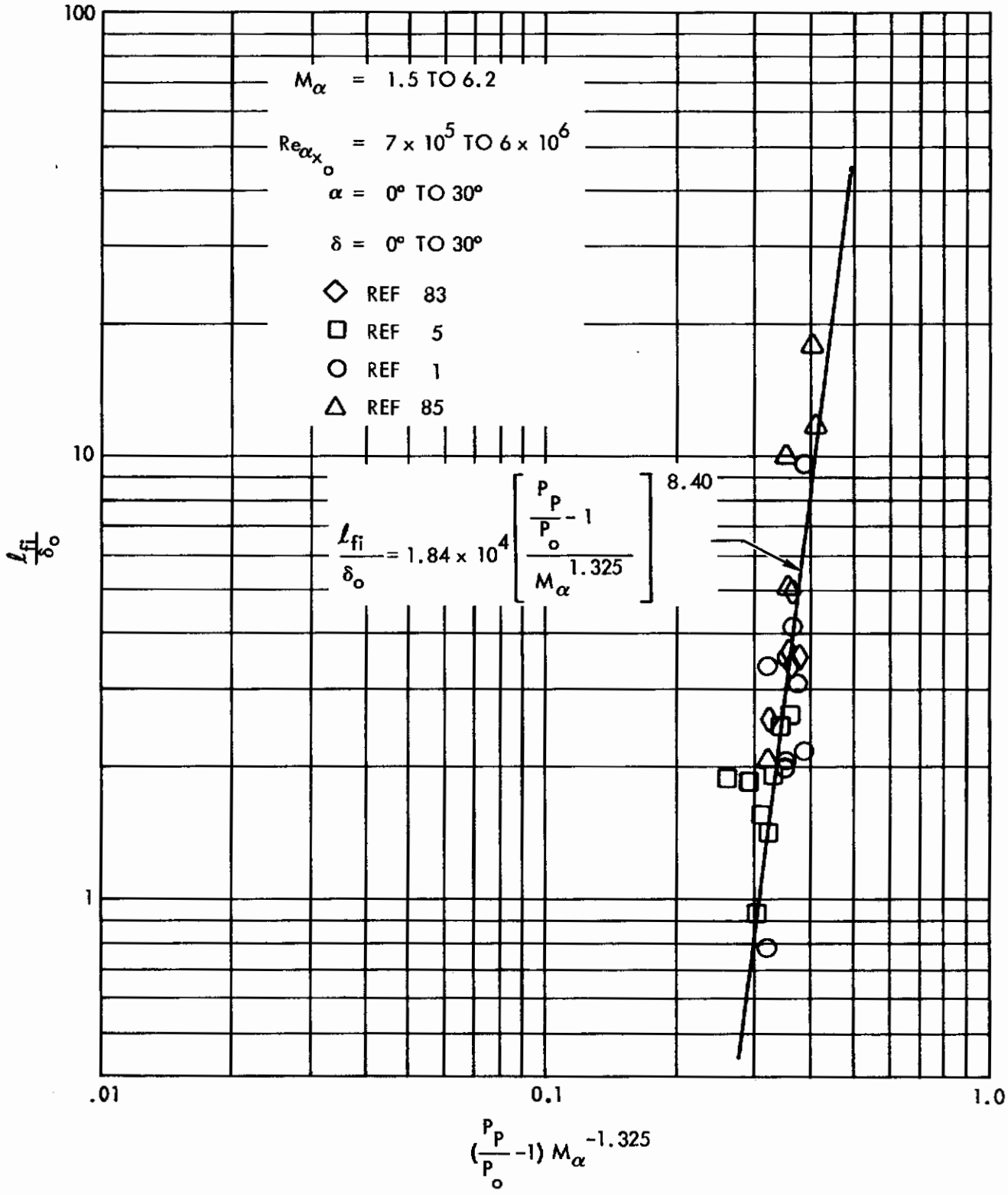

Figure 49. Free Interaction Length Correlation for Turbulent Corner Flow (with Sharp Leading Edge Base Plate)

The best fit to the data was given by

$$\frac{d_2}{d_1} = 2.8 \times 10^{-5} \left[M_\alpha (\delta_f)^{-1.52} \right]^{4.934} \qquad \text{(Figure 50)}_{(33)}$$

where δ_f is expressed in radians. The formula is based on test results for $\delta_f < 15^\circ$, $M_\alpha = 1.5$ to 6.2 and $Re_{\alpha x_o} = 7 \times 10^5$ to 5.6×10^6.

Method 2. An alternate approach leads to an expression for d_2/d_1 as a function of $M_\alpha \delta_f$ and flap length ratio, of the form

$$d_2/d_1 \frac{1}{\sqrt{\frac{C_{flap}}{d_1}}} = 1.16 - 0.33 M_\alpha \delta_f \qquad (34)$$

For meaningful results the following limits are recommended:

For $\frac{C_{flap}}{d_1} \geq 1$: $d_2/d_1 = 1.16 - 0.33 M_\alpha \delta_f$.

For $\frac{C_{flap}}{d_1} \leq 0.25$: $d_2/d_1 = 0.58 - 0.165 M_\alpha \delta_f$.

For $M_\alpha \delta_f \geq 2.4$: $d_2/d_1 \frac{1}{\sqrt{\Gamma}} = 0.37$,

where

$$\Gamma = \begin{cases} 1, \text{ for } \frac{C_{flap}}{d_1} \geq 1 \\ \frac{C_{flap}}{d_1}, \text{ for } 1 \geq \frac{C_{flap}}{d_1} \geq 0.25 \\ 0.25, \text{ for } \frac{C_{flap}}{d_1} \leq 0.25 \end{cases}$$

This formulation may be used for a wider range of flow conditions than that of Method 1.

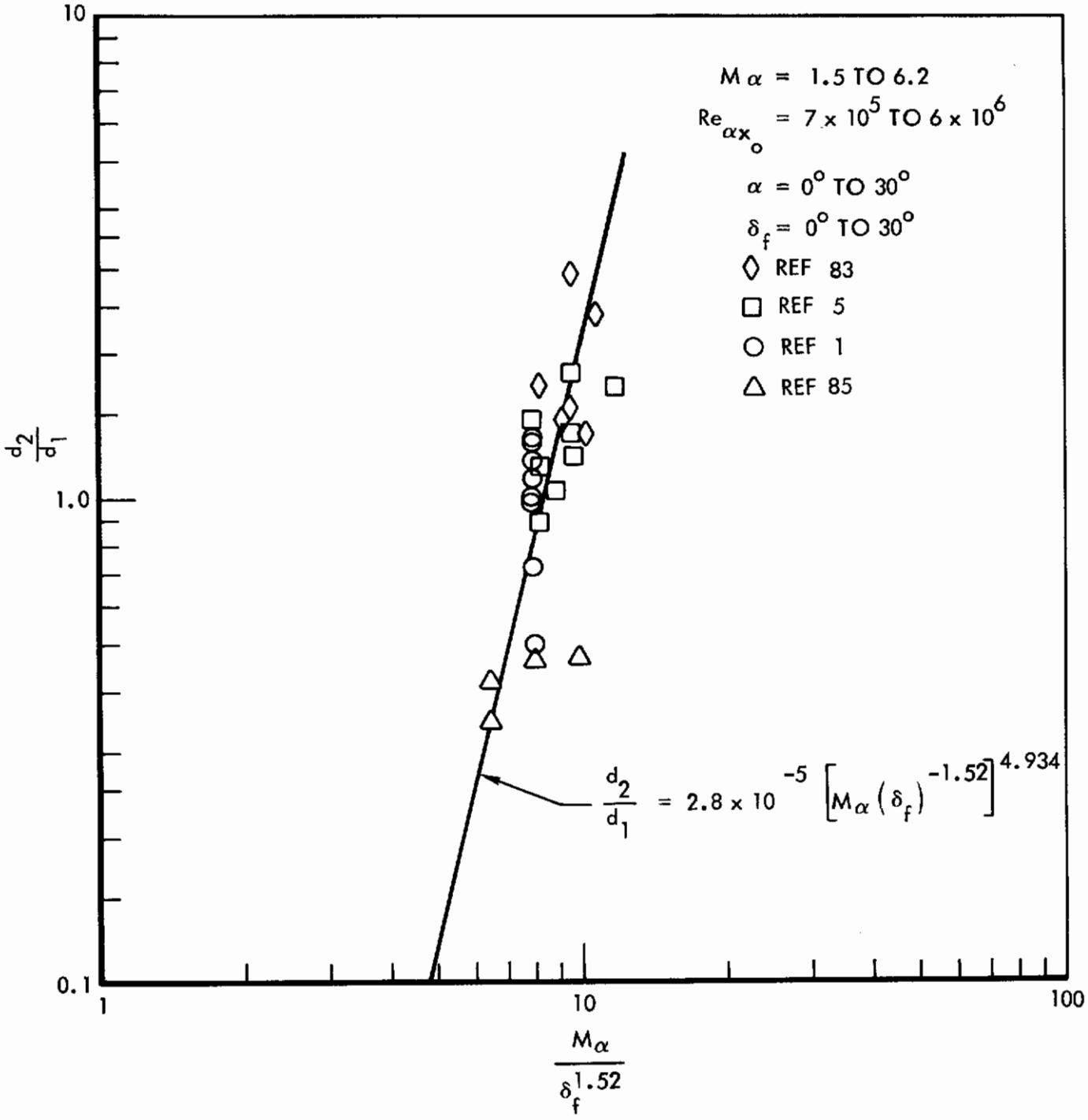

Figure 50. Downstream Interaction Length for Turbulent Corner Flow (with Sharp Leading Edge Base Plate)

Downstream Interaction Length to Pressure Rise, d_3

Examination of the test data used in this study led to the conclusion that d_3 can be taken as zero for the turbulent case. It will be recalled that this parameter indicates the beginning of the rise from the plateau level to the final flap pressure.

Peak Flap Pressure, P_2

The less extensive separation region typical of turbulent flow allows the use of the single shock method to determine the pressure level P_2. This pressure value can therefore be obtained from Reference 36 using the local Mach number value M_{α} as suggested in Section III.

Conditions at Separation, P_s and ℓ_s

The separation position, ℓ_s, again defined by $\left.\frac{\partial u}{\partial y}\right|_w = 0$, may be approximated by d_1 for turbulent flow. The associated pressure coefficient was found to be (Figure 49)

$$(C_{p_{\alpha}})_s = \frac{1.14\,(M^2_{\alpha-1})^{-0.3}}{(Re_{\alpha x_o})^{\frac{1}{10}}} \qquad \text{(Reference 6)} \qquad (35)$$

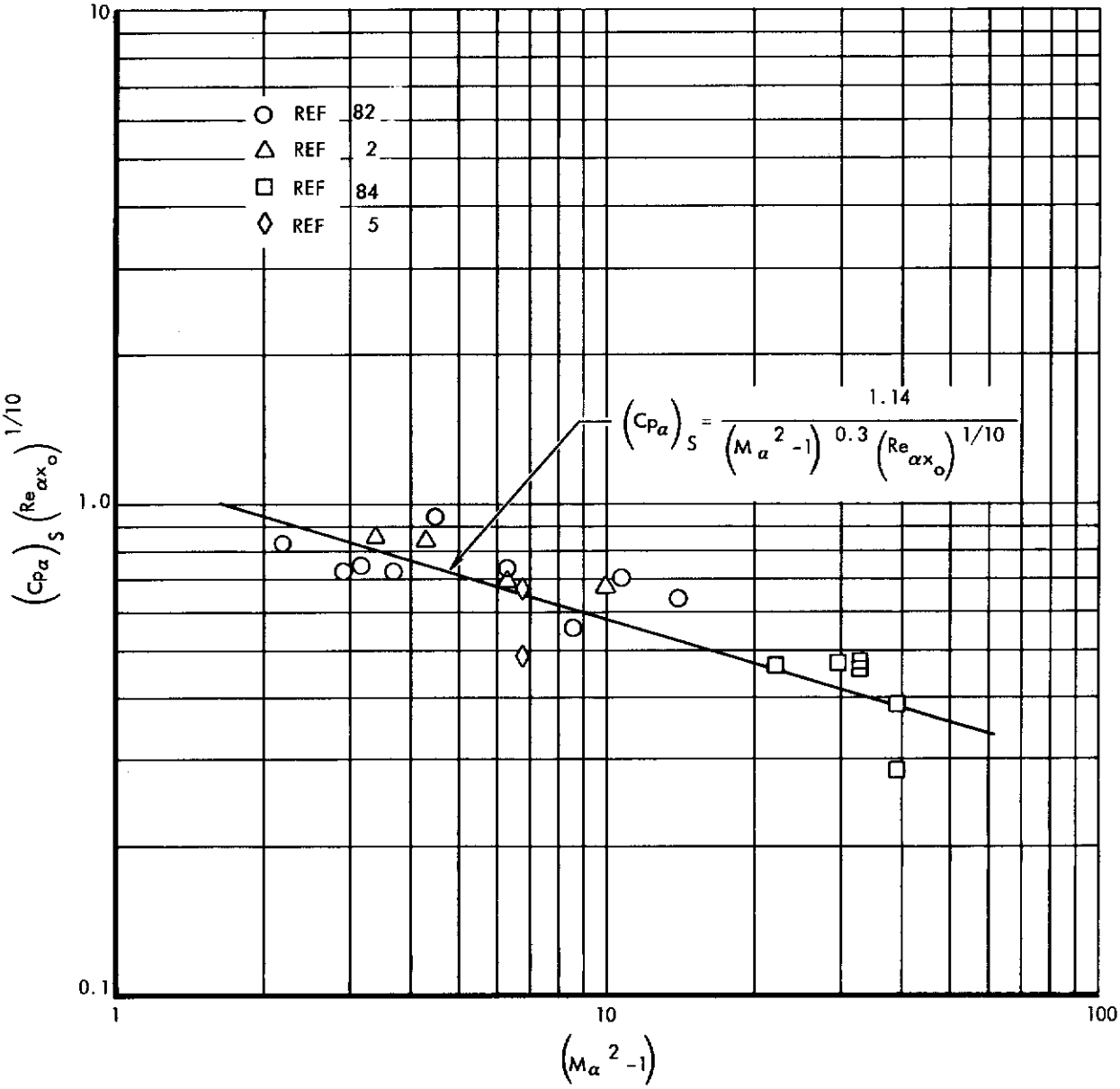

Figure 51. Pressure at Separation for Turbulent Flow

Section V

FLOW SEPARATION ON VARIOUS CONFIGURATIONS

The semi-empirical correlations for separated flow described in the previous section were derived from experimental results for two-dimensional bodies. Although two-dimensional bodies as vehicle elements are of considerable importance, actual vehicles are more complex and the flow is three-dimensional in character. In this section separated flows on fin-plates, flat surfaces with compression flaps and endplates, and delta wings and their variations are discussed. Three-dimensional features of flow about pseudo-two-dimensional bodies of finite size are discussed qualitatively with the aid of visual data.

FIN-PLATE CONFIGURATION

Vertical fins and control surfaces are employed on various types of hypersonic vehicles, such as those designed for aerodynamically maneuverable reentry missions. Shock waves and pressure rises induced by such devices at finite incidence will be transmitted to the adjacent surfaces on the vehicle thus modifying the flow fields there. The problem of a fin-generated shock sheet impinging normally upon a surface with a boundary layer is of interest from both an aerodynamic and thermodynamic point of view. The abrupt pressure rise across the shock in real flow is diffused and spread over some finite distance. Figure 52 shows a simplified model of the interaction region.

Choice of Coordinate System

In attempting to devise a set of correlations for the fin-plate pressure distribution, as was done in the deflected flap case, it must be realized that one is dealing with a basically three-dimensional flow. The impinging shock sheet is considered to be perpendicular to the plate surface, but it is not, in general, normal to the local velocity vector. The question arises as to whether for the correlation purpose one should consider pressure distribution in the initially streamwise direction or proceed in a direction normal to the impinging shock.

Even though the flow behind the shock is not aligned in the original stream direction, the one-dimensional assumption may be a good approximation (as long as the flow deflection angle is not too large).

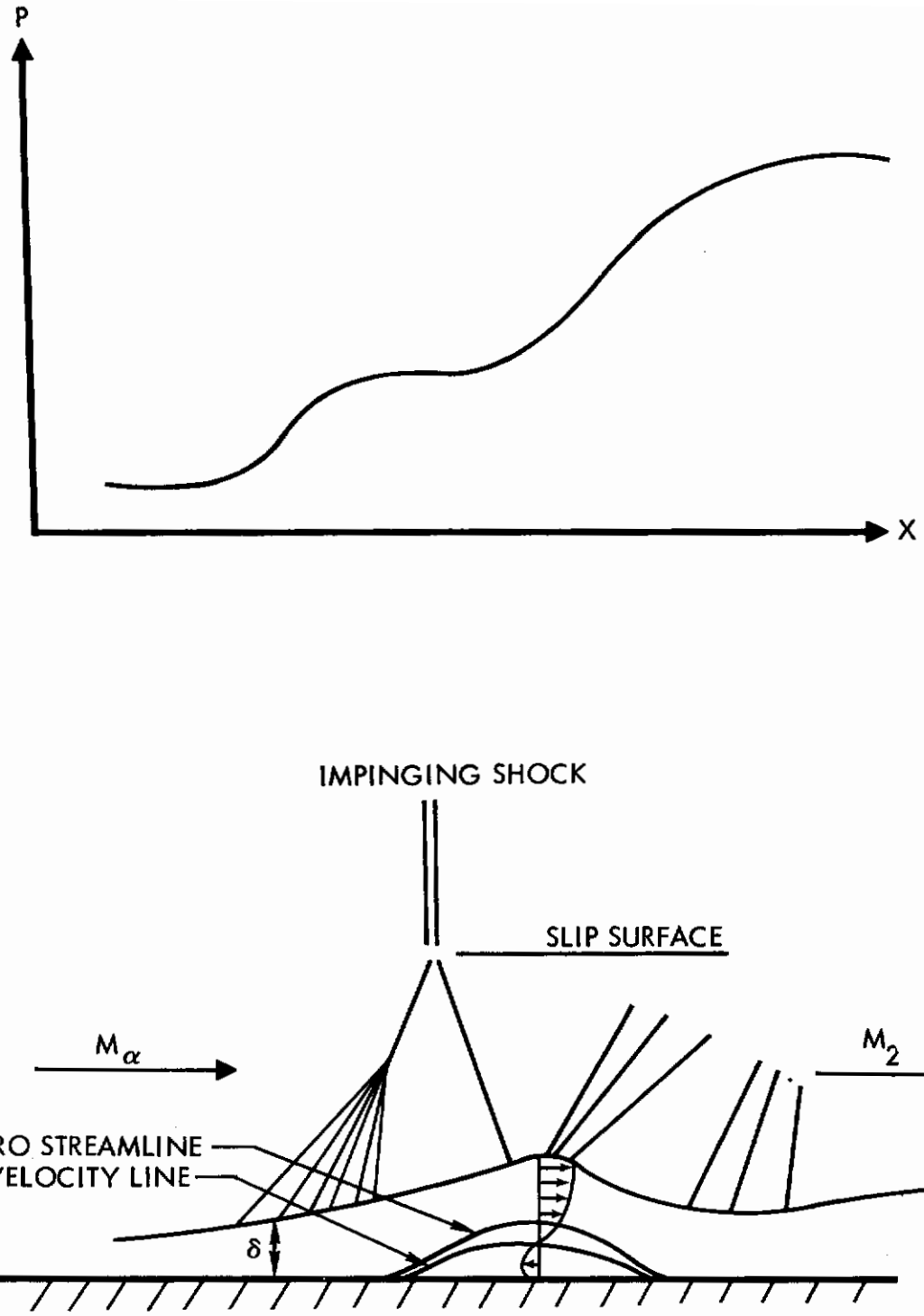

Figure 52. Detail of Shock Impingement Interaction

Correlations in the direction normal to the shock, assuming that the tangential velocity component does not change across the shock and does not have significance for the external inviscid flow (Reference 26), may not be valid for the boundary layer, where the tangential velocity varies.

Analysis of Experimental Results

Experimental Procedure. The model employed in the experimental study of fin-plate interaction (Reference 87) is shown in Figure 53. The fin or wedge which generates the impinging shock has a semivertex angle of 15°. Actually, data have been taken on models of four different configurations, as there are tall and short, sharp and blunted fins. Pressure taps are scattered on one side of the plate surface and one side of the fin (the other half of the model is instrumented with thermocouples). Unit Reynolds numbers are varied moderately, with the Deem-Murphy criterion indicating that boundary layers are probably laminar (Section 4). Considerable variation of the local Mach number is accomplished by angle of attack variation. Because of the pressure instrumentation arrangement, the most informative runs were those of $M_\infty = 5$ and $\alpha = 5°$, i.e., $M_\alpha = 4.5$.

Shock Wave and Boundary Layer Effects. Figure 53 depicts part of the system of shocks that is produced when the model is pitched at some compression angle of attack in the high speed flow. One shock sheet extends downstream from the leading edge of the plate; it will intersect another shock sheet generated by the fin, assuming the fin is tall enough. The intersection ideally results in the production of a new shock system which in general undergoes subsequent impingements and intersections.

It appears that the simple flow regions as noted on Figure 53 are adequate as initial and final conditions for the interaction problem examined here. In particular, the "α" region is considered to be the result of turning the free stream to the plate surface inclination. The "w" region is considered to be the result of turning the free stream to the direction of the fin side. The "2" region is considered to be the result of turning the "α" flow to the direction of the fin side. Therefore the initial and final conditions for the study of the plate pressure distribution through the impinging shock are the conditions of region "α" and the conditions of region "2" (Figure 53). This seems to work fairly well in most cases. There is generally some pressure overshoot before the region "2" conditions are reached. Also, the viscous induced deviation of the pressure ratio P_α/P_∞ from unity in zero angle of attack cases is best represented by isentropic compression for the Mach number range tested.

It will be seen that the boundary layer acts at all times to smooth out pressure differences. Also, the boundary layer on the fin complicates the examination of the interaction on the plate; an effective curvature of the fin surface introduced by the parabolic ($\delta \sim \sqrt{x}$) growth of the boundary layer causes the shock to curve.

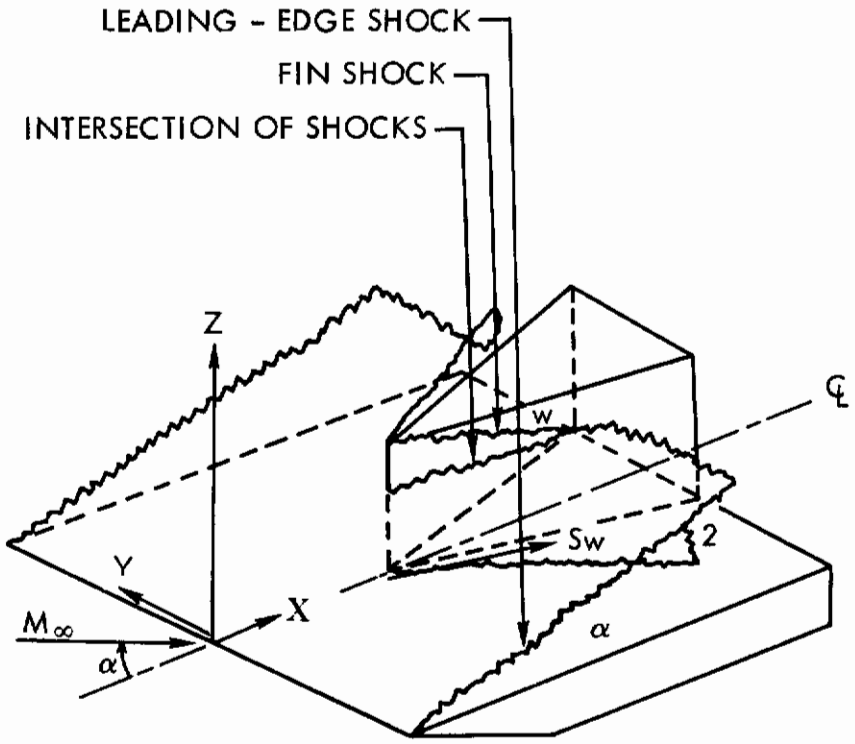

α - FLOW COMPRESSED BY LEADING EDGE SHOCK

w - FLOW COMPRESSED BY FIN SHOCK

2 - FLOW COMPRESSED BY LEADING EDGE SHOCK AND THEN BY FIN SHOCK

Figure 53. Fin-Plate Configuration with Intersecting Shocks and Simple Flow Regions

Plate Pressure Distributions for Sharp Fin. A limiting factor in the analysis of the tests is the spacing between pressure taps; more taps are required in order to get a detailed picture of the pressure distribution through the region of the impinging fin-induced shock..

A combined or aggregate pressure distribution, for deriving the maximum of information from the data, can be constructed as follows. The position of the impinging, fin-produced shock is estimated as well as possible, as the locus of the straight oblique shock that would be produced by turning the "α" flow through the angle δ. Then, all the pressure tap readings are plotted against streamwise or normal-to-shock tap distance from the assumed shock locus, on a single set of axes.

Figures 54 and 55 indicate the effect of fin side boundary layer. The same pressures are plotted in Figure 55 as in Figure 54, but this time against slightly different relative streamwise coordinates, which were obtained by constructing a shock locus modified by introducing slight shock curvature expressed by $X_s(y)$, which gives each pressure tap a new relative position. Figure 56 uses the normal-to-shock direction for constructing the aggregate plate pressure distribution. It should be compared with Figure 57, which shows the distribution in the streamwise direction: the pressure profile normal to the shock shows less scatter and its scale is shorter. Although the plate pressure plots indicate that there is a region characterized by intermediate pressure values, it is not possible to identify a plateau level.

Sharp Fin Pressure Distribution. Figures 54 and 57, which show plate pressure distributions for the small and large fins, respectively, indicate that plate pressure is not influenced by fin height. Figure 53 indicates that pressure distributions up the sides of the fins will show variation between the "2" values and the "w" values. Representative results, shown in Figures 58 and 59, indicate that the pressure rise from P_w to P_2 through the shock interaction is spread out over an appreciable length. Figure 60 shows that the pressure distribution on the fin wall, for $\alpha = 0$, has a definite drop toward the corner. The P_2 value based on displacement effects is not reached at all.

No conclusions are here stated concerning the corner flow between the fin and the plate, as very dense instrumentation is required for a study of this region. (See Reference 61.)

Bluntness Effects. The effects of fin leading edge bluntness are examined through the plots of Figures 61 and 62. Figure 59 shows that the use of the ideal, sharp-leading-edge oblique-shock locus is no longer adequate, for it results in a greatly distorted representation of the plate pressure distribution. Figure 62 indicates higher pressure close to the blunted leading edge as a result of increased strength of the detached bow shock. The inviscid pressure P_2 is exceeded at the station closest to the nose.

Remarks on a High Mach Number Run. In Figures 63 and 60, pressure distributions for the model at zero angle of attack and $M_\infty = 8$ are presented. It is seen that, because of the viscous interaction effect, the pressure on the plate upstream of the fin is substantially larger than the free-stream

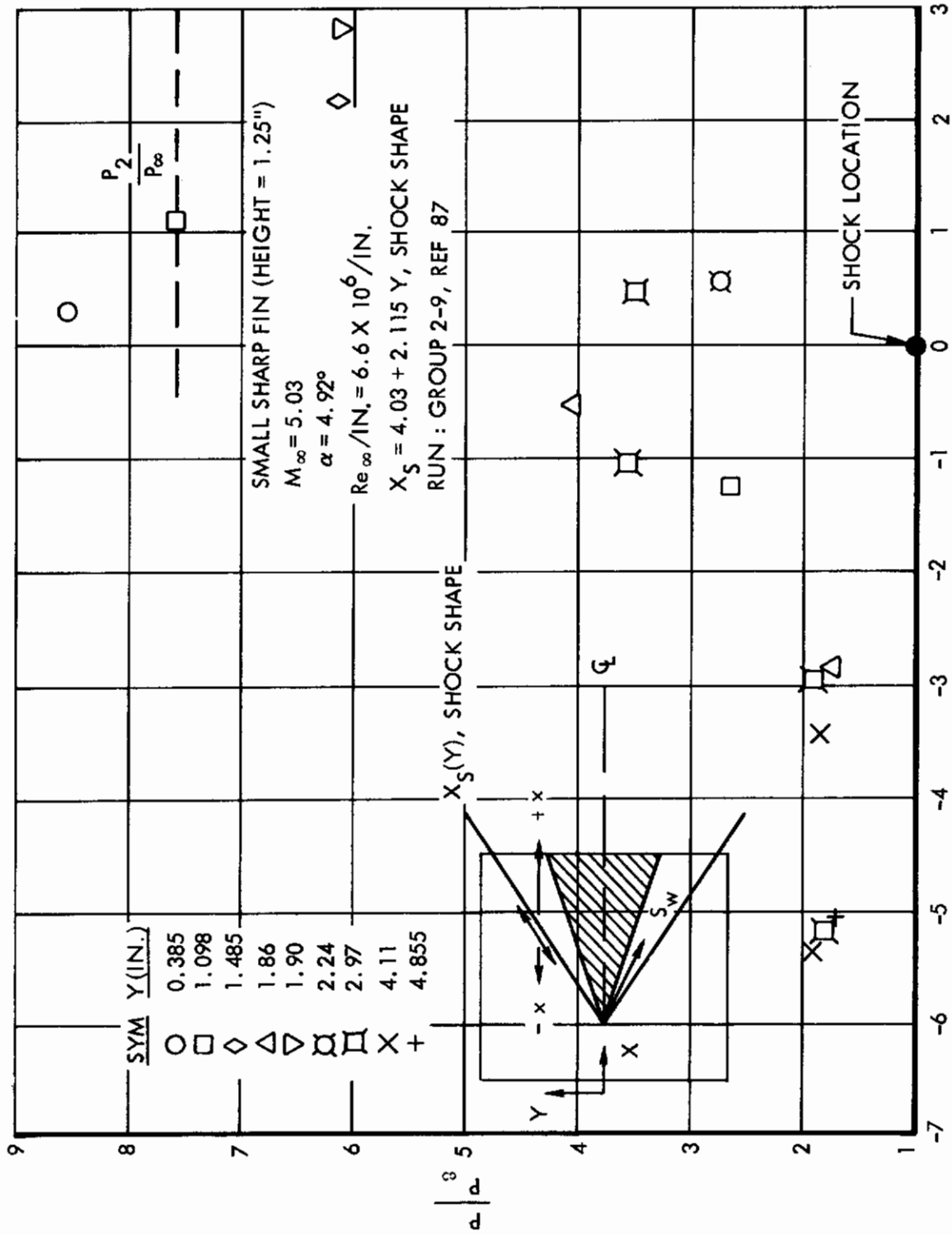

Figure 54. Aggregate Pressure Measurements in Free Stream Direction Along Plate with Impinging Normal Shock

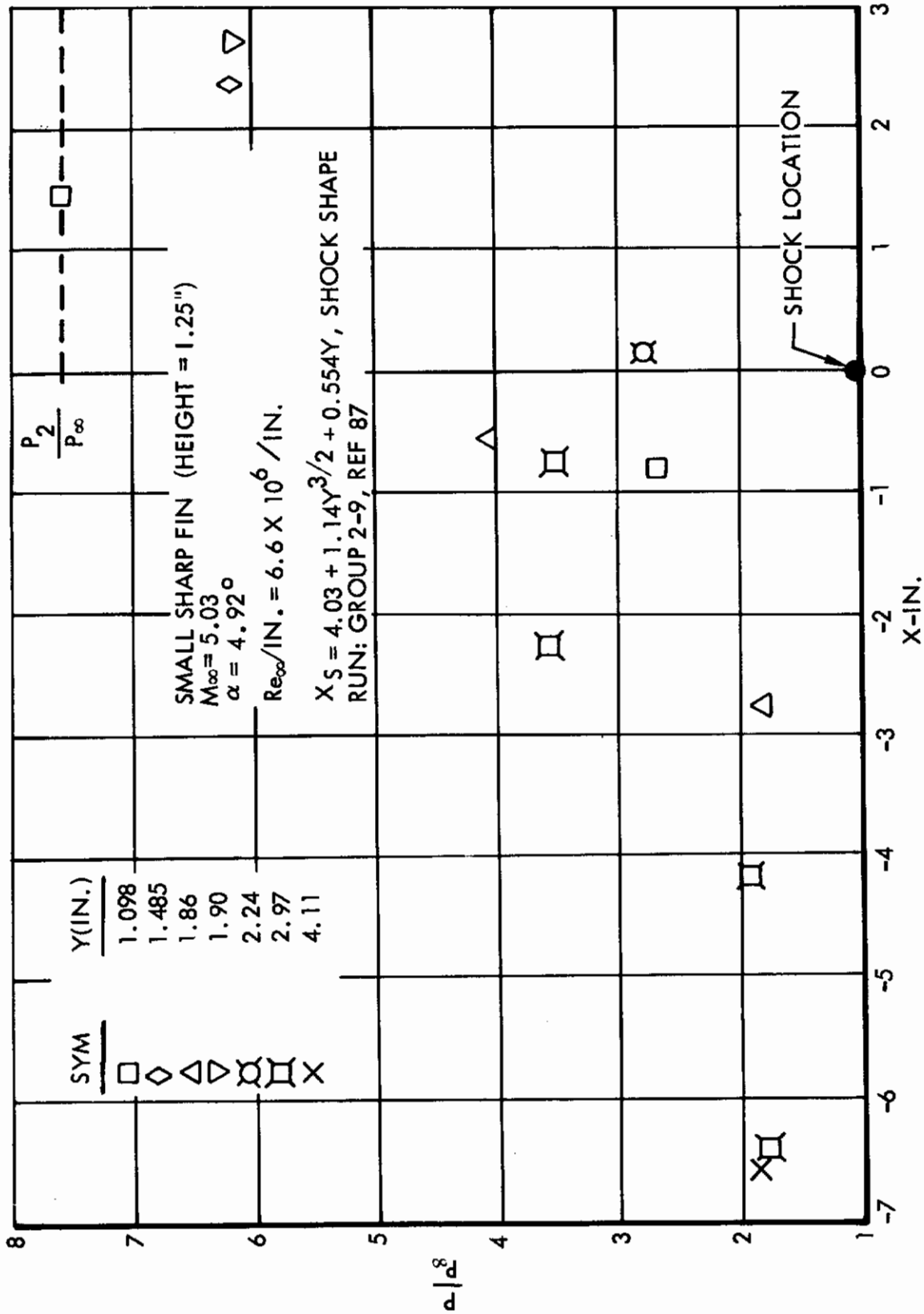

Figure 55. Aggregate Pressure Measurements in Free Stream Direction Along Plate with Impinging Normal Shock (Modified Shock Locus)

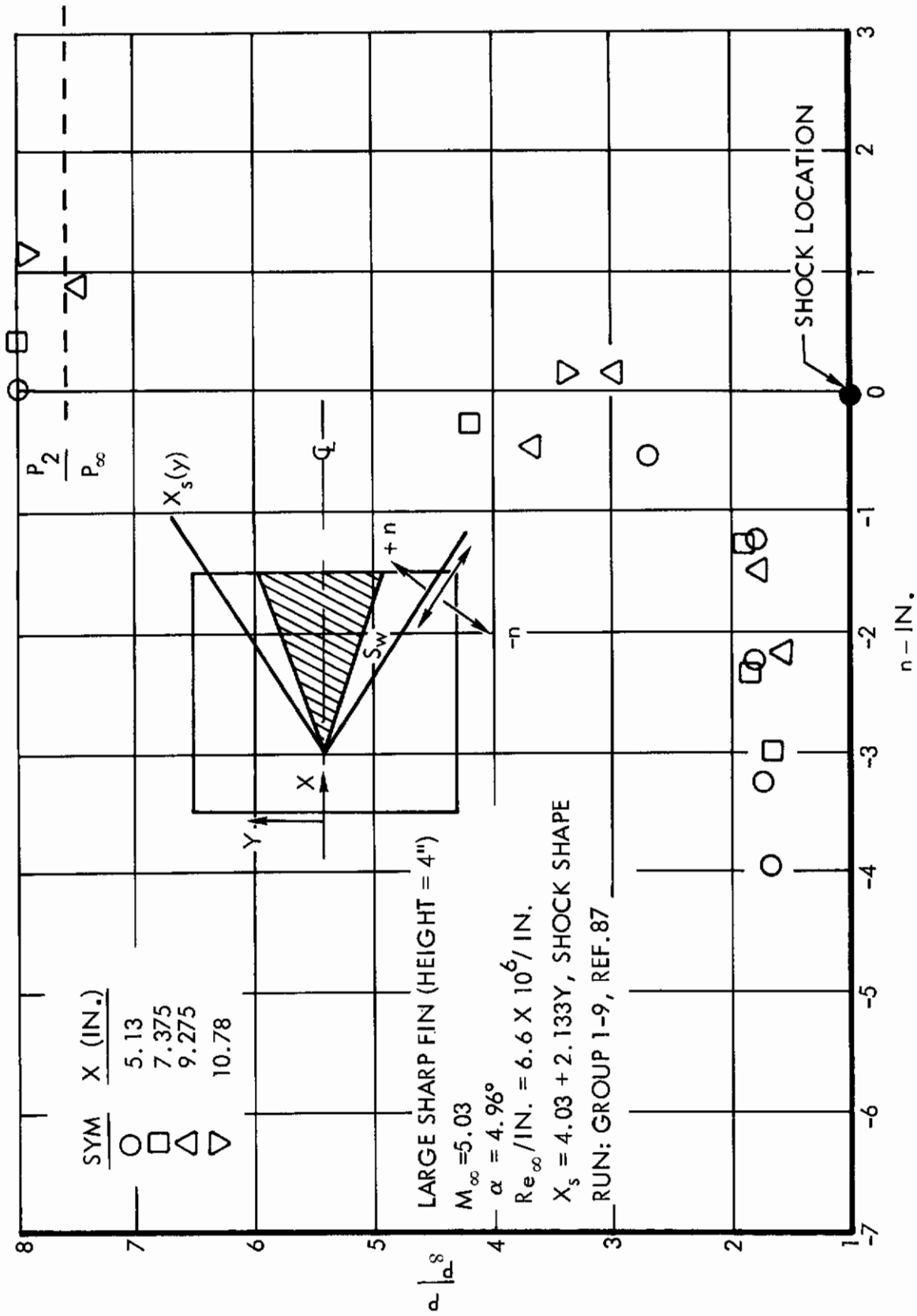

Figure 56. Aggregate Pressure Measurements Along Plate in Direction Normal to Assumed Locus of Impinging Normal Shock

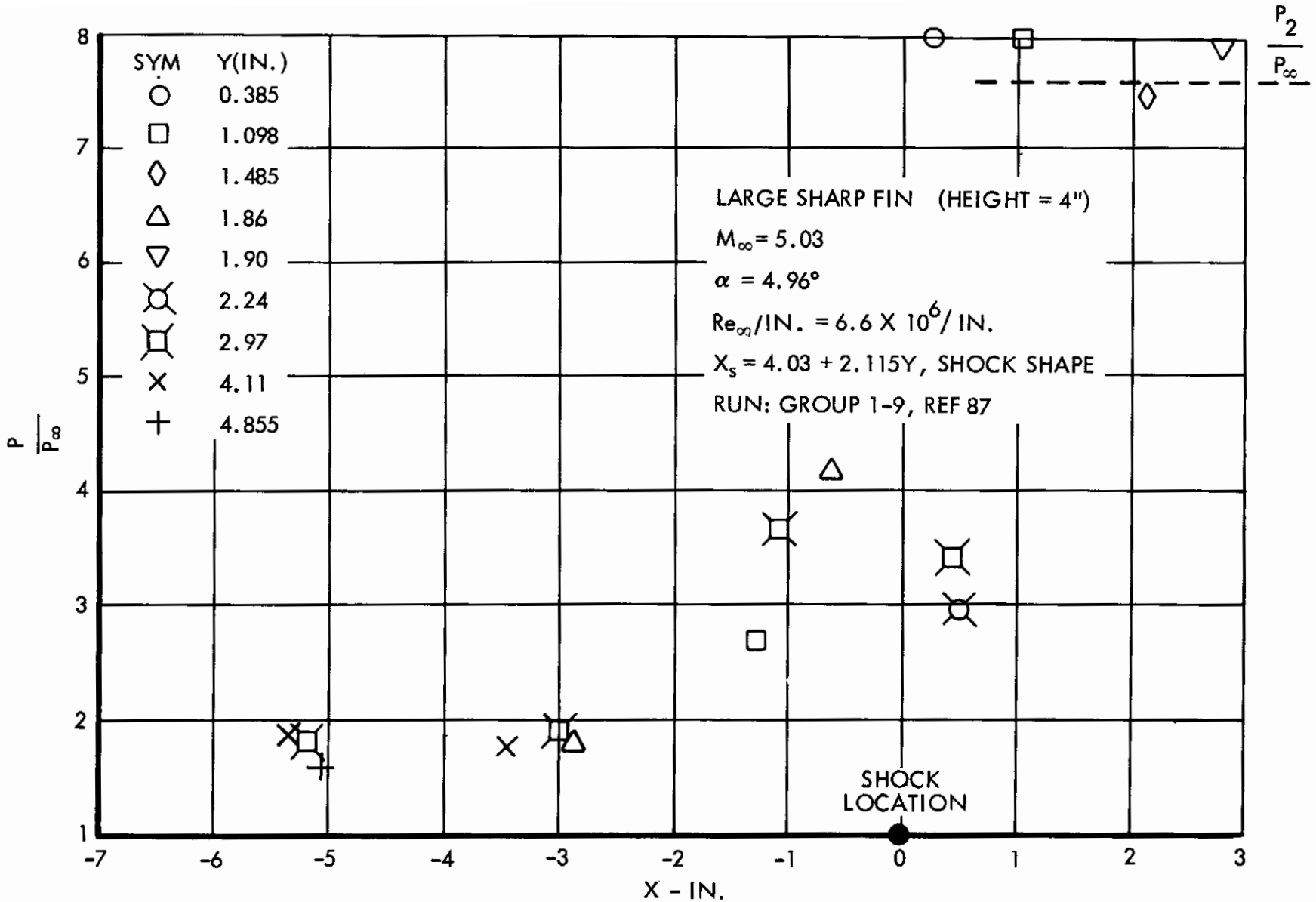

Figure 57. Aggregate Pressure Measurements in Free Stream Direction Along Plate with Impinging Normal Shock

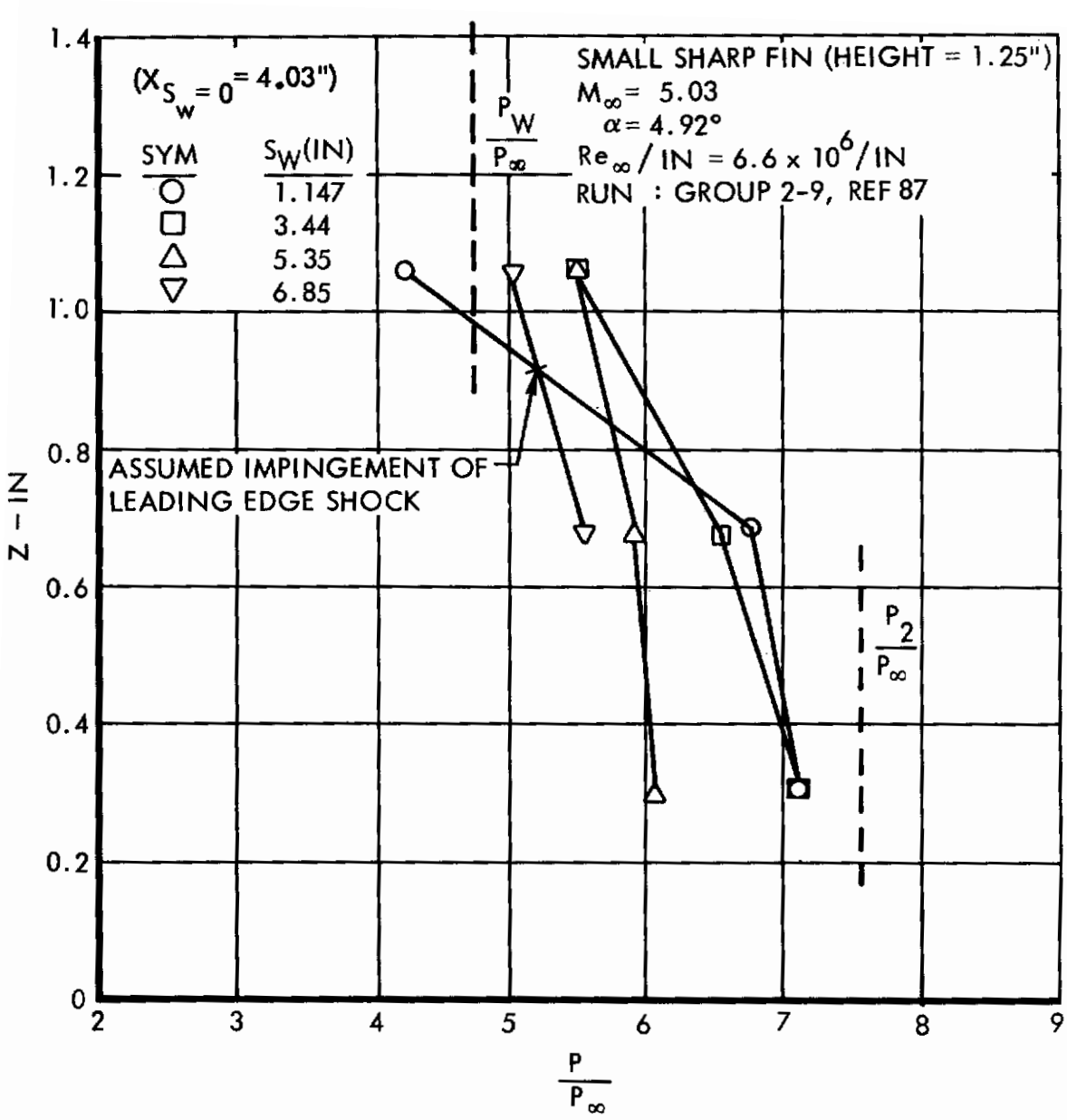

Figure 58. Pressure Distributions Along the Fin Side (Small Fin)

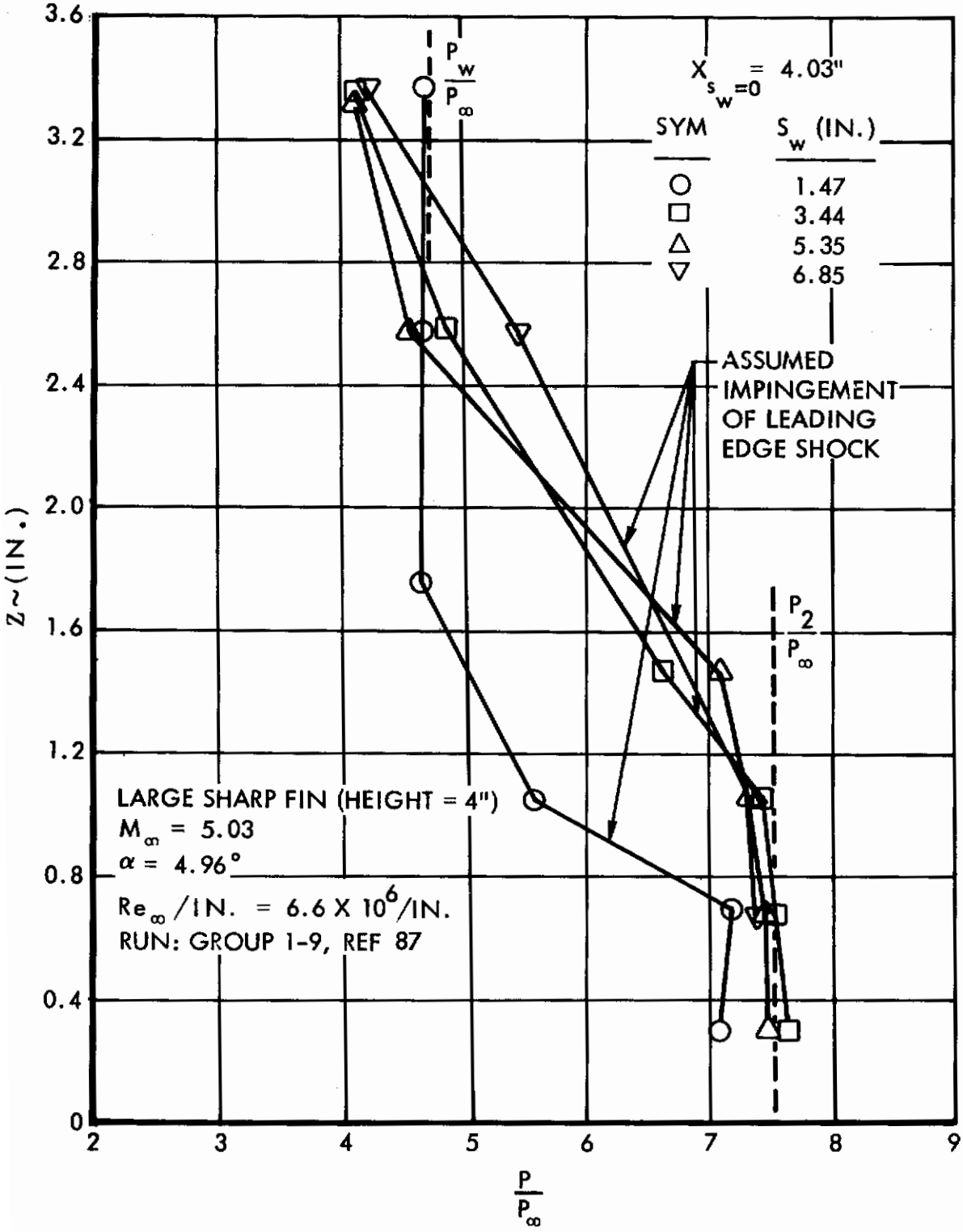

Figure 59. Pressure Distributions Along the Fin Side (Large Fin)

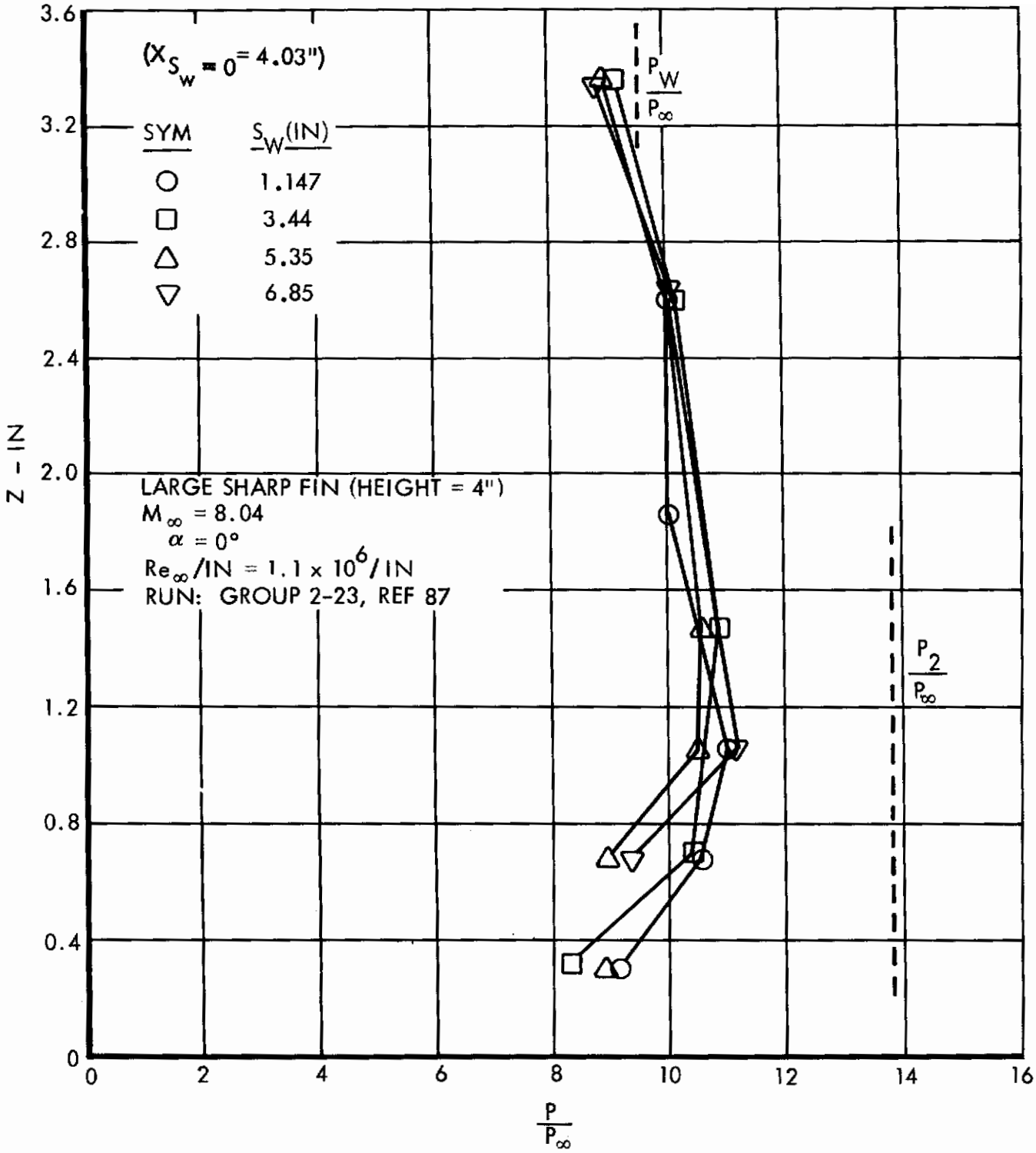

Figure 60. Pressure Distributions Along the Fin Side (High Mach Number)

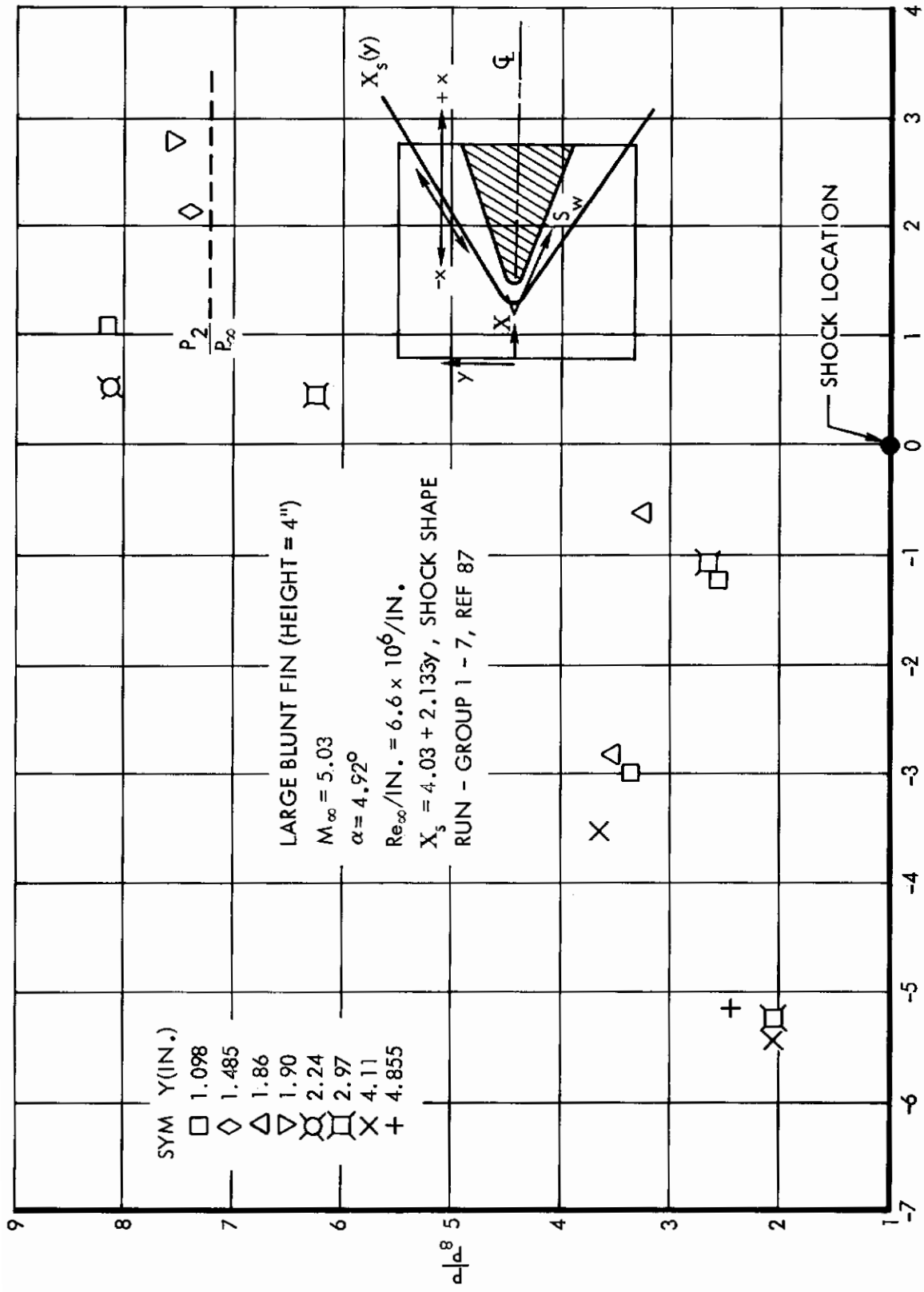

Figure 61. Aggregate Pressure Measurements in Free Stream Direction Along Plate with Impinging Normal Shock (Blunt Fin)

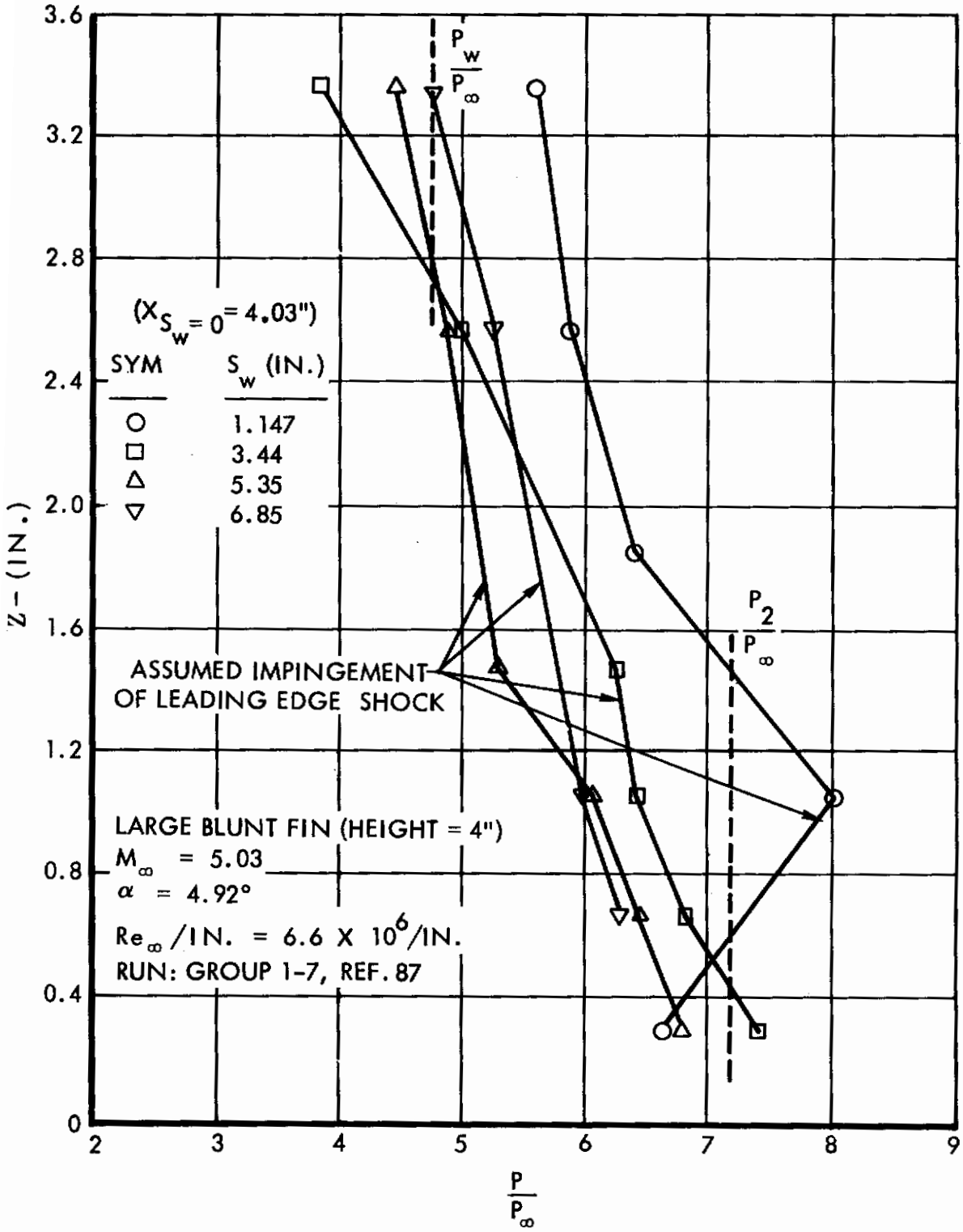

Figure 62. Pressure Distributions Along the Fin Side (Blunt Fin)

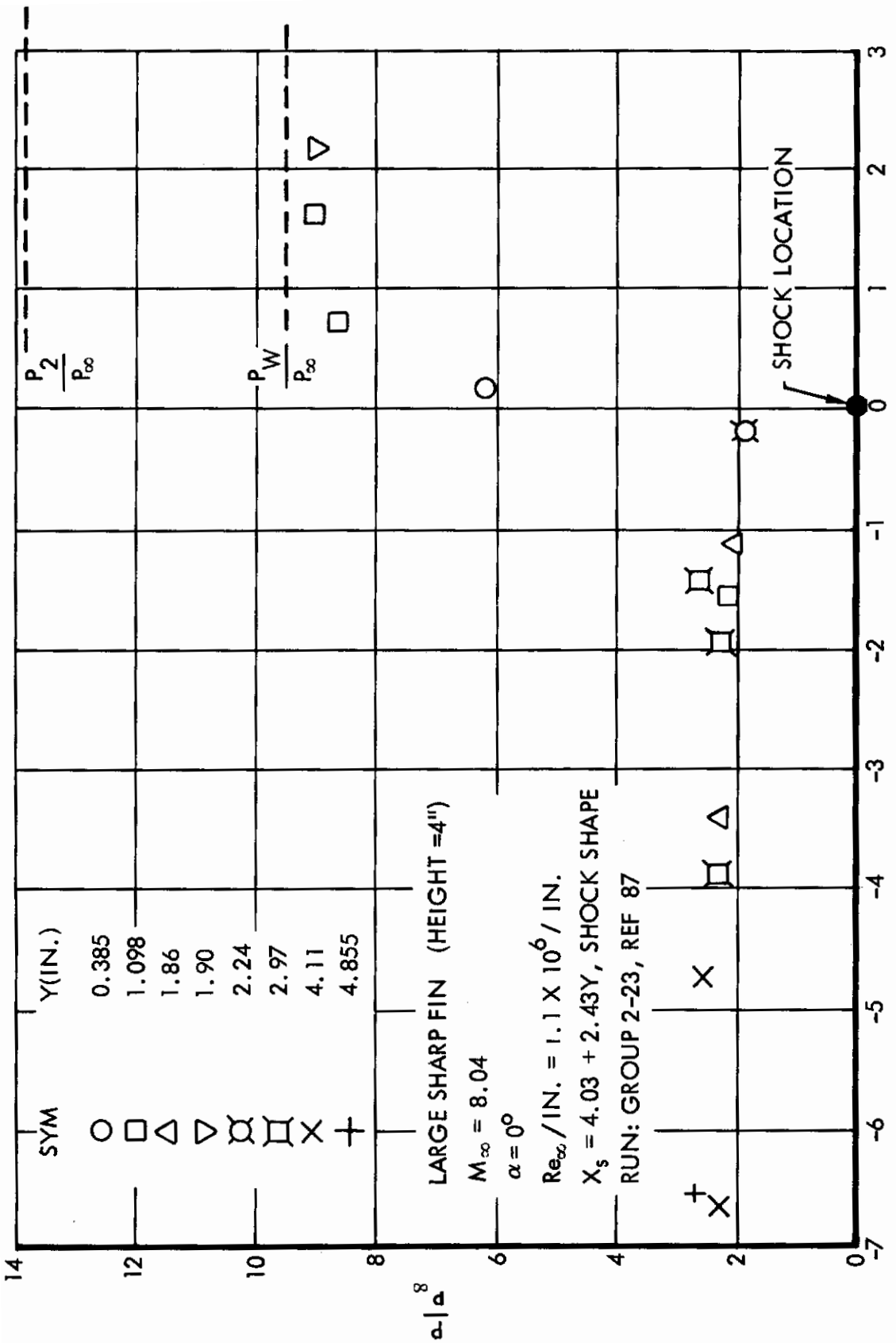

Figure 63. Aggregate Pressure Measurements in Free Stream Direction Along Plate with Impinging Normal Shock (Sharp Fin)

value. However, the dominant pressure downstream is the pressure that would be reached by a single shock turning from the free stream to the direction of the fin wall, i.e., P_w rather than P_2. Apparently the viscous displacement compression is insignificant for these configurations.

The high local Mach numbers in this case mean that shock surfaces are inclined rather acutely with the original free stream direction, and a longer-model with more downstream measuring points would be required to obtain a good view of the shock impingement interaction.

Conclusions. Figures 54 to 60 indicate that the interaction between the plate and fin gives neither a uniform pressure rise nor a single intermediate plateau pressure. Projection of measurements describing the interaction region on a plane normal to the shock plane seems to be feasible. However, a more complete set of measurements on a heavily instrumented model would be required. Understanding of the impinging shock interaction is necessary to allow correlation of the average pressure and overall spread of the interaction.

FLOW ABOUT A FLAT PLATE

Simple shapes are considered two-dimensional if their span-to-chord ratio is very large. However, actual vehicles are of finite dimensions, and body ends cause deviation of an actual flow from the idealized two-dimensional flow.

Flat Plate without End Plates

The tips of a finite "two-dimensional" body in a subsonic stream influence the pressure distribution on the entire body. At supersonic speed finite span effects are also important, but in a different way. For a flat plate at positive angle of attack, higher pressure on the compression side tends to equalize with the lower pressure on the top surface. However, this pressure equalization and propagation of disturbances is confined to the Mach cone. The resulting flow around the longitudinal edges with pressure differential leads to the generation of vortices, similar to those existing in subsonic flow, which are shed downstream and stay within the Mach cone. These vortices emanating at the tips of the body generate a typical circulatory flow indicated by steamlines in Figure 64.

A simple and illustrative example of end effects on a two-dimensional flow is a flow about a flat plate. Figures 65 to 71 are taken from the data of Reference 74. Figure 65 shows an oil flow pattern for a flat plate (with a sharp wedge as the leading edge) at zero angle of attack. This figure indicates a distinct flow dividing line radiating inboard from the tip, with the flow outside of this line directed toward the side edge, and the flow inboard of this line directed toward the centerline. Near the centerline the flow direction approaches the free stream direction. As a result of higher pressure on the bottom surface, a coiled vortex is generated at the tip and the flow spearates near the side edge. The vortex flow re-attaches forming an attachment line. Along this line the flow divides, turning either inward or outward, (Figure 66).

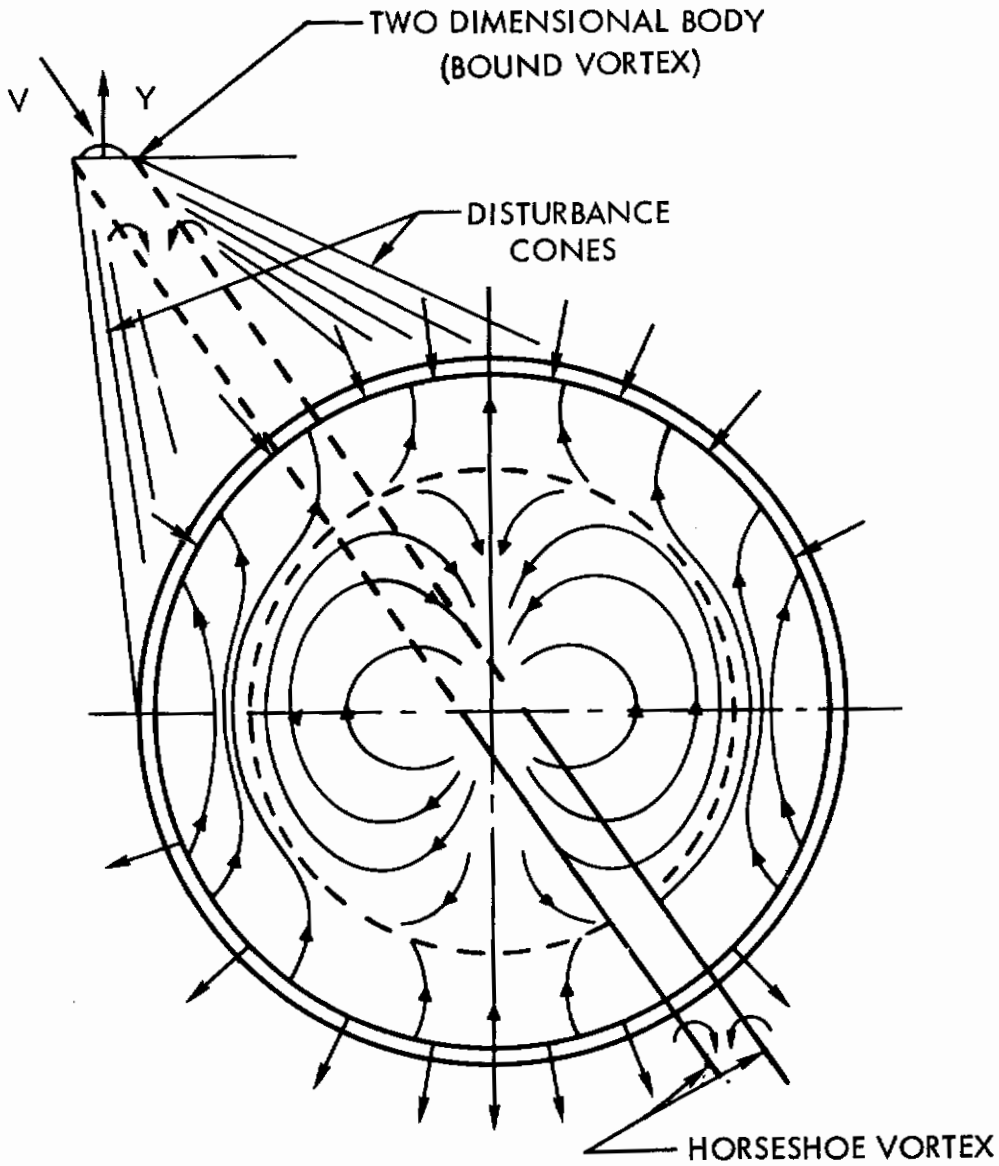

Figure 64. Vortex Flow Behind a Body of Finite Span in Supersonic Flow (Reference 88)

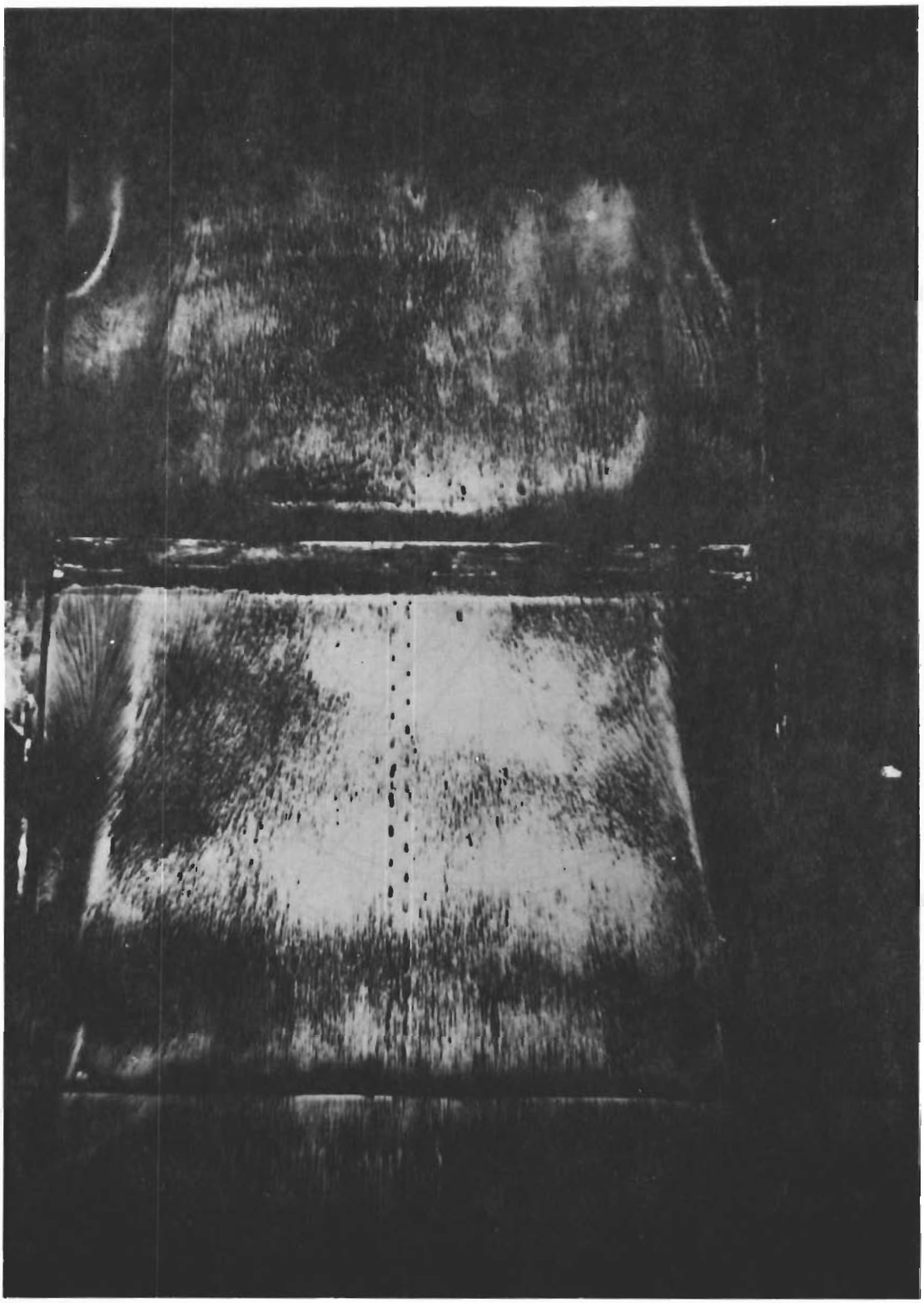

Figure 65. Flat Plate Oil Flow Study (End Plates Off), $\alpha = 0^{\circ}$, $\delta_f = 0^{\circ}$

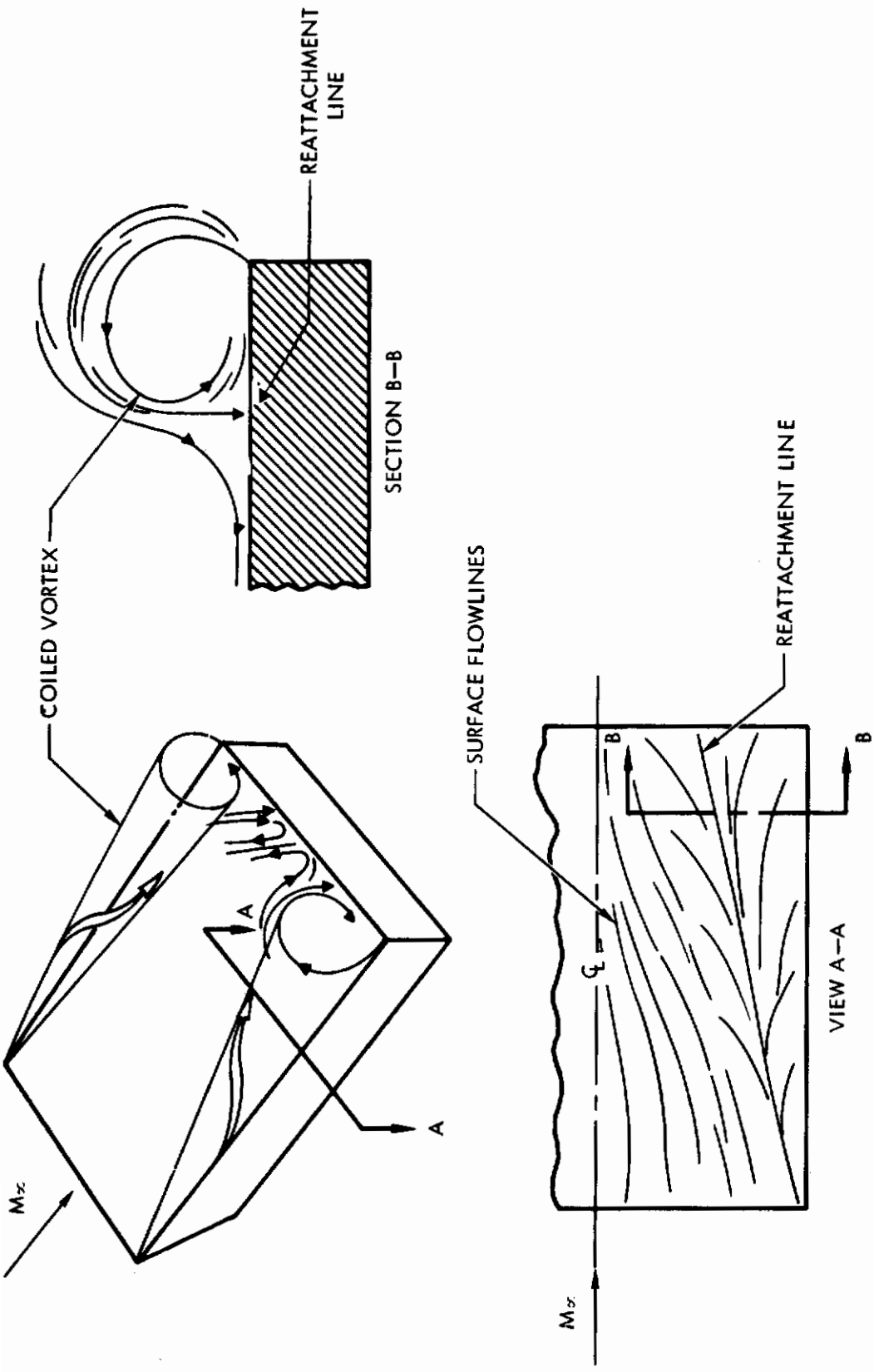

Figure 66. Surface Flow Patterns and Vortex System for Flat Plate Flow

Figure 67 shows a flow pattern on the compression surface of a flat plate at an angle of attack of 25° . High pressure on the compression surface results in a conical flow directed outboard. Figure 68 shows a flow pattern for a ramp at 20° positive angle. Flow on the forward plate at zero angle of attack is basically the same as that shown in Figure 67. Downstream of the hinge line, slight deflection of flow pattern by compression on the ramp is visible. Figure 69 shows a plate inclined at 25° with a ramp at 30° Conical flow on the forward plate is noticeable. An irregular separation line and strong three-dimensional effects due to high flap angle are seen upstream of the hinge line.

Flat Plate with End Plates

The effect of side plates on flat plate flow is shown in Figure 70. The region near the side edges indicates the boundary layer displacement effect and possibly the effect of an oblique shock generated by the side plate. The surface flow lines indicate that this is a region of high shear stresses and high pressure.

Figure 71 shows a flat plate with side plates at zero angle of attack and a flap at an angle of 10°. The forward plate flow is essentially similar to the flow of Figure 70; however, the flap region shows a rather complex flow with three-dimensional features and possibly a multi-vortex system.

The separated flow beneath the boundary layer near the wall is subsonic, and therefore allows the propagation of disturbances in all directions. Effects due to end conditions and the effects of finite plate span are expected to be noted in both the viscous and inviscid flows. The resulting flow field is very complex. An experimental comparison between pressure distribution over a flapped flat plate with and without end plates for identical conditions has been undertaken (References 59 and 60). Pressure measurements were taken in both the longitudinal and transverse directions.

For $M_\infty = 5$, $\alpha = 0$, $\delta_f = 10^\circ$, 20° and $Re_\infty/ft = 1.1 \times 10^6$, and 6.6×10^6 (References 59 and 60), a number of general trends may be noted for the end plates "on" and "off" configurations. The streamwise pressure level on the flap at a flap deflection angle δf of 10° is lower with the end plates on for $Re_\infty/ft = 1.1 \times 10^6$ and 3.3×10^6. At $Re_\infty/ft = 6.6 \times 10^6$ this trend reverses and the pressure level on the flap for the end plates "off" condition is lower. The overall differences are seen to be small (Figure 72).

For the same Mach number and range of Reynolds numbers, identical trends are observed for the $\delta_f = 20^\circ$ cases (Figure 73). If the plateau pressure region extends over a significant distance, the effects of end plates may become important. For the previous flow conditions at $\delta_f = 20^\circ$ and 10° the end plates "on" plateau pressure is slightly higher for all but the $Re_\infty/ft = 6.6 \times 10^6$ cases. For the higher Reynolds number the difference in the pressure level between the end plates "on" and "off" condition disappears (Figures 72 and 73).

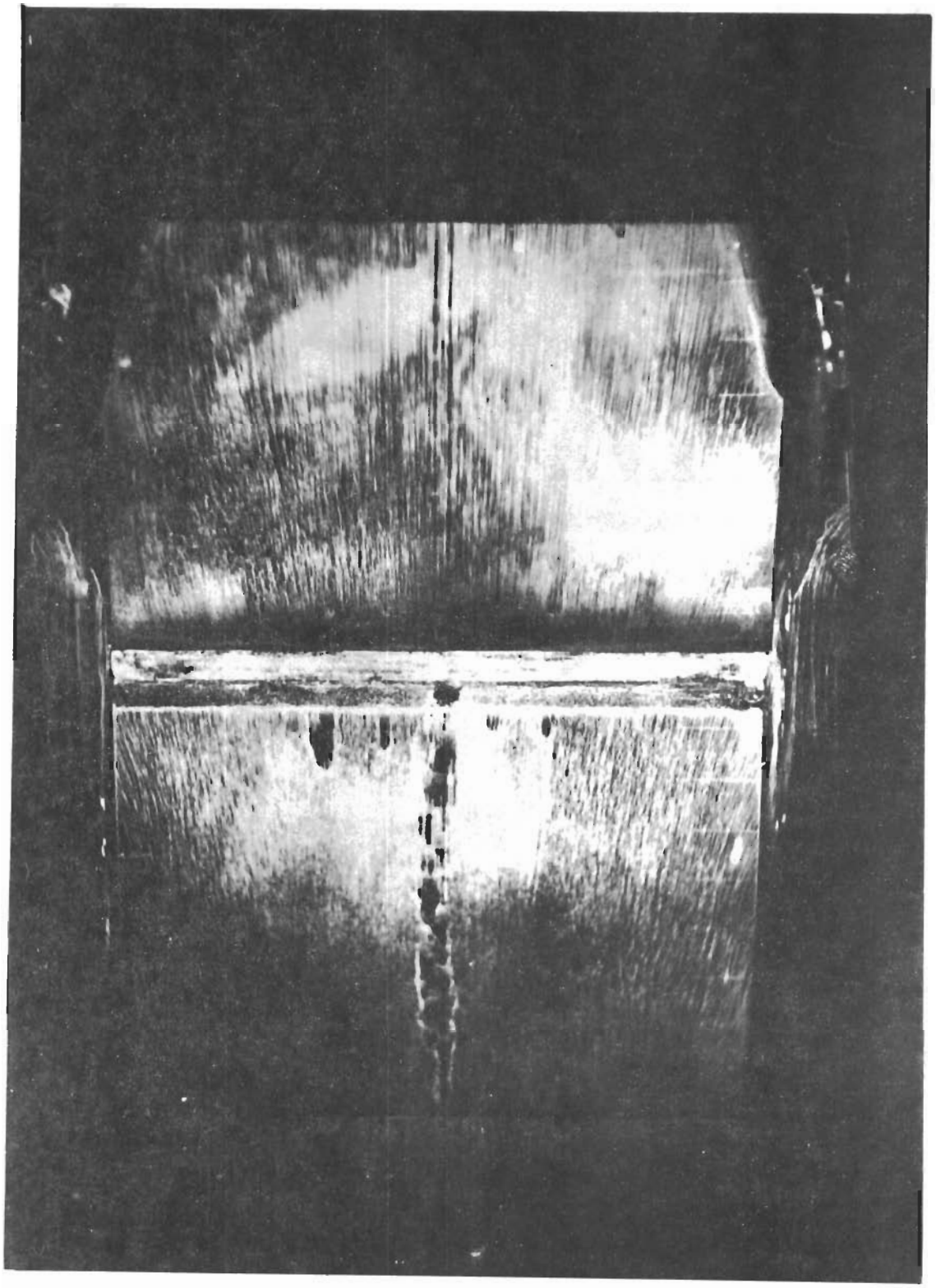

Figure 67. Flat Plate Oil Flow Study (End Plates Off), $\alpha = 25^{\circ}$, $\delta_f = 0^{\circ}$

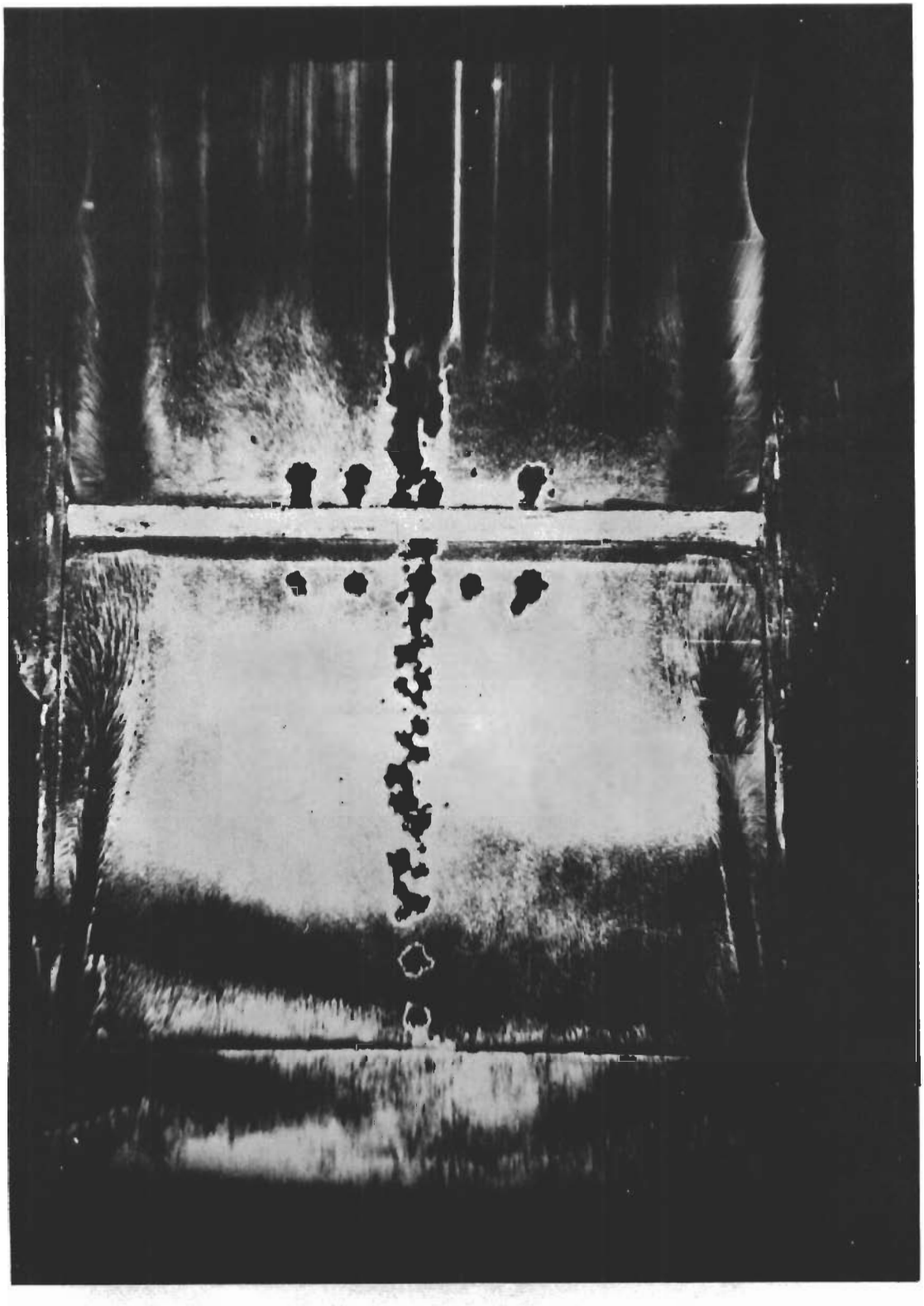

Figure 68. Flat Plate Oil Flow Study (End Plates Off), $\alpha = 0^{\circ}$, $\delta_f = 20^{\circ}$

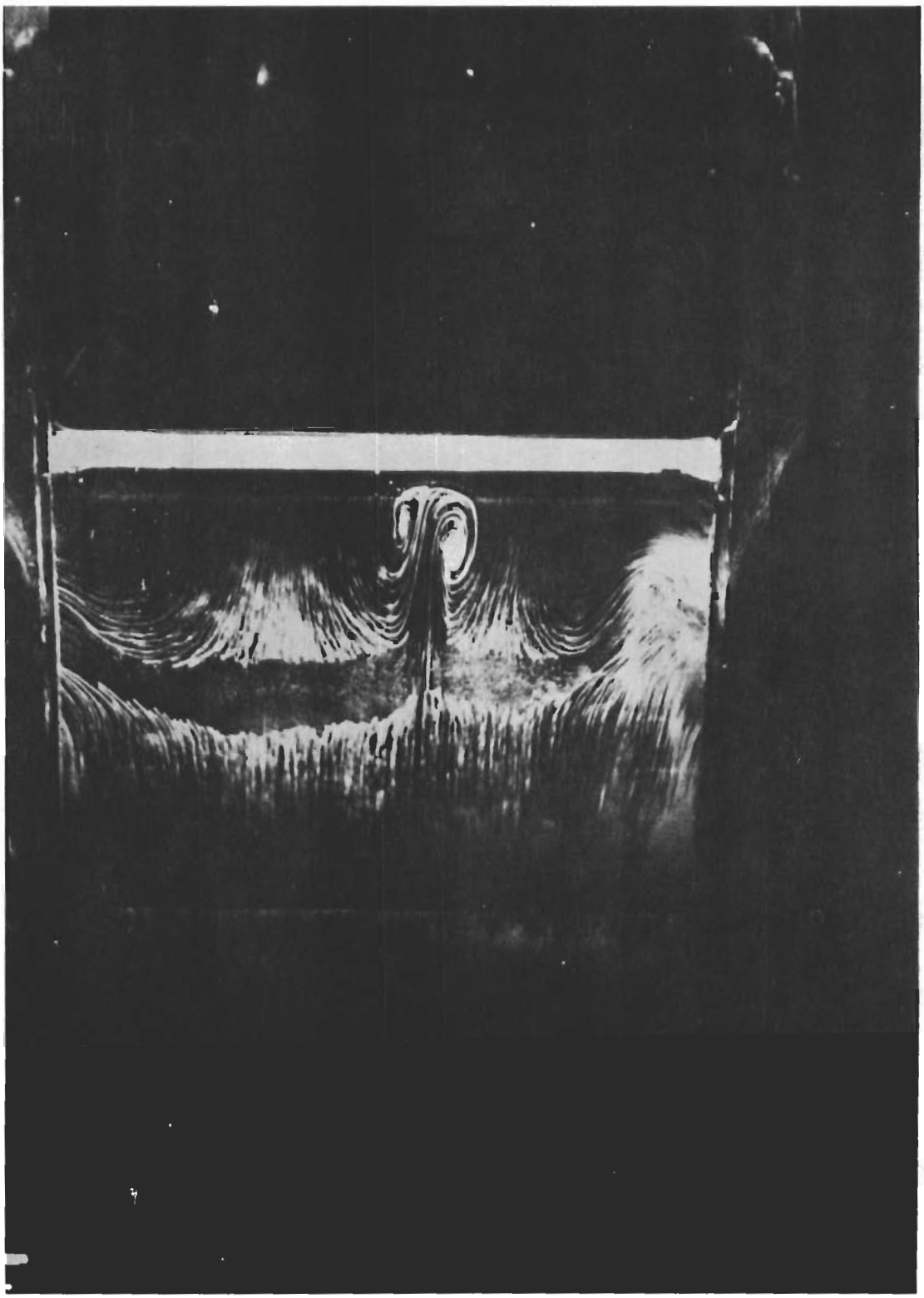

Figure 69. Flat Plate Oil Flow Study (End Plates Off), $\alpha = 25^{\circ}$, $\delta_f = 30^{\circ}$

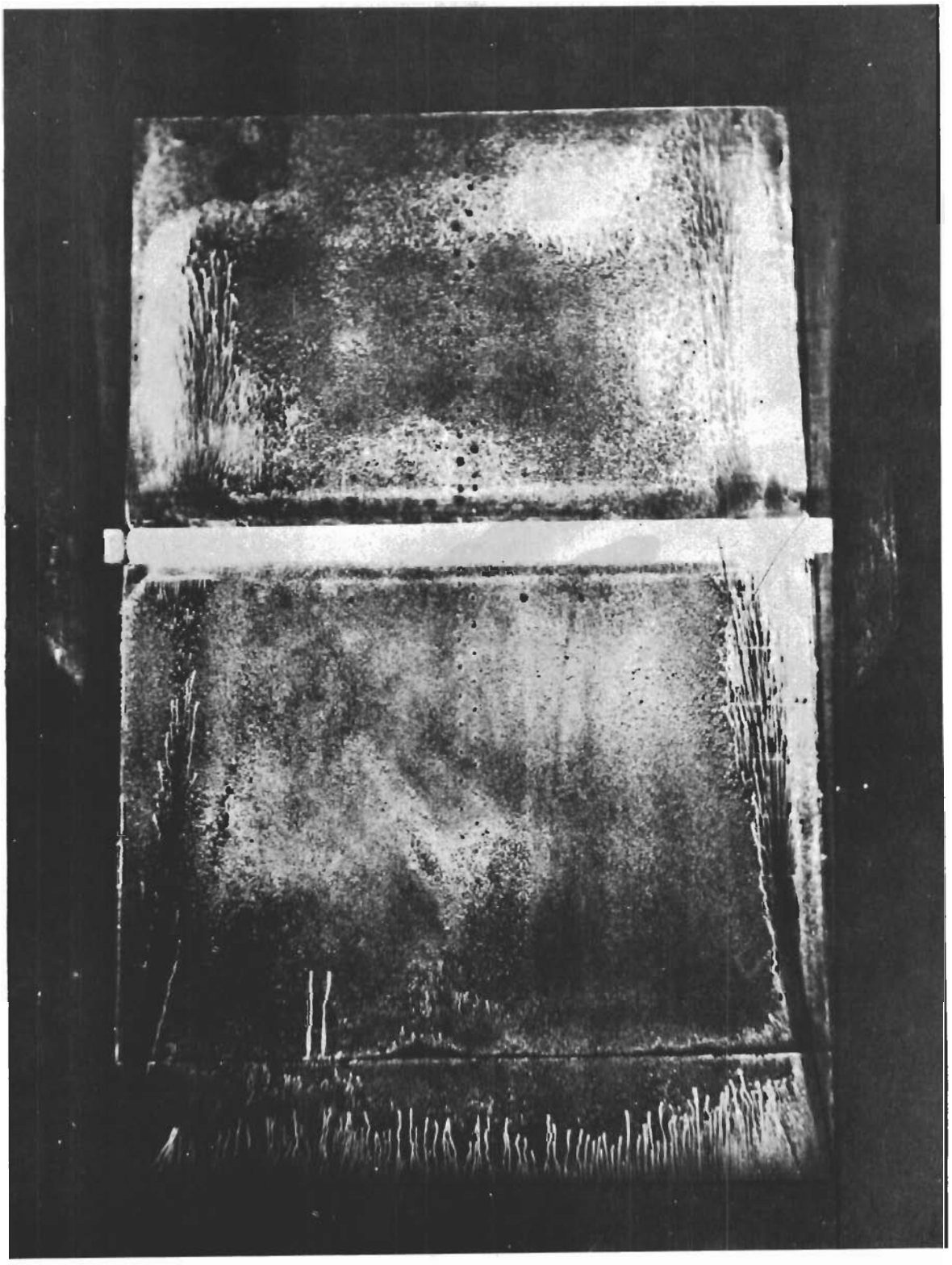

Figure 70. Flat Plate Oil Flow Study (End Plates On), $\alpha = 0^{\circ}$, $\delta_f = 0^{\circ}$

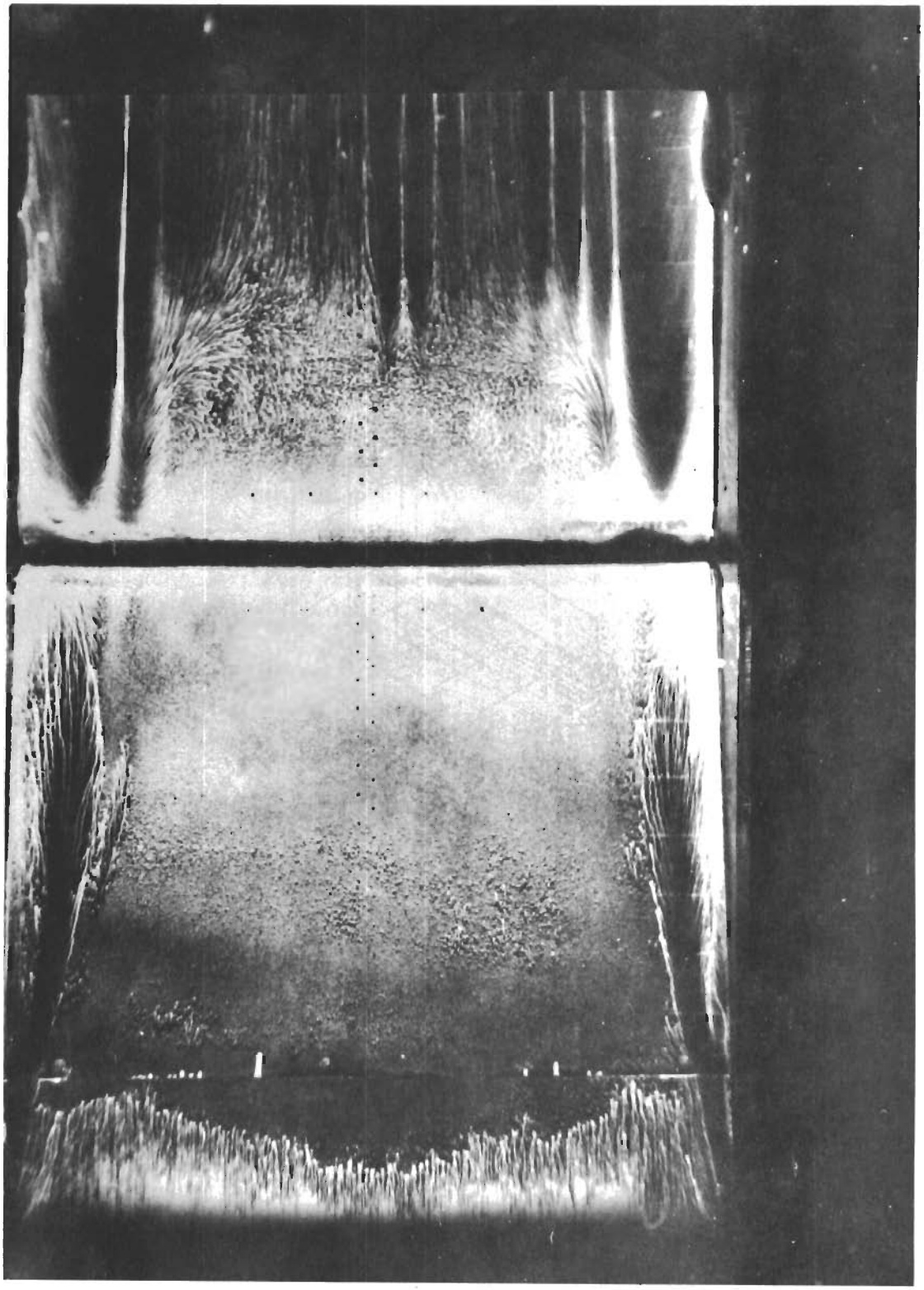

Figure 71. Flat Plate Oil Flow Study (End Plates On), $\alpha = 0^{\circ}$, $\delta_f = 10^{\circ}$

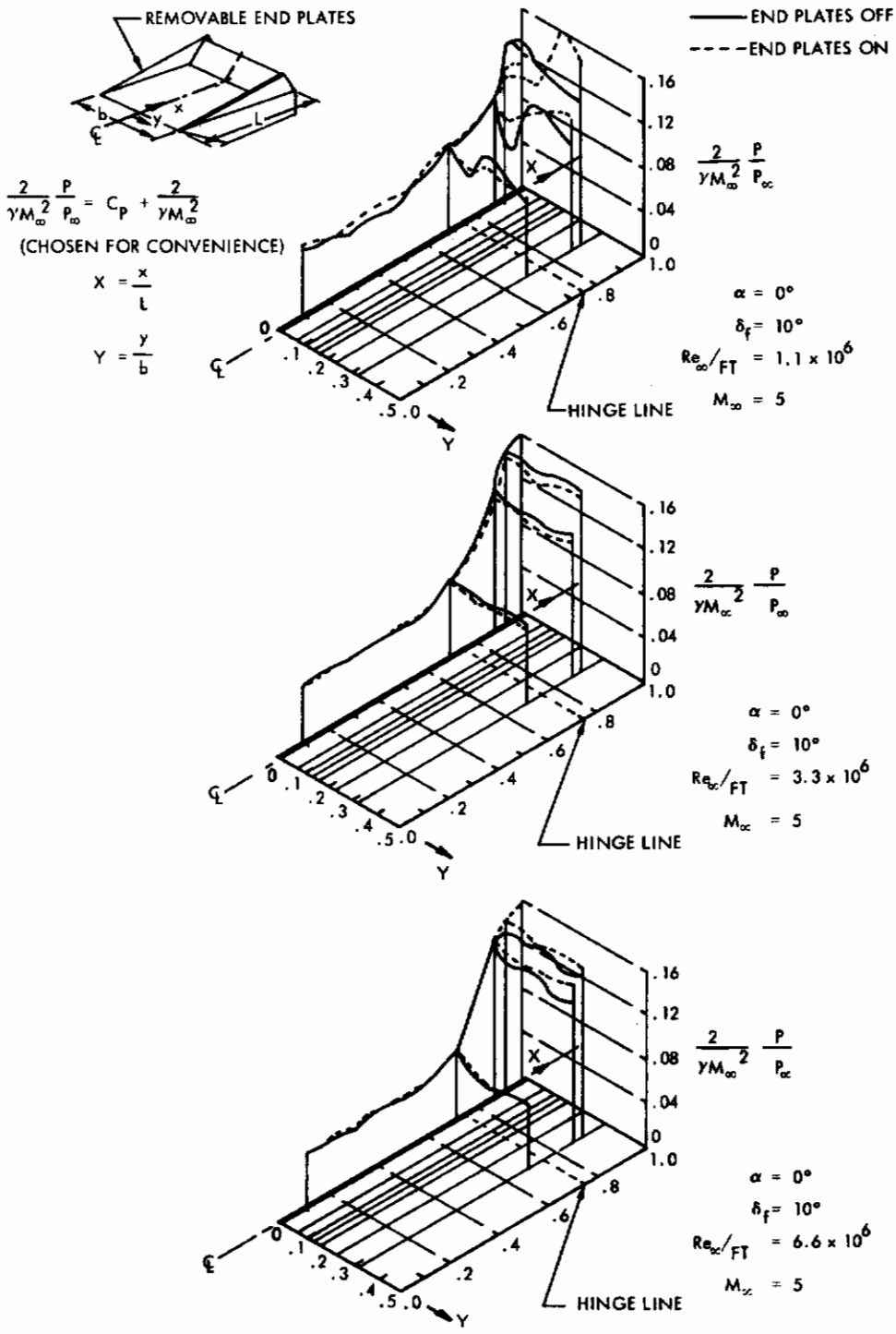

Figure 72. Effect of End Plates on Pressure Distribution, $\delta = 10°$, $M_\infty = 5$

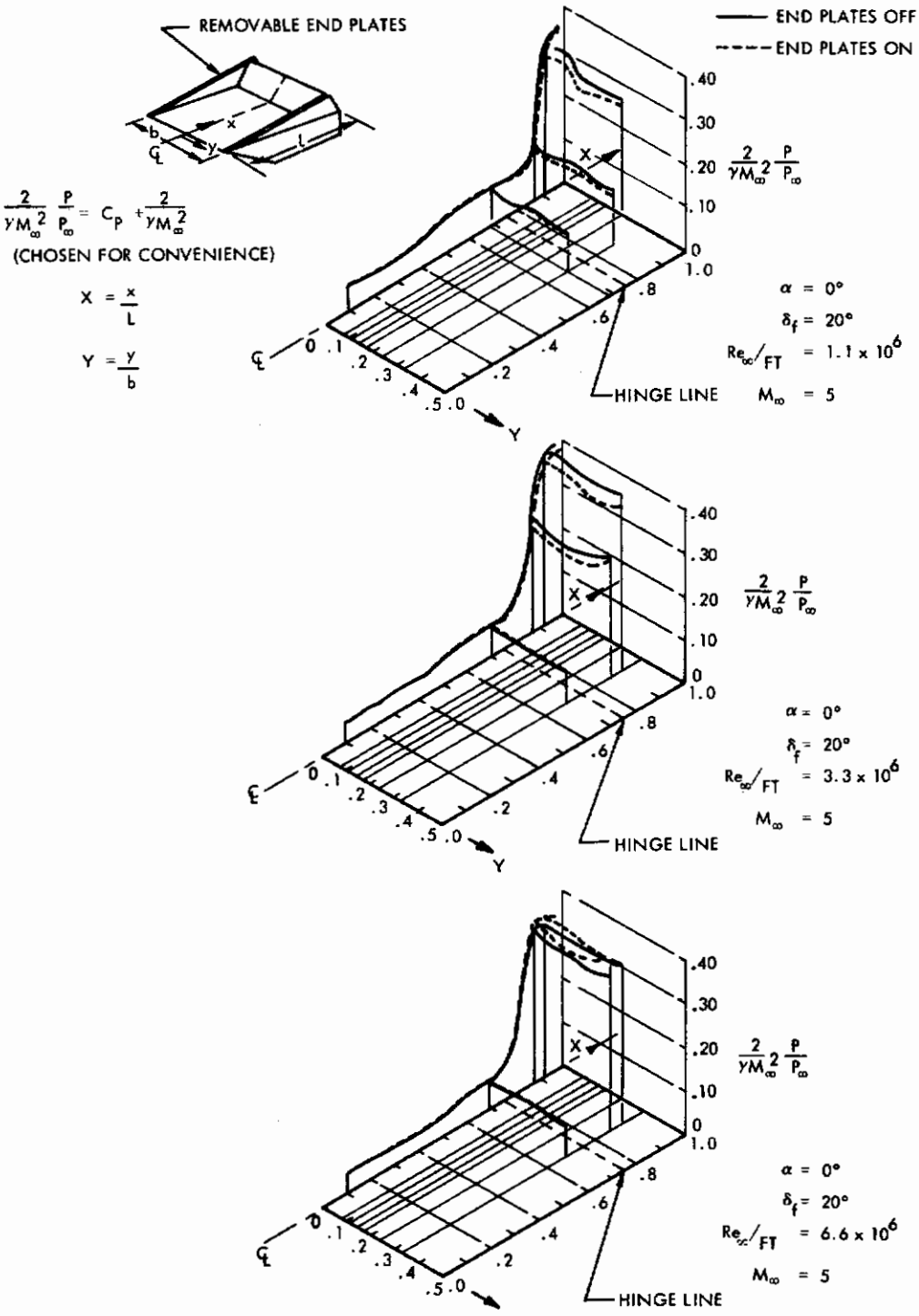

Figure 73. Effect of End Plates on Pressure Distribution, $\delta = 20°$, $M_\infty = 5$

No extensive transverse effects of the endplates on pressure are noted, with the exception of the case with $\alpha = 0°$, $\delta = 10°$ and $Re_\infty/ft = 1.1 \times 10^6$. The characteristic pressure distribution interaction distances in the longitudinal direction remained approximately the same for end plates "on" or "off".

The transverse pressure distribution in the re-attachment region is strongly influenced by decreasing Reynolds number and shows local peaks at both the center of the plate and toward the sides, at least as far as the instrumentation extends (Figures 72 and 73). This trend is particularly well shown in Figure 72 at $Re_\infty/ft = 1.1 \times 10^6$. It appears that a thick boundary layer at low Reynolds numbers promotes the three-dimensionality of the flow. In general, however, the transverse pressure distribution upstream of the hinge line is farily insensitive to Reynolds number (Figures 72 and 73).

For $M_\infty = 8$ and $Re_\infty/ft = 3.3 \times 10^6$ tests were made at $\alpha = 0°$ and $15°$ for $\delta_f = 10°$, $20°$, and $30°$ (Reference 59). It is observed that at the given flow conditions for $\alpha = 0°$ the pressure reached on the flap is higher for the end plates off tests (Figures 74 and 75). At $\alpha = 15°$ and $\delta_f = 30°$ the flap pressures seem independent of end plate pressure (Figure 75). This is consistent with the observations at $Re_\infty/ft = 6.6 \times 10^6$, as the compression angle of attack increased the local Reynolds number ahead of the flap from 3.3×10^6/ft to 5.88×10^6/ft. Extensive pressure variation in the spanwise direction is found both upstream and downstream of the hinge line. For $\alpha = 0°$, the upstream pressure distribution is generally consistent with the $M_\infty = 5$ test results. The plateau region exhibits slightly higher pressures with the end plates on (Figures 74 and 75). No significant change in the upstream and downstream parameters is observed.

DELTA WING CONFIGURATIONS

The generalized correlations for shockwave-boundary layer interaction were derived from experimental data obtained for models with essentially two-dimensional flow: flat plate-ramp, flat plate with incident shock, and flat plate with a step. To examine the general applicability of these results, the flow over various delta configurations is discussed.

Flow About a Delta Wing

The flow about a delta wing configuration is rather complex; however, a number of investigations on delta shapes has been conducted (References 62 through 66). A very useful method of studying complex flow is the oil flow method. Figure 76 shows a surface flow pattern inferred from oil flow photographs on the compression surface of a sharp leading edge delta wing at various angles of incidence (Reference 66). The surface flow and the boundary layer flow at small angles of attack have an inward component which is attributed to the boundary layer induced pressure gradient at the leading edge. Conversely, the external flow is directed away from the centerline. At higher angles of attack the flow turns parallel and eventually diverges. At an incidence of about 10° the flow divides along a line at about 90% of the span, with the outboard flow directed toward the leading edge. At higher angle of attack, the dividing line moves inboard and reaches the centerline of the body at $\alpha \cong 18°$ Beyond

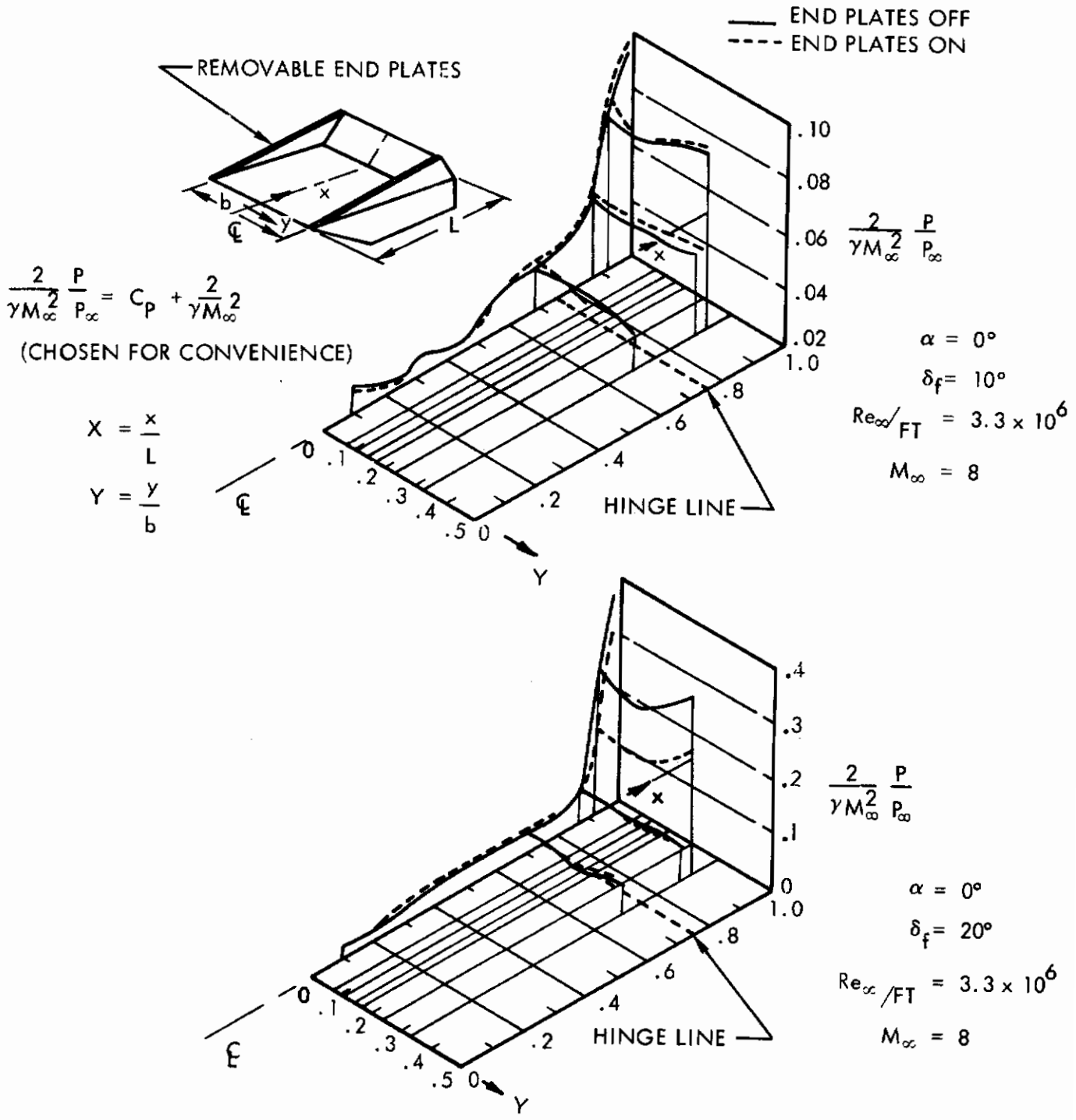

Figure 74. Effect of End Plates on Pressure Distribution, $\delta_f = 10°$ and $20°$, $M_\infty = 8$

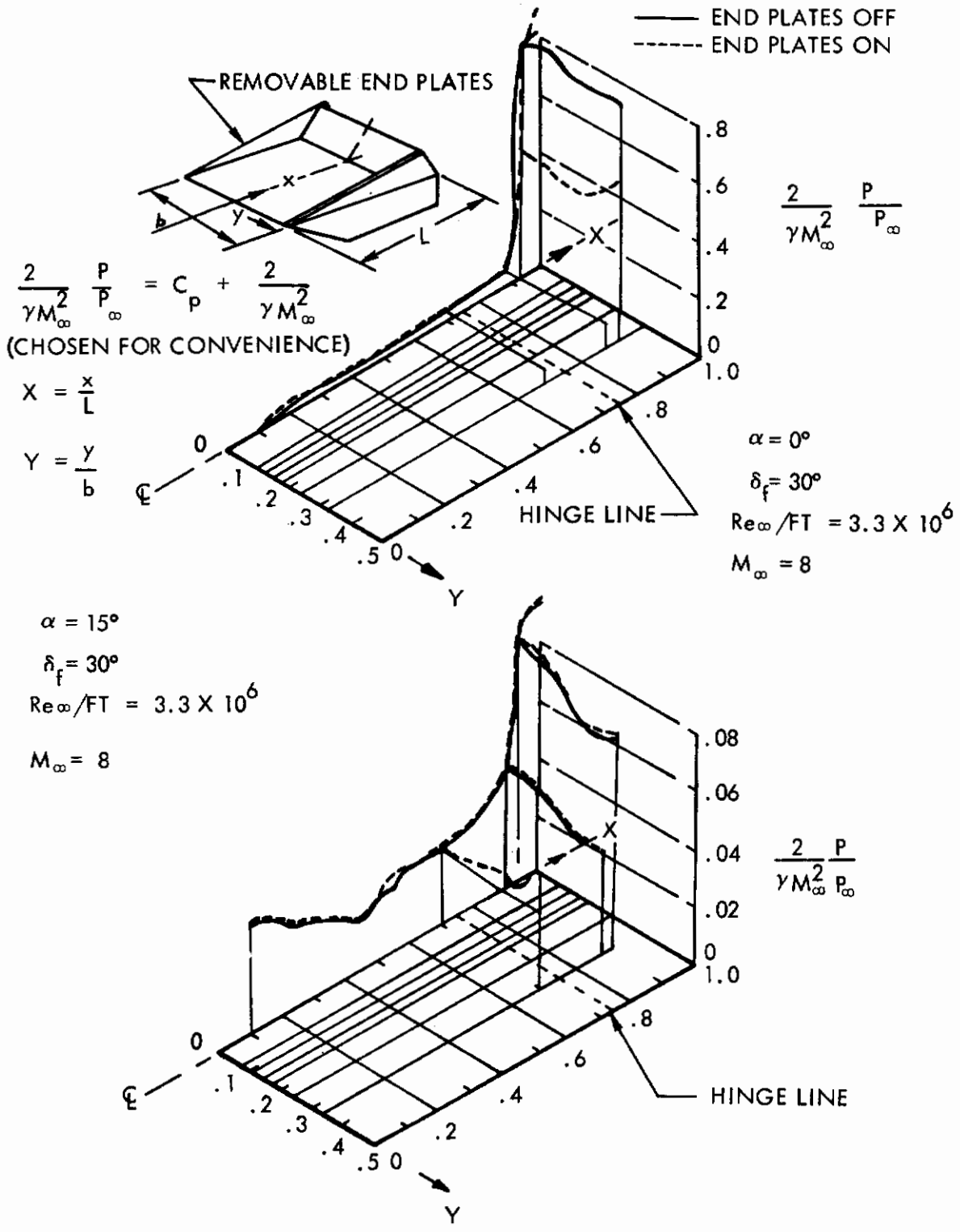

Figure 75. Effect of End Plates on Pressure Distribution, $\delta_f = 30°$, $M_\infty = 8$

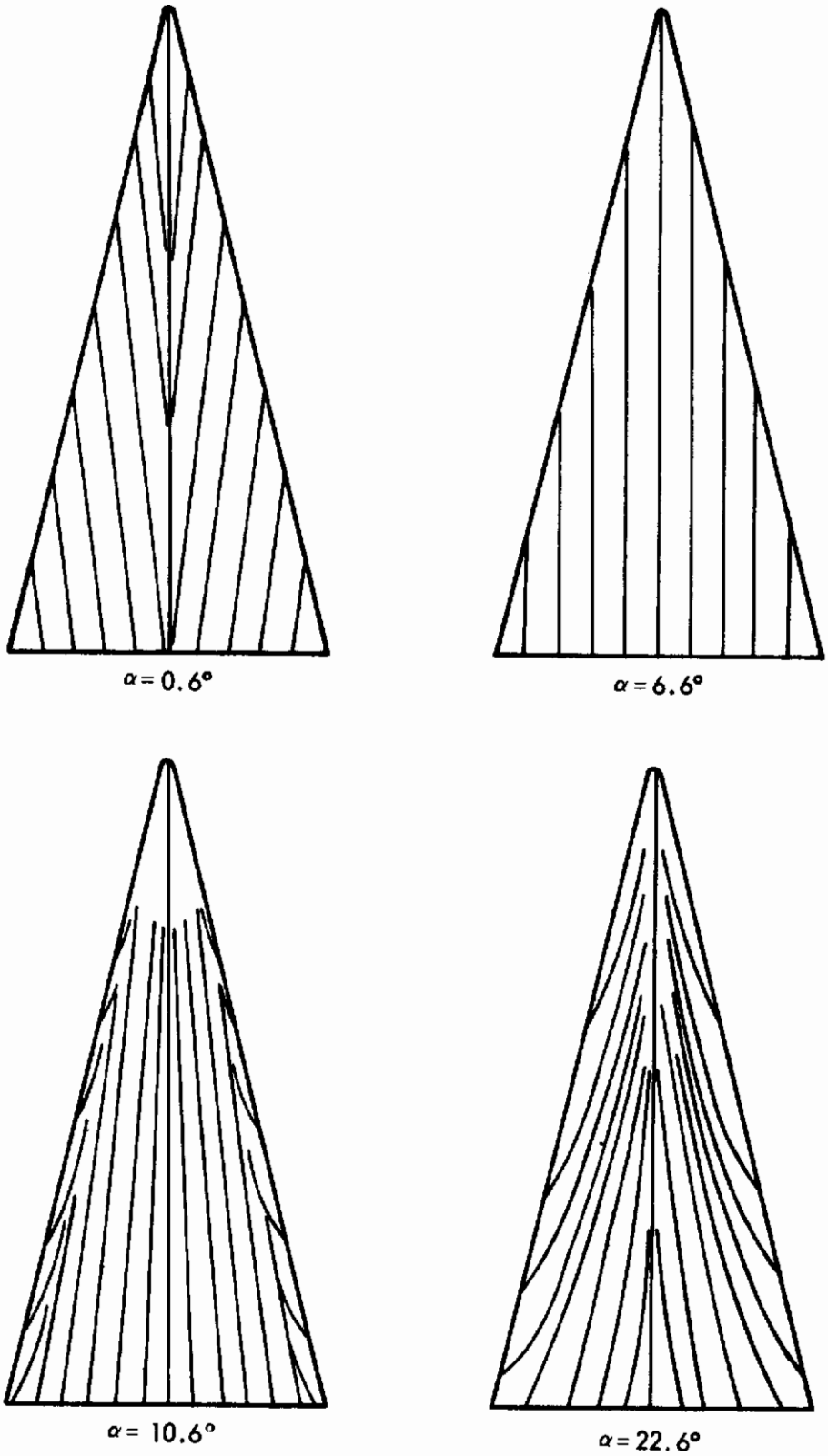

Figure 76. Compression Surface Flow Patterns for a Delta Wing with Dihedral, $M_\infty = 7.1$, $Re_{\infty L} = 3.5 \times 10^5$ (Ref. 66)

$\alpha \cong 20°$ the flow field is such that the leading edge of the delta wing may become a trailing edge. This outboard flow is a result of shock losses which are predominant at higher incidence.

Flow patterns on the lee surfaces of delta wings at various angles of attack and Mach numbers have been examined in Reference 62. At small angles of incidence the flow was noted to be attached over the entire upper surface. This is observed in Figure 77 for lower Mach numbers and in Figure 77 at higher Mach numbers.

As the angle of attack increases for the low Mach number case the flow separates from the leading edge. A coiled vortex sheet is thus formed which lies across the expansion surface along the leading edges (Figure 77). A spanwise outflow is induced beneath the vortex and a secondary separation occurs along the leading edge (Figure 77). At lower sweep angles the vortex sheet re-attaches, forming a long separation bubble.

For higher Mach numbers, the flow is attached at lower angles of attack. A weak shock is noted to emanate from the vortex region and deflect the flow. When this shock attains sufficient strength the boundary layer separates and forms a coiled vortex sheet (Figure 77). Again, at lower angles of attack, the boundary layer re-attaches to the surface and forms a separation bubble.

On the expansion surface of a thick delta wing at incidences at which suction is developed, separation lines become noticeable and moves outboard as the incidence is increased (Figure 78). The area between the separation lines on both sides of the centerline is an area of reduced shear and thus the flow is inclined away from the centerline. At $\alpha \geq 25°$ re-attachment of the separated flow occurs at the centerline of the body.

At $\alpha \cong 19°$ there is visible a concentration of oil filaments from the turning of the flow away from the plane of symmetry. This indicates a flow retardation due to a presence of an external shock wave. Deviation from conical flow is seen from the curvature of the separation line near the trailing edge. This is attributed to the upstream propagation through the thick laminar boundary layer of strong pressure gradients generated by compression at the trailing edge.

The flow structure of the resulting conical flow is shown in the spanwise cross-section in Figure 79. This figure identifies the location of the bow shock and expansion flow field emanating from the leading edge. The boundary layer is thick and the adverse pressure gradient due to external compression is propagated toward the leading edge.

The position of separation determined from the oilflow photographs is shown in Figure 80 (Reference 66). Although flow details near the centerline are lacking, it is suggested that rolling up of the separated flow promotes a new expansion of the external flow which then turns parallel to the surface and gives rise to compression at the centerline. An idealized flow over such configurations has been analyzed and verified by Fowell (Reference 63). It was shown that a Prandtl-Meyer expansion centered at the leading edge turns

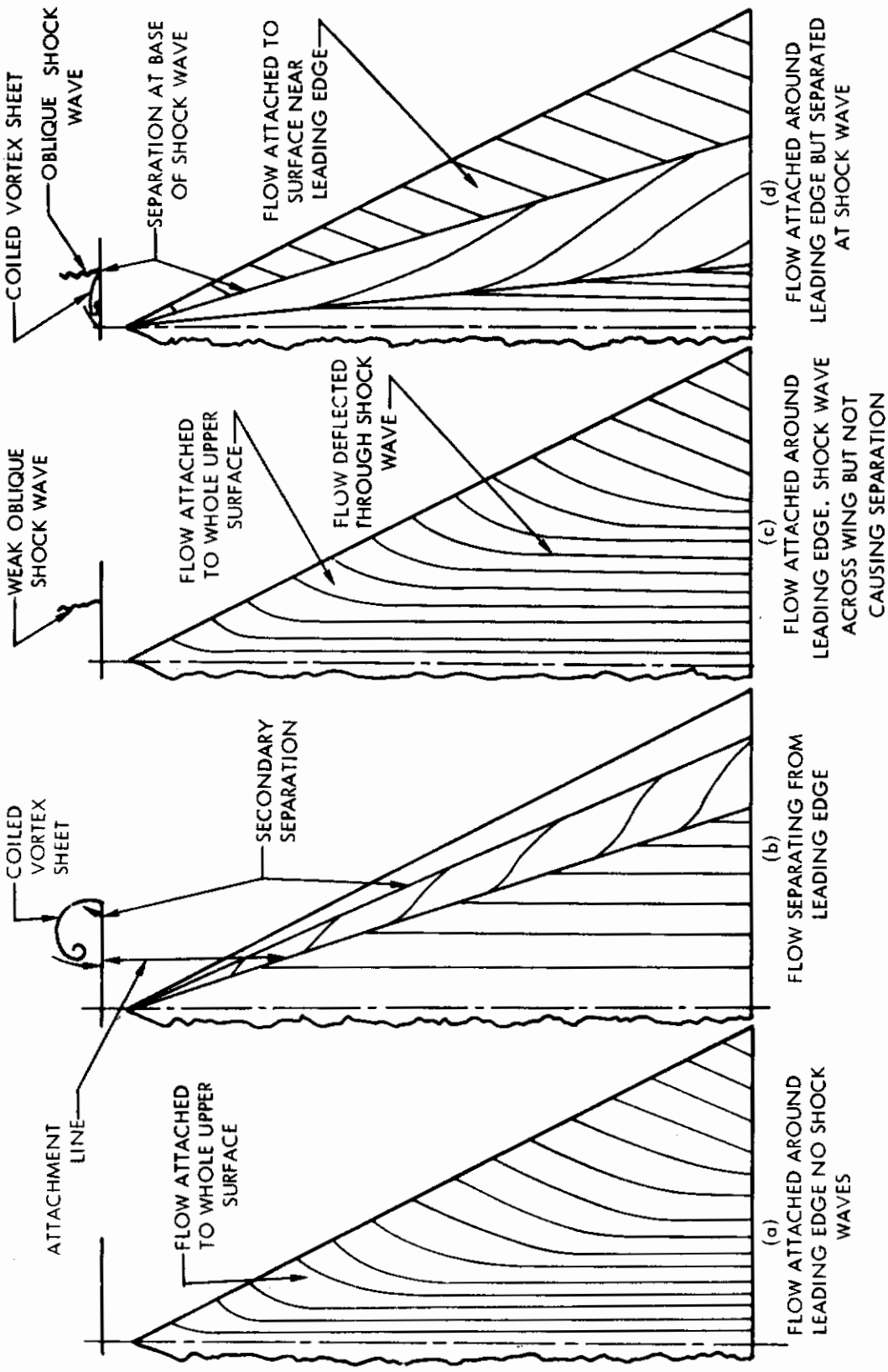

Figure 77. The Main Types of Flow Around Highly-Swept Edges (Ref. 62)

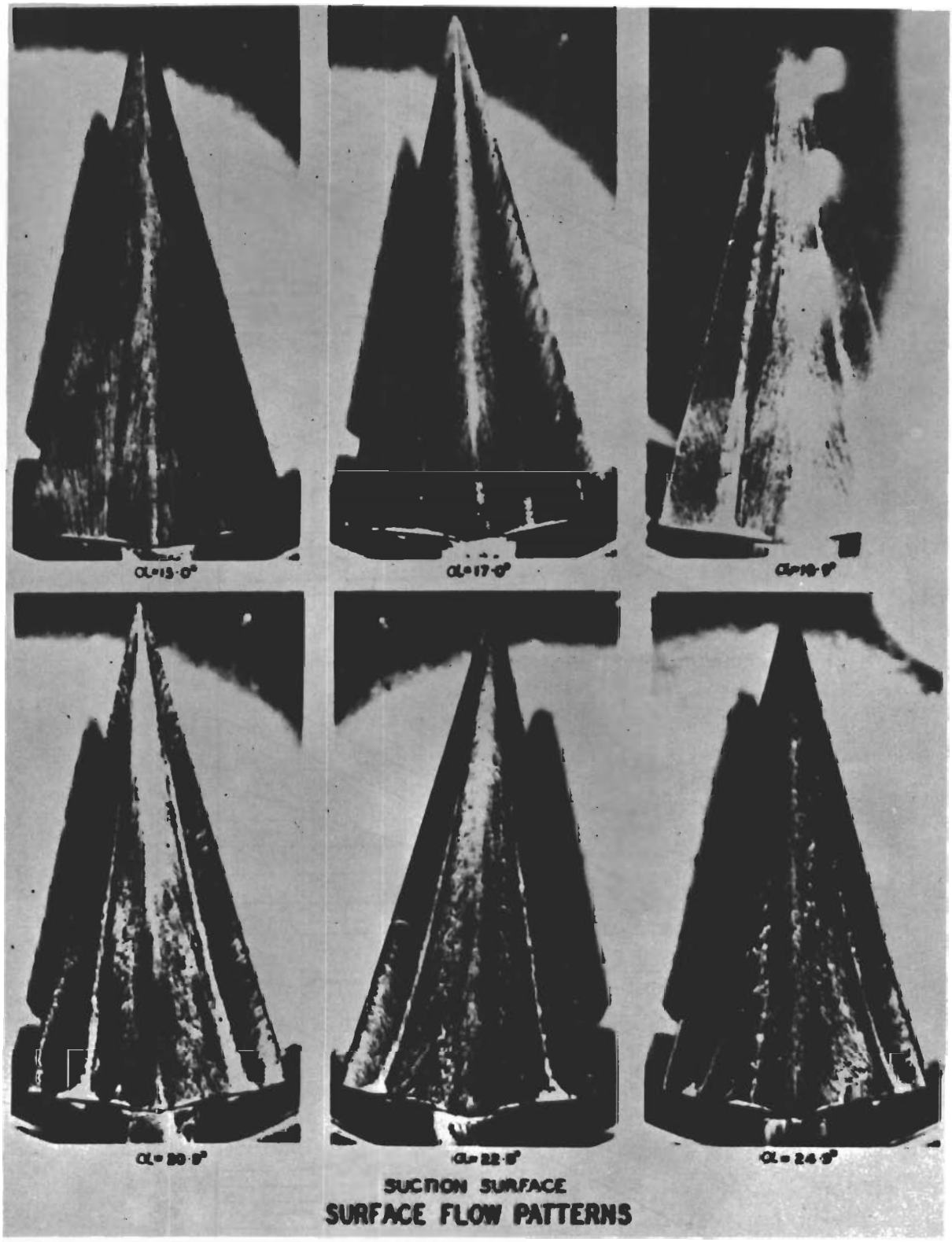

Figure 78. Expansion Surface Flow Patterns on a Delta Wing with Dihedral (Ref. 66)

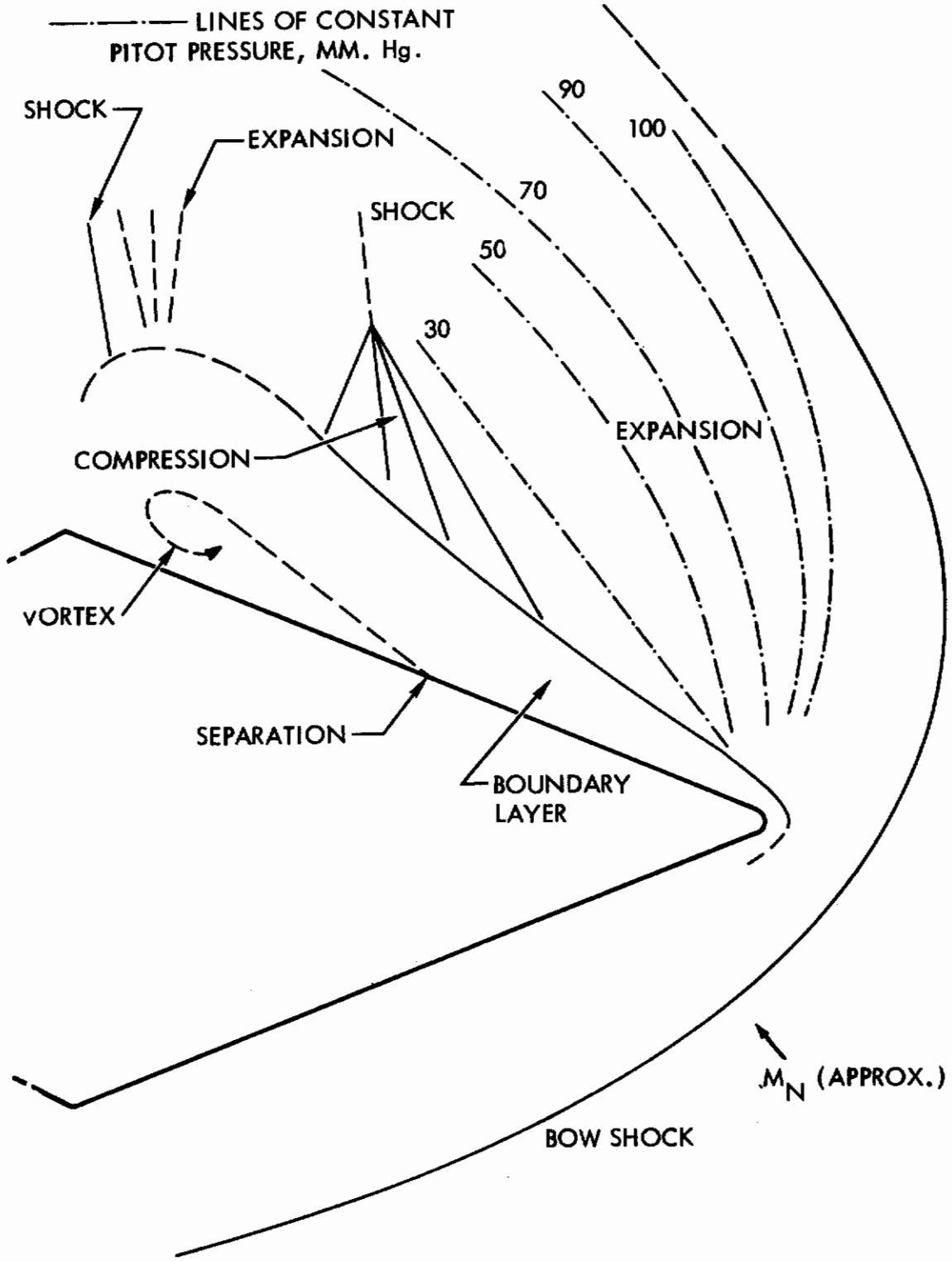

Figure 79. Spanwise Cross-Section of Flow Around Delta Wing at $\alpha = 17.6^{\circ}$ (Ref. 66)

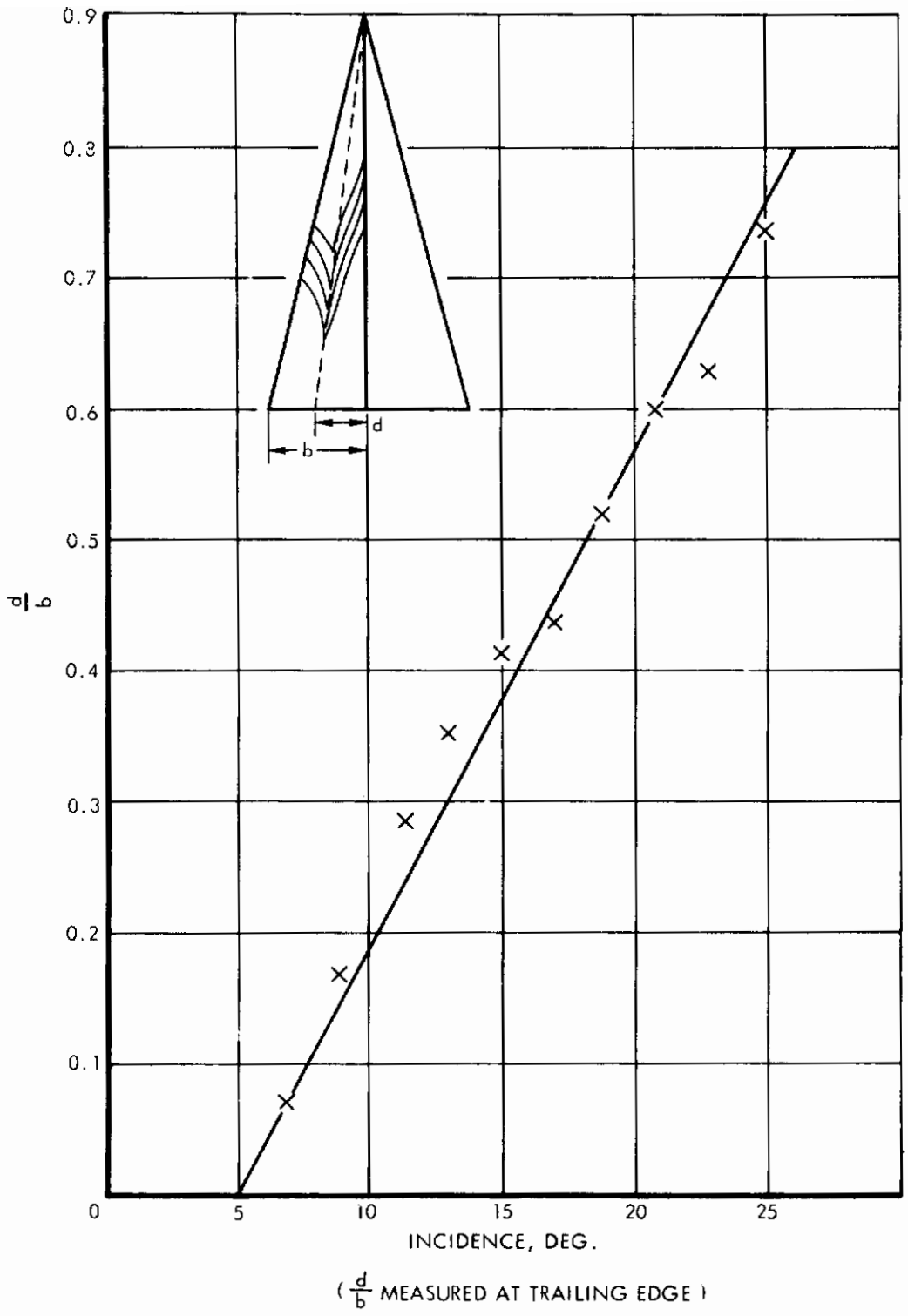

Figure 80. Position of Separation as a Function of Incidence (Ref. 66)

the flow inward and at some distance inboard recompression takes place through an oblique shock wave which turns the flow parallel. Considering viscous effects in a real flow, a strong recompression may cause flow separation and formation of a vortex. The flow outside of the vortex may reattach, and inboard of the reattachment, flow is turned parallel to the centerline.

The flow patterns exhibited by the blunt delta wing are roughly similar to those presented for the sharp leading edge (Reference 65). The flow pattern at $\alpha = 0^{o}$ is characterized by central outflow as a result of high induced pressure at the apex, and is contained by the shock and the induced high pressure along the leading edges (Figure 81). Surface flow on cylindrical edges is inward and follows the pressure gradient. At increasing angle of attack an inward flow develops until $\alpha \geq 20^{o}$ where an outward flow occurs (Figure 81).

An investigation of blunted delta wings with deflected flaps is presented in Reference 67. The existence of deflected flaps on the model surface modifies the flow over a substantial portion of the configuration. The oil film patterns for this model disclose a very complex flow field. The surface flow on the compression surface shows a strong influence of the blunt apex in the central area of the model (Figure 82). A definite "blast" region clear of oil is observed in the central high pressure area. Separation lines upstream of both flaps are well developed and symmetrical. A flow pattern at $\alpha = 0^{o}$ is shown in Figure 83. Attached flow exists near the leading edges. Further inboard, flow separation occurs with reattachment along the centerline. Flow separation upstream of the flaps is well outlined. Separation effects propagate upstream and form complex flow patterns a significant distance ahead of the flaps. Similar flow with more details exists on the expansion surface at $\alpha = -30^{o}$ (Figure 84).

Pressure Distribution on Flat Delta Wing

The general applicability of the two-dimensional correlations for separated flow to more complex configurations will now be investigated.

A blunted flat-bottom delta wing from Reference 67 is considered first (Figure 85). In order to verify the existence of two-dimensional flow, the experimental pressure distribution in the streamwise and spanwise directions is considered. For the flat-bottom delta configuration, the streamwise and spanwise experimental distribution at 33^{o} angle of attack ($M_{\infty} = 8$, $\Lambda = 70^{o}$) is shown in Figures 86 and 87. It is noted that the pressure distribution downstream of the nose agrees very closely with the two-dimensional oblique shock value obtained from Reference 36. This indicates that conditions in the separated region upstream of the flaps may be determined by using two-dimensional correlations.

The local Mach number in the vicinity of the flap was determined from the ratio of flap pressure P_{flap} to undisturbed pressure, P_{α}. This was accomplished by finding $M_{\alpha}\sin\theta$, where θ is the shock angle, through the use of

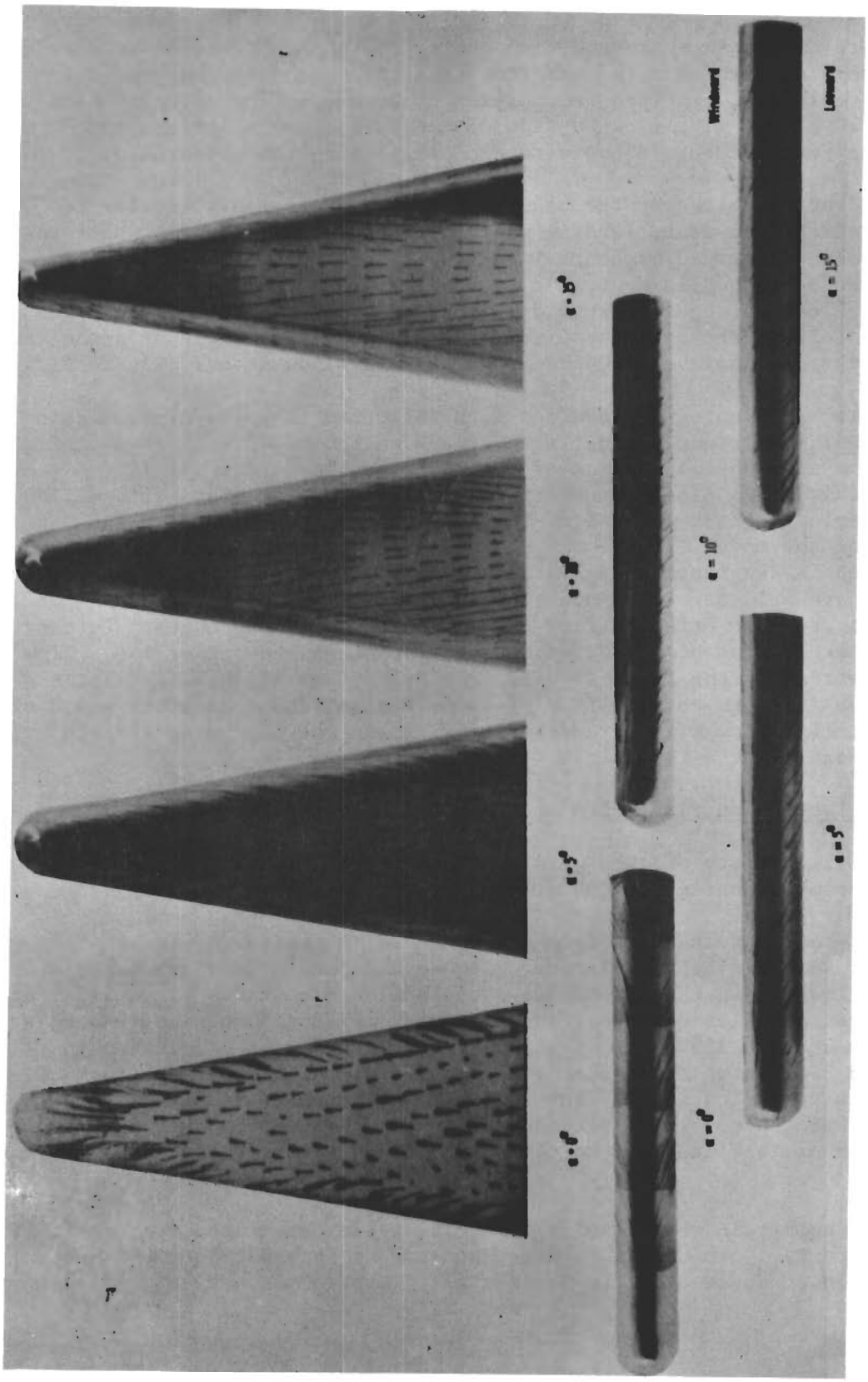

Figure 81. Surface Flow Studies on a Blunt Delta Wing for $M_\infty = 6.8$ (Ref. 65)

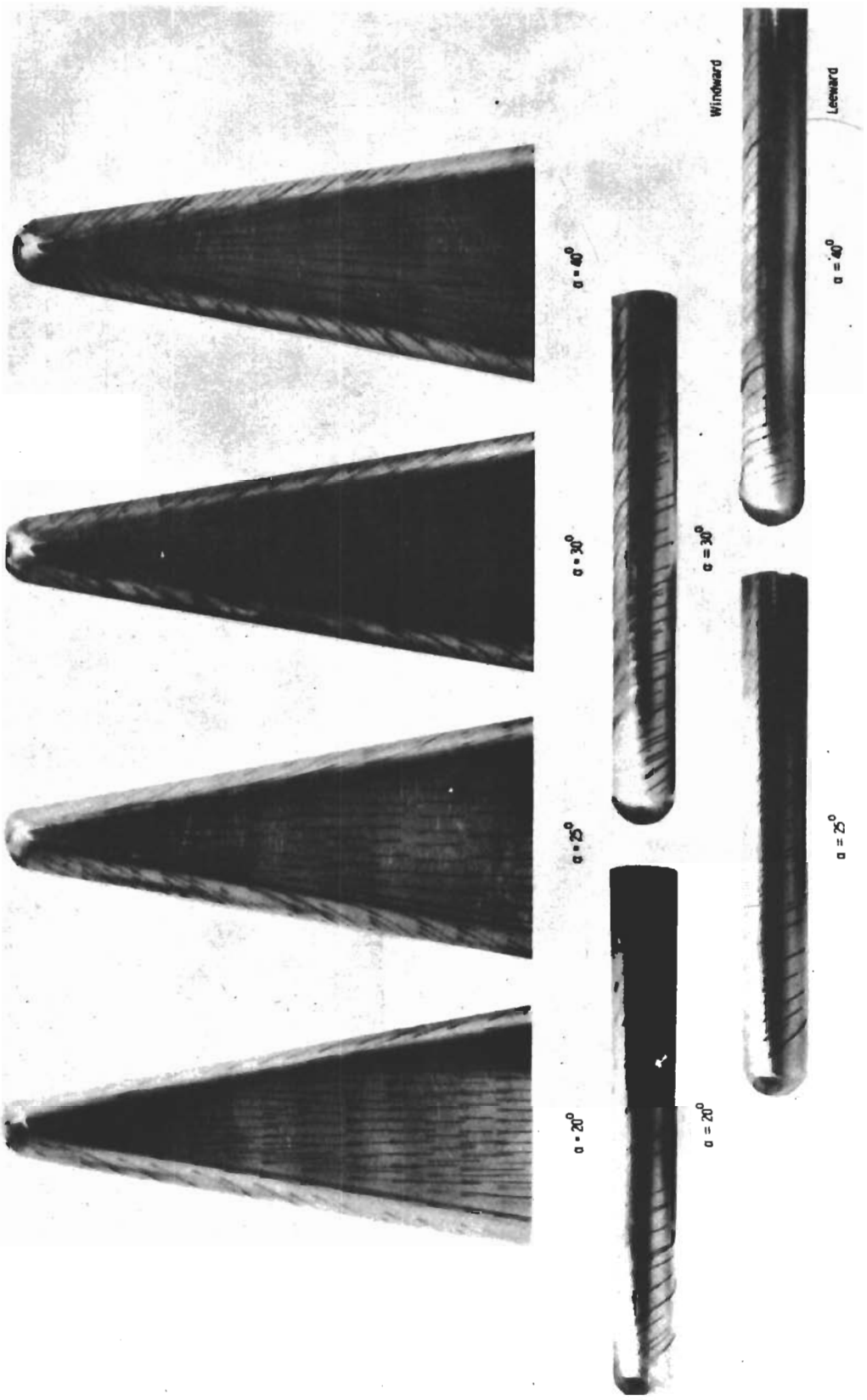

Figure 81. Surface Flow Studies on a Blunt Delta Wing for $M_\infty = 6.8$ (Ref. 65) (Concluded)

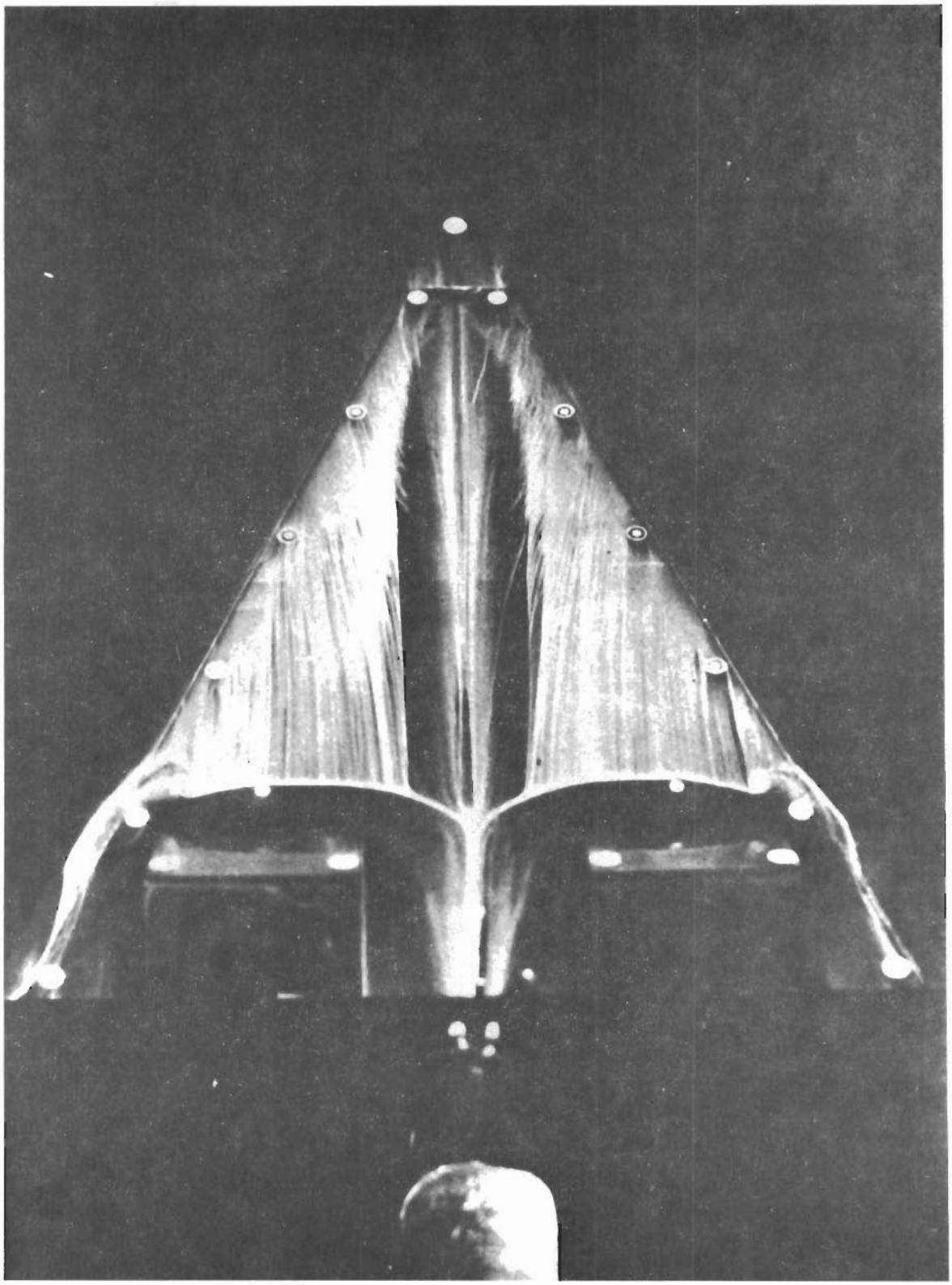

Figure 82. Oil Film Photograph of Lower Surface of Blunt Pyramidal Configuration (Ref. 67); $M_\infty = 5$, $\alpha = 14.3^\circ$ $\delta_f = 40^\circ$

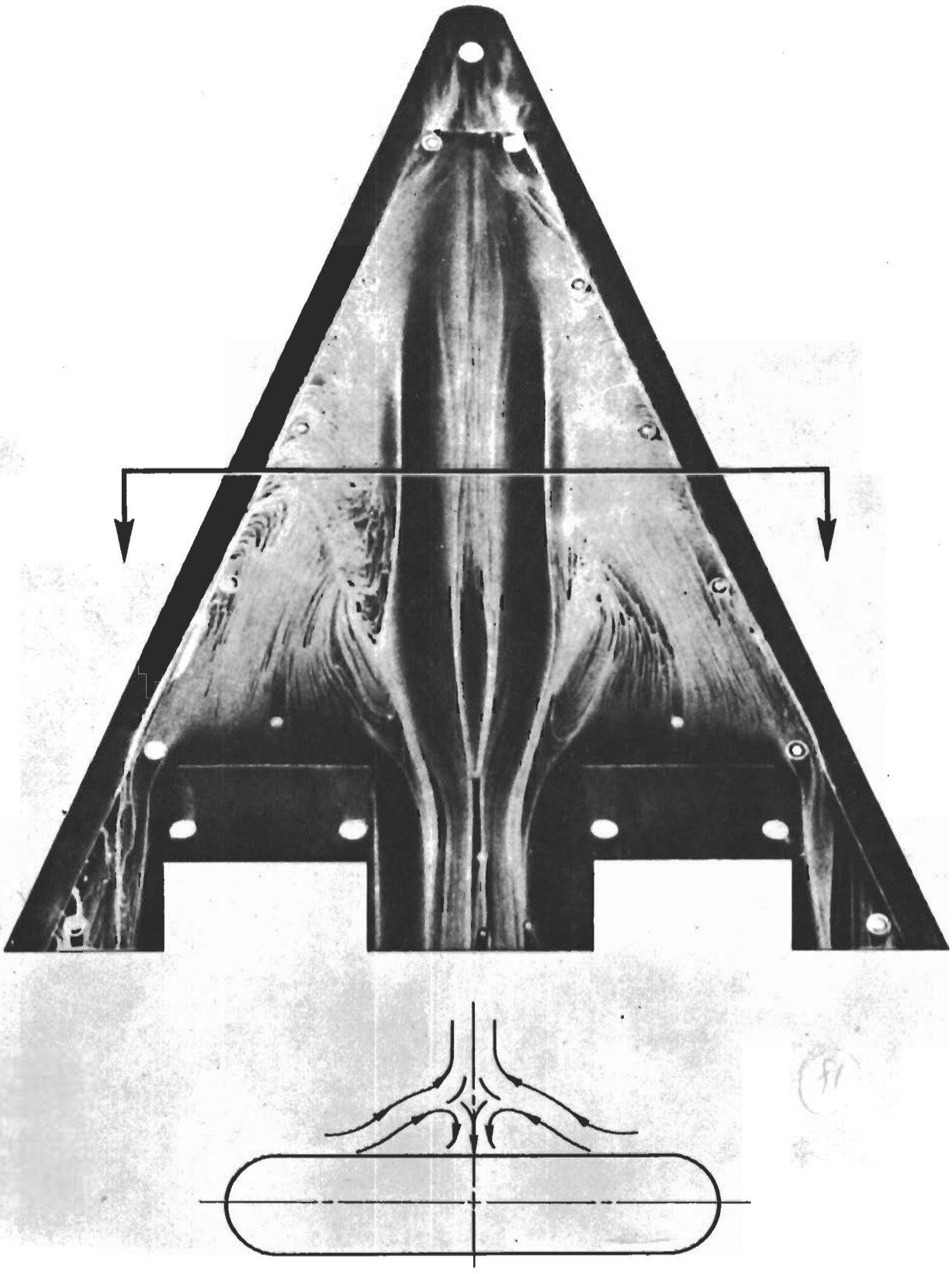

Figure 83. Oil Film Photograph of Lower Surface of Blunt Pyramidal Configuration (Ref. 67), $M_\infty = 5$, $\alpha = 0^\circ$, $\delta_f = 40^\circ$

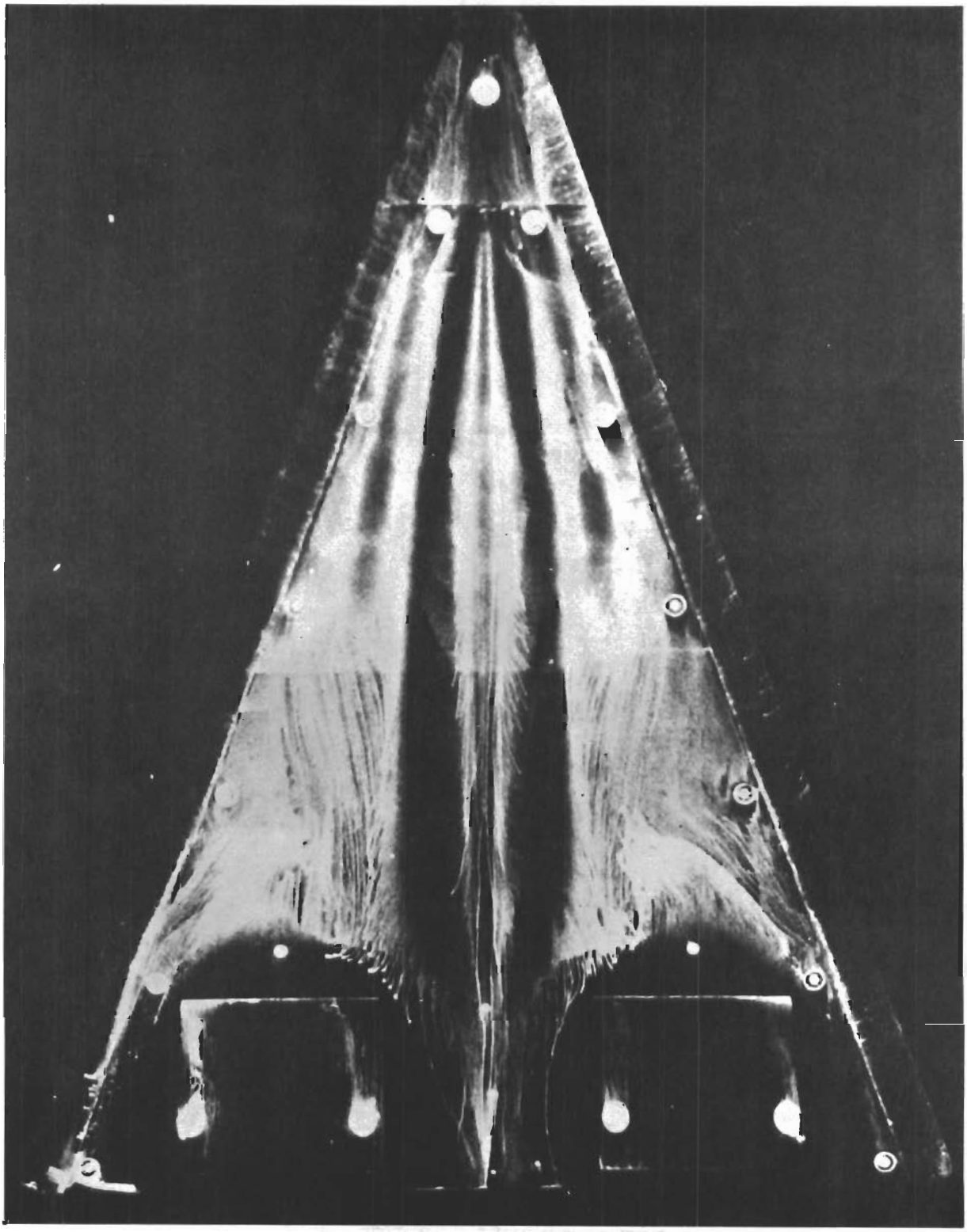

Figure 84. Oil Film Photograph at Lower Surface of Blunt Pyramidal Configuration (Ref. 67); $M_\infty = 5$, $\alpha = -30^\circ$, $\delta_f = 40^\circ$

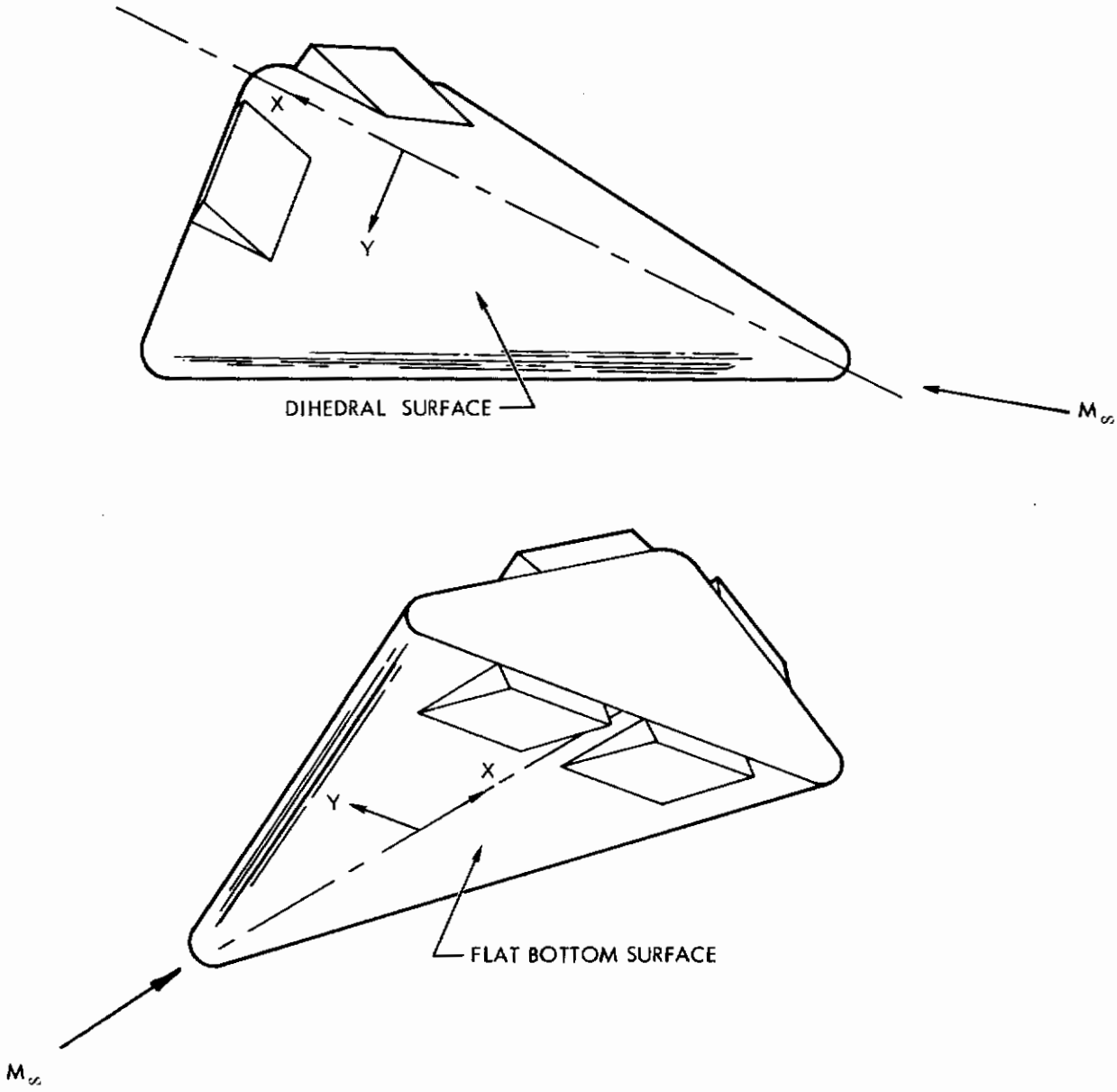

Figure 85. Blunt Pyramidal Configuration

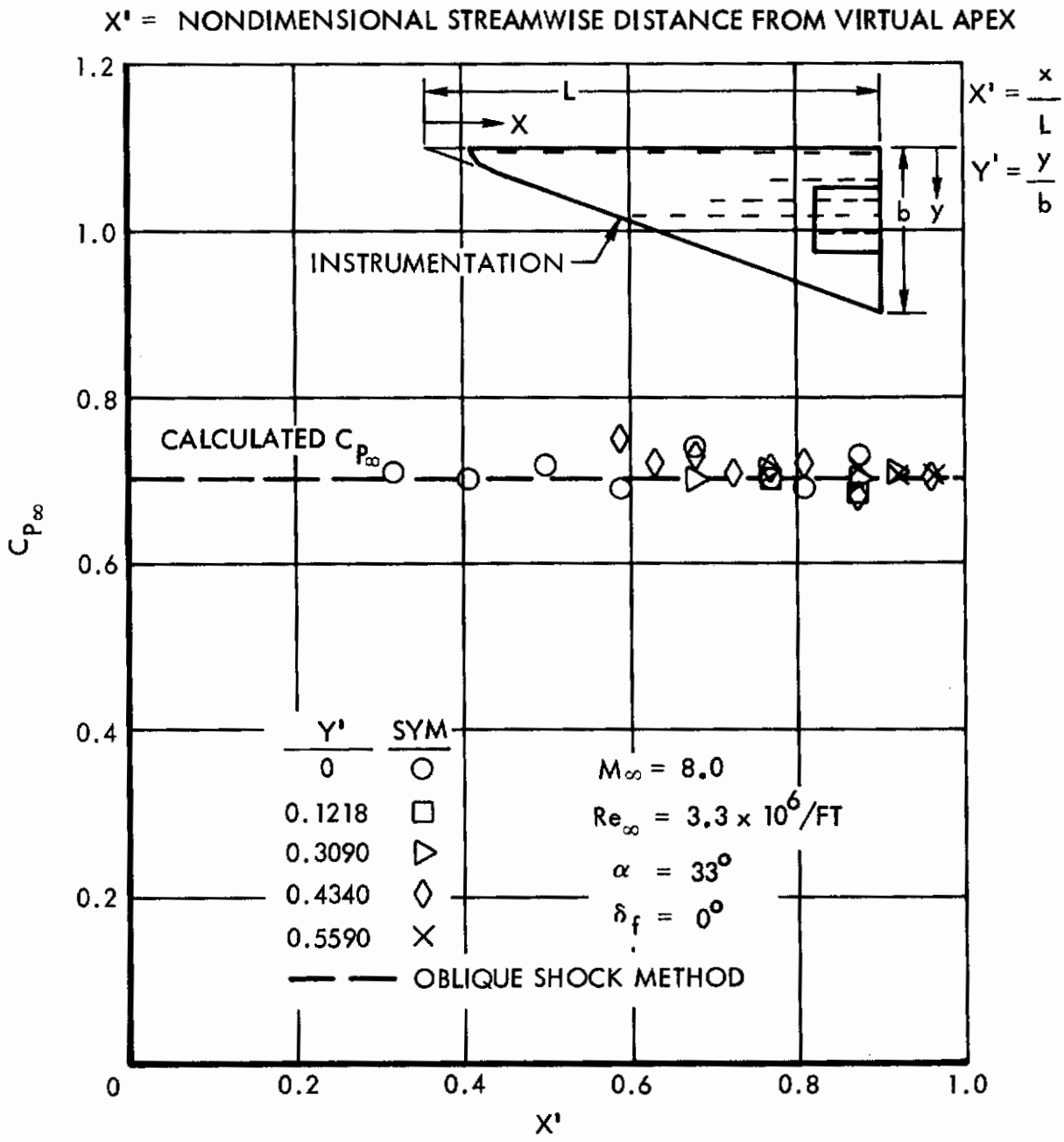

Figure 86. Lengthwise Pressure Distribution Over Pyramidial Configuration (Flat Bottom Surface)

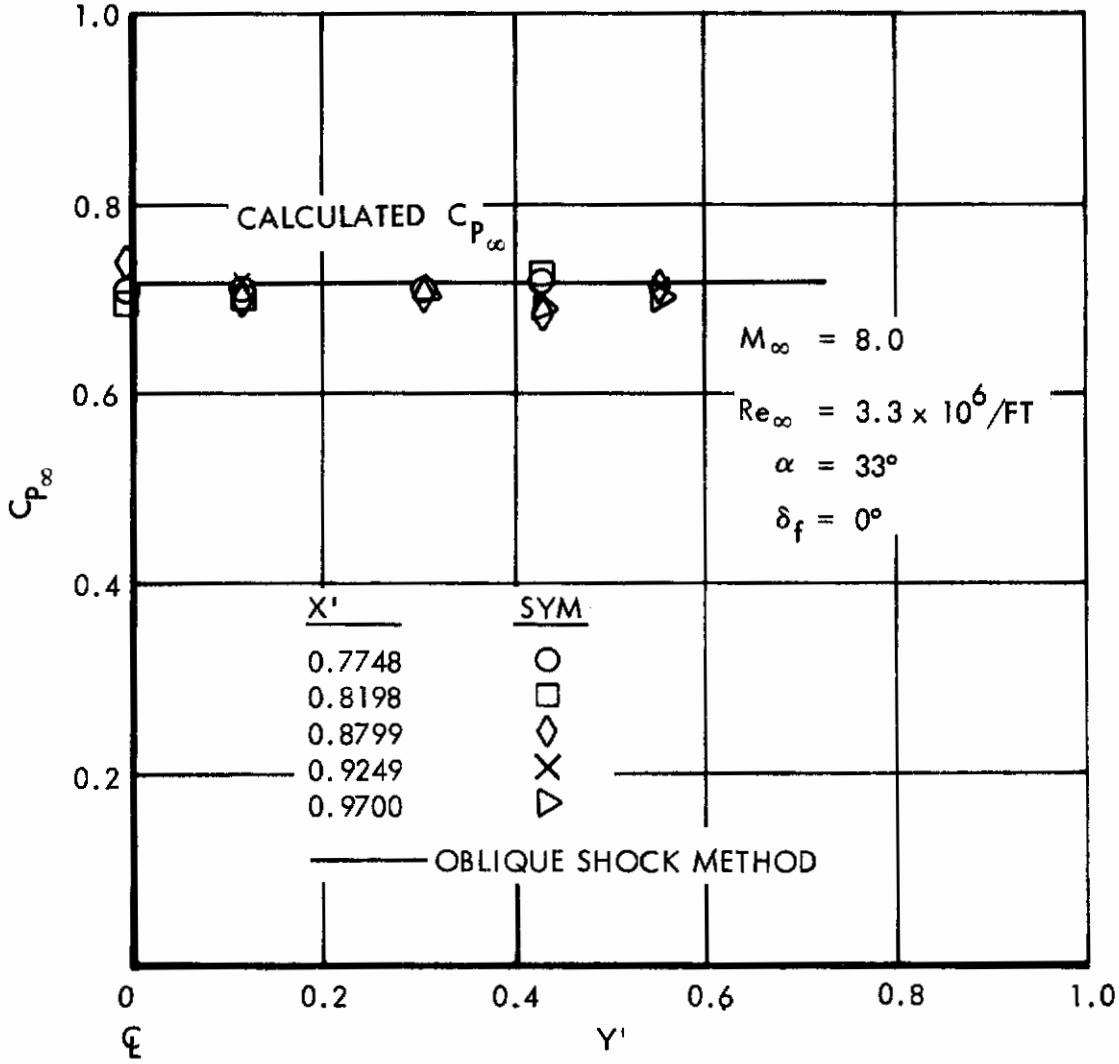

Figure 87. Spanwise Pressure Distribution Over Pyramidal Configuration (Flat Bottom Surface)

$\frac{P_{flap}}{P_\alpha}$ in the normal shock tables of Reference 36. M_α is then obtained by iteration with the aid of Chart II of the same reference. The value for M_α was found to be almost identical to the two-dimensional value corresponding to the given angle of attack. Therefore the local Reynolds number is found through the use of the oblique shock tables of Reference 36.

The distance and pressure parameters d_1, ℓ_{f_i}, C_{P_P}, and C_{P_2} for separated flow upstream of the flaps were calculated as noted in Section IV. The existence of laminar flow ($Re_{\alpha X_0} = 7.81 \times 10^5$, $M_\alpha = 4.79$) was verified by the Deem Murphy formula (Equation 17).

Reasonable agreement with the experimental values of Reference 67 was obtained (Figures 88 through 91). Since the $Re_{\alpha X_0}$ changes in the spanwise direction, the calculated parameters will be a function of y. It is therefore recommended that an average $Re_{\alpha X_0}$ be taken to determine the pressure profile. For small values of Λ and for downstream flap positions this will not be necessary. In cases where the control surfaces are located in the region of influence of the blunt leading edge, bluntness effects must be considered for moderate angles of attack. The blast wave analysis of Reference 34 may be used to find the pressure increment due to the blunt leading edge. Therefore,

$$\frac{P_b}{P_\infty} = (1/2)^{2/3} (C_\gamma) C_D^{2/3} \frac{M_\infty^2 \cos^2 \Lambda_{effective}}{\left(\frac{x}{d}\right)^{2/3}}$$

where

$$\Lambda_{effective} = \arcsin (\cos \alpha \sin \Lambda)$$

The inviscid pressure distribution is thus:

$$\frac{P_o}{P_\infty} = \frac{P_\alpha}{P_\infty} + \frac{P_b}{P_\infty}$$

This may be solved for P_o/P_∞ at each x_o position. If viscous effects are found to be important by the previously mentioned criteria (Section III), they may be accounted for by the methods presented in that section. The preceding analysis assumes the flow to be two dimensional in the sense that strip theory is applicable.

Flow About a Delta Wing with Dihedral

The dihedral surface of the pyramidal configuration (Figure 83) exhibits a significantly different flow pattern from that of the flat bottom surface.

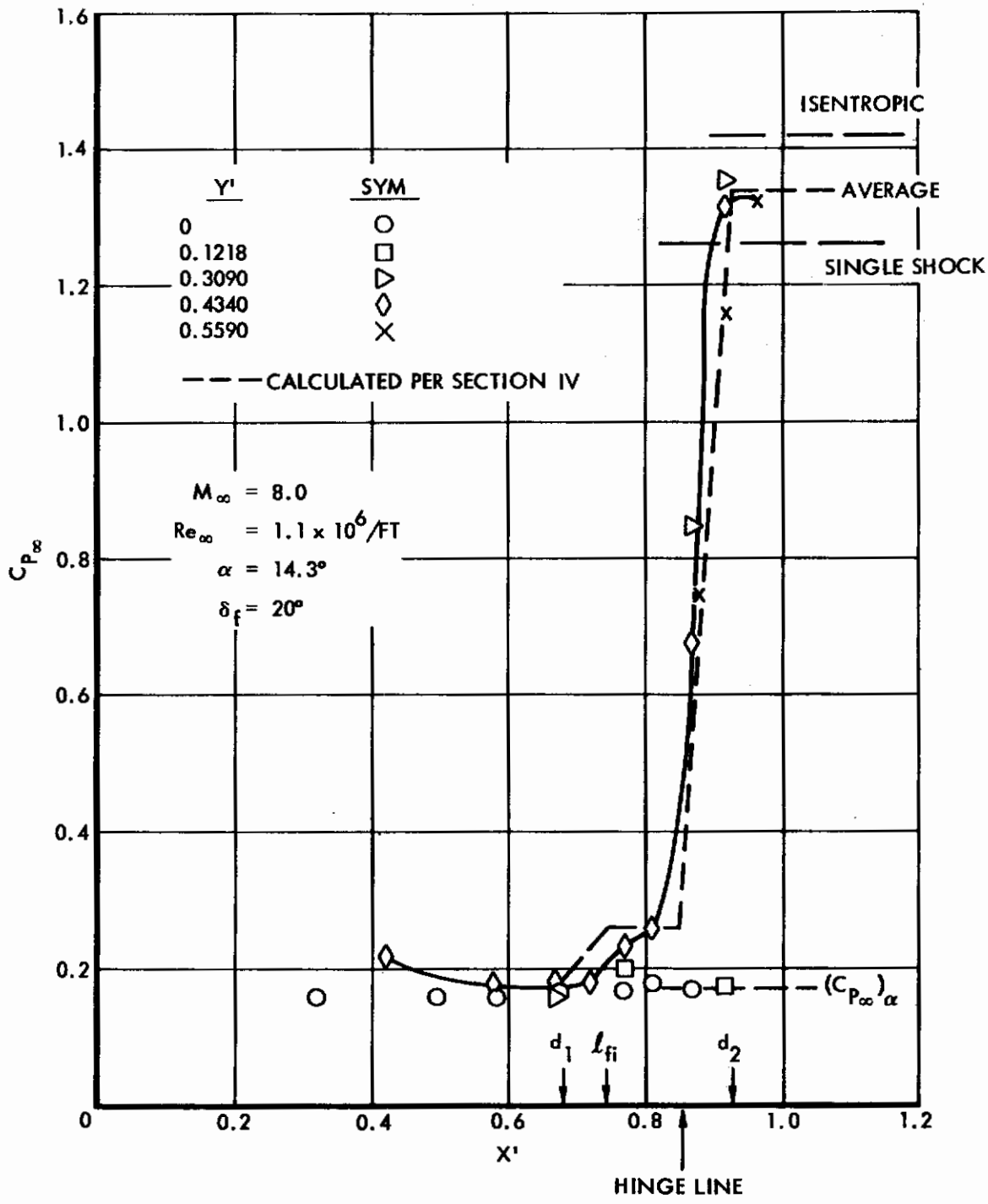

Figure 88. Pressure Distribution Over Pyramidal Configuration (Flat Bottom Surface)

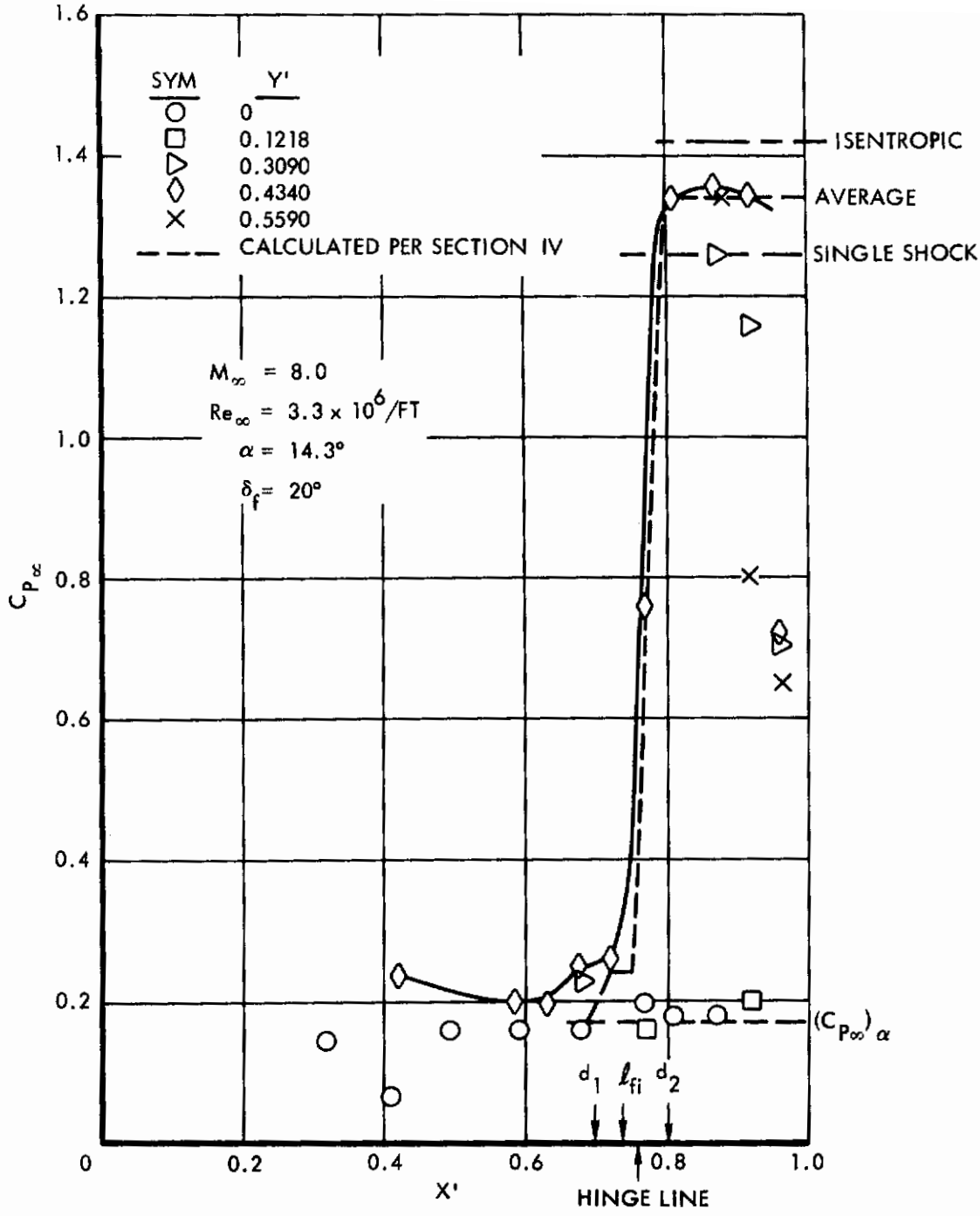

Figure 89. Pressure Distribution Over Pyramidal Configuration (Flat Bottom Surface), $Re_\infty = 3.3 \times 10^6$/ft

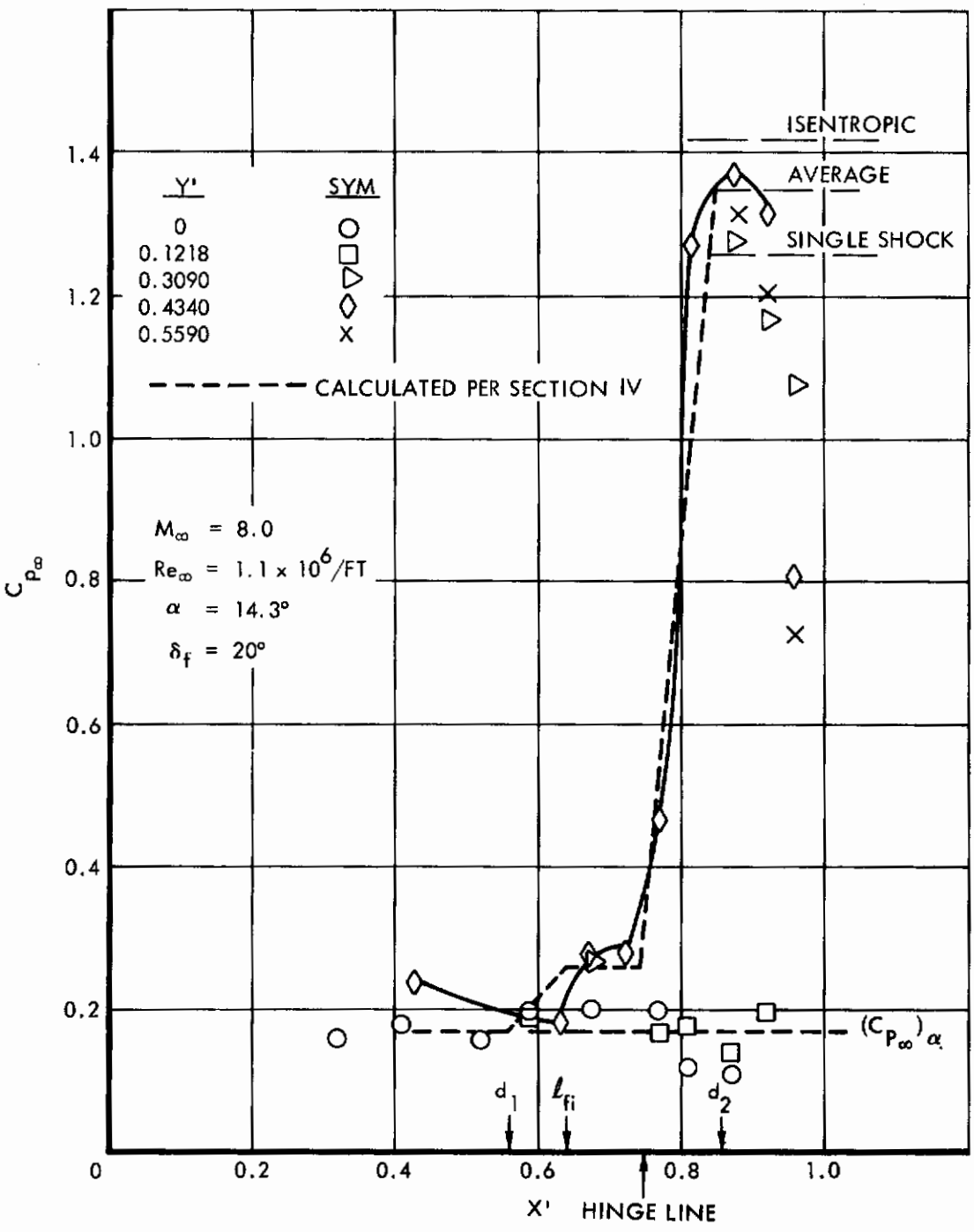

Figure 90. Pressure Distribution Over Pyramidal Configuration (Flat Bottom Surface), X'_{HL} = 0.75, R_e = 1.1 X 10^6/ft, δ_f = 20°

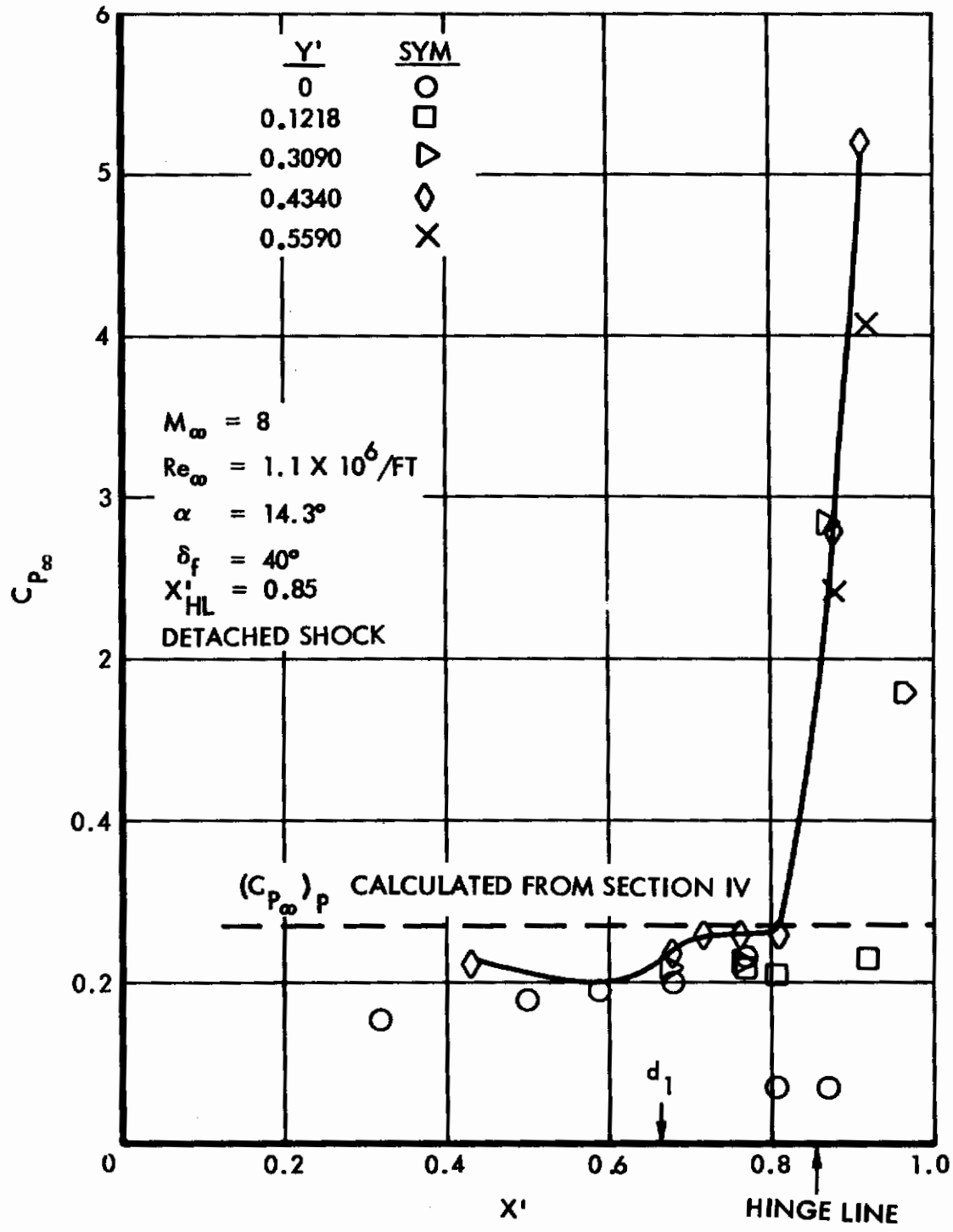

Figure 91. Pressure Distribution Over Pyramidal Configuration (Flat Bottom Surface), $\delta_f = 40°$, $X'_{HL} = 0.85$, $Re_\infty = 1.1 \times 10^6$/ft

The oil flow pattern (Figures 4 through 7, Reference 67) indicates outboard flow on both sides of the ridge. A well defined blast region no longer exists. The interaction region ahead of the flap undergoes a severe distortion in the transverse direction. The separated region is swept outward and is noted to flow over the blunt edges.

An outflow is seen to exist all along the leading edges for all angles of attack at which the pressures on the dihedral surfaces exceed those on the lower surface. Consequently, the resultant flow field around the model is rather complex and the application of certain approximations in calculating the flow properties seems well justified. The accuracy of these approximations will be established by comparison with experimental values.

Pressure Distribution on a Delta Wing with Dihedral

To test the applicability of the two-dimensional analysis to a blunt delta wing ($\Lambda = 70°$) with dihedral, the local flow conditions on dihedral surfaces were examined. It was found that the pressure in the streamwise direction is almost constant and decreases only slightly in the spanwise direction as shown on Figures 92 and 93 for $\alpha = 29°$; conical flow may be more applicable as concluded from the conical shock shape appearing at higher angles of attack (Reference 68). The instrumentation density in the interaction region was not sufficient to allow the determination of the characteristic parameters d_1, ℓ_{f_i}, and C_{P_P}.

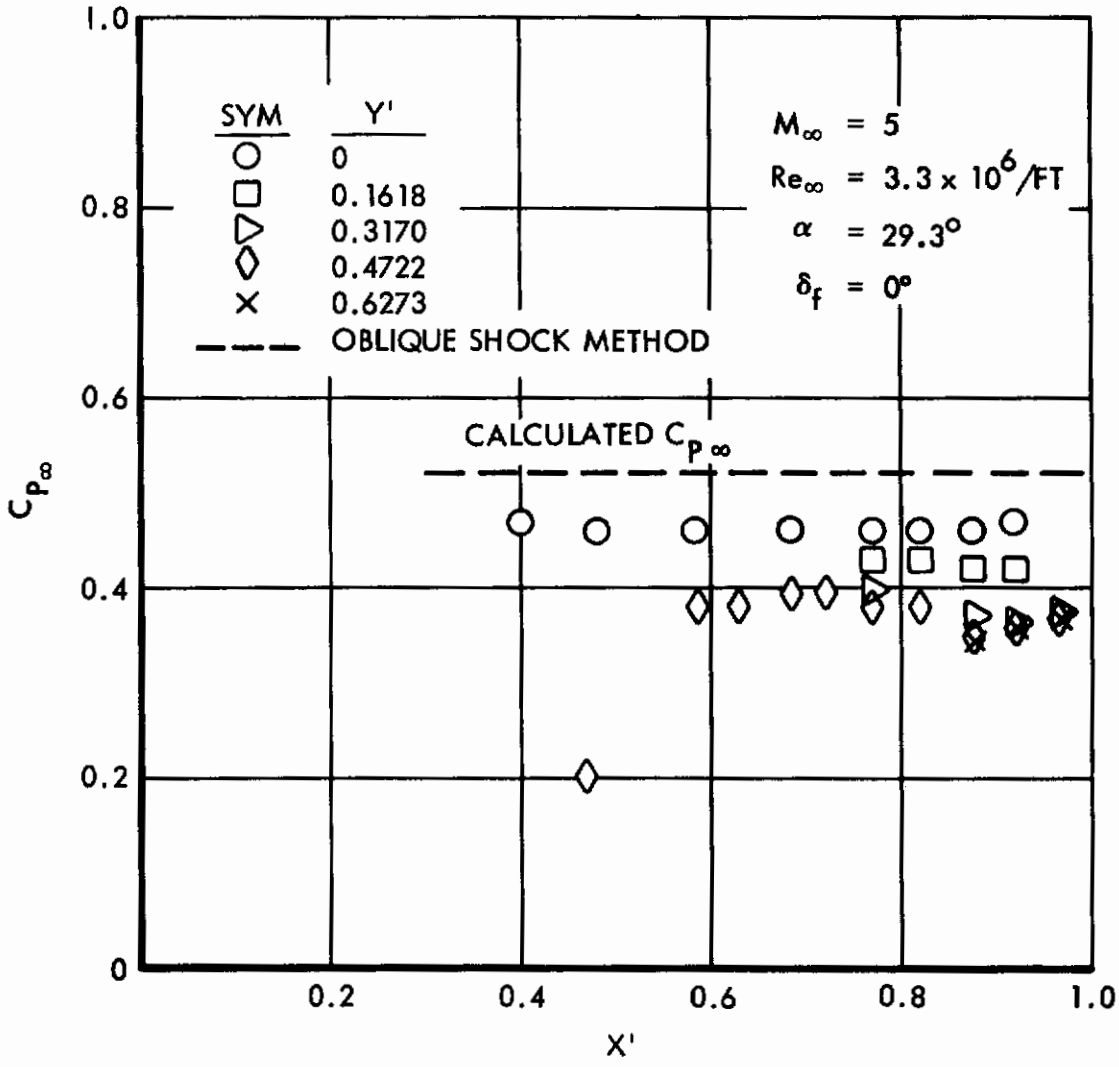

Figure 92. Lengthwise Pressure Distribution Over Pyramidal Configuration (Dihedral Surface)

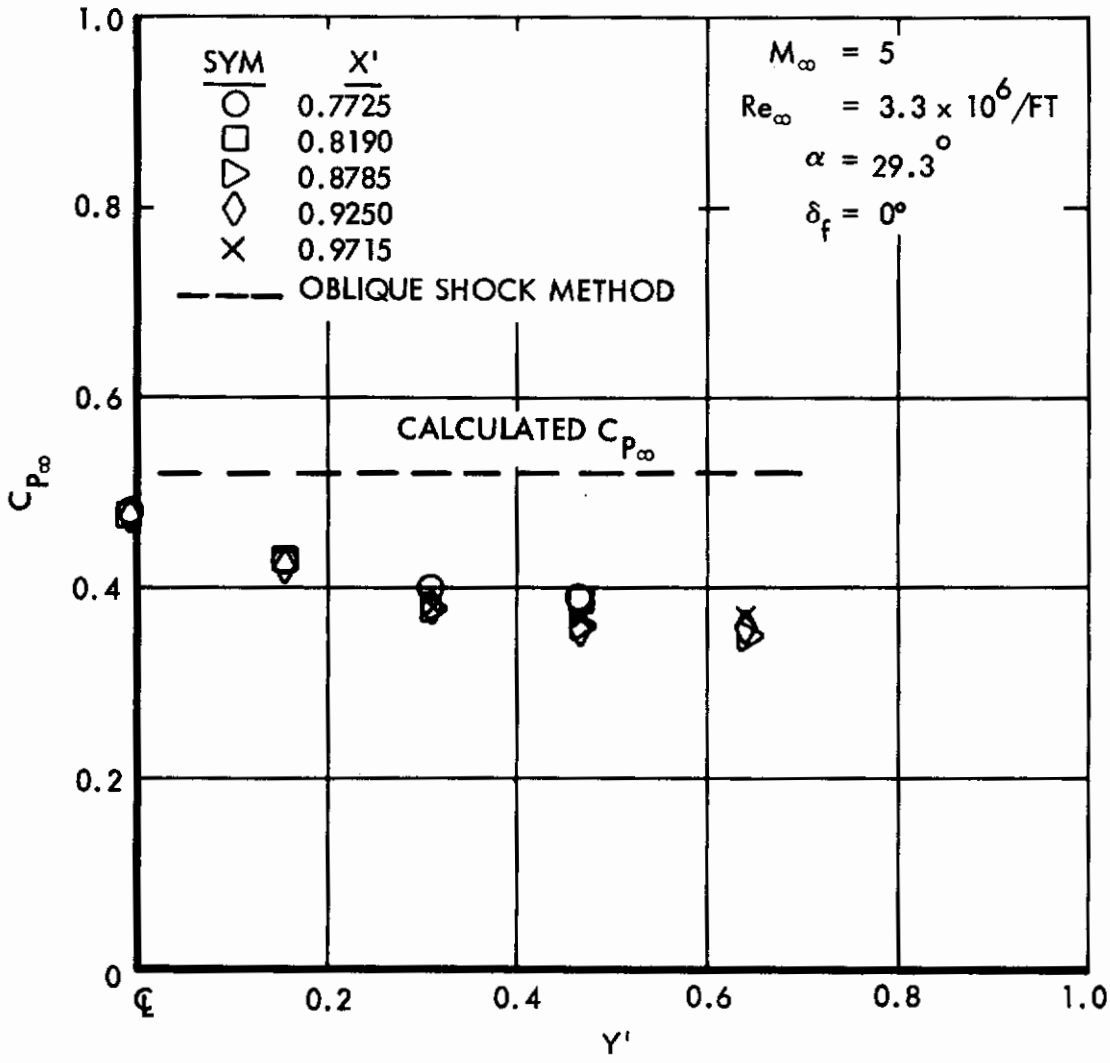

Figure 93. Spanwise Pressure Distribution Over Pyramidal Configuration (Dihedral Surface)

Section VI

PREDICTION OF EFFECTIVENESS OF AERODYNAMIC CONTROLS

This section develops a systematic procedure for the application of correlation results presented in preceding sections to the prediction of hypersonic control effectiveness. Wherever practicable, design charts are developed to facilitate the calculation procedure. The methods are intended for use over the broad range of flight conditions encountered by a typical hypersonic cruise/glide vehicle. It is to be emphasized, however, that the methods are based upon data obtained for a finite range of experimental conditions and that the validity of an extrapolation of the methods for conditions far outside the experimental range is yet to be established. The range of variables covered by the experimental data is indicated in the correlation figures (Section IV) and prediction charts. Application of the procedure described in this section for calculation of control effectiveness is illustrated in the sample problems presented in Appendix II.

FLIGHT CONDITIONS

The altitude-velocity envelope of a vehicle defines the range of free-stream conditions which are encountered during flight. For a given velocity, the maximum altitude at which a vehicle can fly is determined by the minimum dynamic pressure which will sustain flight, and the minimum altitude is restricted by the capability of a vehicle to withstand aerodynamic heating. The aerodynamic and heating boundary curves for a typical hypersonic cruise/glide vehicle were obtained from Reference 50 and are presented in Figure 94 The information developed in this section is confined to freestream flight conditions in the altitude-velocity envelope for Mach numbers greater than 5.

The angle of attack at which a vehicle flies is limited by vehicle performance and structural heating considerations. The angle of attack below which the lift/drag ratio is favorable and structural heating is not excessive is approximately 20 degrees. Since this study is concerned primarily with flat plate surfaces, angle of attack also represents flow deflection angle. Therefore, angle of attack is used to denote flow deflection angle and is limited to the range from 0 to 20 degrees.

The range of control surface deflection angle from 0 to 30 degrees relative to the forward surface is assumed to encompass most cases of practical interest.

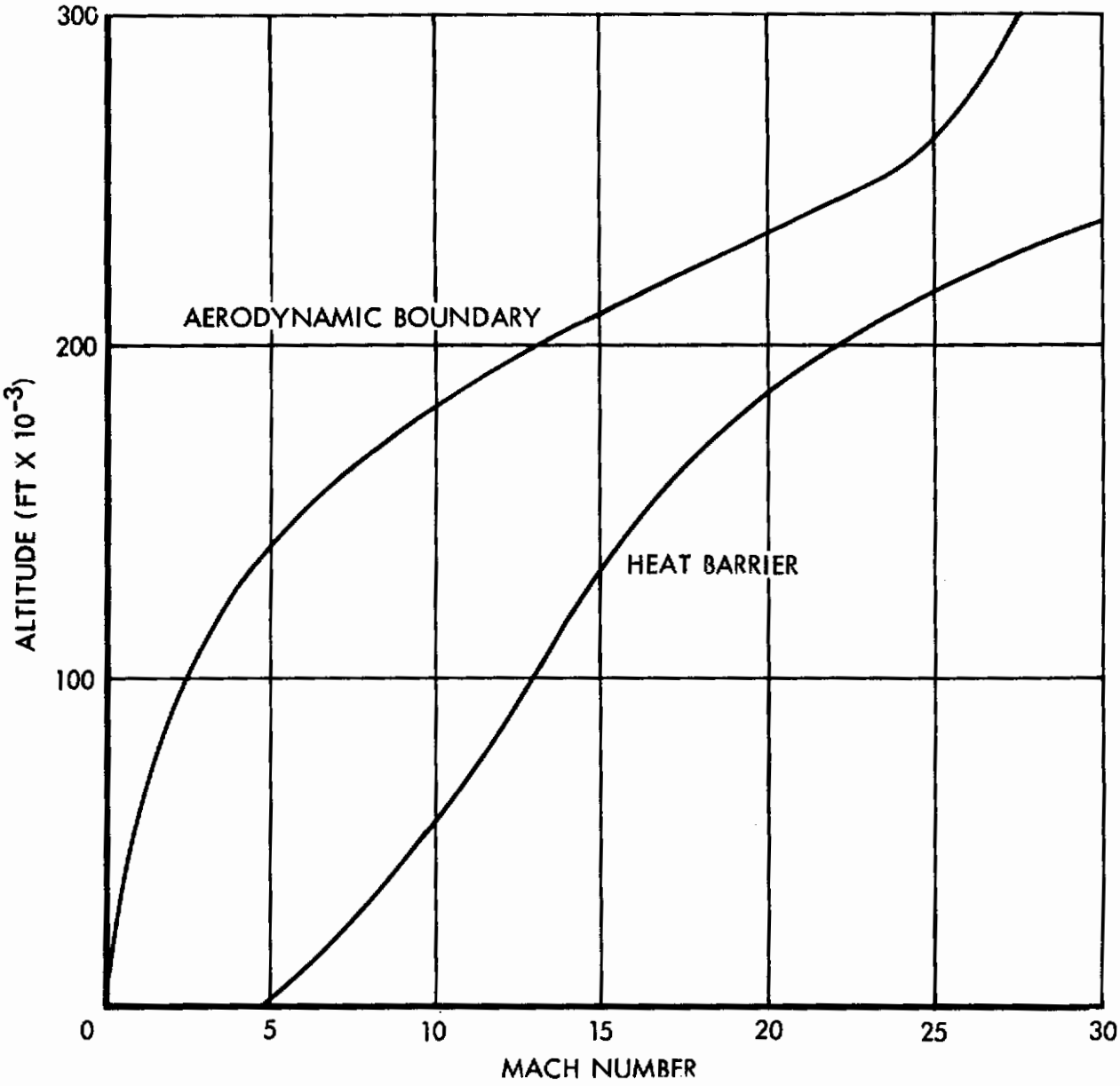

Figure 94. Typical Flight Envelope for Lifting Hypersonic Vehicles

LOCAL FLOW CONDITIONS

Local flow properties are used to define the parameters which describe compression corner flow separation. The first problem, then, in a control effectiveness analysis is the determination of flow conditions upstream of the control surface. Section III provides a discussion of methods for predicting local flow properties along blunted, planar surfaces. It was shown that on windward surfaces far downstream of the leading edge, local flow properties are approximately the same as flow conditions behind an oblique shock.

For many practical reentry configurations, control surfaces are located near the trailing edge of essentially planar surfaces and are sufficiently far from the leading edge for bluntness effects to be negligible. Also, since leeward surfaces in hypersonic flow are generally ineffective, the problem is reduced to investigation of compression corner flow separation on windward surfaces. Therefore, in many cases the flow properties forward of a control surface can be assumed to be approximately the same as conditions behind an oblique shock.

Since oblique shock assumptions are often valid, oblique shock properties have been determined for a number of flight conditions in the altitude-velocity envelope (Figure 94). Section 3.4 recommends that either perfect gas or equilibrium real gas assumptions be used for an oblique shock depending on velocity-altitude conditions and flow deflection angle.

For the flight regimes where flow properties deviate from those given by oblique shock theory for a perfect gas, equilibrium real gas effects were determined by means of similarity parameters from approximate theory and effective ratio of specific heats presented in Reference 69. This reference presents the effective ratio of specific heats, γ_e, at various altitudes (based on ARDC 1959 model atmosphere) as a function of the component of the Mach number normal to the shock wave. The solution for the correct γ_e to be used in the calculations involved an iterative procedure for determining the shock wave angle and corresponding normal component of the Mach number. For the first iteration, the Mach number component normal to a perfect gas oblique shock angle was assumed for determining the initial γ_e (Reference 69, Figure 12). This value of γ_e was used to calculate the value of the parameter $(\gamma_e + 1)\frac{M_\infty^2}{\beta}\sin\alpha$. Figure 4 of Reference 69 presents curves which correlate the normal Mach number component as a function of this parameter. The normal Mach number obtained from these curves was used for the second iteration. This procedure was repeated until the initial and final normal Mach number components converged.

Having determined the effective ratio of specific heats, the oblique shock correlations of Reference 69 were used for rapid calculation of the flow properties for an equilibrium real gas.

The oblique shock Reynolds number ratio was determined from the following expression:

$$\frac{Re_\alpha}{Re_\infty} = \frac{\rho_\alpha u_\alpha}{\rho_\infty u_\infty} \left(\frac{T_\infty}{T_\alpha} \right)^{0.67}$$

This expression is derived using an exponential viscosity-temperature relation with a power of 0.67. Comparison of the exponential viscosity-temperature relation for various powers with Sutherland's formula is shown in Figure 95. This comparison indicates that over the range of temperature of practical interest, the 0.67 power provides sufficient accuracy for this application. Although a lower power provides better agreement at high temperature, the disagreement is increased in the intermediate range of temperature where most of the design conditions are expected to occur.

The Mach number behind an oblique shock for a real gas was evaluated with the aid of References 69 and 70 using the relation

$$M_\alpha = M_\infty \frac{u_\alpha}{u_\infty} \frac{a_\infty}{a_\alpha}$$

The oblique shock velocity ratio was determined from equation 25a of Reference 69.

$$\frac{u_\alpha}{u_\infty} = \frac{1}{\cos \alpha} \left[1 - \left(1 - \frac{\rho_\infty}{\rho_\alpha} \right) \sin^2 \theta \right]$$

The speed of sound ratio was obtained from data presented in Table IV of Reference 70.

Figures 96 through 99 present the pressure, temperature, Mach number, and Reynolds number behind an oblique shock for flow deflection angles from 0 to 20 degrees for the following altitude and Mach number conditions:

Altitude (feet)	Mach Number
50,000	5, 7
100,000	5, 7, 10
150,000	10, 15
200,000	15, 20, 30
250,000	20, 30
300,000	20, 30

The selection of Mach number is restricted to those Mach numbers in the vicinity of the flight envelope for which Reference 69 presents data.

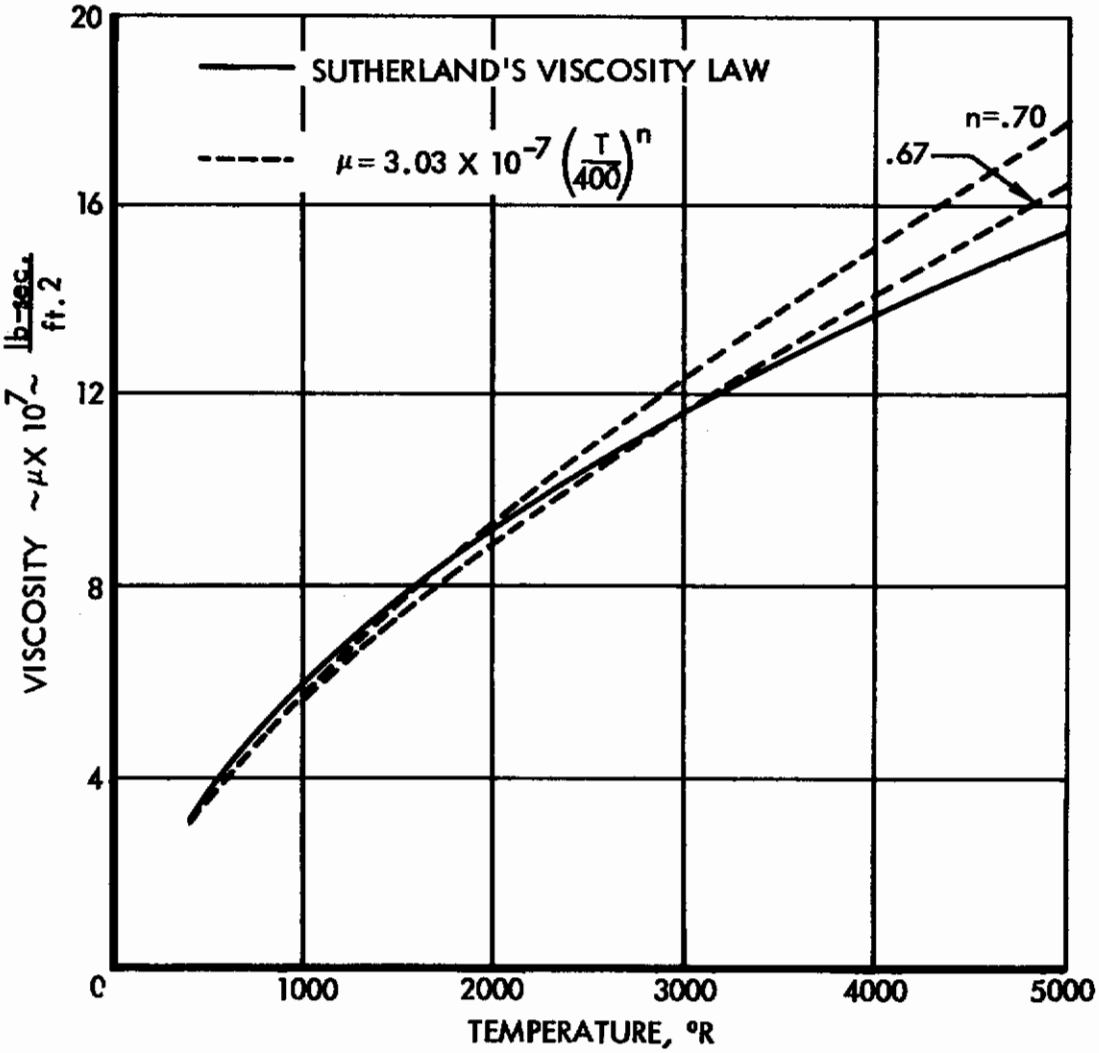

Figure 95. Comparison of Sutherland's Viscosity Law with Exponential Viscosity - Temperature Relation

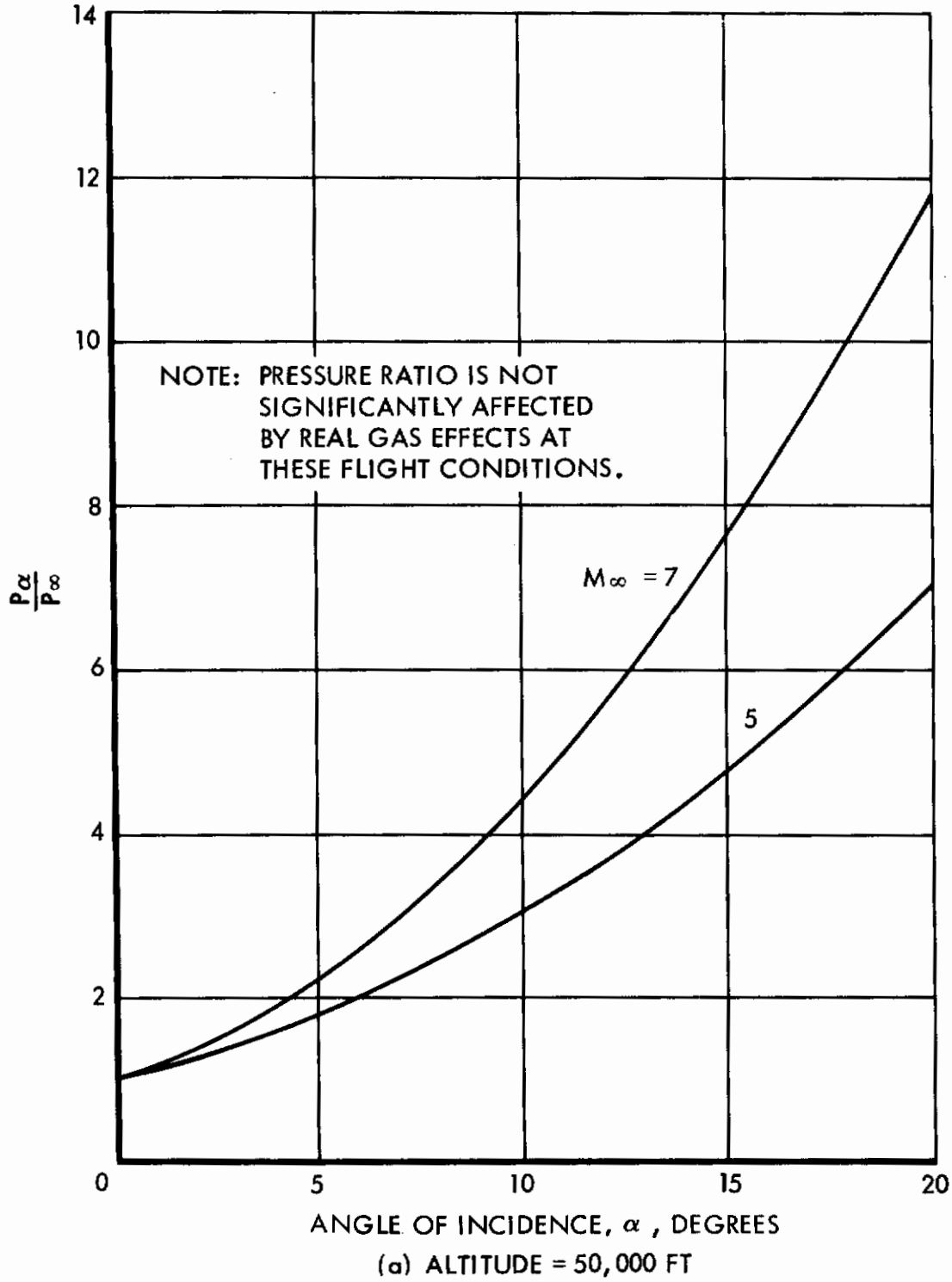

Figure 96. Oblique Shock Pressure Ratio Including Real Gas Effects

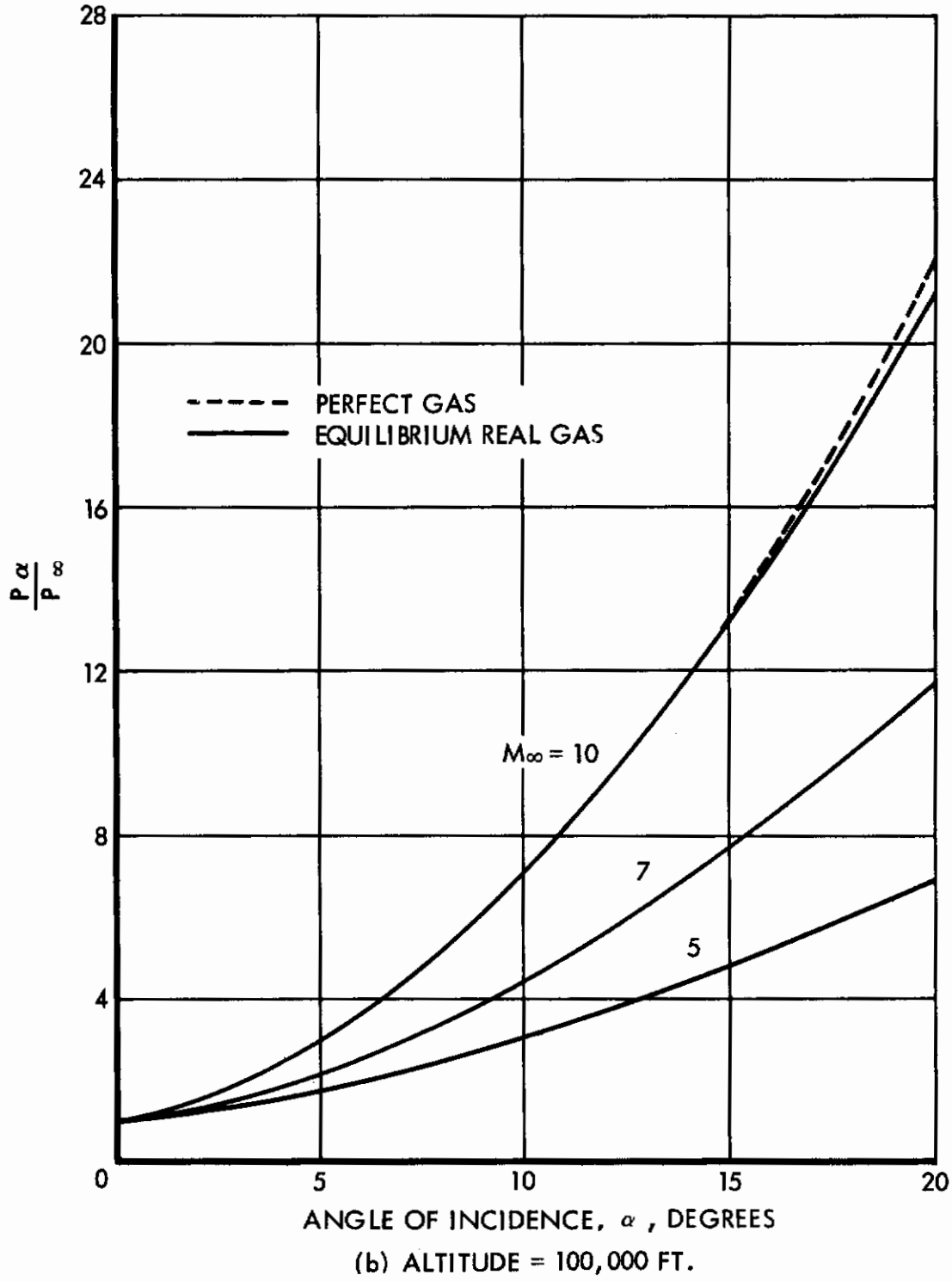

Figure 96. Oblique Shock Pressure Ratio Including Real Gas Effects (Continued)

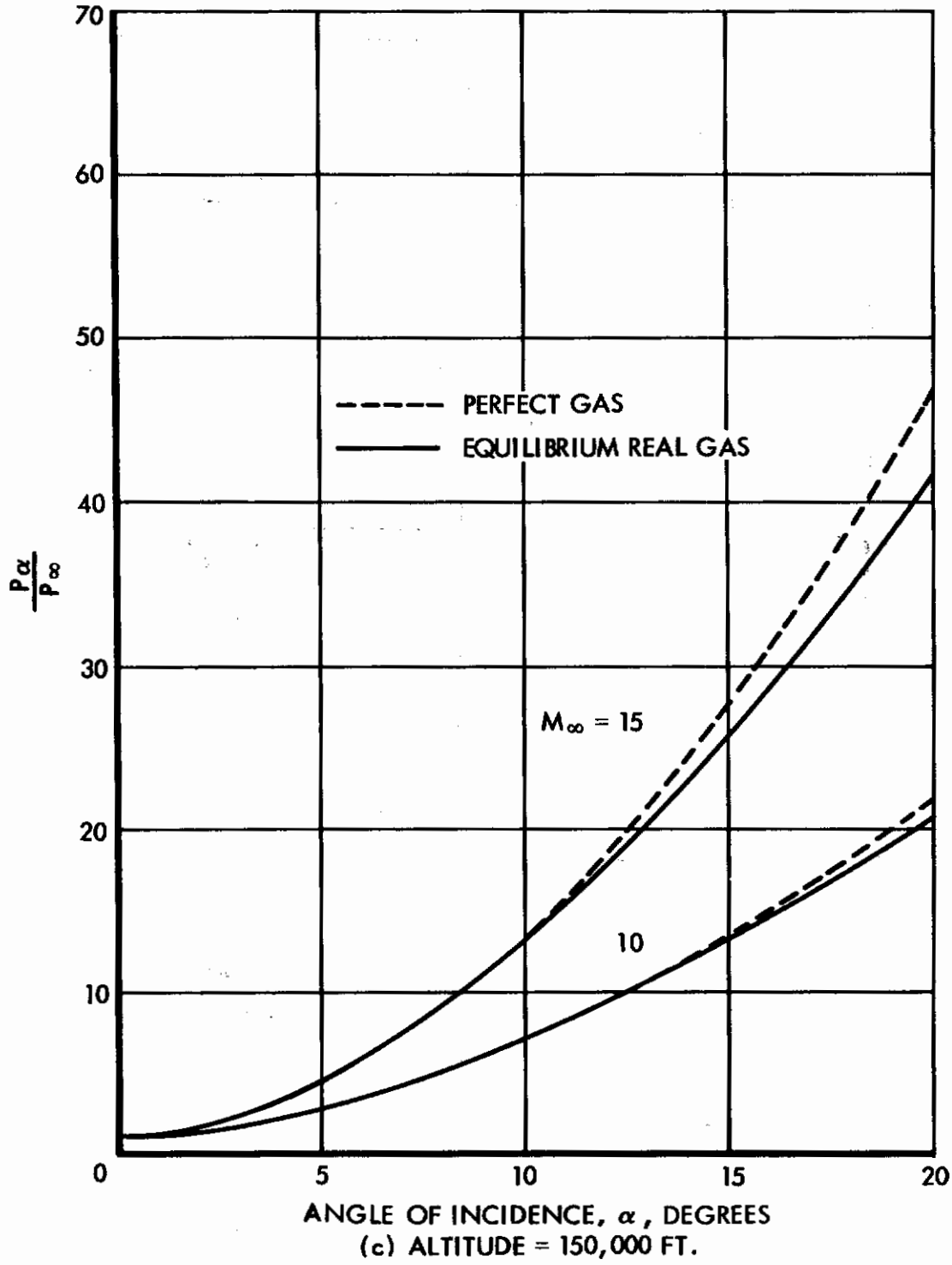

Figure 96. Oblique Shock Pressure Ratio Including Real Gas Effects (Continued)

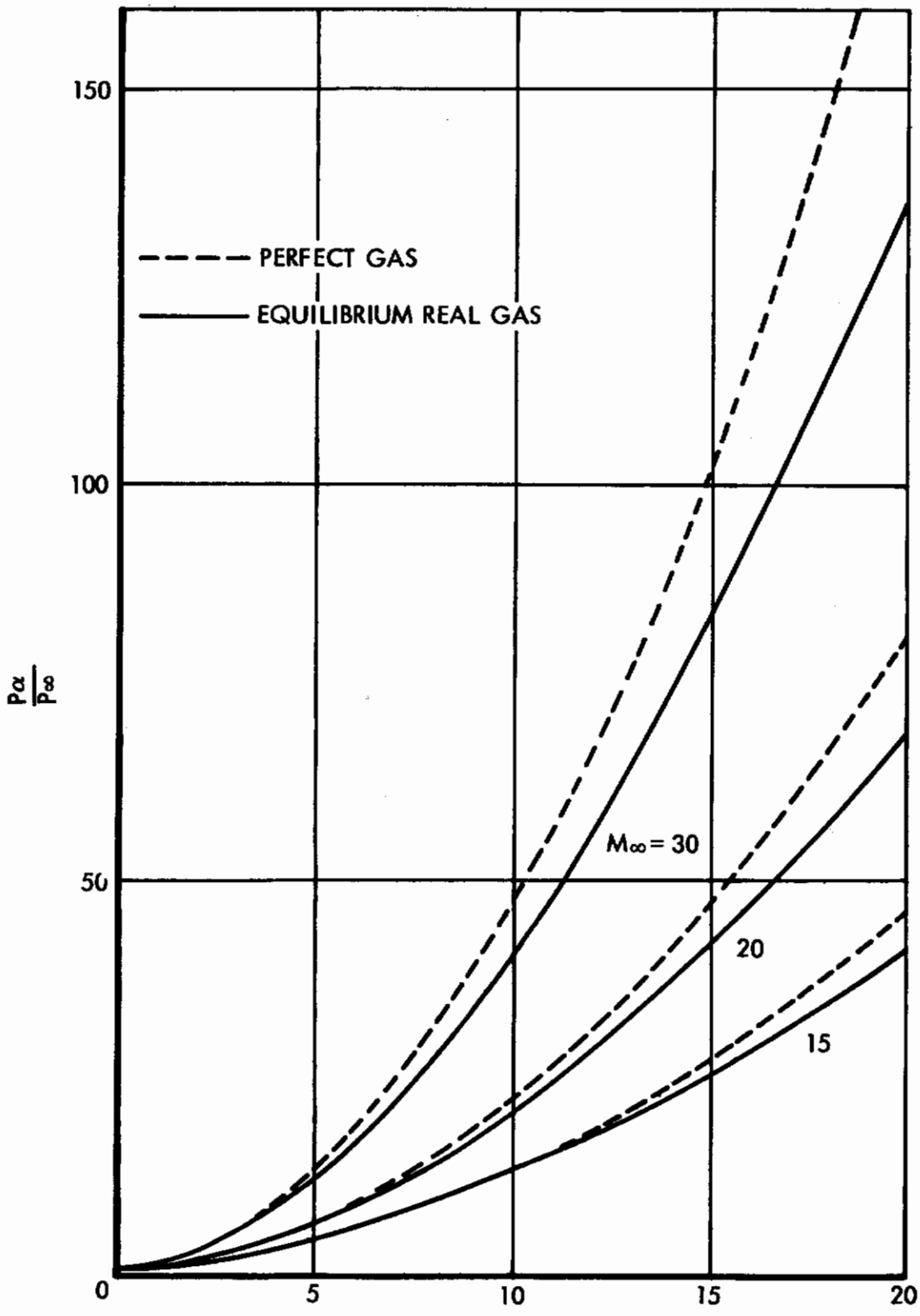

(d) ALTITUDE = 200,000 FT.

Figure 96. Oblique Shock Pressure Ratio Including Real Gas Effects (Continued)

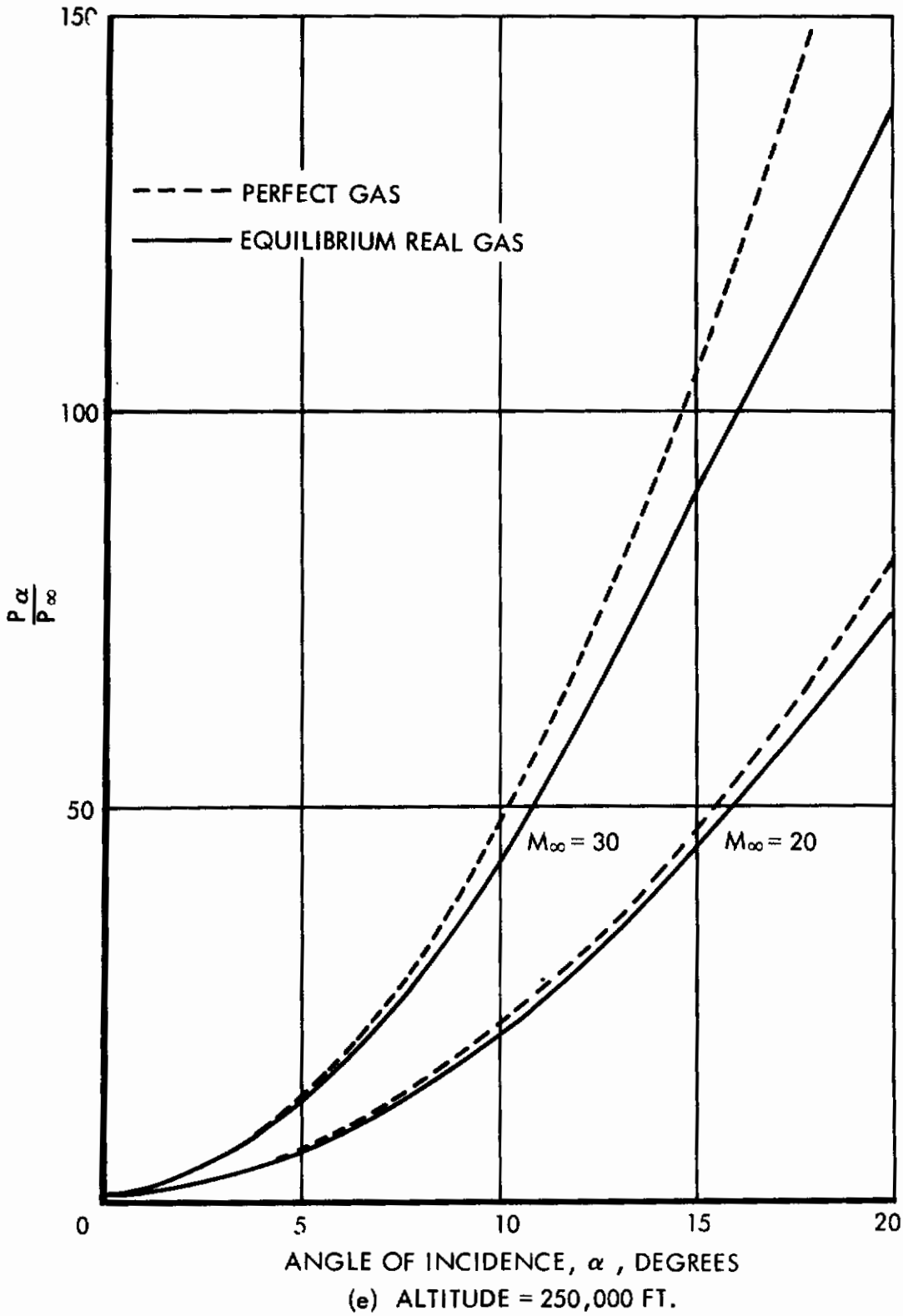

(e) ALTITUDE = 250,000 FT.

Figure 96. Oblique Shock Pressure Ratio Including Real Gas Effects (Continued)

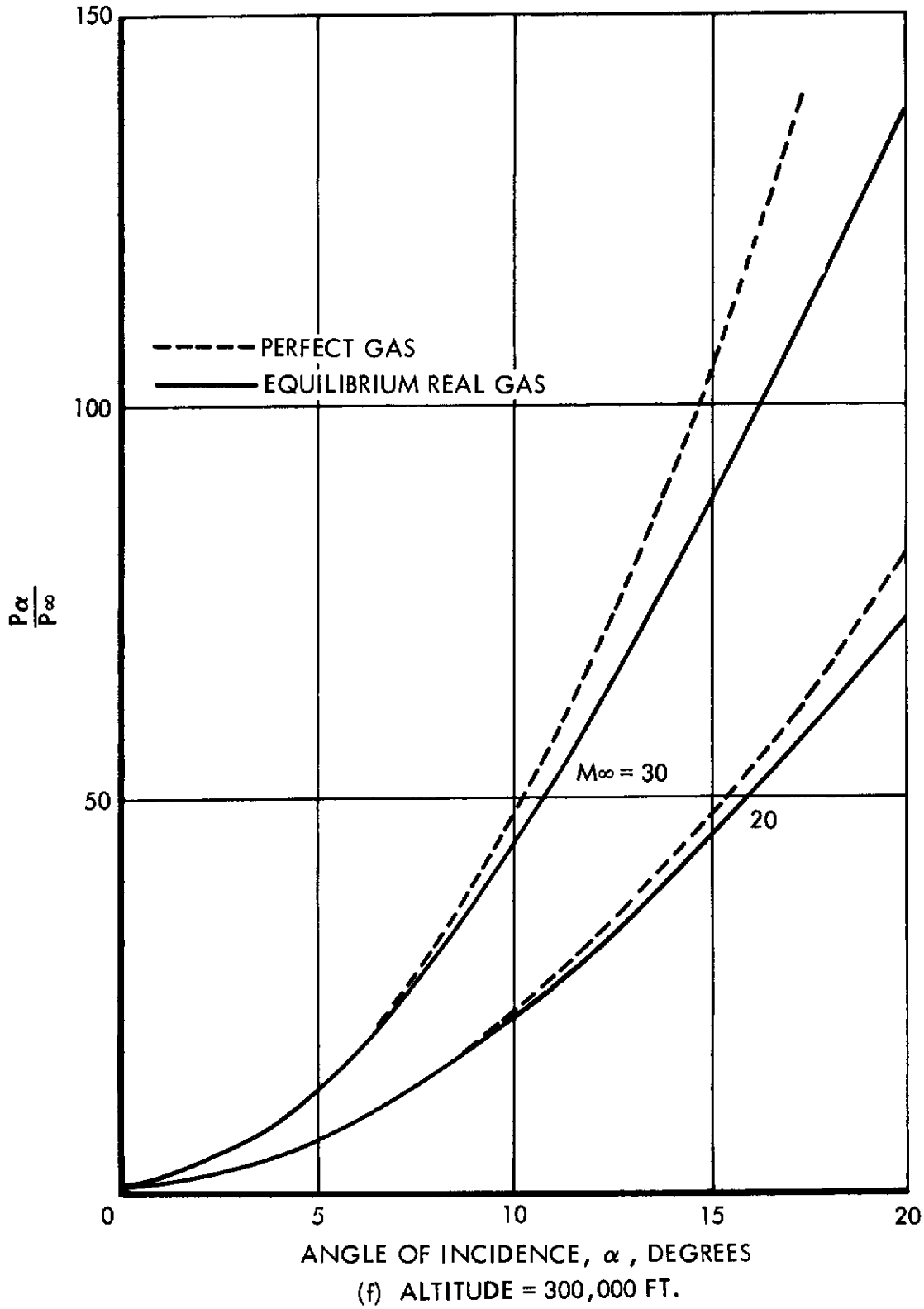

(f) ALTITUDE = 300,000 FT.

Figure 96. Oblique Shock Pressure Ratio Including Real Gas Effects (Concluded)

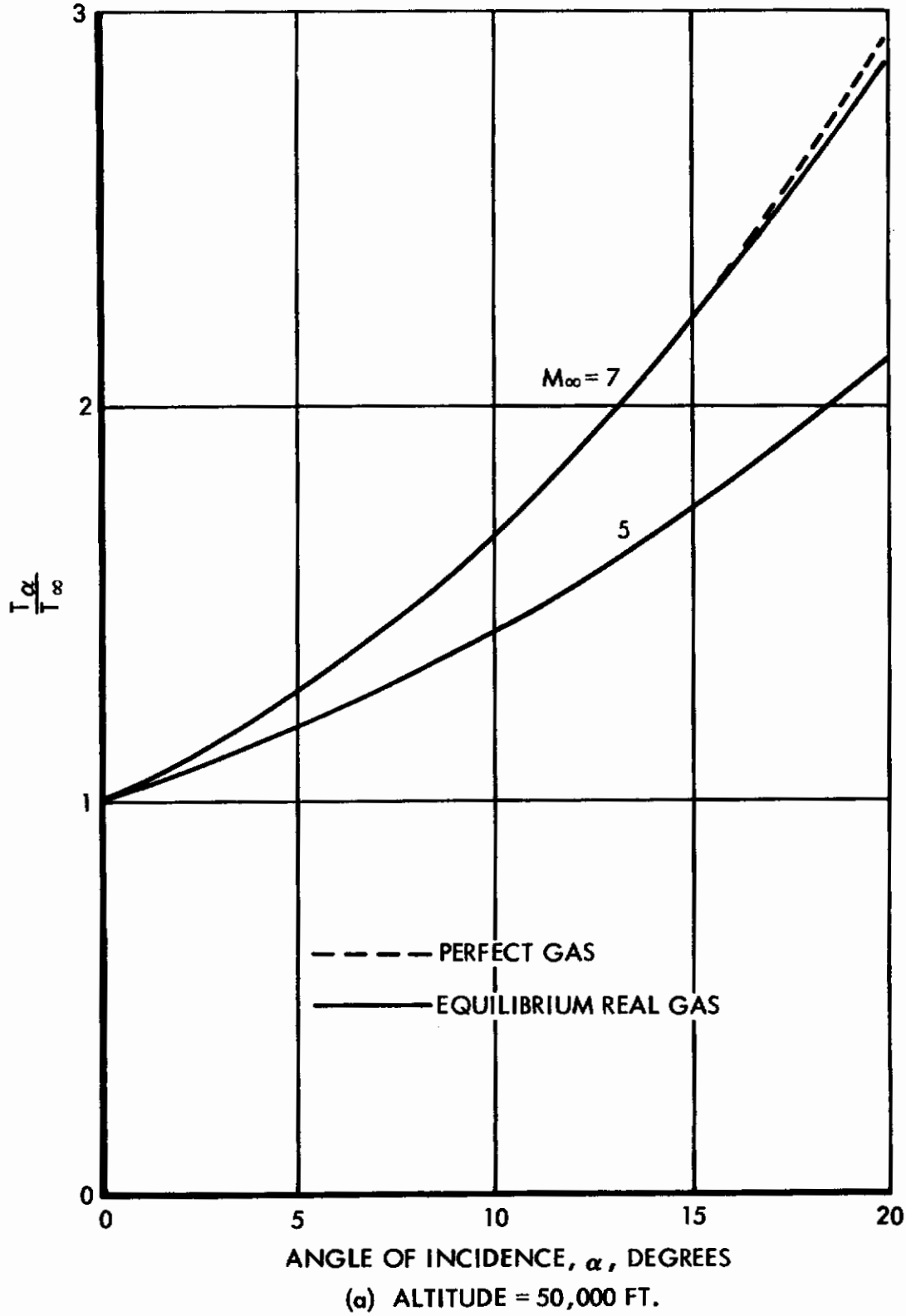

(a) ALTITUDE = 50,000 FT.

Figure 97. Oblique Shock Temperature Ratio Including Real Gas Effects

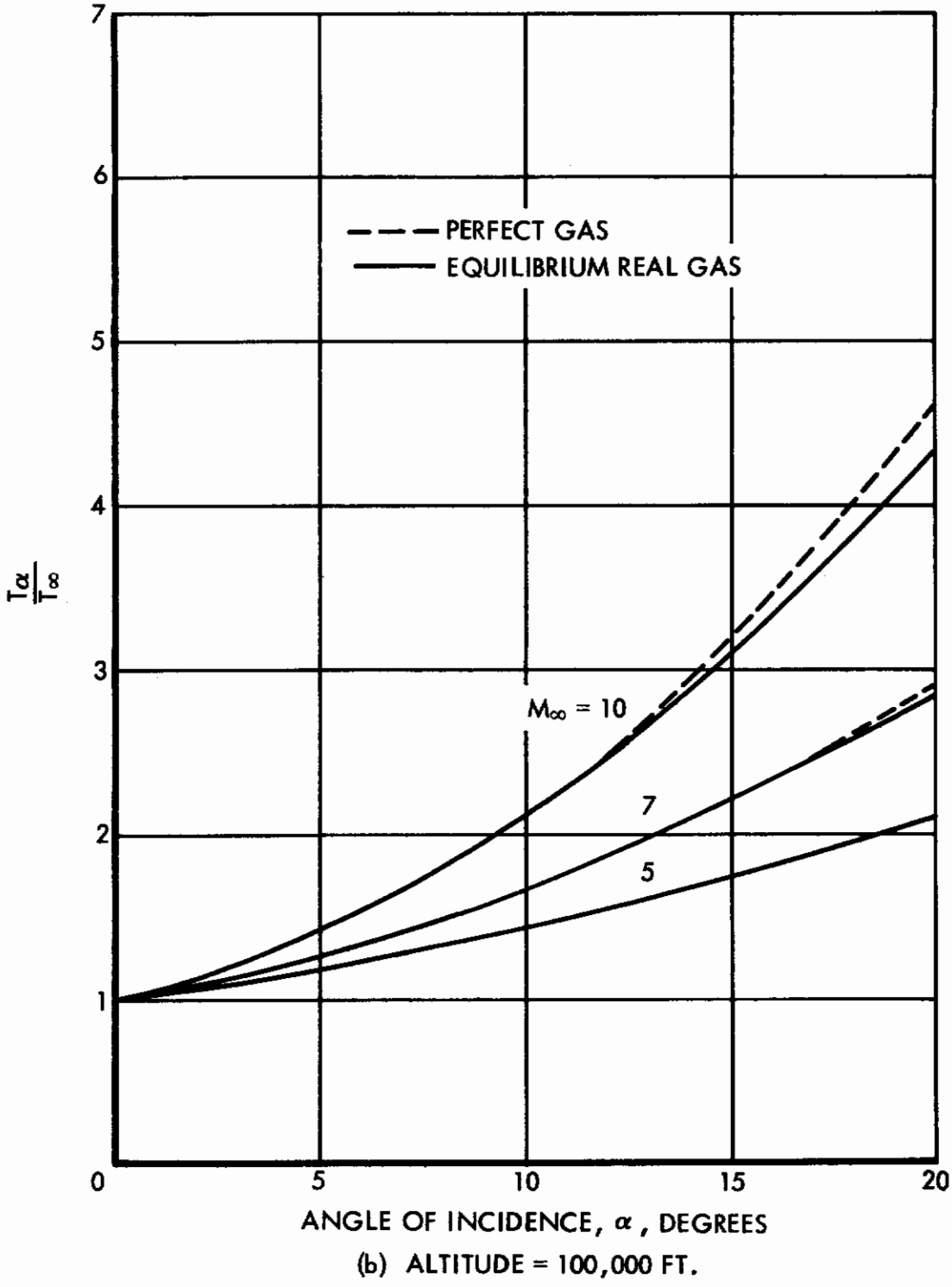

Figure 97. Oblique Shock Temperature Ratio Including Real Gas Effects (Continued)

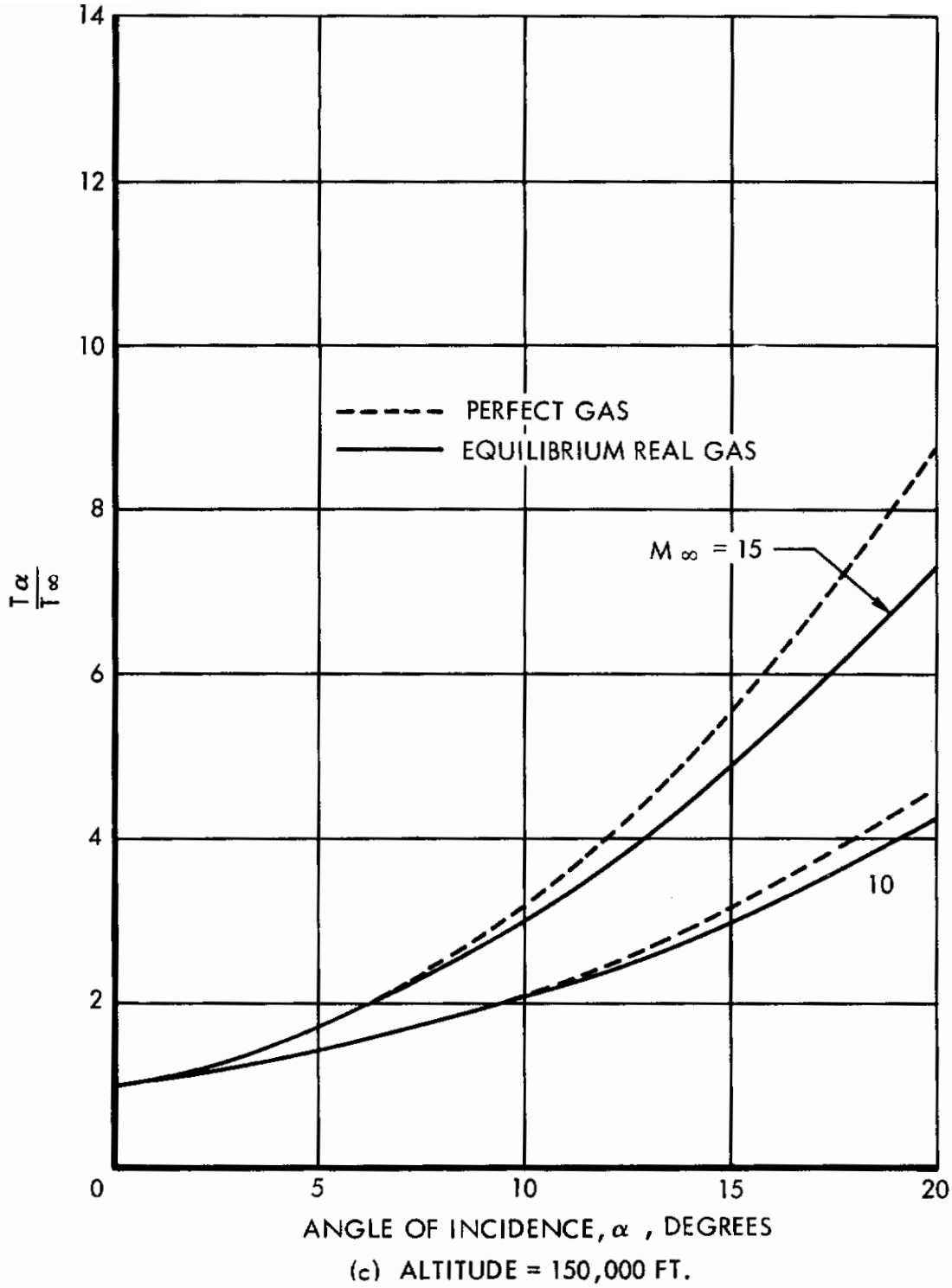

Figure 97. Oblique Shock Temperature Ratio Including Real Gas Effects (Continued)

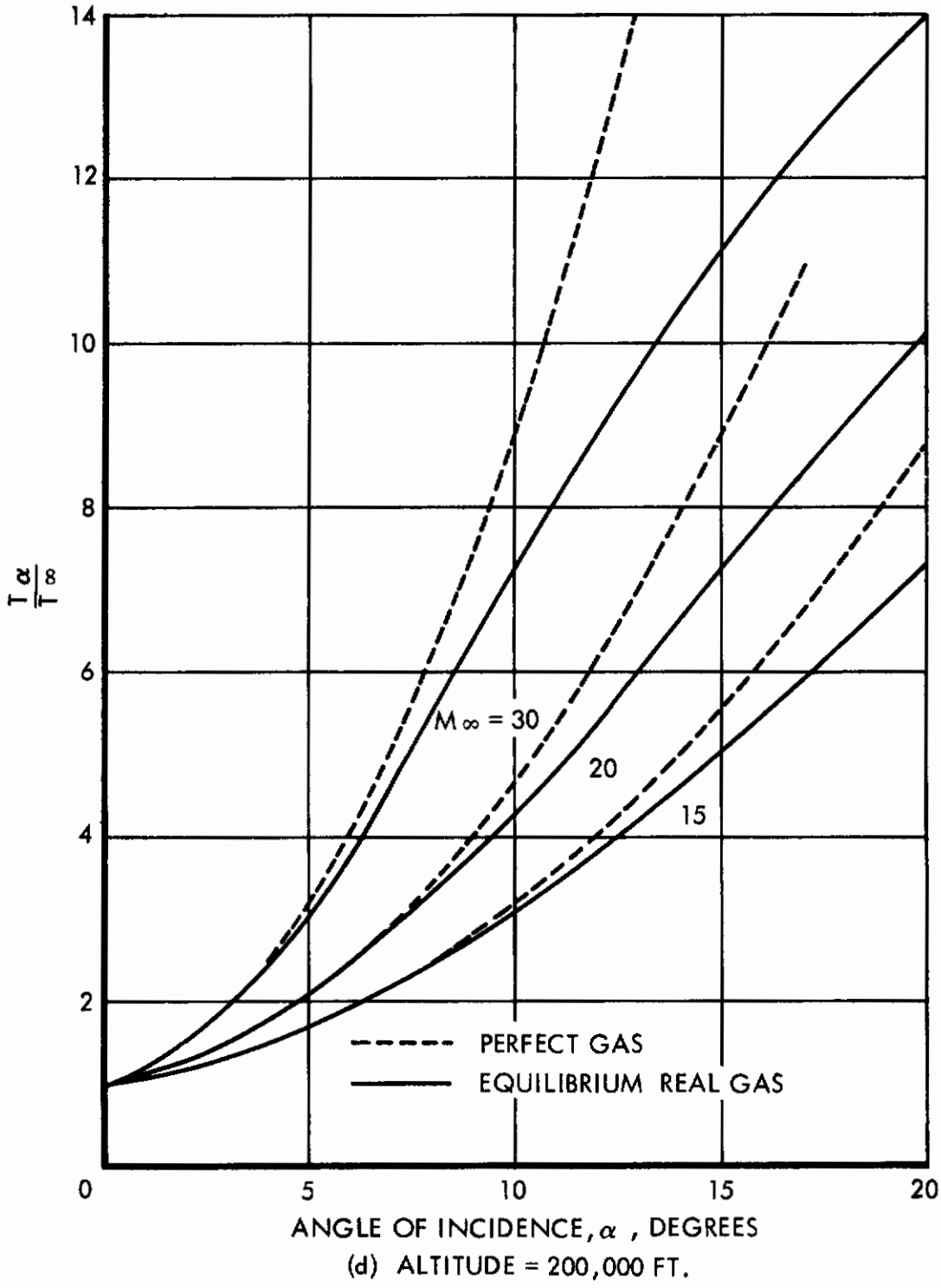

Figure 97. Oblique Shock Temperature Ratio Including Real Gas Effects (Continued)

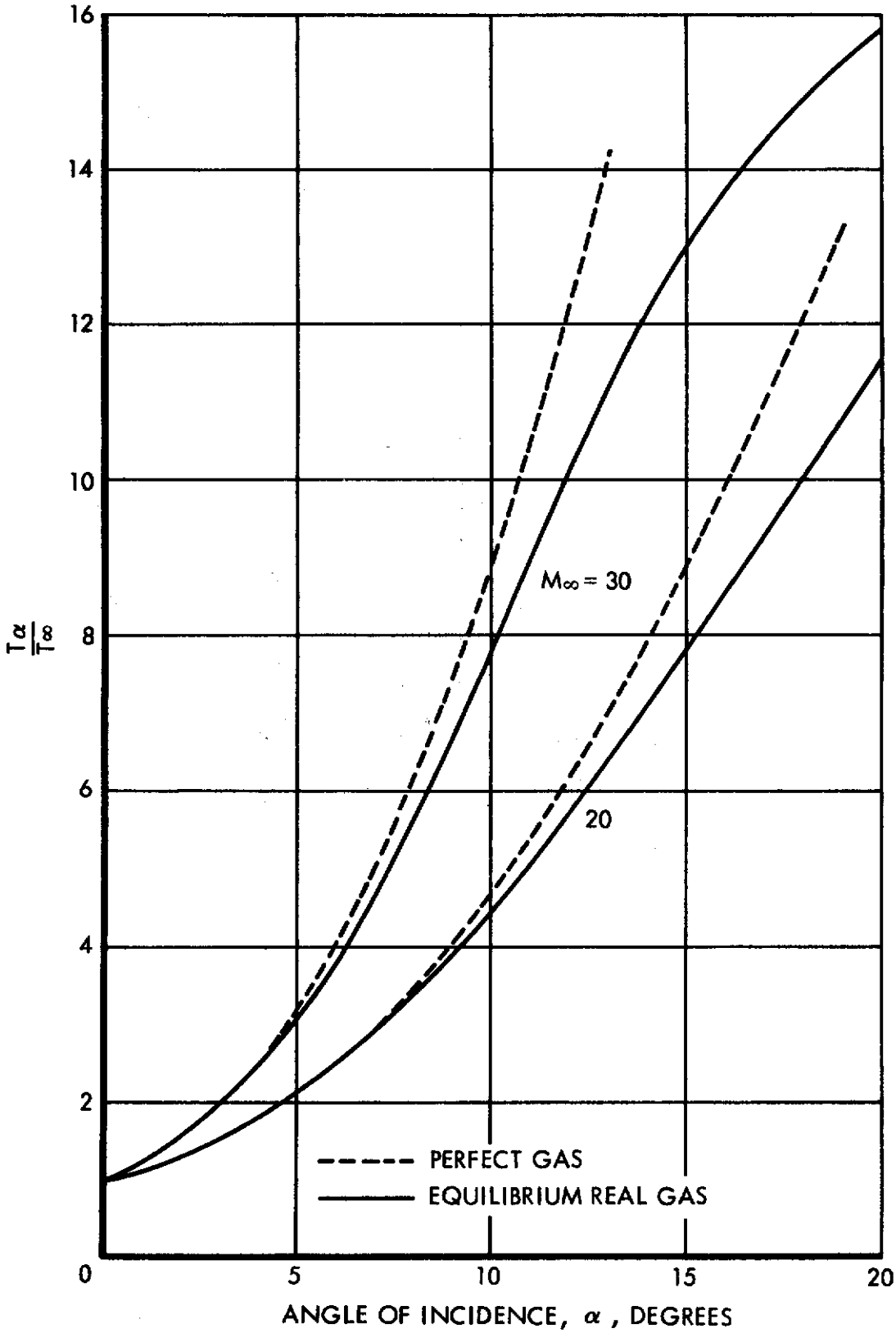

(e) ALTITUDE = 250,000 FT.

Figure 97. Oblique Shock Temperature Ratio Including Real Gas Effects (Continued)

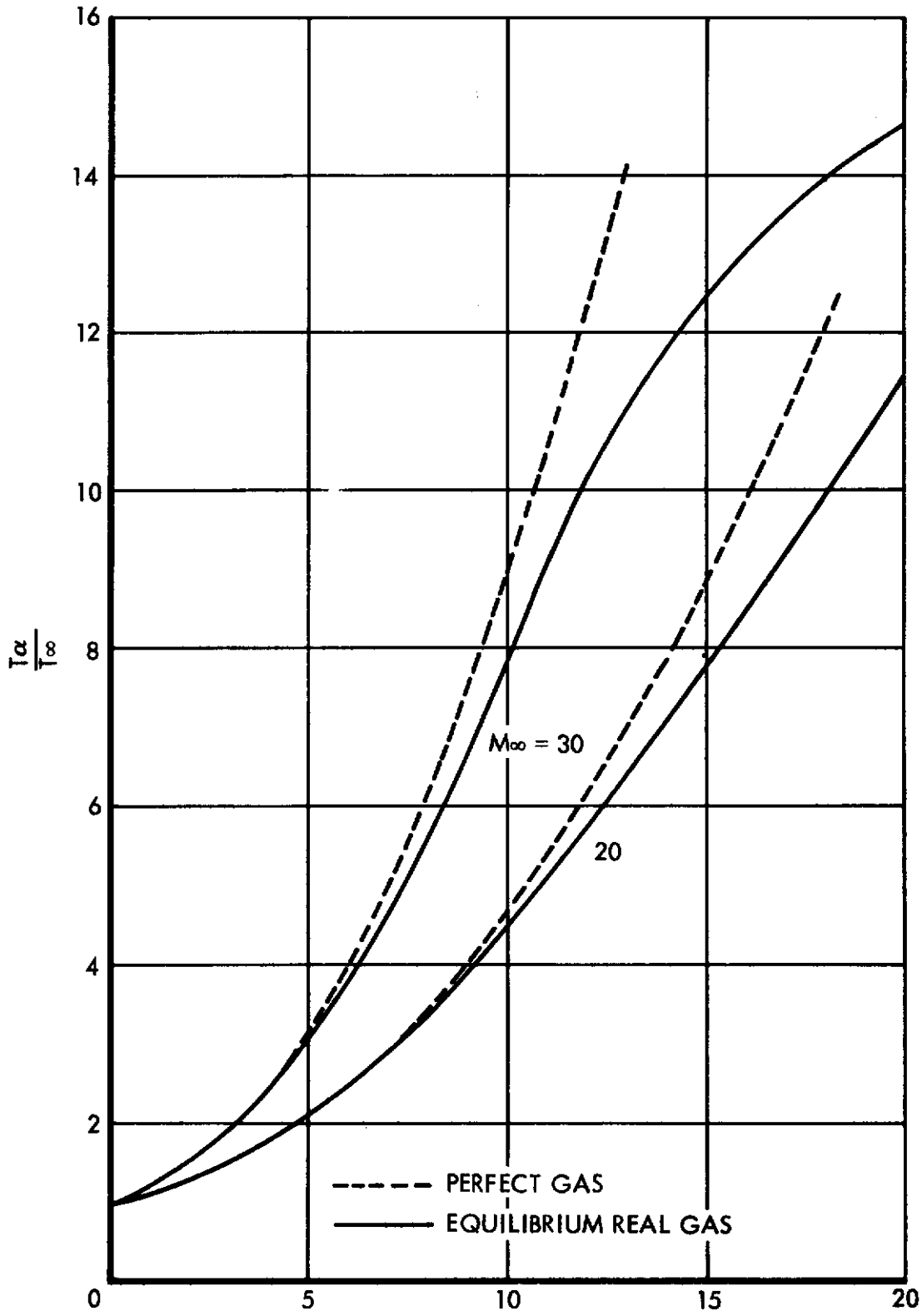

(f) ALTITUDE = 300,000 FT.

Figure 97. Oblique Shock Temperature Ratio Including Real Gas Effects (Concluded)

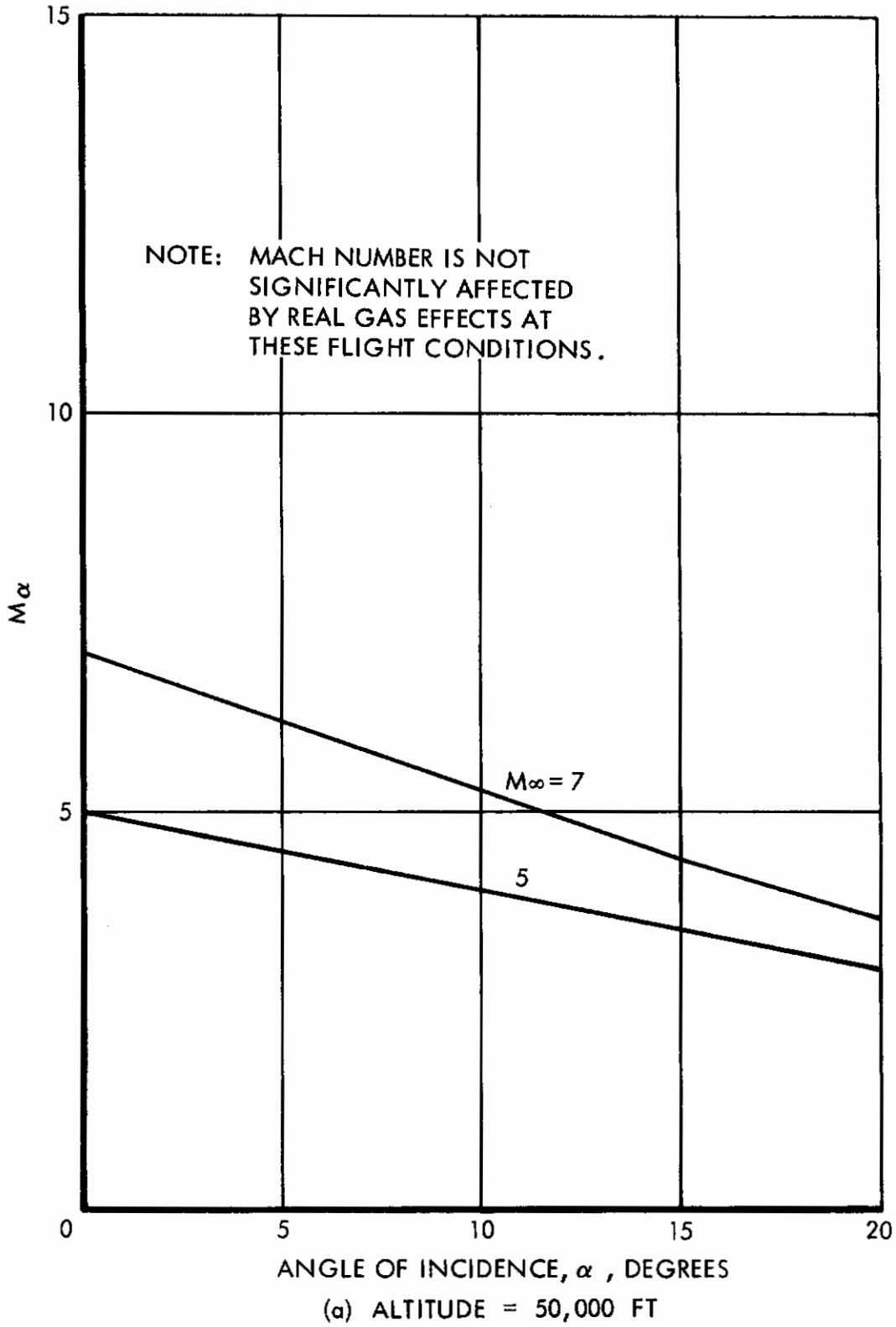

Figure 98. Mach Number Behind an Oblique Shock Including Real Gas Effects

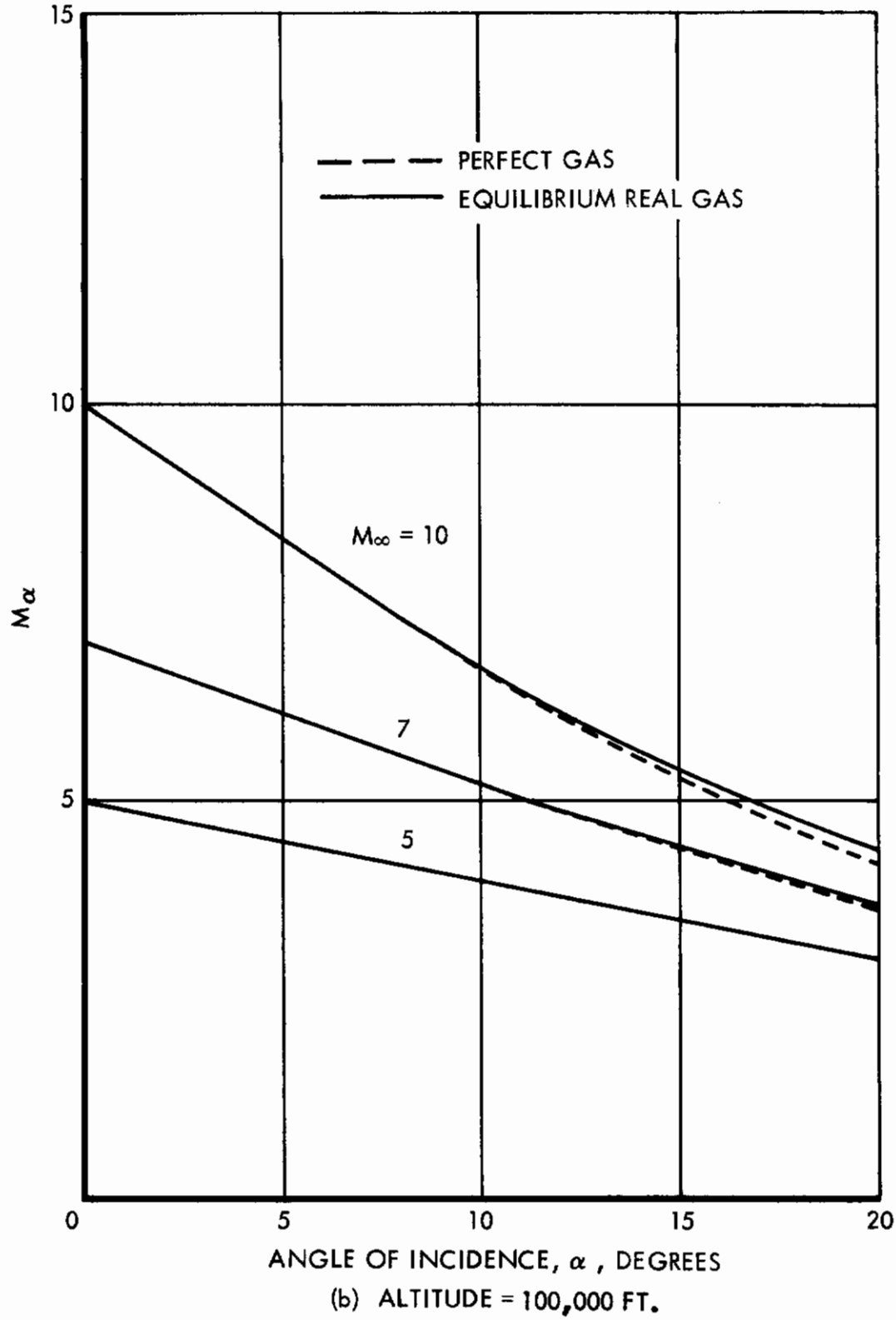

(b) ALTITUDE = 100,000 FT.

Figure 98. Mach Number Behind an Oblique Shock Including Real Gas Effects (Continued)

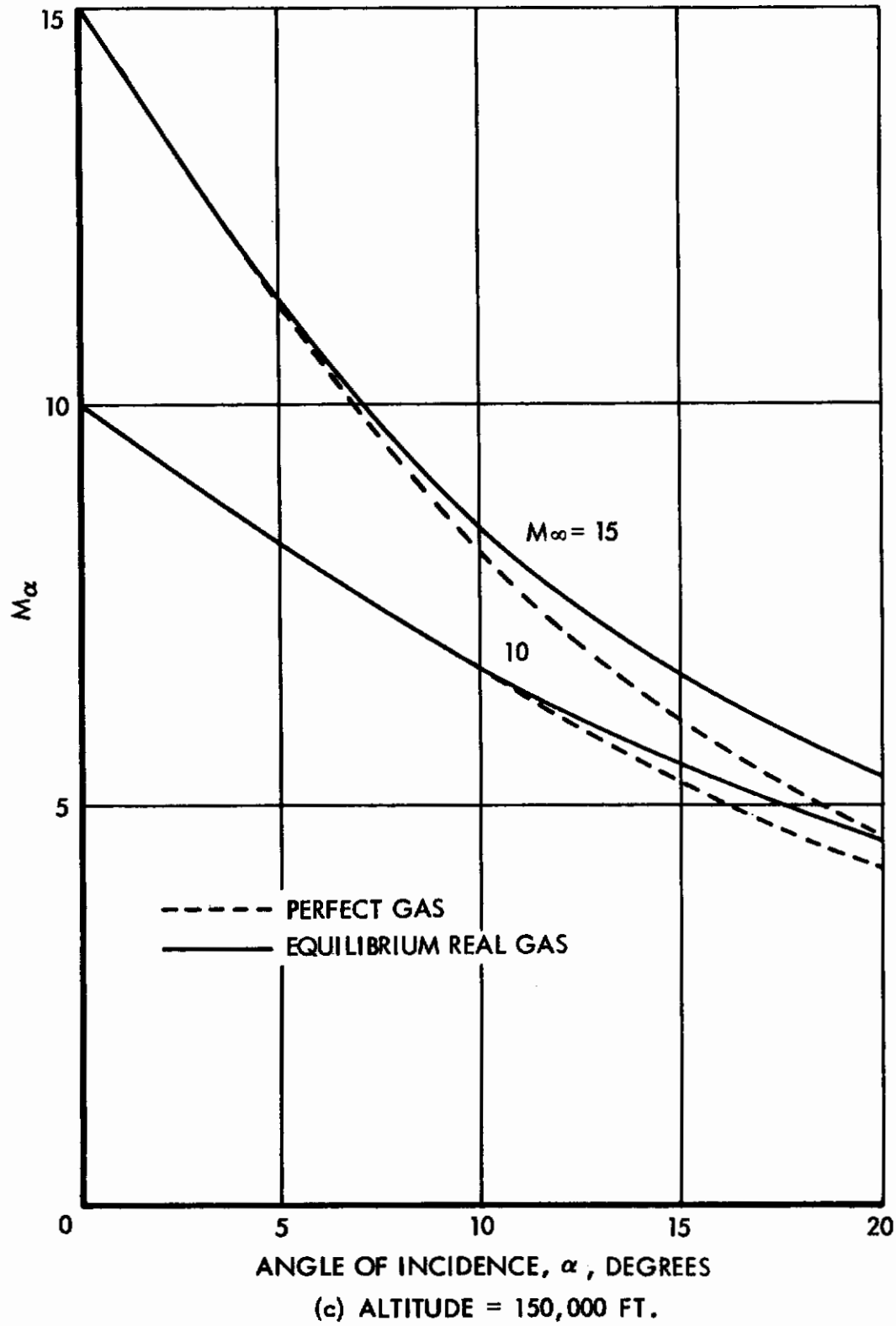

(c) ALTITUDE = 150,000 FT.

Figure 98. Mach Number Behind an Oblique Shock Including Real Gas Effects (Continued)

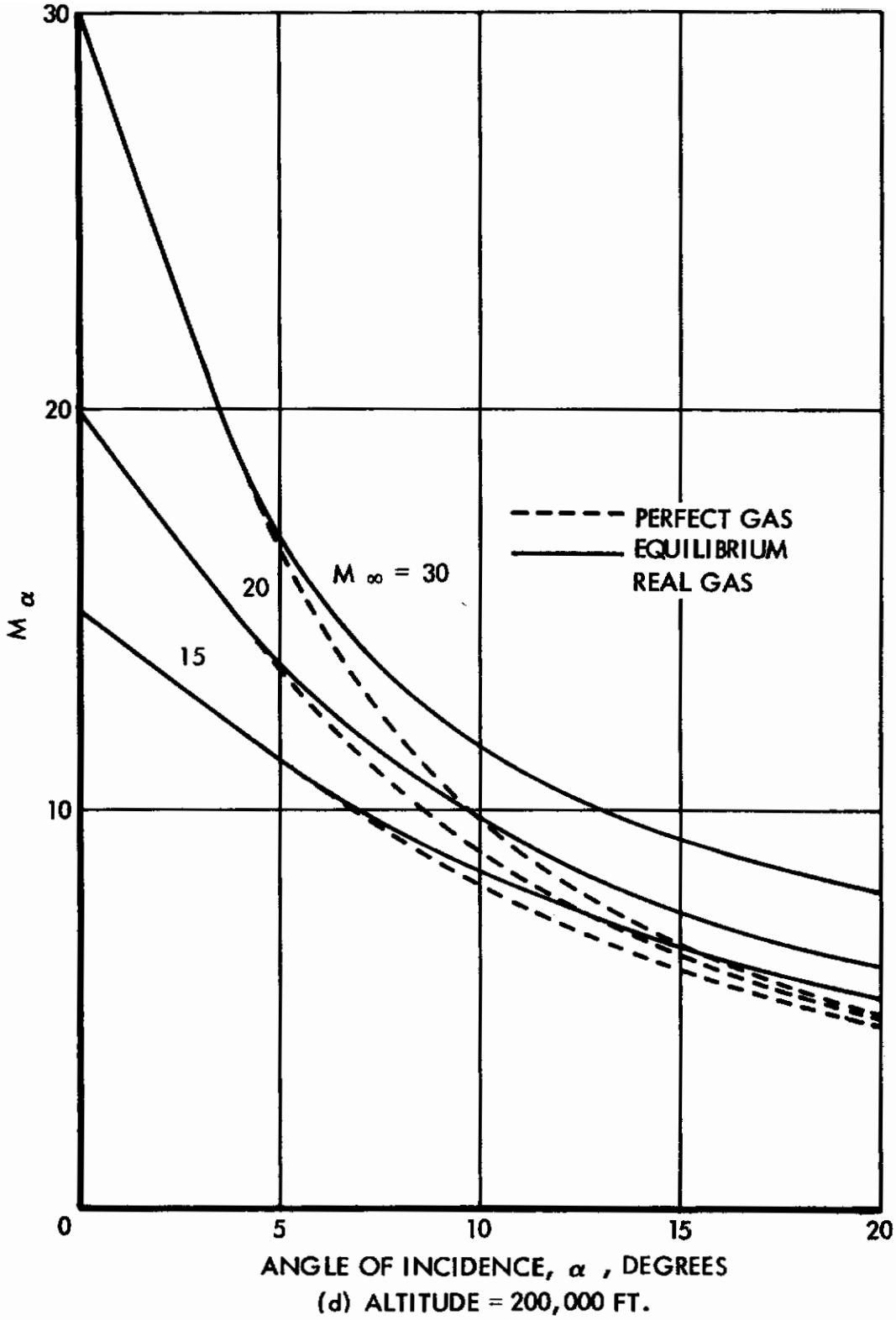

Figure 98. Mach Number Behind an Oblique Shock Including Real Gas Effects (Continued)

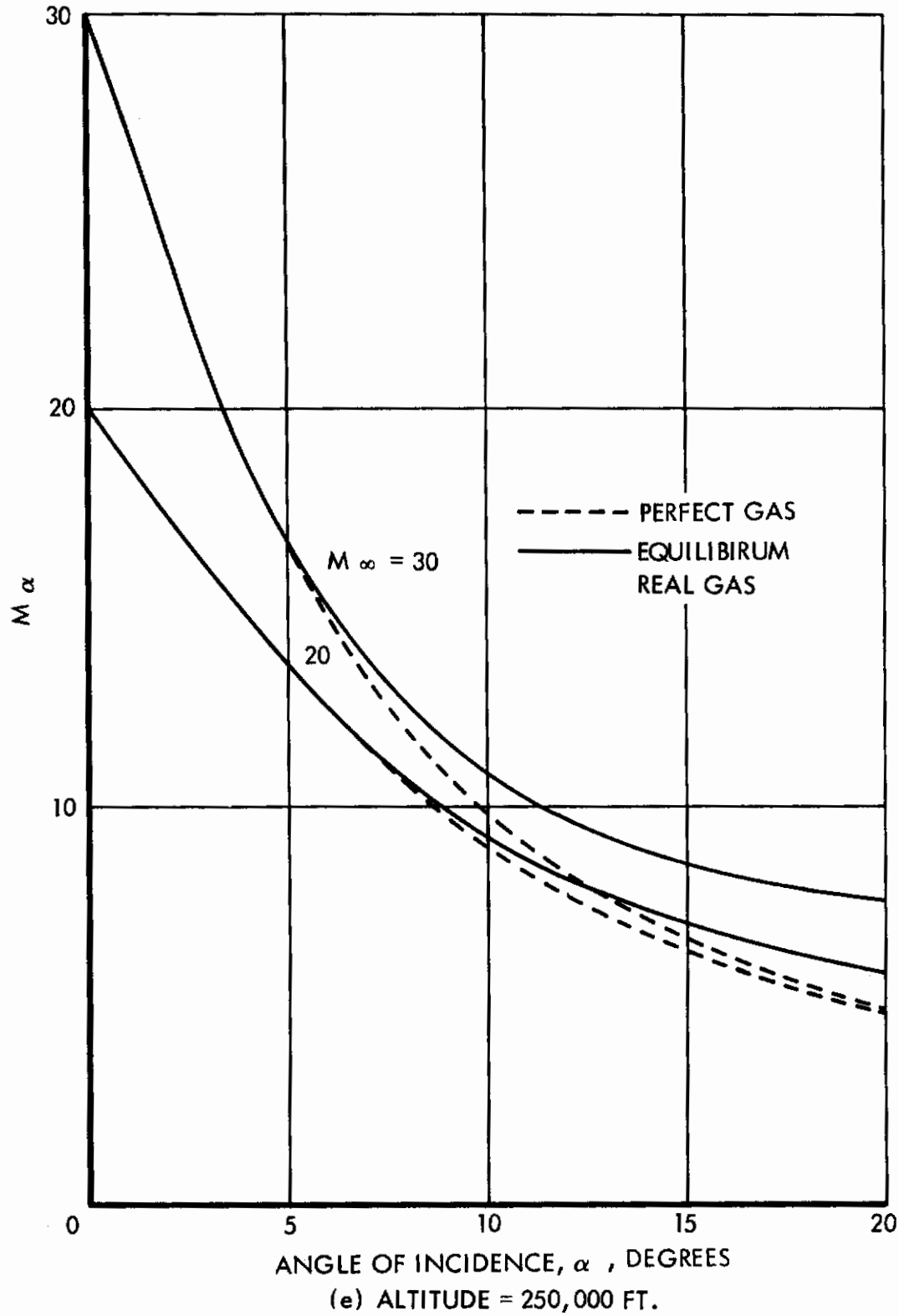

Figure 98. Mach Number Behind an Oblique Shock Including Real Gas Effects (Continued)

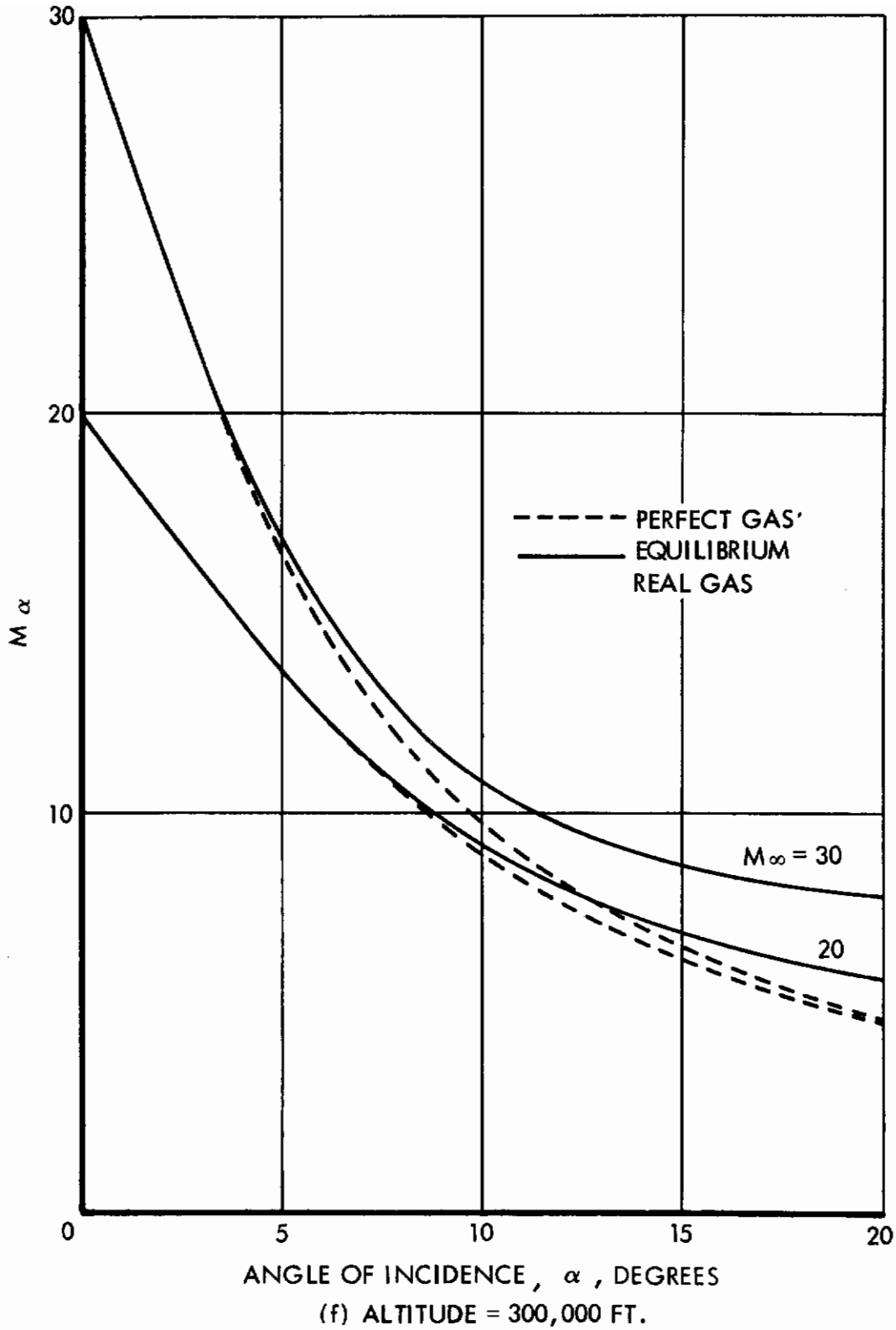

(f) ALTITUDE = 300,000 FT.

Figure 98. Mach Number Behind an Oblique Shock Including Real Gas Effects (Concluded)

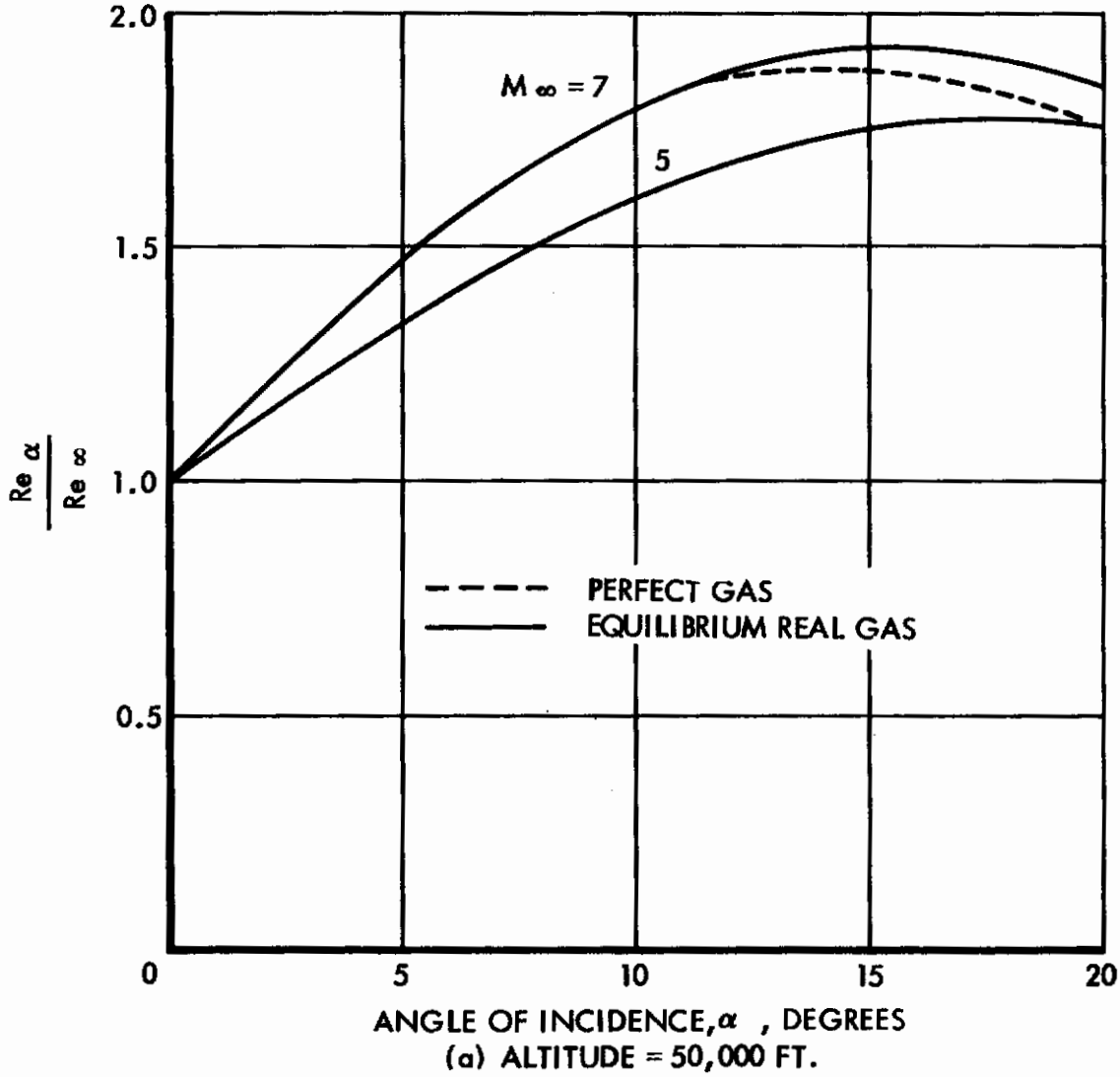

Figure 99. Oblique Shock Reynolds Number Ratio Including Real Gas Effects

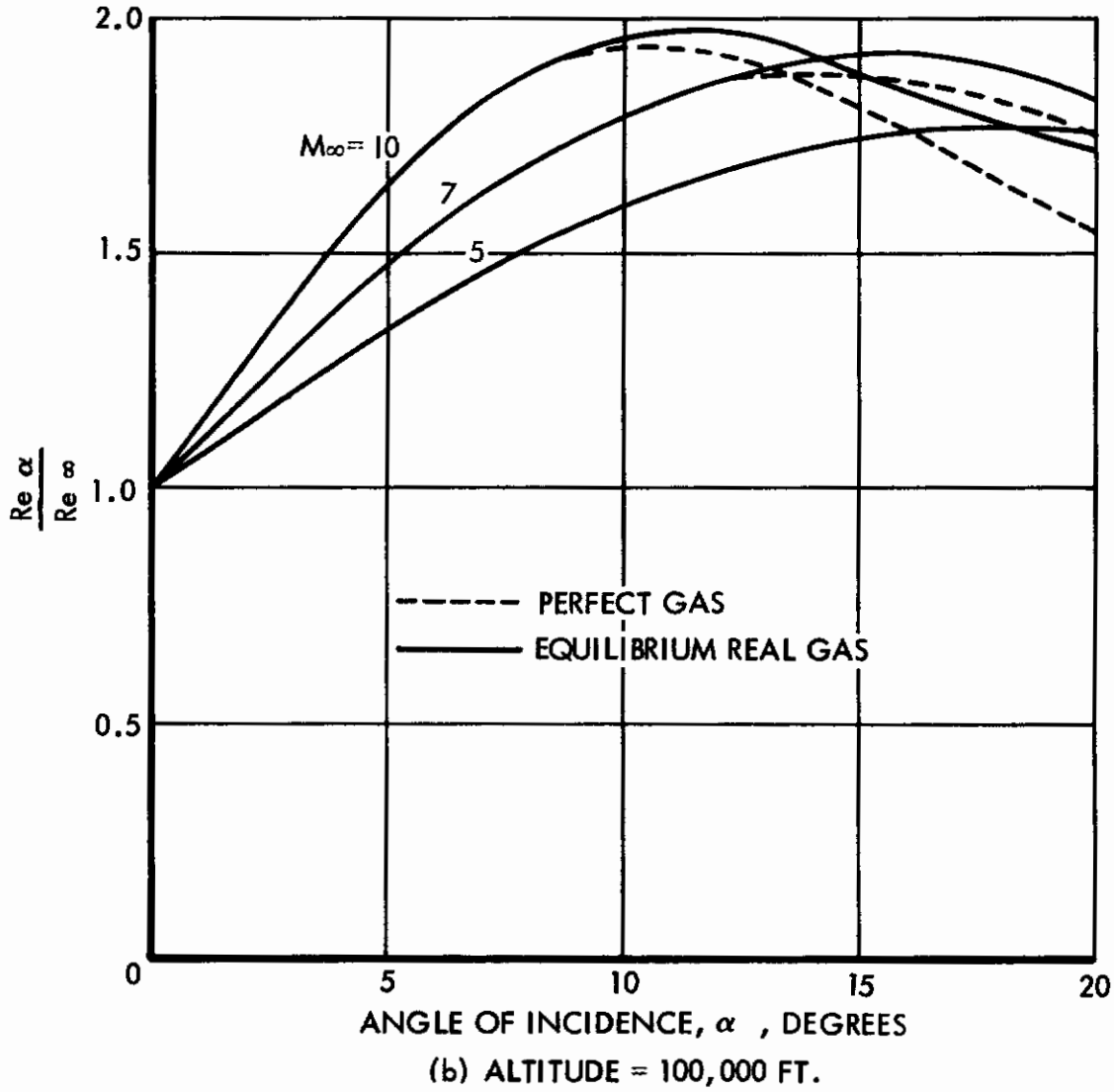

Figure 99. Oblique Shock Reynolds Number Ratio Including Real Gas Effects (Continued)

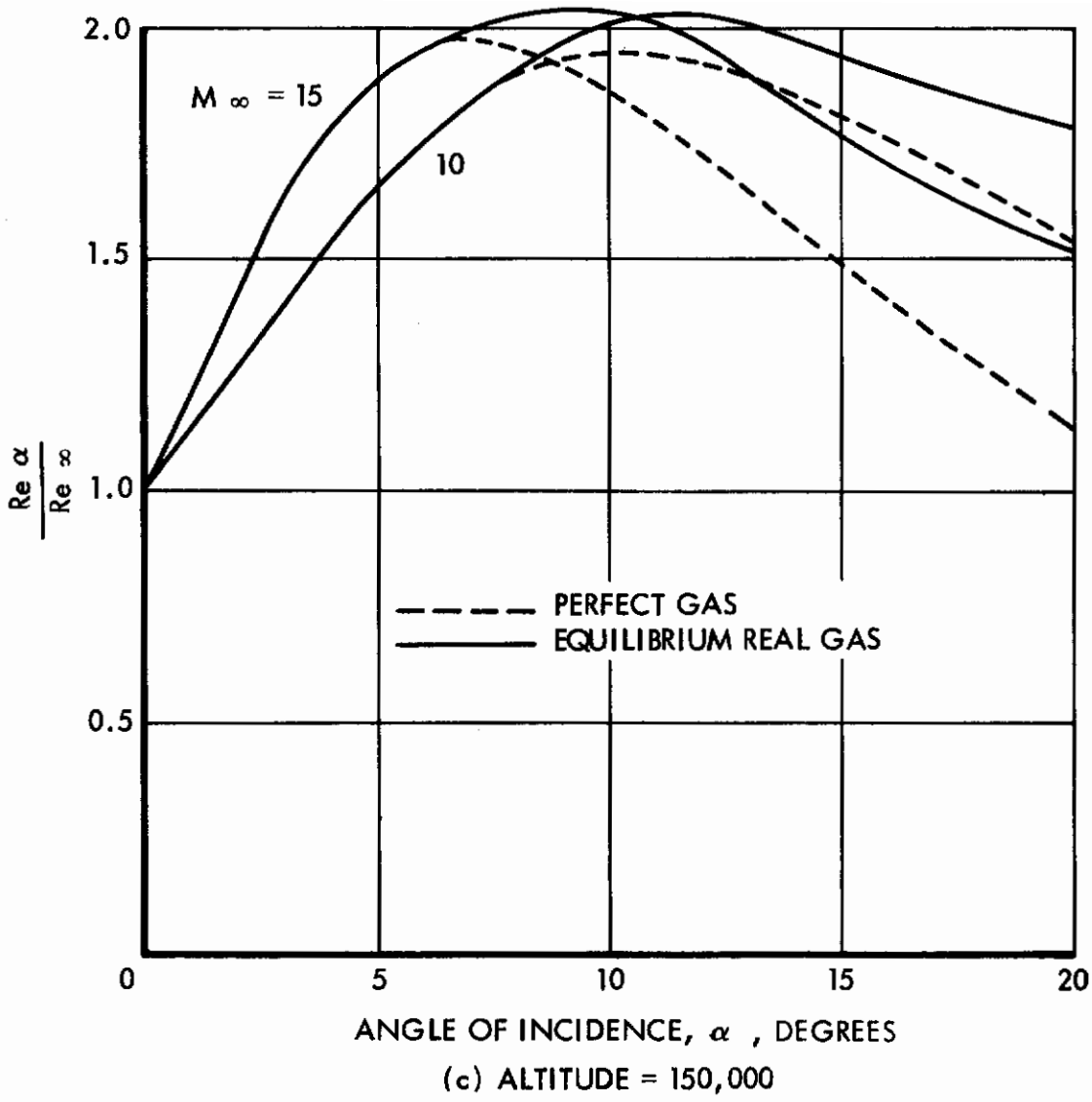

Figure 99. Oblique Shock Reynolds Number Ratio Including Real Gas Effects (Continued)

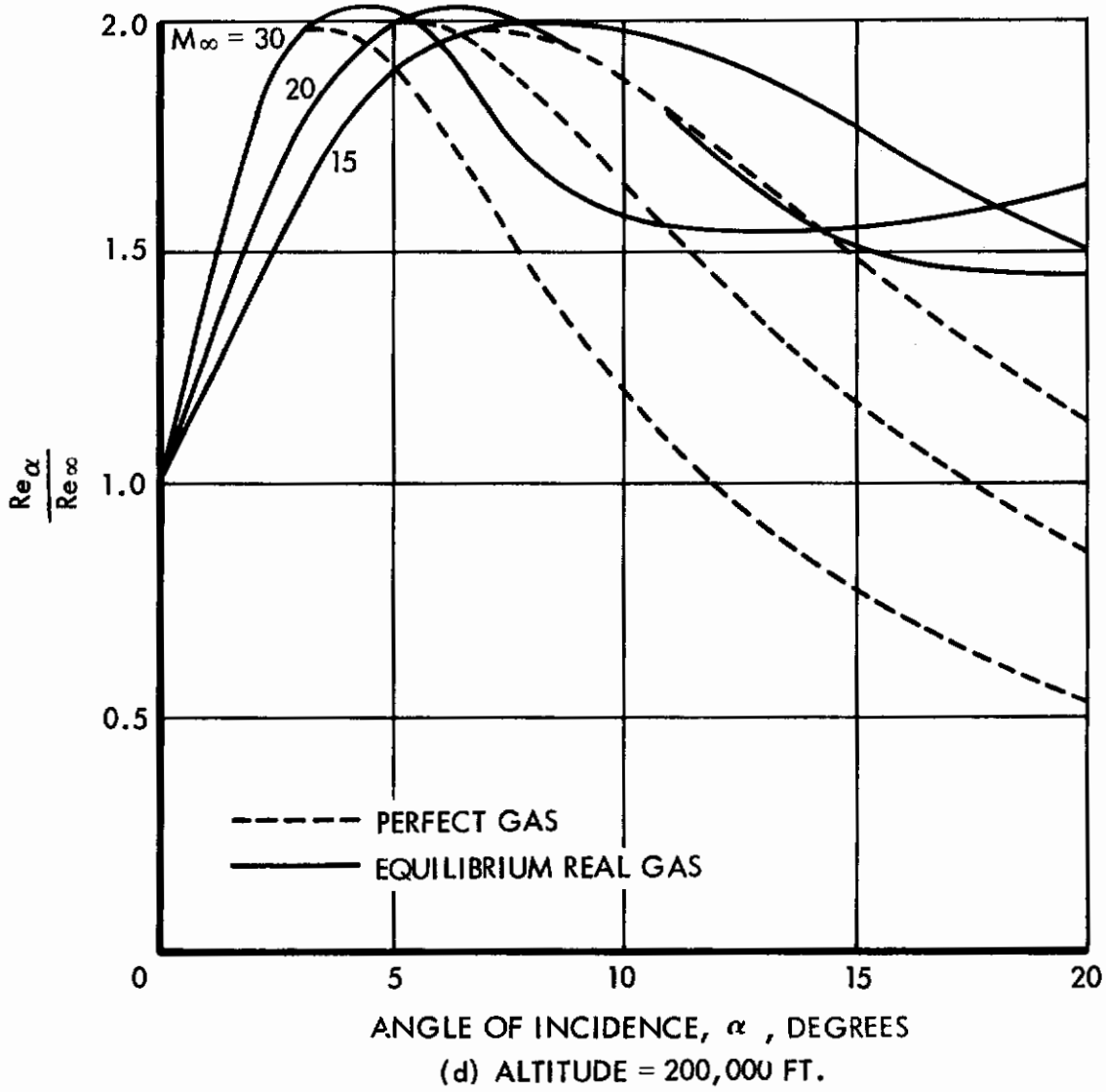

Figure 99. Oblique Shock Reynolds Number Ratio Including Real Gas Effects (Continued)

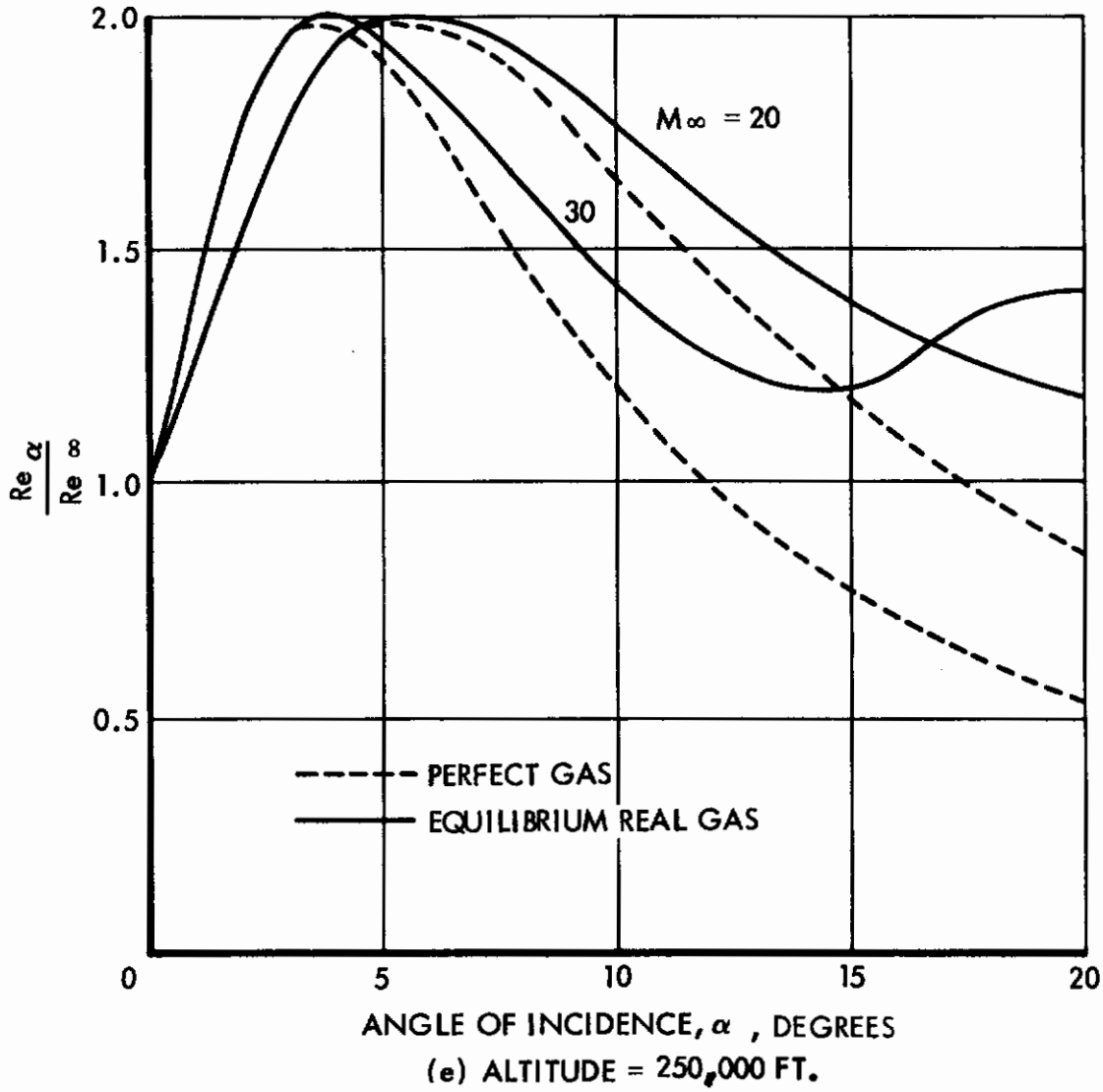

Figure 99. Oblique Shock Reynolds Number Ratio Including Real Gas Effects (Continued)

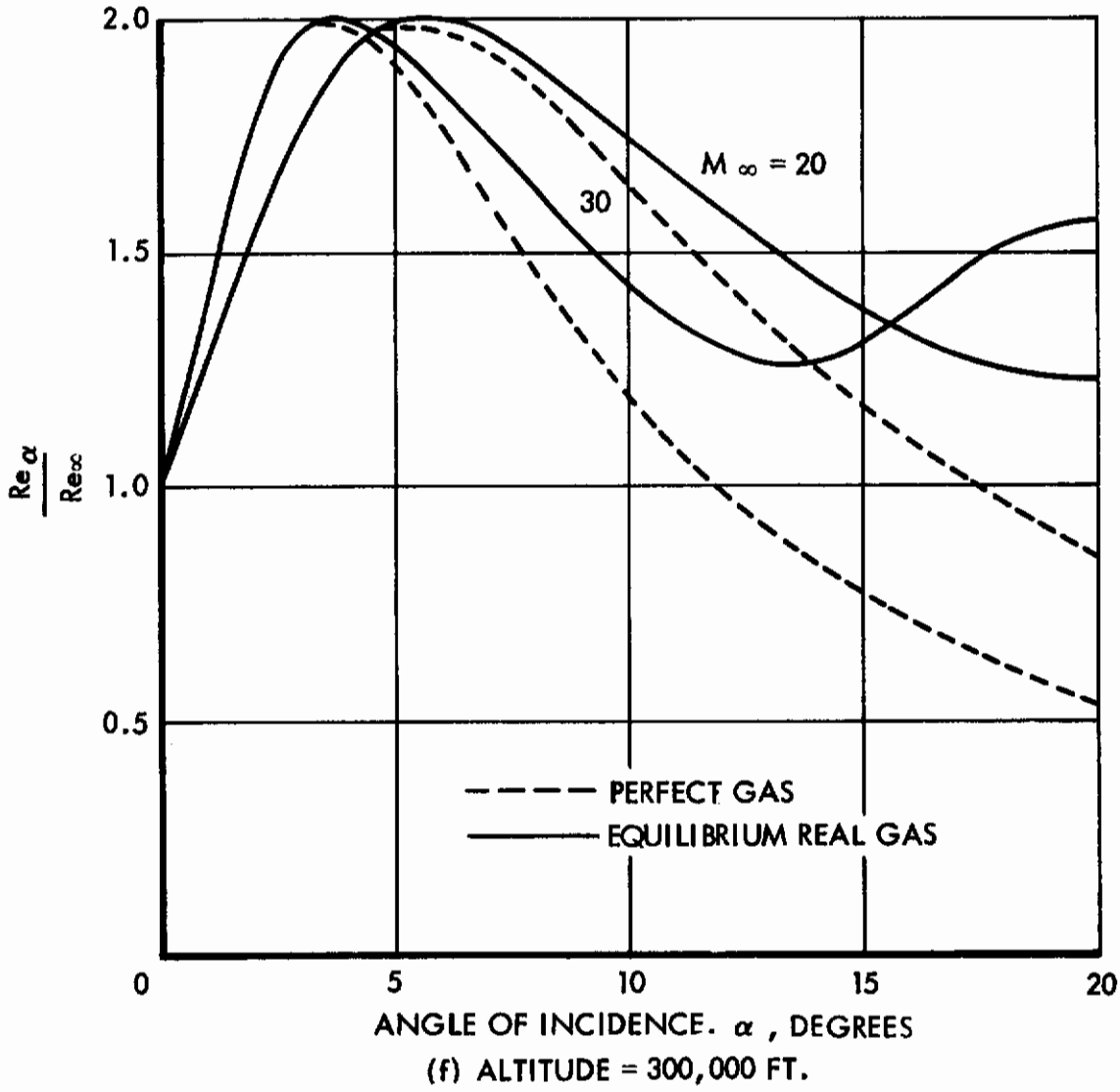

Figure 99. Oblique Shock Reynolds Number Ratio Including Real Gas Effects (Concluded)

BOUNDARY LAYER THICKNESS

Since boundary layer thickness is the parameter used for non-dimensionalizing the interaction distances of a separated flow field, charts have been constructed to simplify the procedure for calculating boundary layer thickness.

Section III shows that hypersonic boundary layer thickness may be determined using Reynolds number obtained by the reference temperature method (Ref. 71). Using the 0.67 power viscosity-temperature relation, the ratio of reference temperature Reynolds number to local Reynolds number reduces to the following form:

$$\frac{Re^*_\alpha}{Re_\alpha} = \left(\frac{T_\alpha}{T^*}\right)^{1.67}$$

Substitution of the equations which define reference temperature and adiabatic wall temperature into the above equation results in the expression

$$\frac{Re^*_\alpha}{Re_\alpha} = \left[0.28 + 0.5\,\frac{T_W}{T_\alpha} + 0.22\left\{1 + \left(\frac{\gamma - 1}{2}\right) M_\alpha^{\,2} Pr^n\right\}\right]^{-1.67}$$

Reference temperature Reynolds number calculations were based upon a Prandtl number of 0.72 with n equal to 1/2 for laminar flow and to 1/3 for turbulent flow. Wall temperatures were restricted to the expected range of practical interest ($1 \leq T_w/T_\alpha \leq 10 \leq T_{aw}/T_\alpha$). Figures 100 and 101 present the reference temperature Reynolds number ratio for laminar and turbulent flow as a function of local Mach number for various ratios of wall to local stream temperature.

Plots of the laminar and turbulent boundary layer thickness equations, based on reference temperature Reynolds number, are presented in Figures 102 and 103. The equations shown omit the pressure correction factor which should be included in the case of significant viscous interaction or bluntness induced pressure gradient (See Section III).

PRESSURE DISTRIBUTION

The development of semi-empirical correlations for describing the pressure distribution in the laminar and turbulent separated region was discussed in Section IV. The pertinent expressions have been presented in the form of working charts to facilitate calculation of the surface pressure distribution in the region of separated compression corner flow. The charts are shown in Figures 104 through 114. The procedure for using the charts is discussed below, and their use is illustrated in the sample calculations presented in Appendix II.

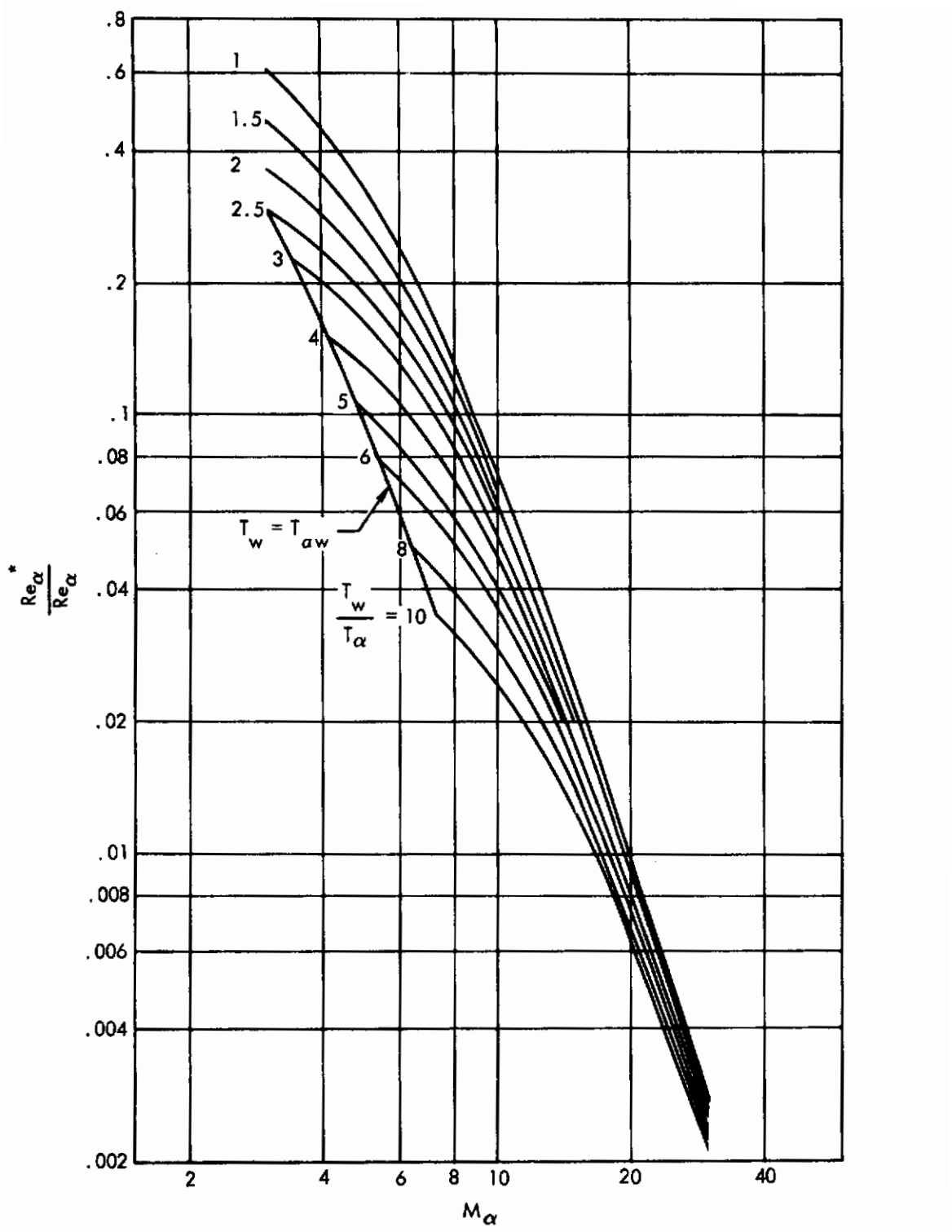

Figure 100. The Effects of Mach Number and Wall Temperature on Local Reference Temperature Reynolds-Number Ratio (Laminar)

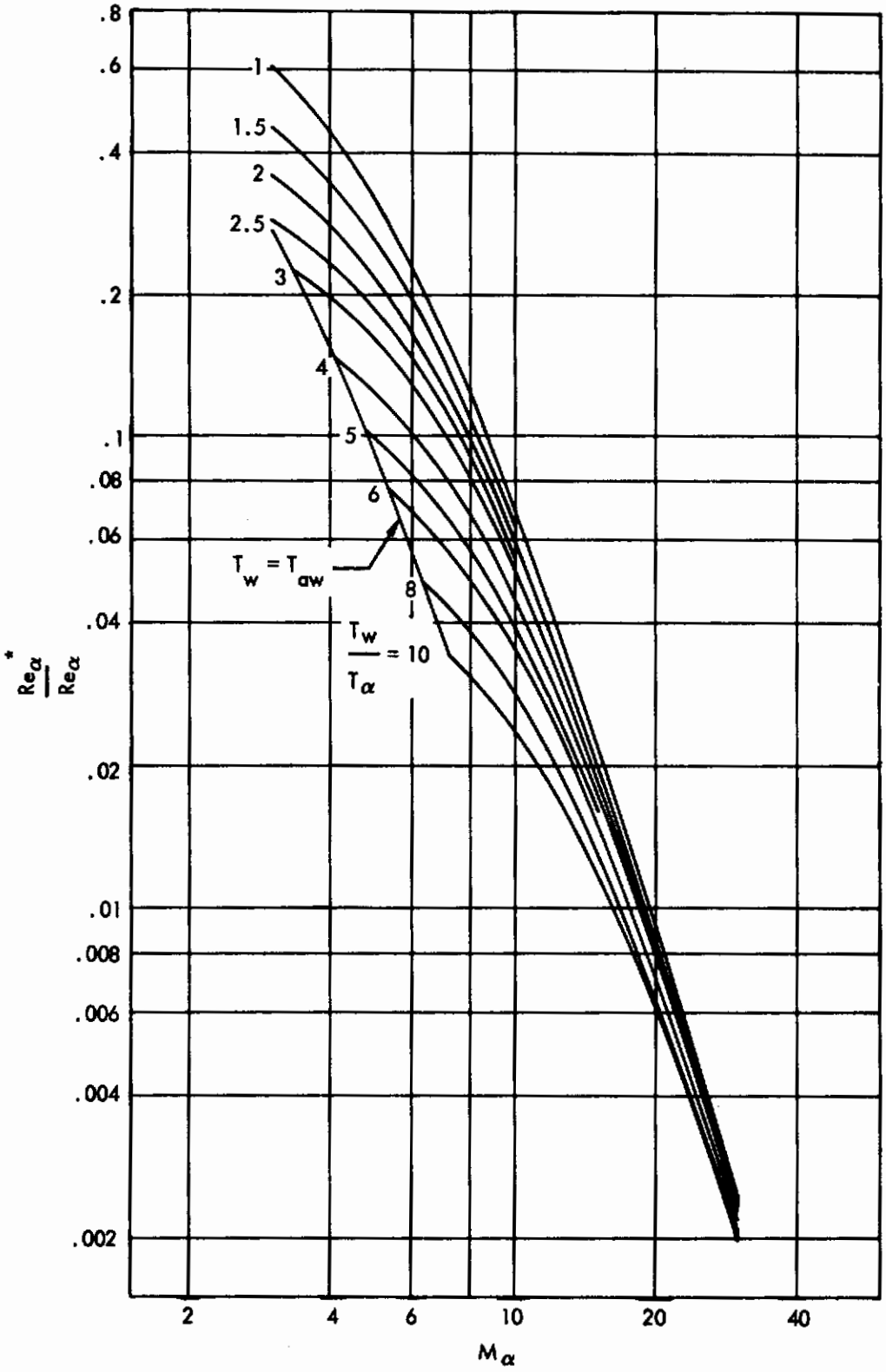

Figure 101. The Effects of Mach Number and Wall Temperature on Local Reference Temperature Reynolds Number Ratio (Turbulent)

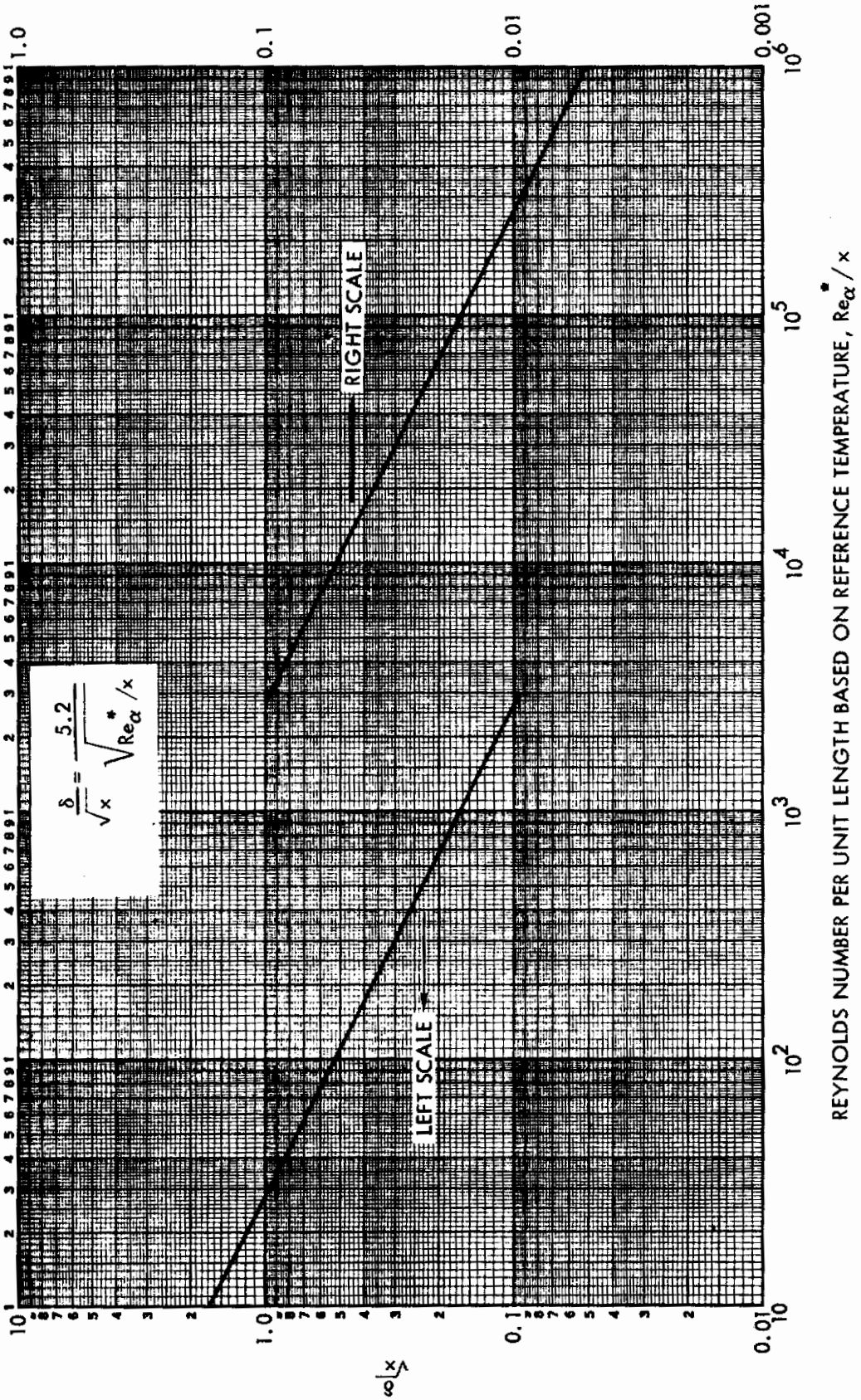

Figure 102. Laminar Boundary Layer Thickness

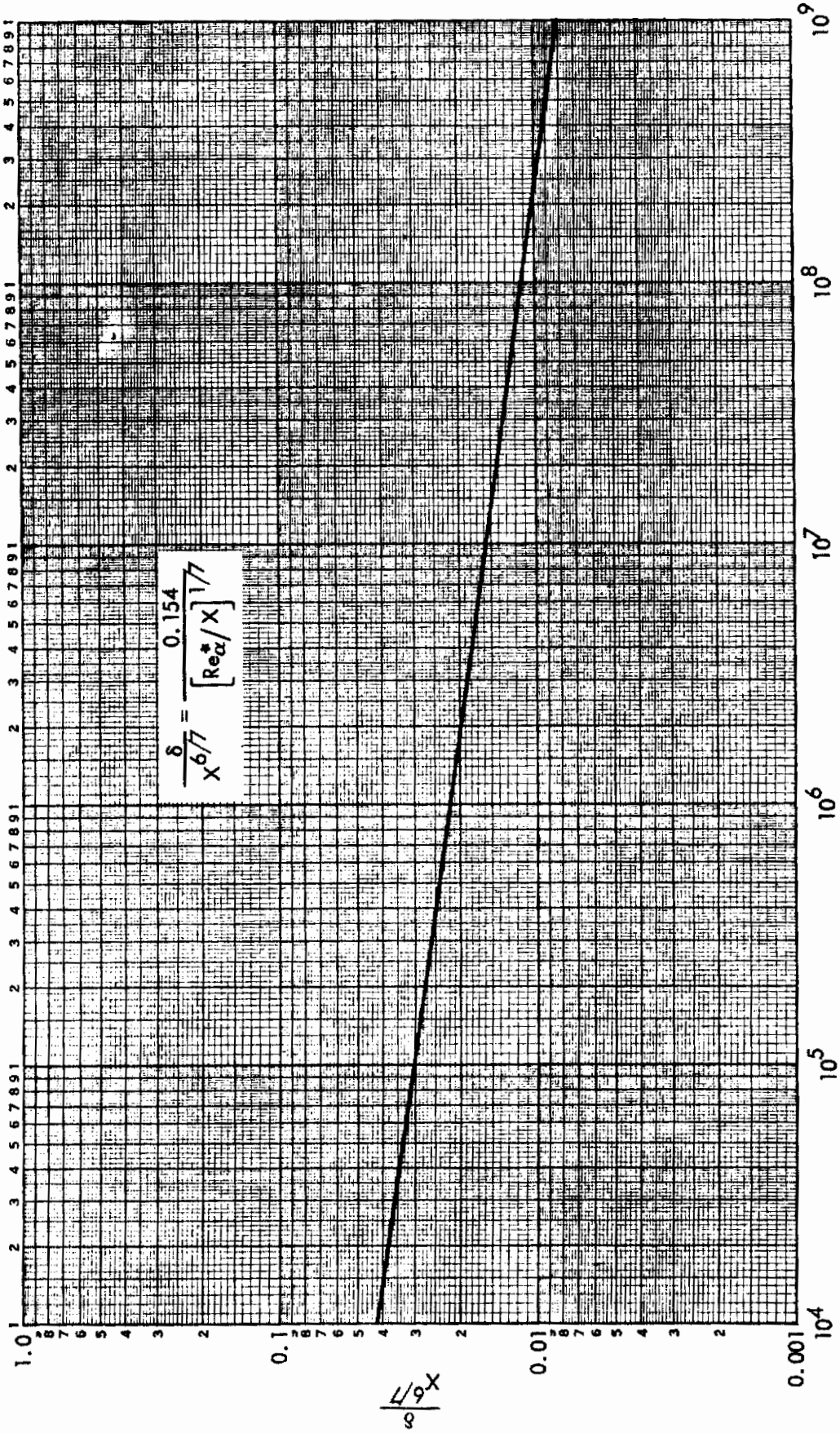

Figure 103. Turbulent Boundary Layer Thickness

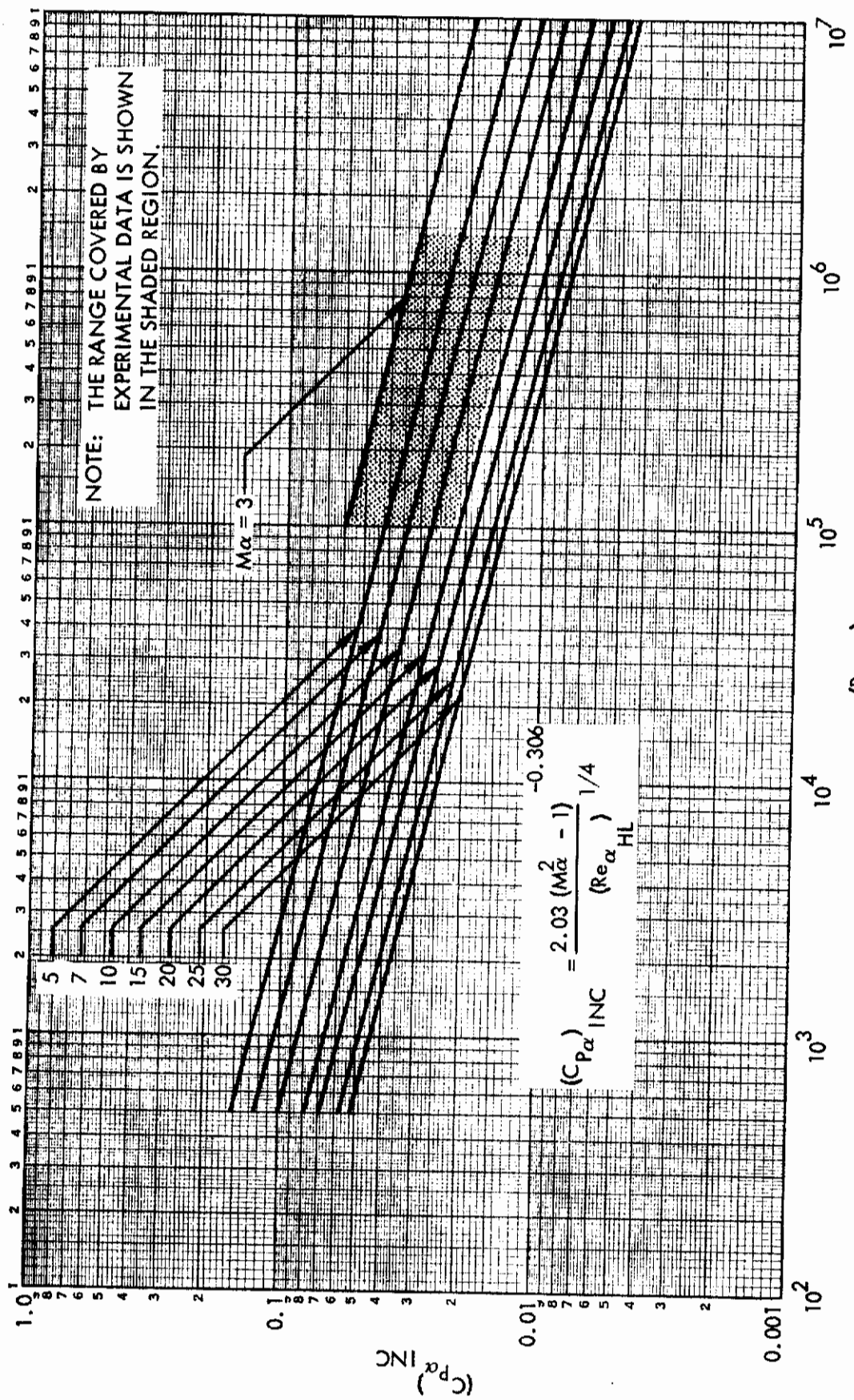

Figure 104. Pressure Coefficient for Incipient Boundary Layer Separation in Laminar Flow

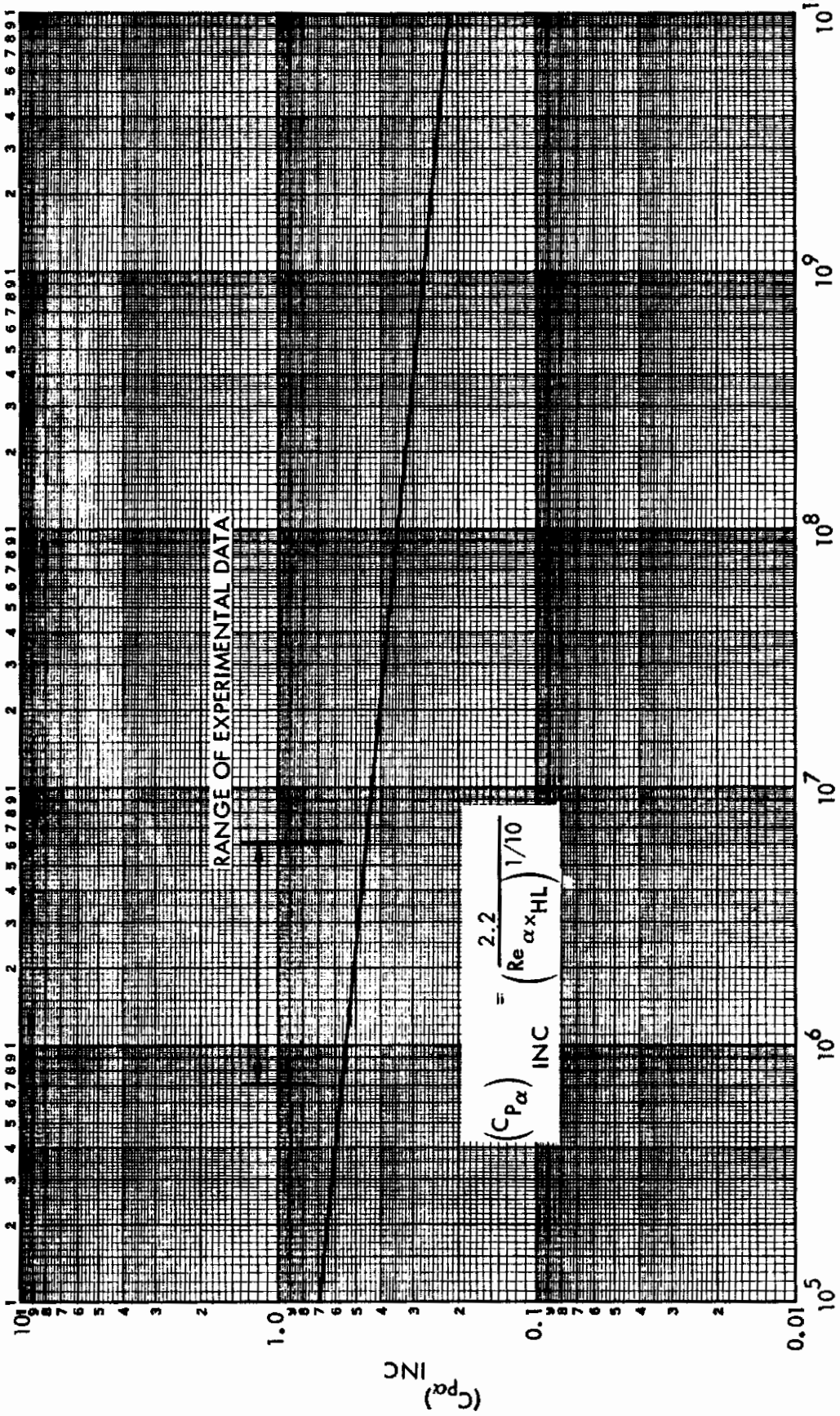

Figure 105. Pressure Coefficient for Incipient Boundary Layer Separation in Turbulent Flow

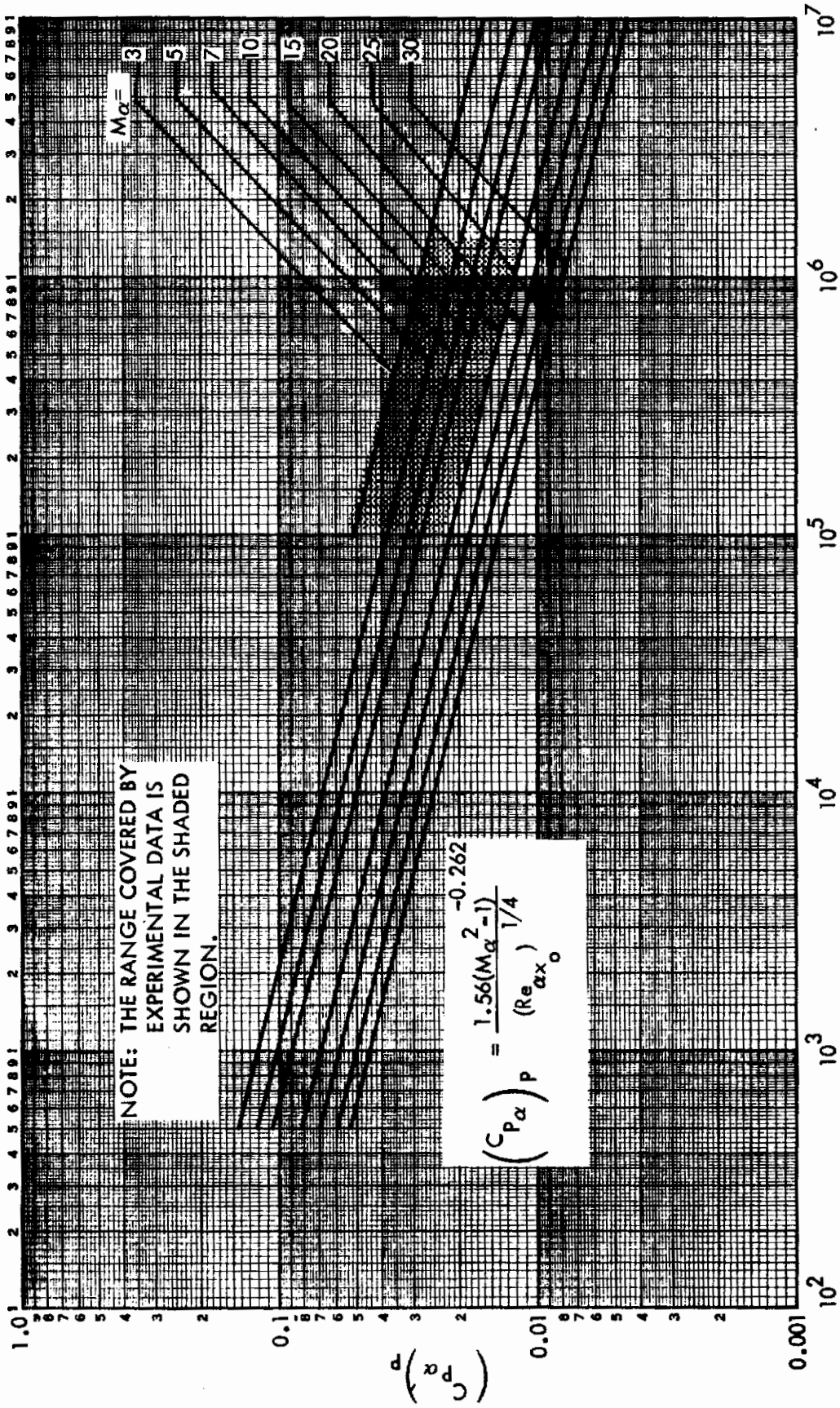

Figure 106. Laminar Plateau Pressure Coefficient

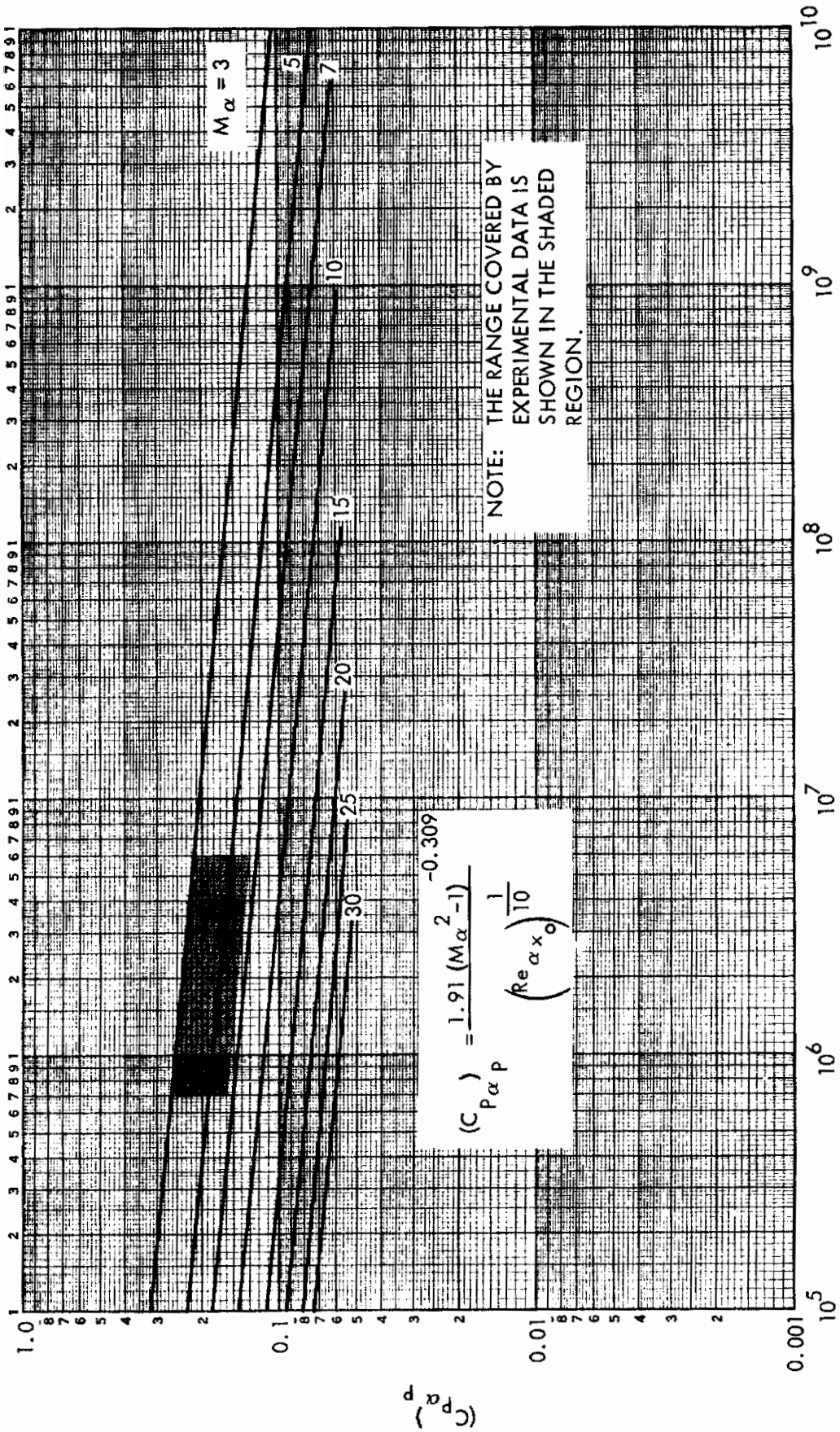

Figure 107. Turbulent Plateau Pressure Coefficient

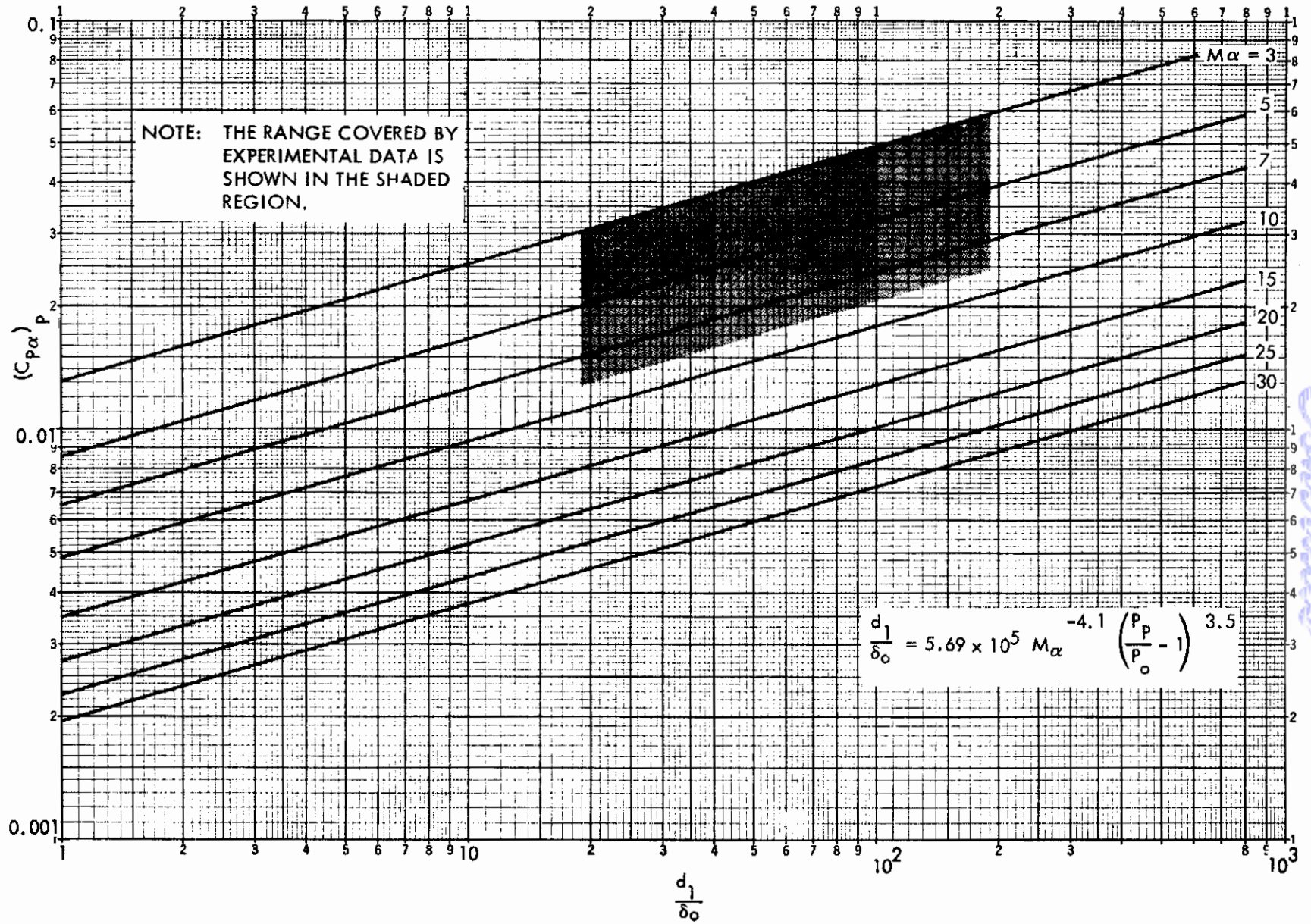

Figure 108. Upstream Interaction Distance for Laminar Flow

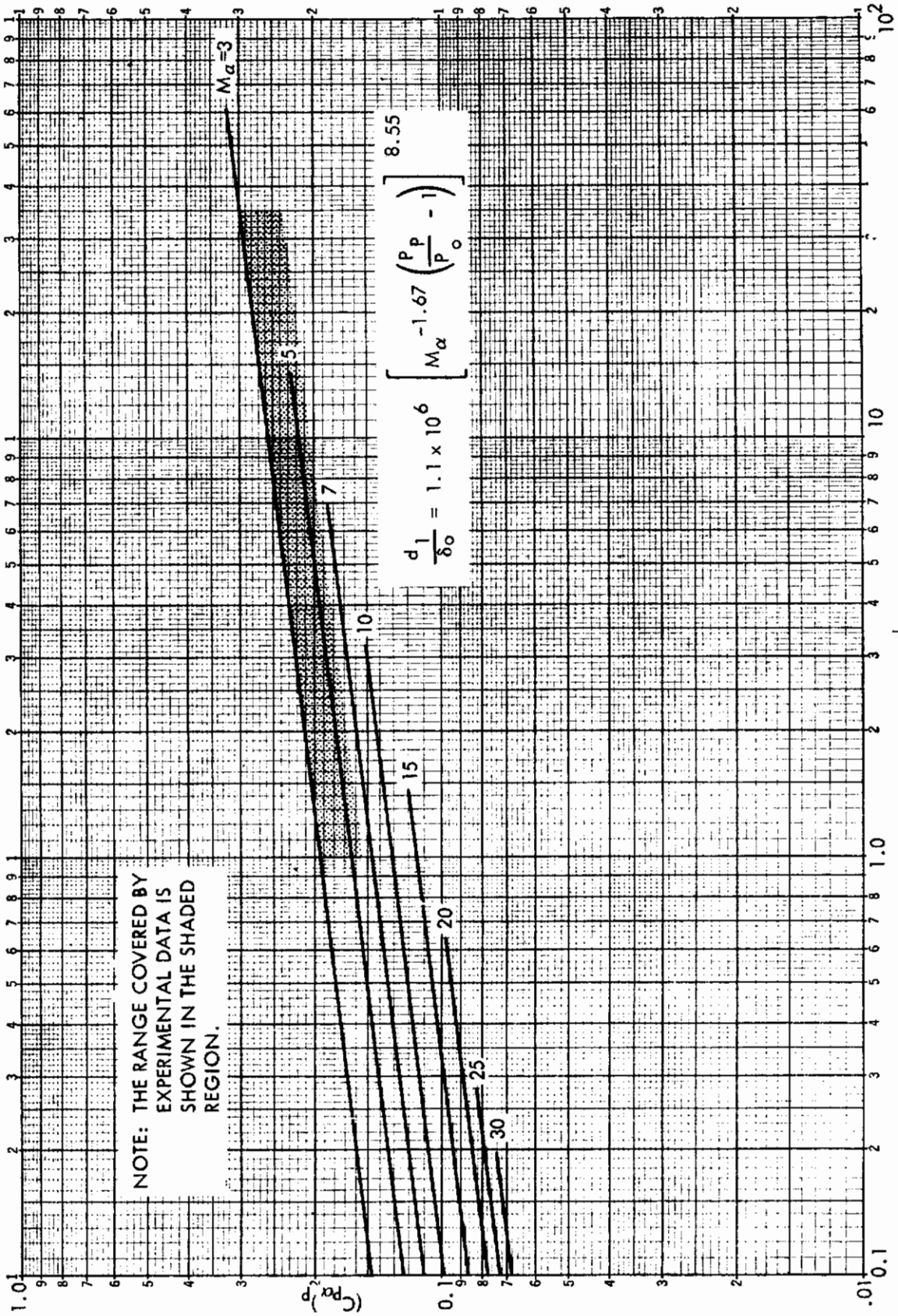

Figure 109. Upstream Interaction Distance for Turbulent Flow

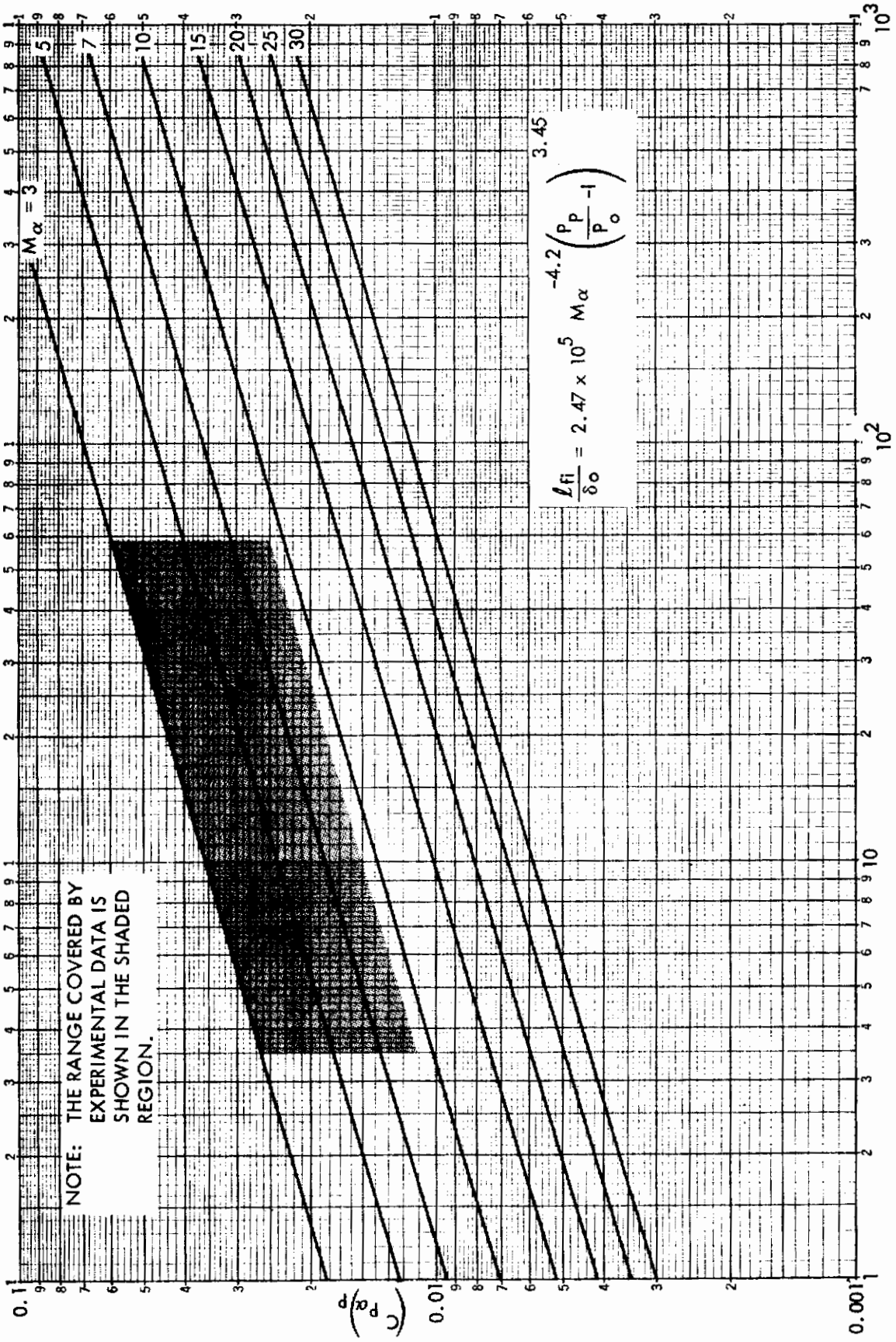

Figure 110. Free Interaction Length for Laminar Flow

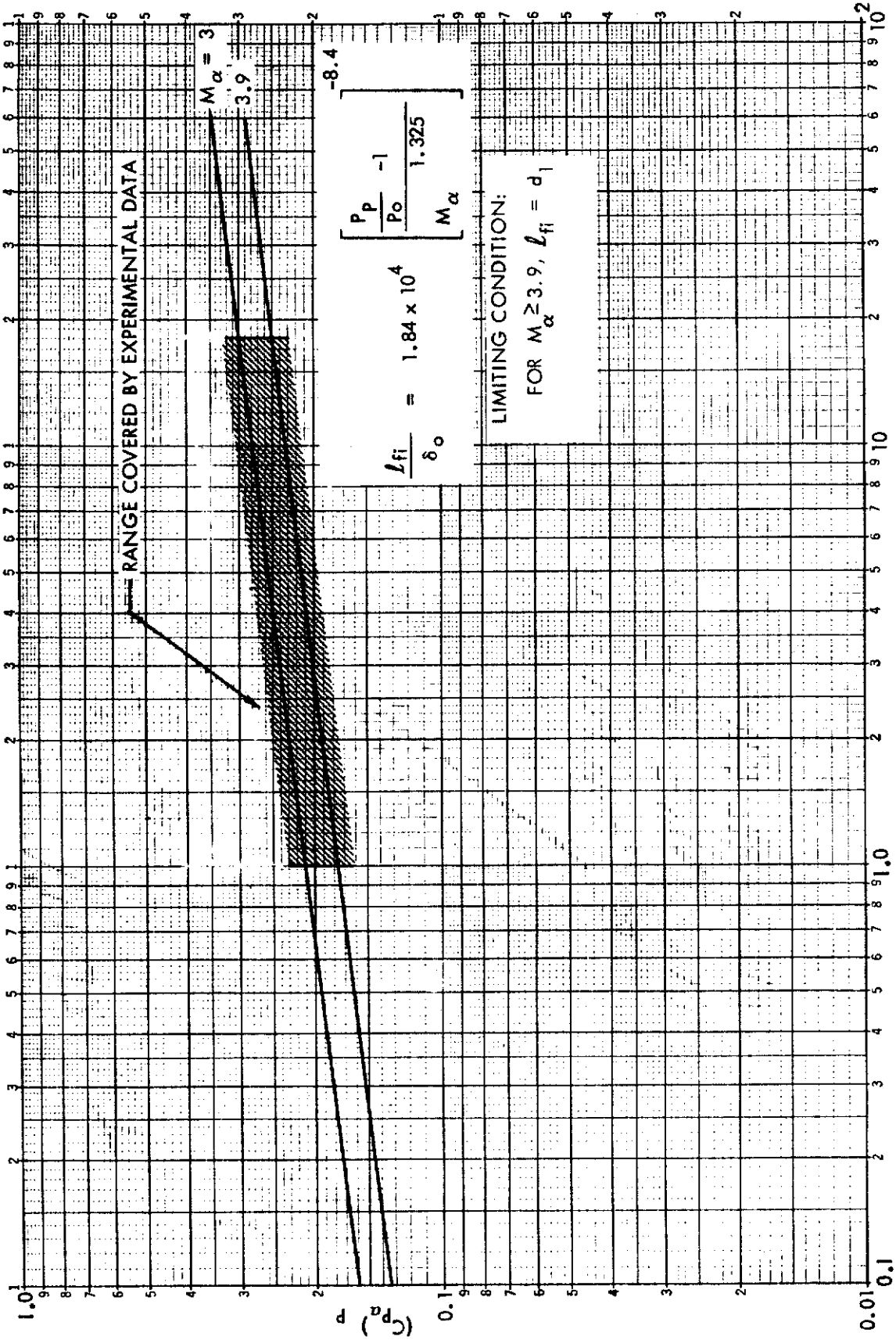

Figure 111. Free Interaction Length for Turbulent Flow

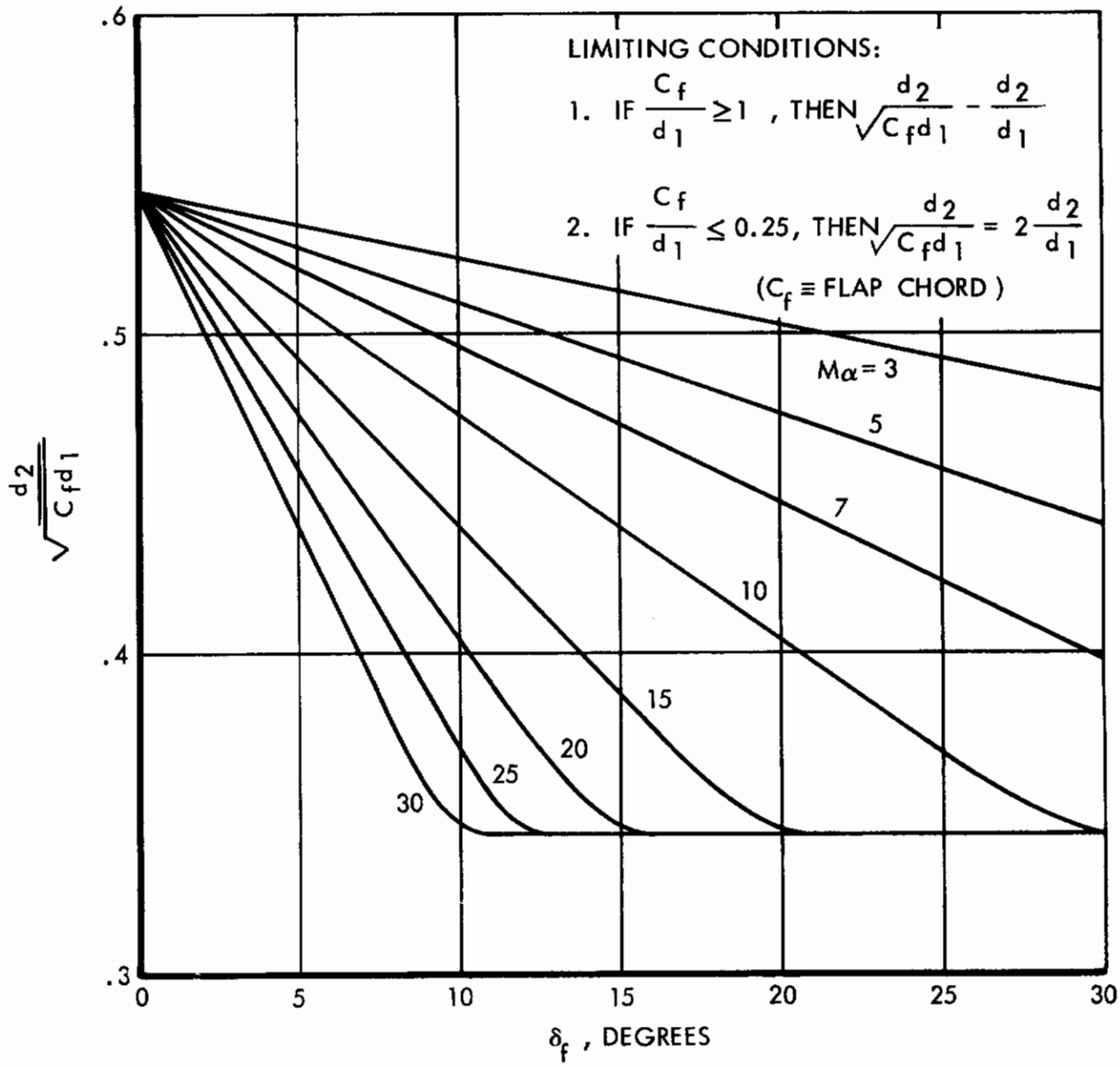

Figure 112. Downstream Interaction Distance to Peak Pressure on Flap for Laminar Flow, d_2

LIMITING CONDITIONS:

1. IF $\frac{C_f}{d_1} \geq 1$, THEN $\frac{d_2}{\sqrt{C_f d_1}} = \frac{d_2}{d_1}$

2. IF $\frac{C_f}{d_1} \leq 0.25$, THEN $\frac{d_2}{\sqrt{C_f d_1}} = 2\frac{d_2}{d_1}$

($C_f \equiv$ FLAP CHORD)

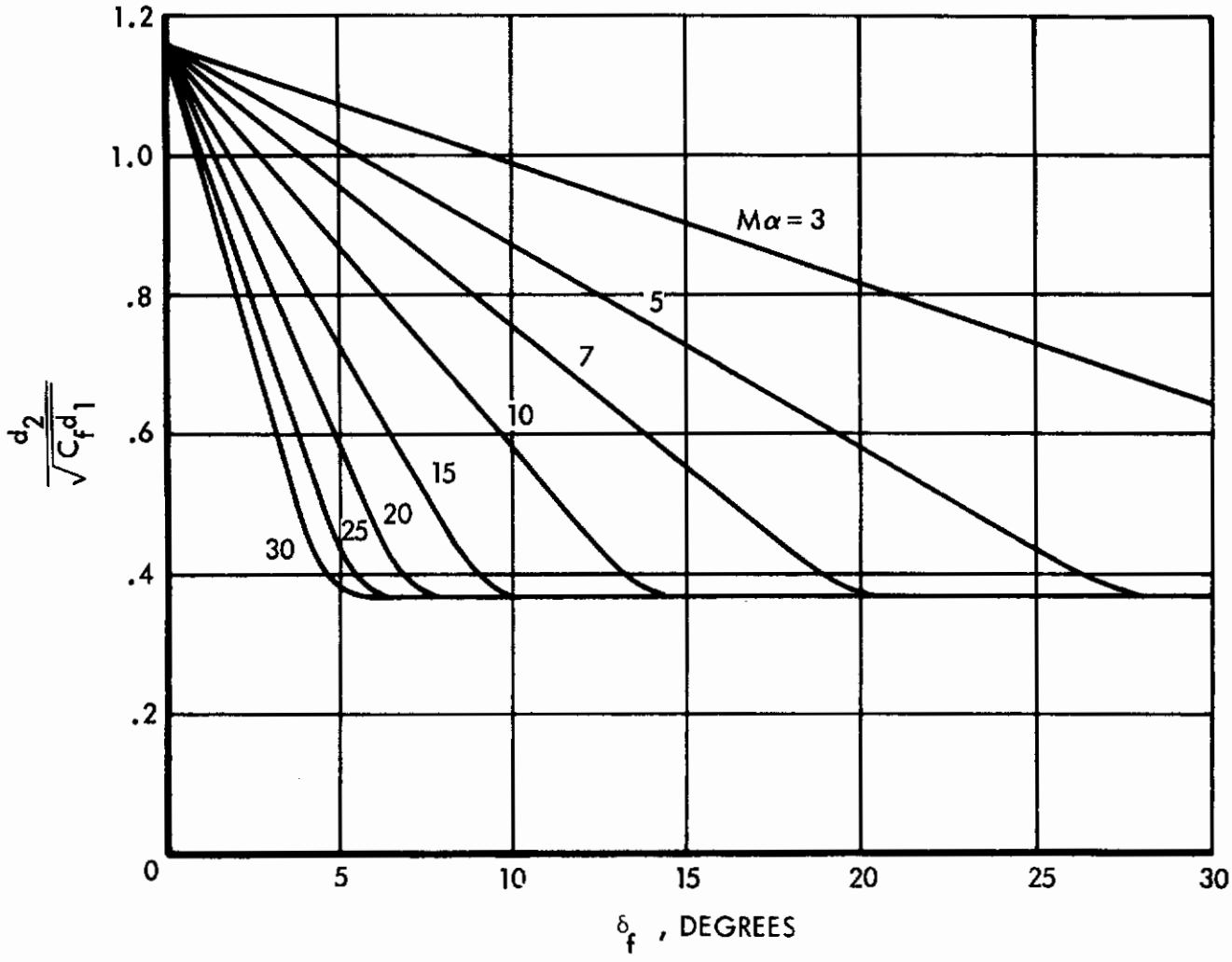

Figure 113. Downstream Interaction Distance to Peak Pressure for on Flap Turbulent Flow, d_2

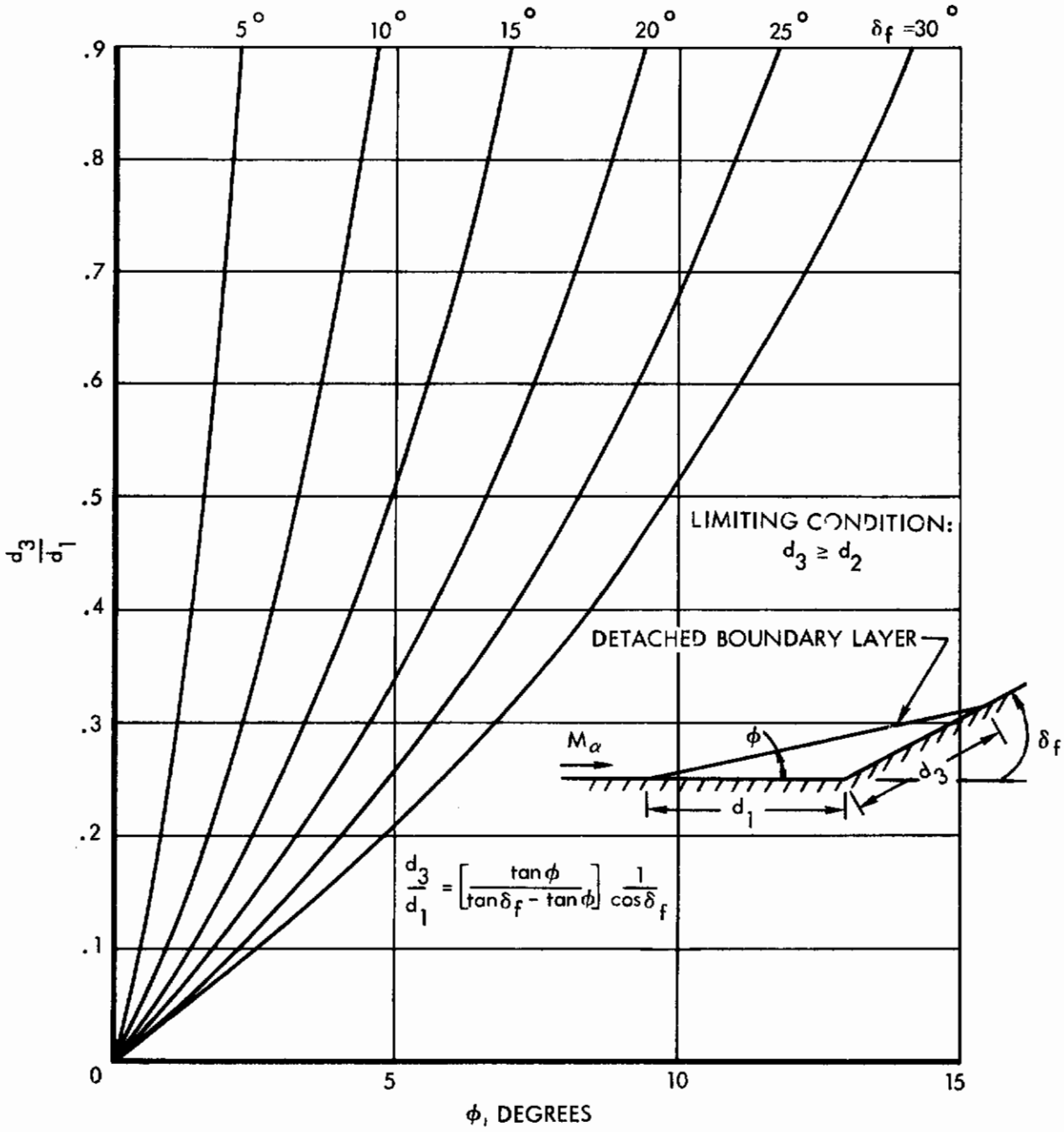

Figure 114. Downstream Interaction Distance to Pressure Rise on Flap for Laminar Flow, d_3

The first step in defining the pressure distribution is to determine if flow separation exists. The pressure coefficient data recommended for predicting incipient boundary layer separation in laminar or turbulent flow are presented in Figure 100.

It has been verified (Section 4.1) that the existence of laminar or turbulent flow can be predicted with adequate accuracy by the Deem-Murphy criterion (Reference 51).

If flow separation exists, an iterative procedure is required to determine the separation location. For a given local Mach number, the upstream interaction distance is a function of the plateau pressure level, which is a function of the Reynolds number at the separation point. (The interaction flow model is discussed in Section IV and is shown in Figure 28.) Therefore, for any separation location a corresponding plateau pressure level and upstream interaction distance is defined. In solving for the separation location, the upstream interaction distances corresponding to a number of assumed separation locations are calculated until the point is found for which the sum of the downstream distance to the separation point and the upstream interaction distance is equal to the distance to the hinge line. The procedure is as follows:

1. Assume a separation location X'_0 (the prime superscript denotes distance measured from an effective starting point for equivalent flat plate boundary layer generation), and calculate the Reynolds number.

2. Read the plateau pressure coefficient from Figure 106 or 107.

3. Obtain the upstream interaction distance, d_1, non-dimensionalized by boundary layer thickness, from Figure 108 or 109.

4. For a given wall temperature, calculate the reference temperature Reynolds number from Figure 100 or 101 and the corresponding boundary-layer thickness from Figure 102 or 103.

5. Compute d_1 and $X'_0 + d_1$. If $X'_0 + d_1 \neq X'_{HL}$, repeat procedure.

Figures 110 through 114 present the remaining interaction distances (ℓ_{fi}, d_2, and d_3) which define the pressure distribution, as functions of the plateau pressure level, upstream interaction distance, and boundary layer thickness.

INCREMENTAL FORCE AND MOMENT EQUATIONS

Equations have been derived for the two-dimensional force and moment increments produced by separated compression corner flow. The force and moment equations were developed in terms of the distances and pressure levels which define the pressure distribution. A body fixed coordinate axes system with origin at an arbitrary vehicle moment reference point (MRP) was used in the

derivation. The coordinate axes system and convention for positive sense of the forces and moments are shown in Figure 115. The equations are summarized below. The complete derivation of the equations is presented in Appendix I. It is to be emphasized that the following equations represent the force and moment increments produced on the windward surface of a deflected control and that increments produced on the leeward surface are not included; the subscript w is used to denote this fact. In many cases, however, the leeward contribution is negligible. Also, the effect of skin friction control effectiveness was not included. Note that all force increments and pitching moment increments are based on the pressure on the windward side at the beginning of interaction. Windward component of elevon hinge moment is based on absolute pressure distribution.

1. Normal force increment:

$$\frac{\Delta C_N S\big]_w}{b} = \left[(C_{p_\infty})_p - (C_{p_\infty})_\alpha\right]\left[d_1 - \frac{\ell_{fi}}{2} + \cos\delta_f C_f\right] + \left[(C_{p_\infty})_2 - (C_{p_\infty})_p\right](\cos\delta_f)\left[C_f - \frac{d_2}{2} - \frac{d_3}{2}\right] \tag{36}$$

2. Increment of pitching moment about HL due to normal force increment:

$$\frac{\Delta C_{m_{HL}} SL\big]_{\Delta N_w}}{b} = \left[(C_{p_\infty})_p - (C_{p_\infty})_\alpha\right]\left[\frac{\ell_{fi}^2}{6} - \frac{\ell_{fi} d_1}{2} + \frac{d_1^2}{2} - \frac{(\cos^2\delta_f) C_f^2}{2}\right] - \left[(C_{p_\infty})_2 - (C_{p_\infty})_p\right](\cos^2\delta_f)\left[\frac{C_f^2}{2} - \frac{d_2^2}{6} - \frac{d_2 d_3}{6} - \frac{d_3^2}{6}\right] \tag{37}$$

3. Center of pressure of normal force increment:

$$X_{cp_{\Delta N_w}} = X_{HL} + \frac{\Delta C_{m_{HL}} L\big]_{\Delta N_w}}{\Delta C_{N_w}} \tag{38}$$

4. Axial force increment:

$$\frac{\Delta C_A S\big]_w}{b} = (\sin\delta_f)\left\{\left[(C_{p\infty})_p - (C_{p\infty})_\alpha\right] C_f + \left[(C_{p\infty})_2 - (C_{p\infty})_p\right]\left[C_f - \frac{d_2}{2} - \frac{d_3}{2}\right]\right\} \tag{39}$$

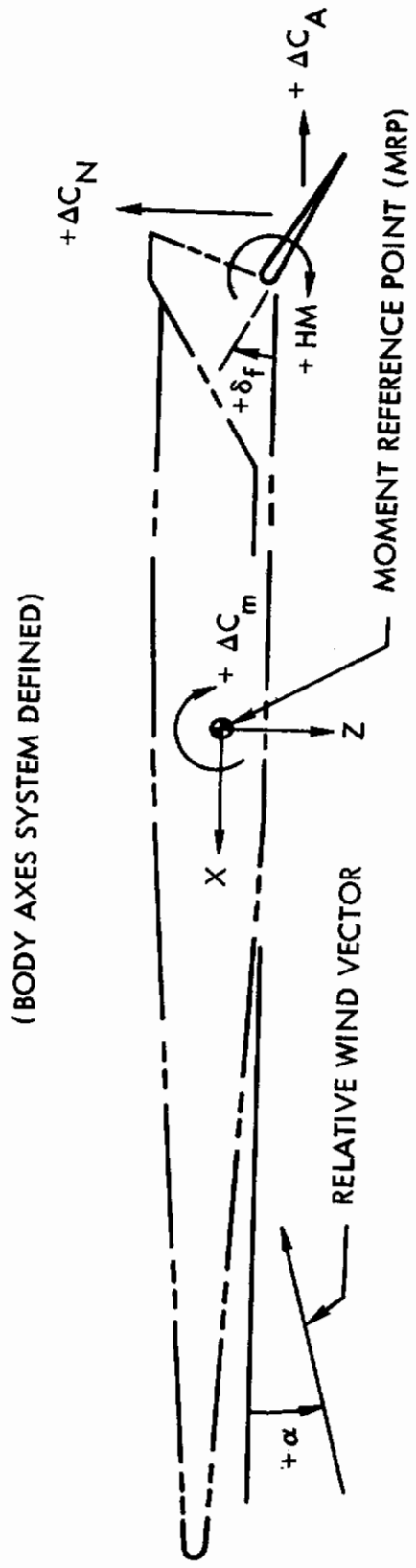

Figure 115. Two-Dimensional Force and Moment Convention for Symmetrical Elevon Deflection

5. Increment of pitching moment about HL due to axial force increment:

$$\frac{\Delta C_{m_{HL}}\Big|_{\Delta A_w}}{b} = -\left(\sin^2\delta_f\right)\left\{\left[(C_{p\infty})_p - (C_{p\infty})_\alpha\right]\frac{C_f^2}{2}\right. \tag{40}$$

$$\left. + \left[(C_{p\infty})_2 - (C_{p\infty})_p\right]\left[\frac{C_f^2}{2} - \frac{d_2^2}{6} - \frac{d_2 d_3}{6} - \frac{d_3^2}{6}\right]\right\}$$

6. Center of pressure of axial force increment:

$$Z_{cp_{\Delta A_w}} = Z_{HL} - \frac{\Delta C_{m_{HL}}\Big|_{\Delta A_w}}{\Delta C_{A_w}} \tag{41}$$

7. Increment of pitching moment about vehicle MRP:

$$\Delta C_{m_{MRP}}\Big|_w = \Delta C_{N_w} X_{cp_{\Delta N_w}} - \Delta C_{A_w} Z_{cp_{\Delta A_w}} \tag{42}$$

8. Windward component of elevon hinge moment (based on absolute pressure):

$$\frac{HM}{bq}\Big|_w = -\left\{(C_{p\infty})_2 \frac{C_f^2}{2} - \frac{1}{6}\left[(C_{p\infty})_2 - (C_{p\infty})_p\right]\left[d_2^2 + d_2 d_3 + d_3^2\right]\right\} \tag{43}$$

These equations provide a direct means of calculating the two-dimensional, windward effectiveness of a control surface once the idealized pressure distribution for compression corner flow is known.

COMPARISON OF EXPERIMENTS WITH PREDICTIONS

To illustrate the applicability of the prediction methods for estimating control effectiveness, incremental force and moment coefficients have been calculated for a test configuration and compared with the experimental data. Reference 72 presents force test results taken at Mach numbers 5 and 8 for a pyramidal configuration with trailing edge control surfaces. A sketch of the test configuration is shown in Figure 85. Calculations for the bottom surface of this configuration were performed for angles of attack of 0 and 10 degrees and control surface deflection angles of 20 and 40 degrees. The average distance of the control surface hinge line from the leading edge was used to compute the Reynolds number. No attempt was made to account for the leading

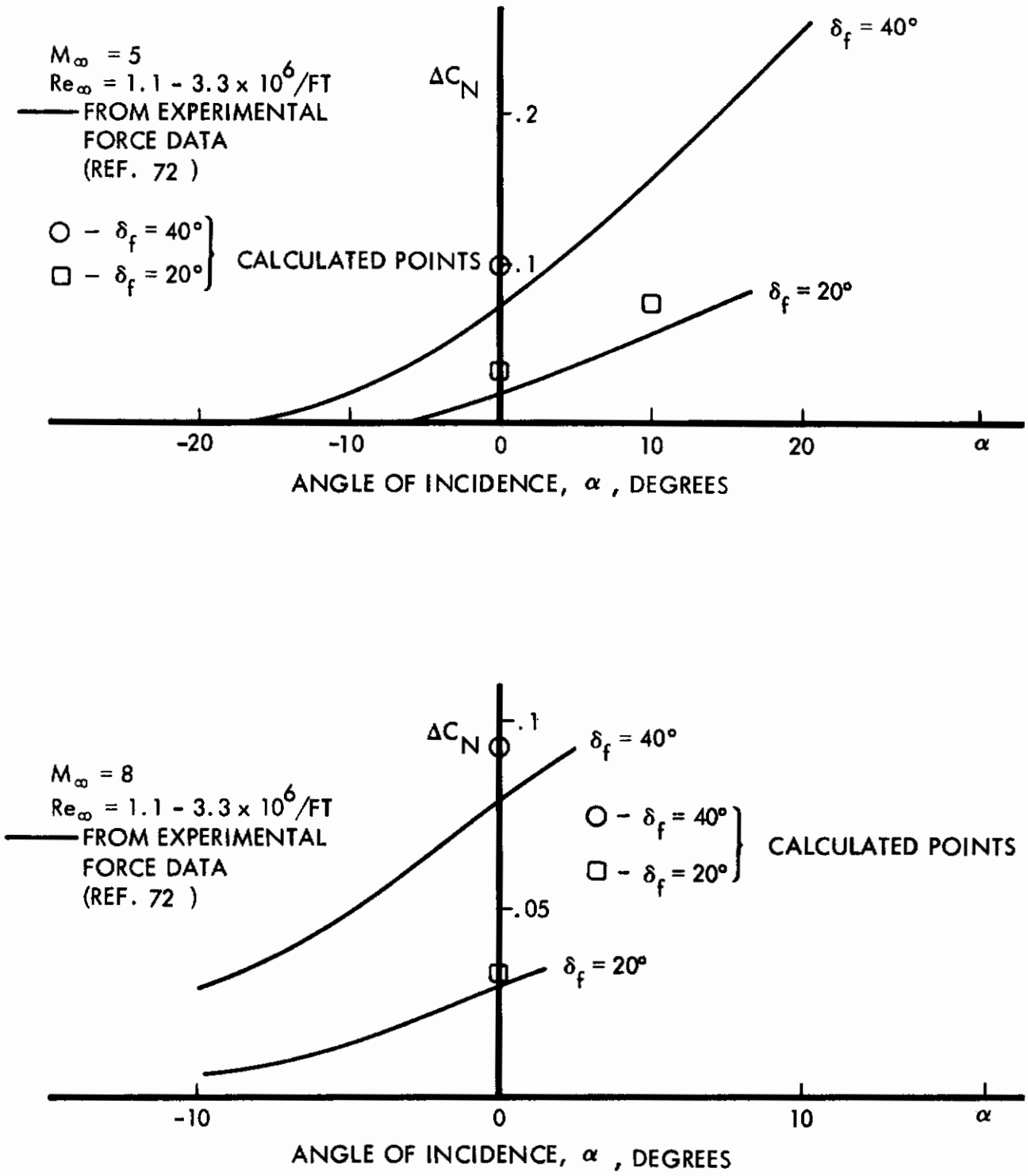

Figure 116. Comparison of Experimental Data with Predicted Results for Blunted Pyramidal Configuration

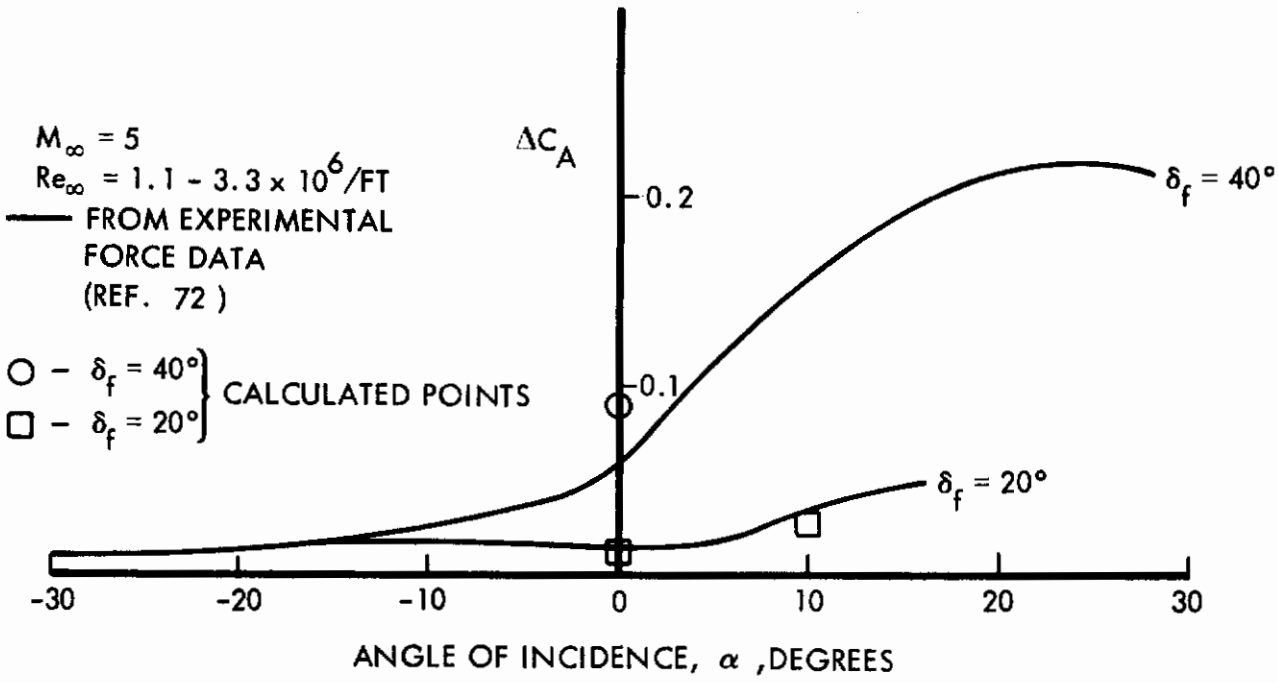

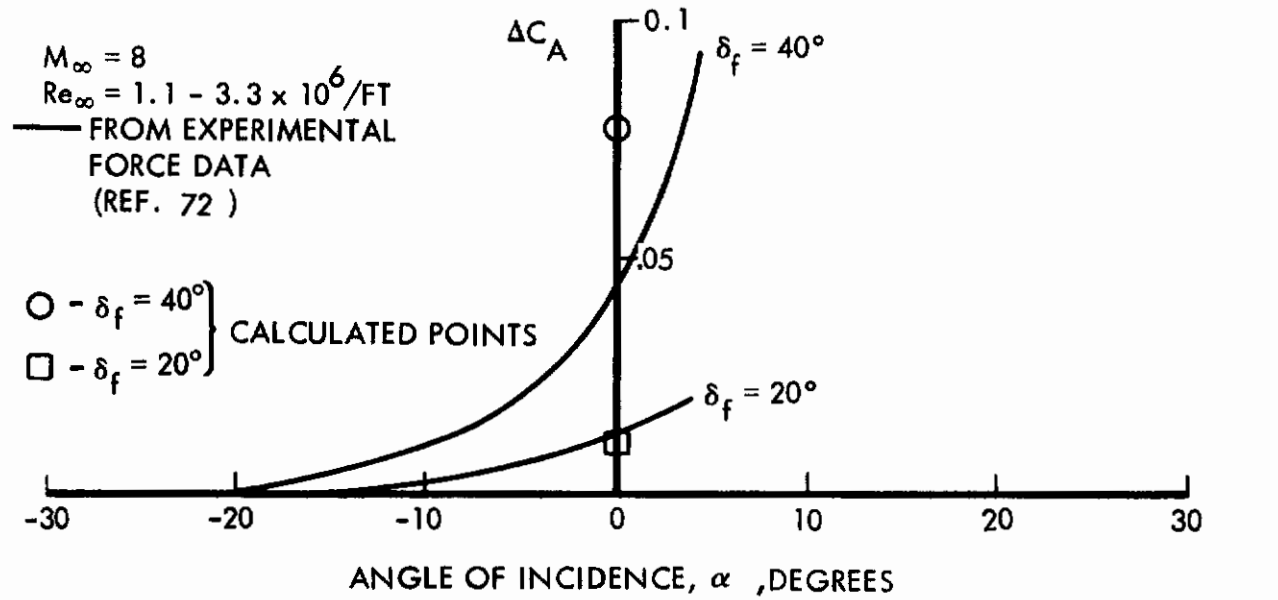

Figure 116. Comparison of Experimental Data with Predicted Results for Blunted Pyramidal Configuration (Continued)

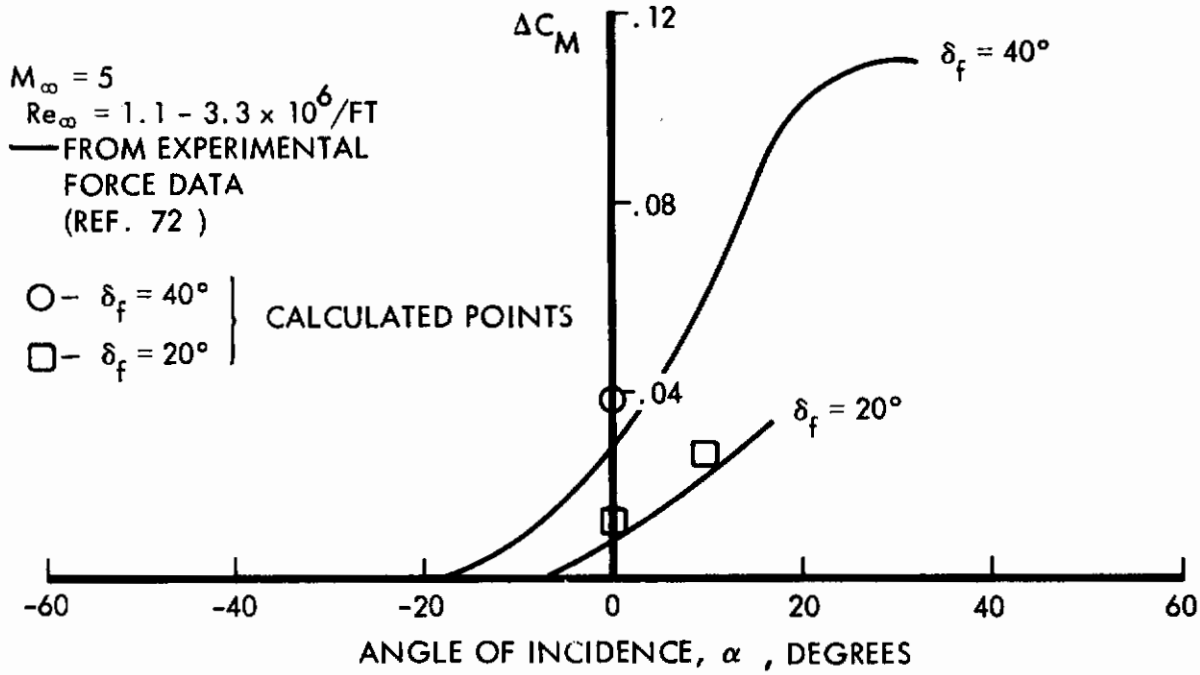

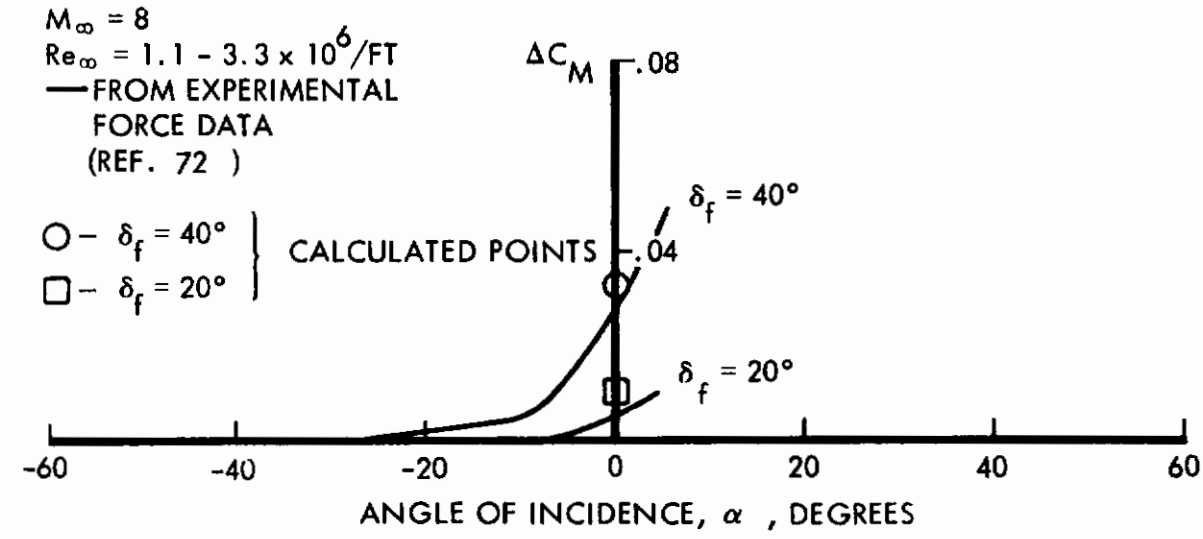

Figure 116. Comparison of Experimental Data with Predicted Results for Blunted Pyramidal Configuration (Concluded)

edge bluntness or the sweepback. Figure 116 shows a comparison of the analytical results with experimental data. The comparison indicates that the calculated data slightly overpredict the control effectiveness; however, in view of the fact that finite span effects were not considered, generally good agreement is shown.

Section VII

AERODYNAMIC HEATING IN SEPARATED FLOW

Flow separation brings about changes in pressure and heat transfer distribution. A typical heat transfer distribution, including the parameters used in the succeeding correlations, is shown in Figure 117. Heat transfer rates depend on the pressure field. It is well established that surfaces beneath separated regions experience reduced rates, while greatly increased local rates are experienced in regions of reattachment. For a long enough axisymmetric body, total integrated heat flux tends to approximate the flux that would exist if there were no separation (Ref 73).

An investigation of the heat transfer in separated laminar and turbulent flow is described in this section. The model geometries considered are: a sharp leading edge flat plate with a deflected trailing edge flap in compression, and a flat plate with an incident shock generated by an external wedge. Data (obtained from various test facilities) along the plate centerline have been correlated into expressions describing the magnitude and distribution of heat transfer in the separated region.

DATA PRESENTATION

The local experimental heat transfer coefficients were non-dimensionalized by local theoretical heat transfer values for a flat plate at zero incidence, evaluated by means of the reference temperature method.

Using the reference temperature relation (Reference 71):

$$\frac{T^*}{T_\infty} = 0.5\left(\frac{T_w}{T_\infty} + 1\right) + 0.044r\,M_\infty^2$$

where $r = Pr^{1/2} = 0.85$ for laminar flow

and $r = Pr^{1/3} = 0.90$ for turbulent flow

The theoretical heat transfer coefficients were obtained from (Reference 71)

$$\frac{h_x}{K^*} = Nu_x^* = 0.332\,Re_x^{*\,1/2}\,Pr^{*1/3} \text{ for laminar flow}$$

and $$\frac{h_x}{K^*} = Nu_x^* = 0.029\,Re_x^{*\,4/5}\,Pr^{*1/3} \text{ for turbulent flow.}$$

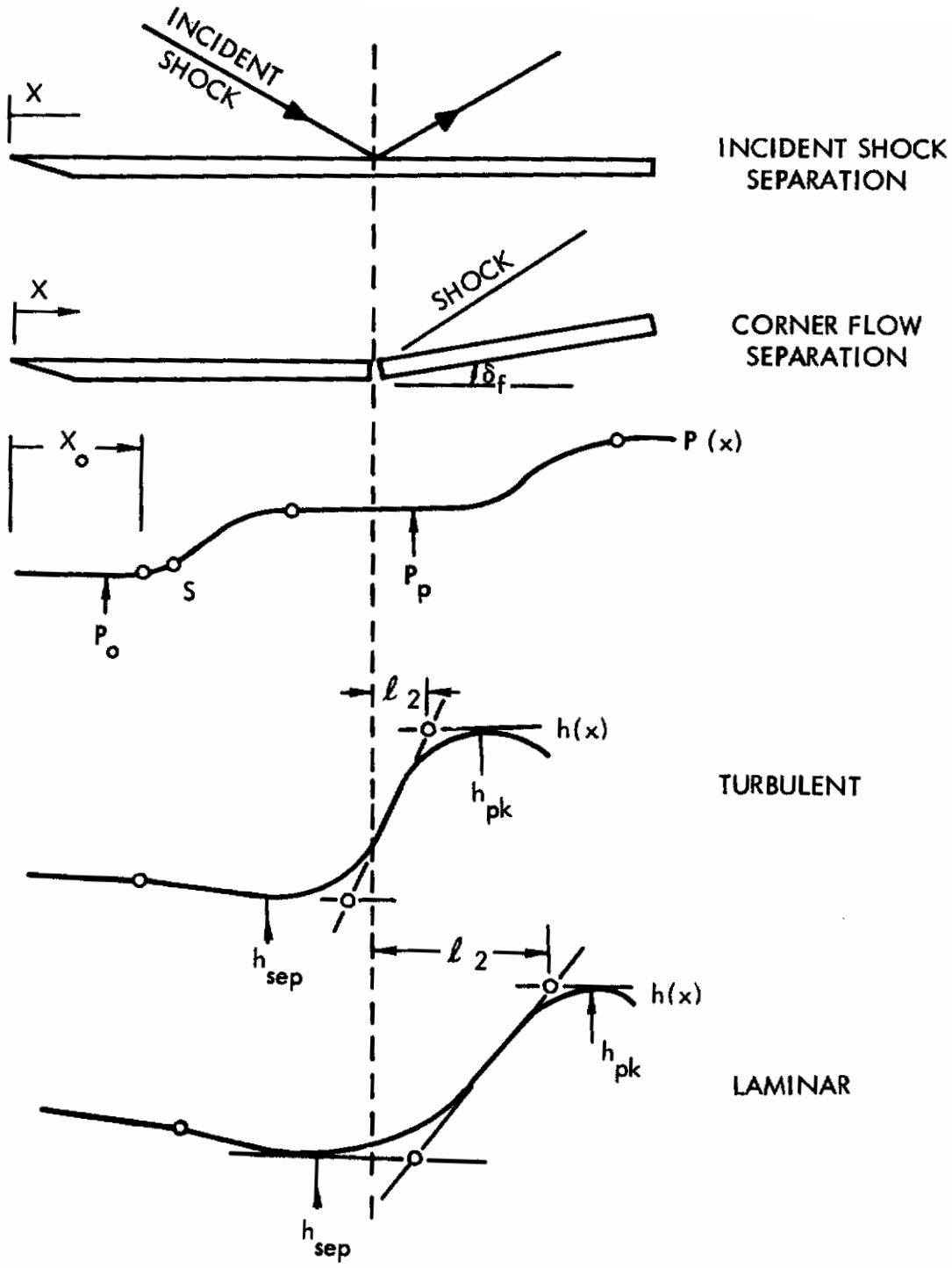

Figure 117. Definition of Interaction Parameters for Shock-Induced Separation

The downstream heat transfer interaction length was non-dimensionalized by the attached boundary layer thickness at X_o, defined by the following simple relations for laminar and turbulent flow, respectively:

$$\delta_{o_B} = 5.2\, X_o Re_{x_o}^{-\frac{1}{2}} \quad \text{Laminar}$$

$$\delta_{o_B} = 0.38\, X_o Re_{x_o}^{-\frac{1}{5}} \quad \text{Turbulent}$$

The evaluated experimental data were obtained from References 74 - 80 and the aerodynamic heating rates on the test plates were obtained utilizing the thin wall transient temperature technique with correction for heat conduction.

HEAT TRANSFER CORRELATIONS

It was inferred from experimental data that the peak heat transfer h_{pk} and the downstream heat transfer interaction length ℓ_2 can be expressed by the following relationships:

$$\frac{\ell_2}{\delta_{o_B}} = f\left[Re_{x_o}^{n},\ M_\infty^{a}\left(\frac{P}{P_o}\right)^{b}\right]$$

$$\frac{h_{pk}}{h_{fp}} = f\left[Re_{x_o}^{n},\ M_\infty^{c}, \left(\frac{P}{P_o}\right)^{d}\right]$$

where: $n = \frac{1}{2}$ for laminar flow

$n = \frac{1}{5}$ for turbulent flow

Groups of dimensionless parameters were plotted on log-log paper and the data correlations were obtained by fairing a straight line representing an average through the data distribution. An equation of the form $y = A\, x^m$, where A is the ordinate-intercept and m is the slope of the line, was obtained for various groups of parameters, subsequently arriving at a correlation function.

LAMINAR SEPARATED FLOW

It was established that the heat transfer rate decreases over the separated region and reaches a maximum value in the reattachment region. The magnitude of the peak heat transfer rate, location of peak heating, and heat rate in the separated region are discussed in the following sections.

Peak Heating Rate

An attempt was made to obtain some semi-empirical relations describing the magnitude of the peak heat transfer. An evaluation of experimental heat transfer results leads to the following parametric relation for peak heat transfer (Ref. 81).

$$\frac{h_{pk}}{h_{fp}} = f\left(Re, M_\infty, \frac{P}{f\alpha}\right)$$

Figures 118 and 119 present the peak heat transfer parameter for laminar separated corner flow as a function of pressure rise from the plateau value to the oblique shock value and from the undisturbed value to the oblique shock value, respectively. The figures illustrate that peak heating magnitudes increase with decreasing Mach number, and are proportional to pressure ratio. The variation of peak heat transfer is easily obtained from Figures 118 and 119. In order to determine the heat transfer dependence on Mach number, a grouped parameter (heat transfer, Reynolds number and pressure) is shown plotted in Figures 120 and 121 versus Mach number. A straight line representing an average was faired through the data, resulting in two expressions for peak heating correlation functions:

$$\frac{h_{pk}}{h_{fp}} = 5.8 \times 10^5 \left(\frac{P_2}{P_P} - 1\right)^{0.89} Re_{x_o}^{-\frac{1}{2}} M_\infty^{-2.4} \qquad (44)$$

$$\frac{h_{pk}}{h_{fp}} = 5.0 \times 10^6 \left(\frac{P_2}{P_0}\right)^{0.88} Re_{x_o}^{-\frac{1}{2}} M_\infty^{-3.70} \qquad (45)$$

Downstream Heat Transfer Interaction Length

The location of the peak heat transfer relative to the reference line is described by the length ℓ_2 which is illustrated in Figure 117. Figure 122 presents the downstream heat transfer interaction length for M = 6 and M = 8 conditions as a function of pressure rise. The correlation of downstream heat transfer interaction length for laminar corner flow including the Mach number dependence is presented in Figure 123 and is given as follows:

$$\frac{\ell_2}{\delta_{o_B}} = \left(\frac{P_2 - P_P}{P_0}\right)^{-0.188} Re_{x_o}^{\frac{1}{2}} M_\infty^{-1} \qquad (46)$$

Heat Transfer in the Separated Region

The ratio of heat transfer (h_s/h_{fp}) in the separated region covering a range of Mach numbers from 6 to 10 is shown in Figure 124 as a function of pressure rise from the plateau to the inviscid value. The rate of heat transfer from a separated laminar mixing layer is less than that from an attached laminar

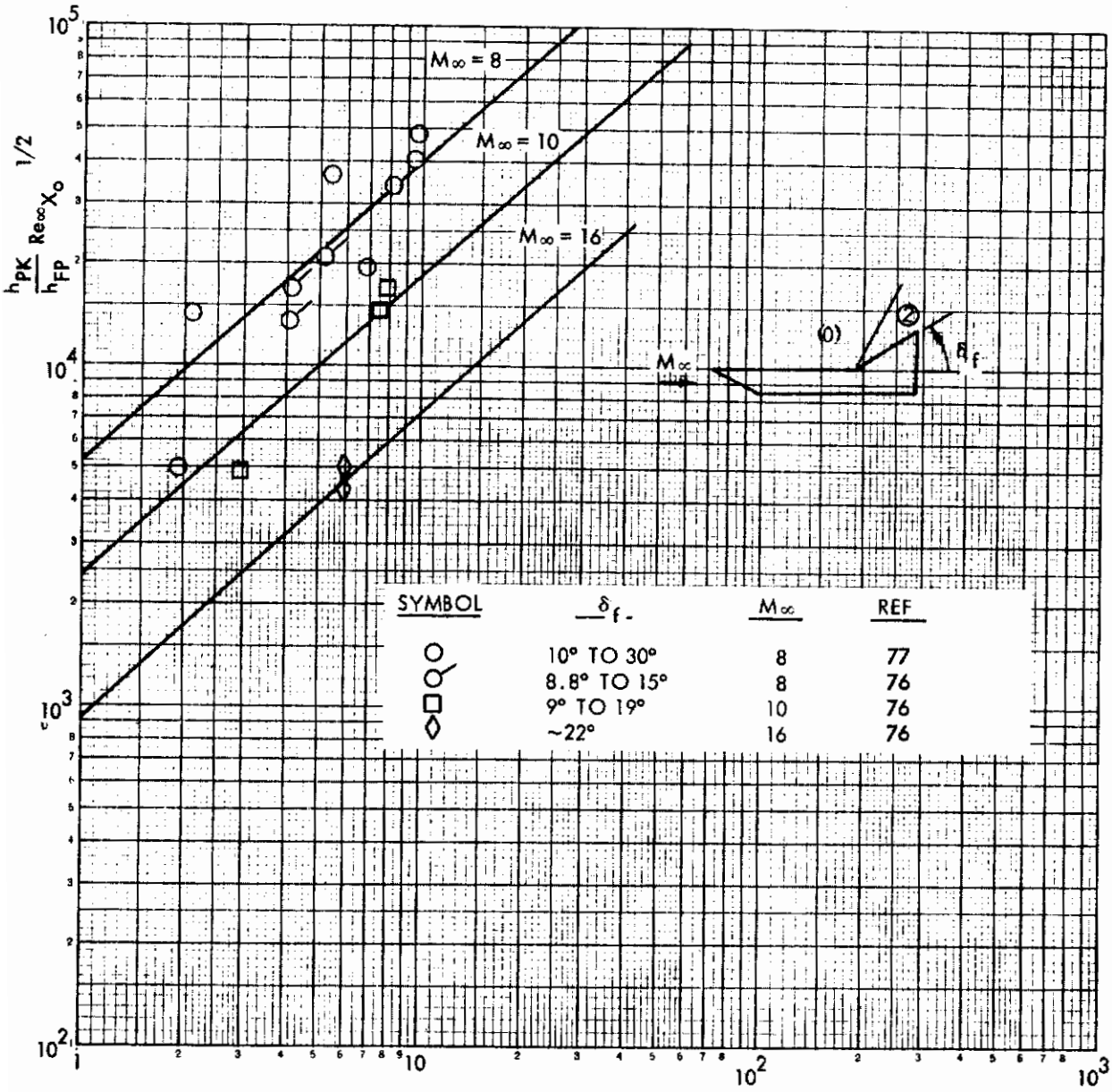

Figure 118. Peak Heat Transfer for Separated Laminar Corner Flow vs $\frac{P_2}{P_P} - 1$

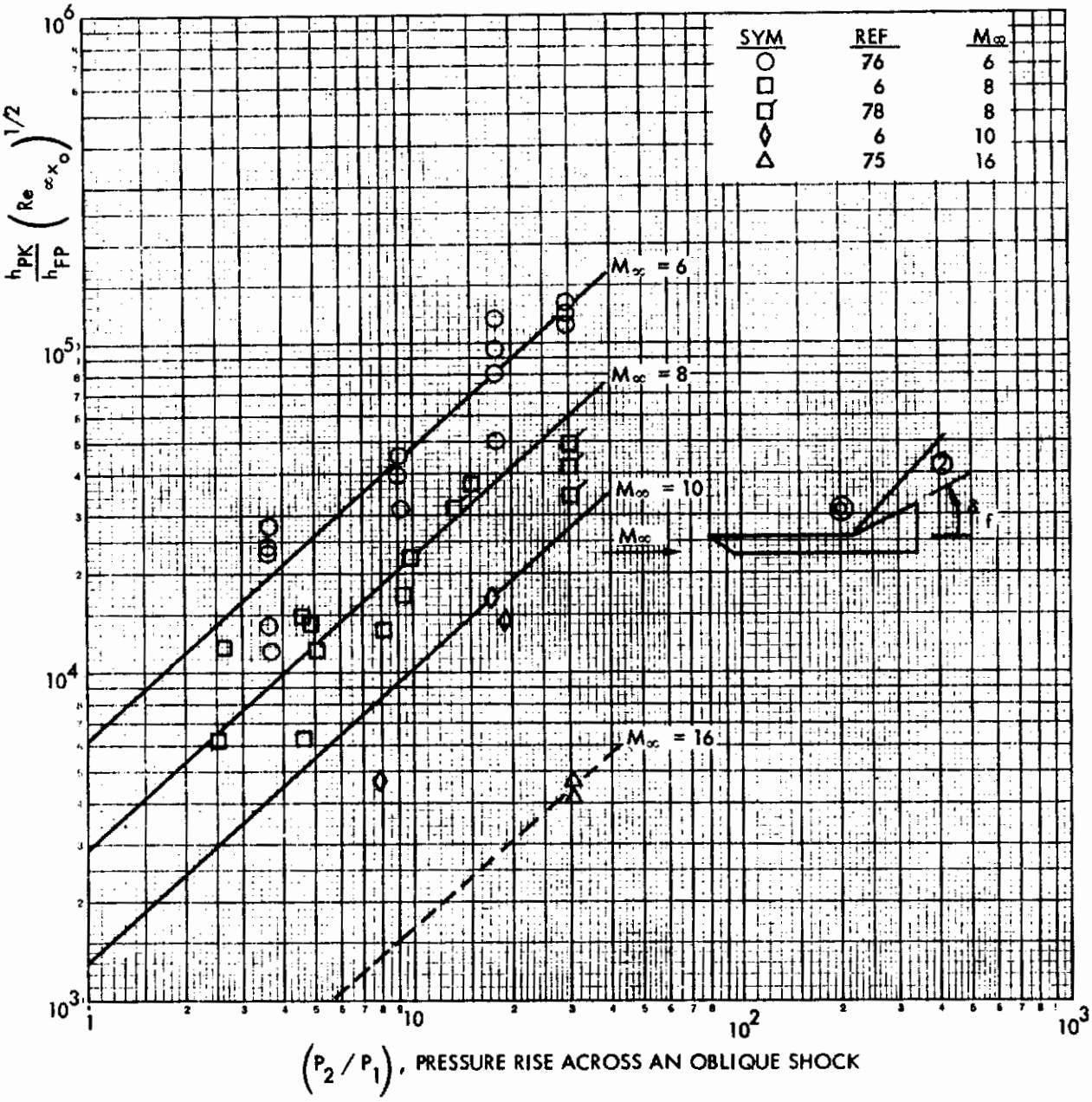

Figure 119. Peak Heat Transfer for Separated Laminar Corner Flow vs $\frac{P_2}{P_P}$

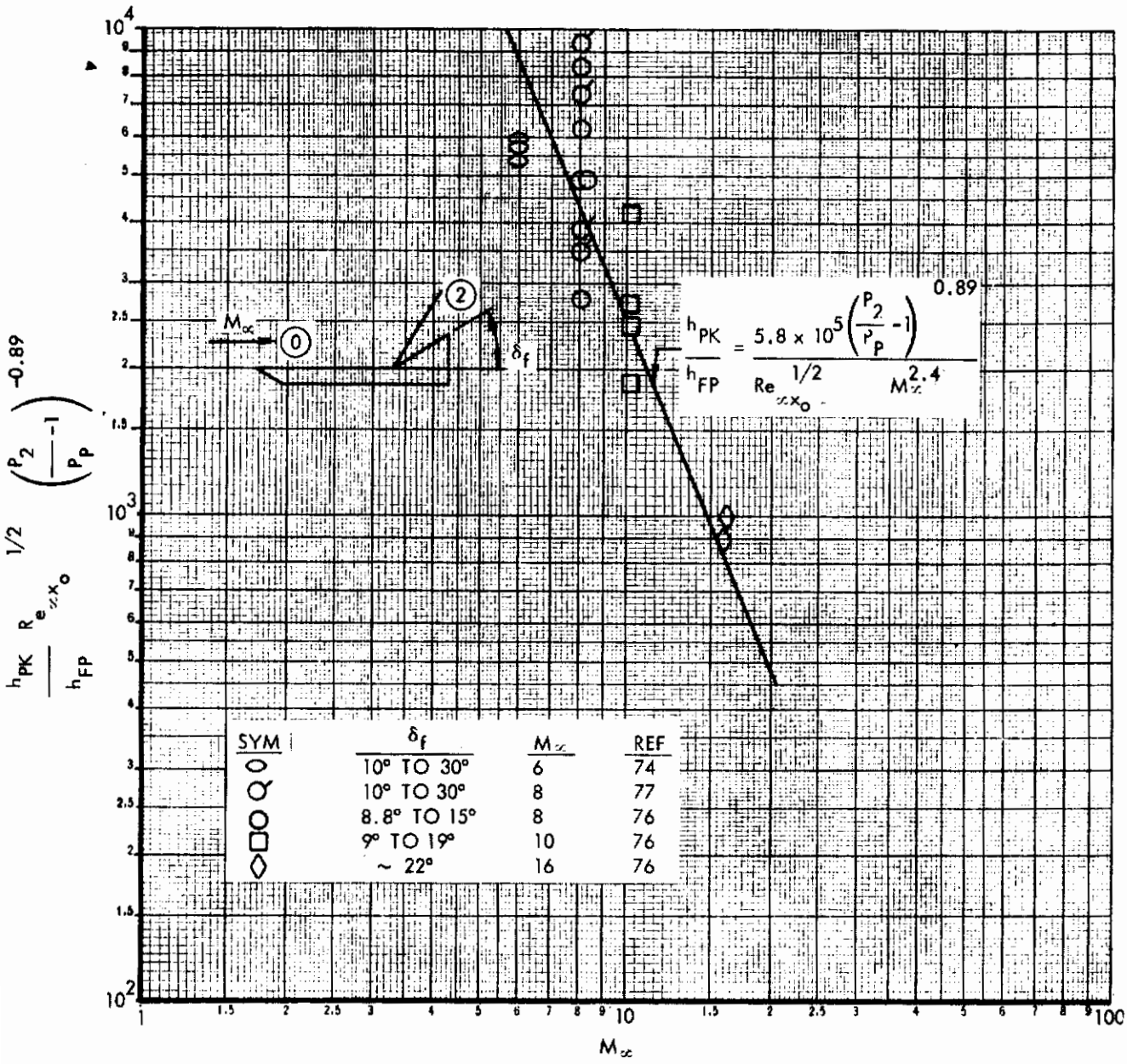

Figure 120. Peak Heat Transfer for Laminar Separated Corner Flow vs Mach Number

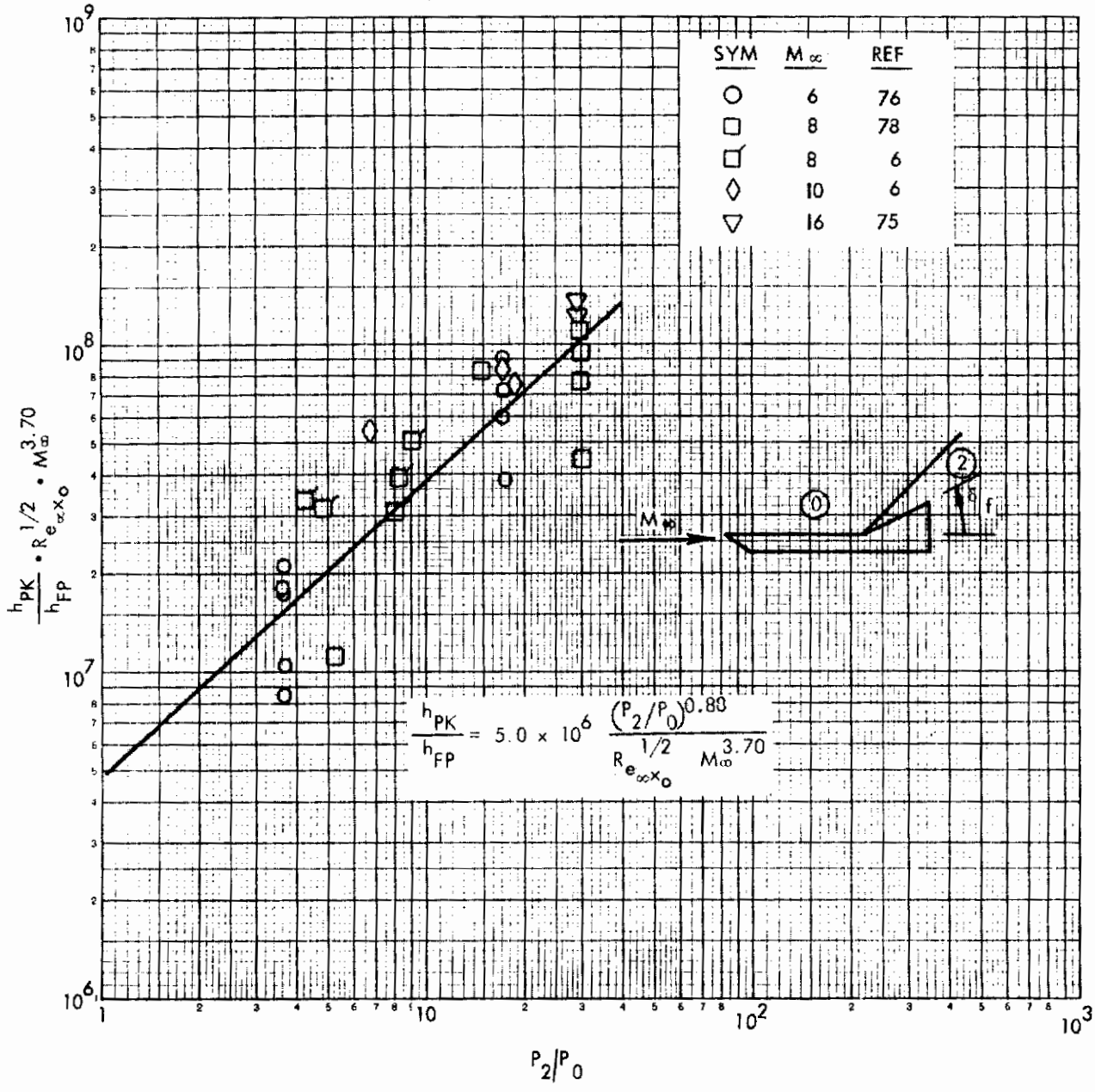

Figure 121. Grouped Peak Heat Transfer Parameter for Laminar Separated Corner Flow

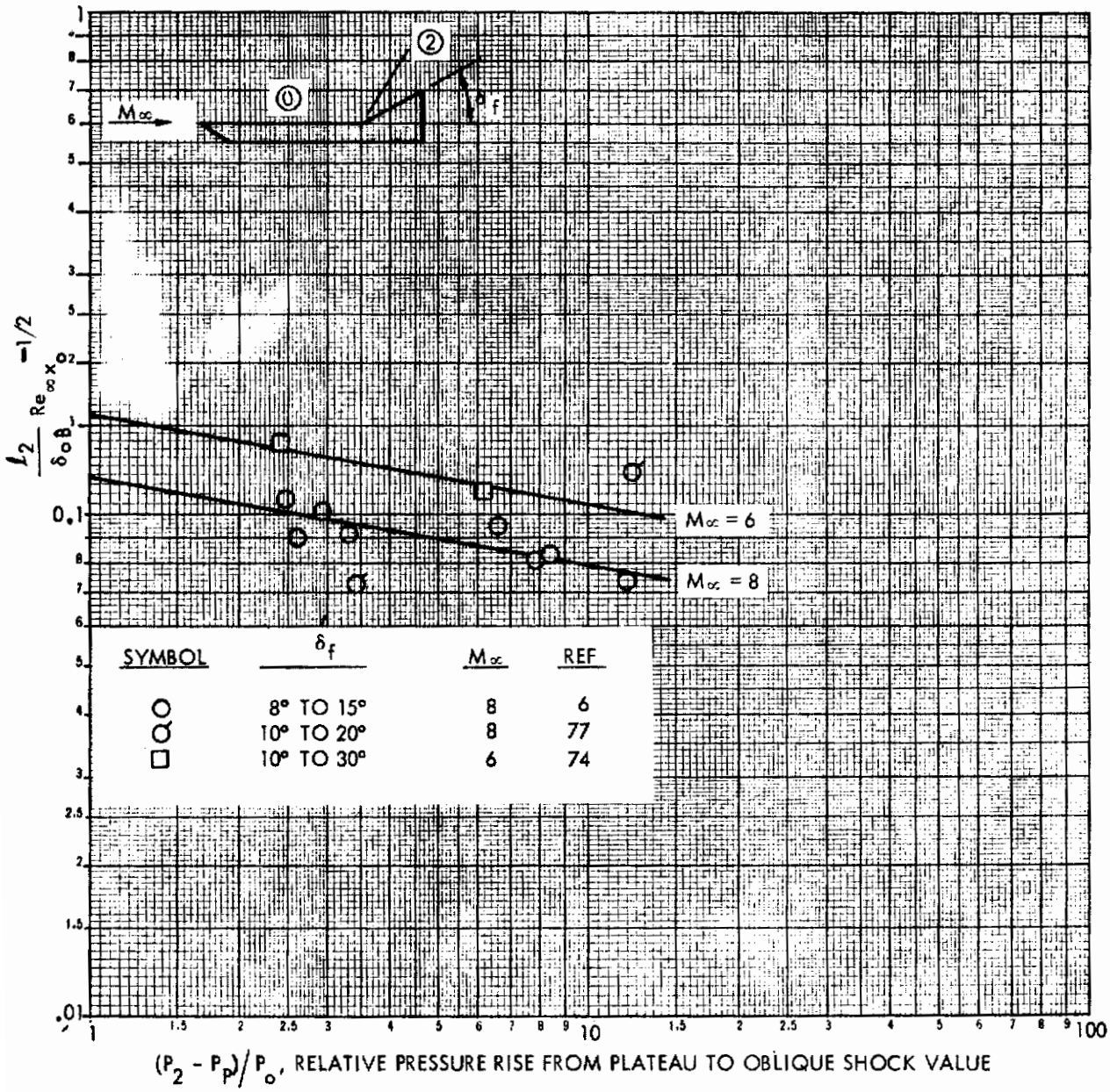

Figure 122. Downstream Heat Transfer Interaction Length for Laminar Separated Corner Flow

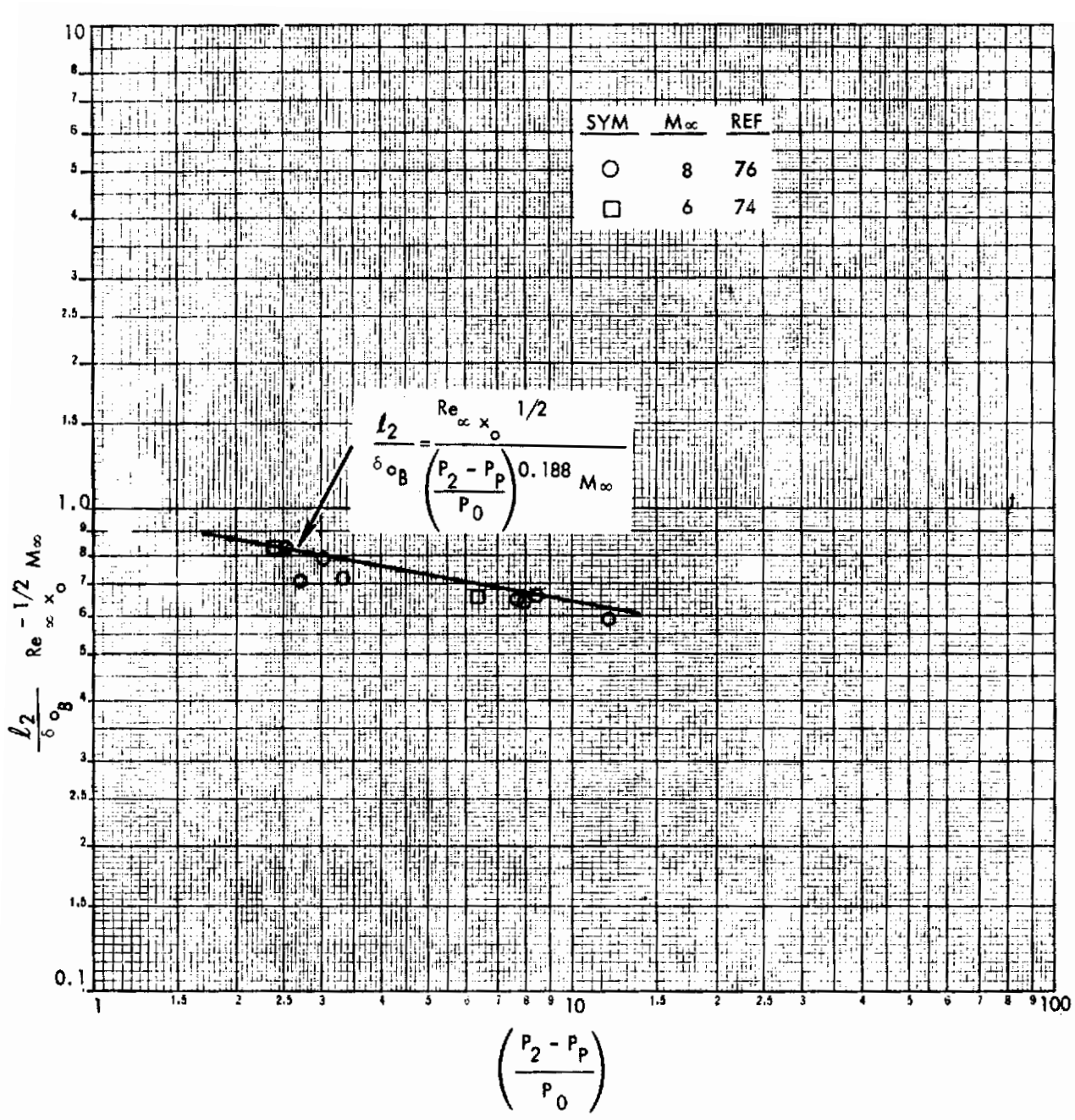

Figure 123. Grouped Downstream Interaction Length Parameter for Laminar Separated Corner Flow

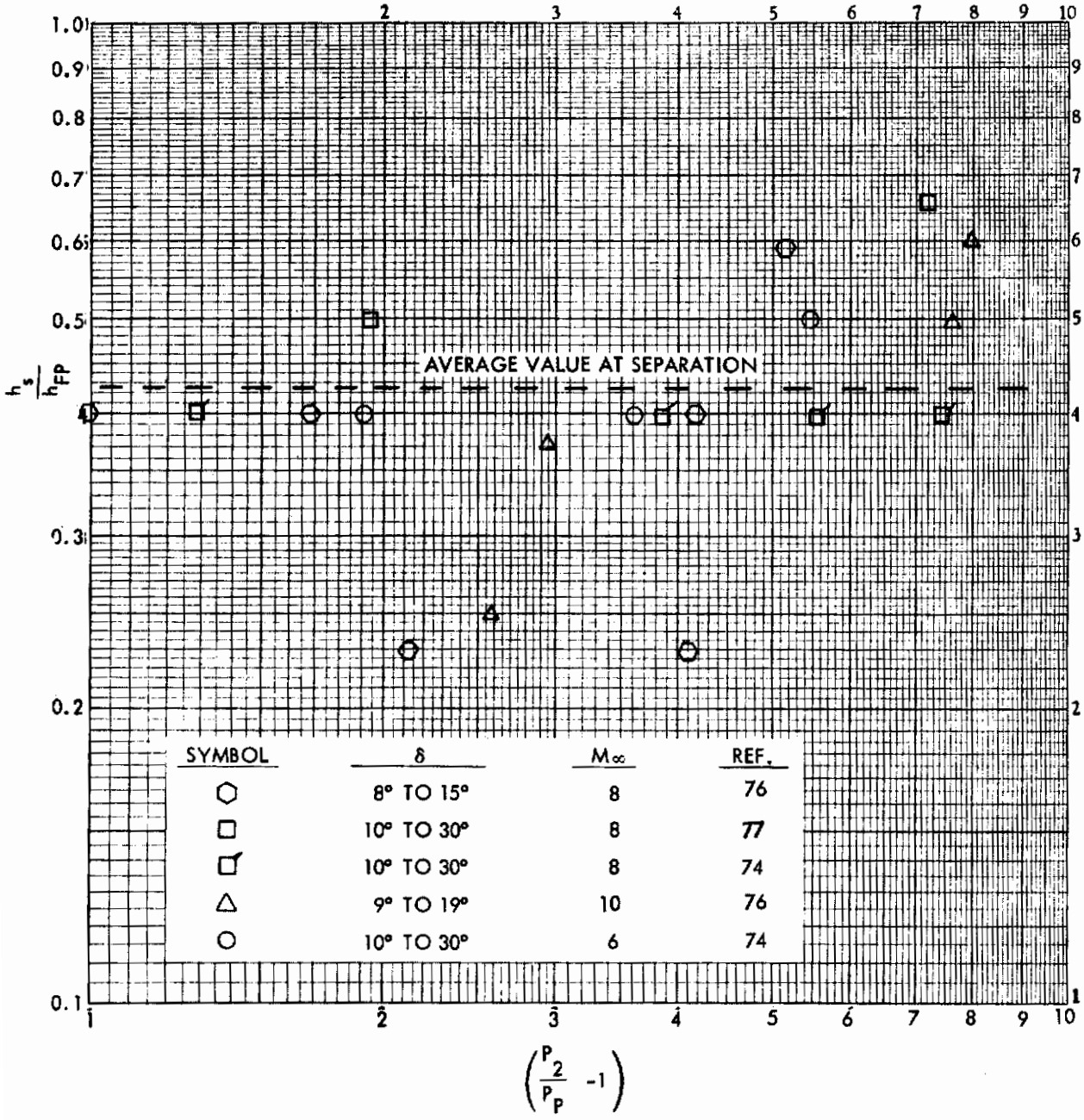

Figure 124. Heat Transfer Coefficient in the Separated Region for Laminar Corner Flow

boundary layer at corresponding values of Mach number, Reynolds number, and wall-to-stream temperature ratio. The ratio of heat flux in the separated flow to that in the attached flow is a function only of Prandtl number and has been found to be equal to a value of 0.56 for Pr = 0.72 (Ref. 82). An average value of heat transfer ratio equal to 0.425 was obtained in Figure 124.

TURBULENT SEPARATED FLOW

Peak Heating Rate

Figures 125 and 126 present data correlations for peak heating magnitude as a function of a characteristic pressure rise. The plot of $\frac{h_{pk}}{h_{fp}} Re_{x_o}^{1/5}$ versus pressure ratio $\frac{P_3}{P_0}$ of Figure 125 leads to the following expression for peak heat transfer:

$$\frac{h_{pk}}{h_{fp}} = 32.0\left(\frac{P_3}{P_0}\right)^{0.62} \left(Re_{x_o}\right)^{-\frac{1}{5}} \qquad (47)$$

This expression does not show an explicit Mach number dependence; however, a Mach number influence is contained in the P_3/P_0 ratio. A correlation of $\frac{h_{pk}}{h_{fp}}$ as a function of pressure parameter $\frac{P_3 - P_P}{P_o}$ shown in Figure 126 results in a relation for peak heat transfer

$$\frac{h_{pk}}{h_{fp}} = 1.18 \left(\frac{P_3 - P_P}{P_o}\right)^{0.18} M_\infty \qquad (48)$$

This expression does not contain a Reynolds number term; however, the Reynolds number effect is included implicitly in $\frac{P_3 - P_P}{P_o}$.

Downstream Heat-Transfer Interaction Length

The downstream location of the peak heat transfer rate relative to the reference line is determined by the length ℓ_2. A parametric correlation of ℓ_2 is shown in Figure 127 and it is expressed by

$$\frac{\ell_2}{\delta_{o_B}} = 0.02 \frac{\left(Re_{x_o}\right)^{\frac{1}{5}}}{M_\infty^{5.78} \left(\frac{P_3 - P_P}{P_o}\right)^{3.175}} \qquad (49)$$

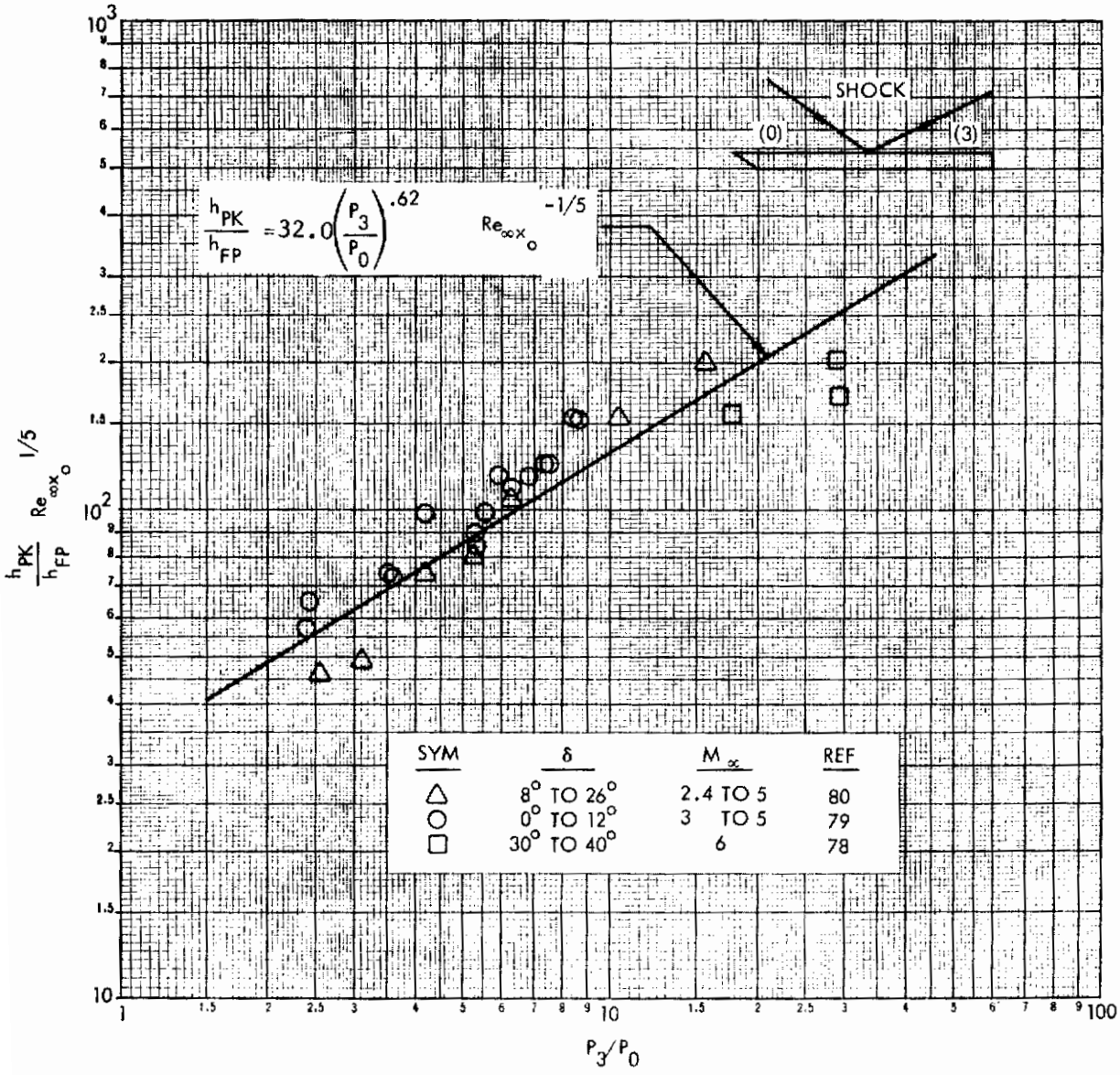

Figure 125. Peak Heat Transfer for Turbulent Flat Plate Flow with and without Separation

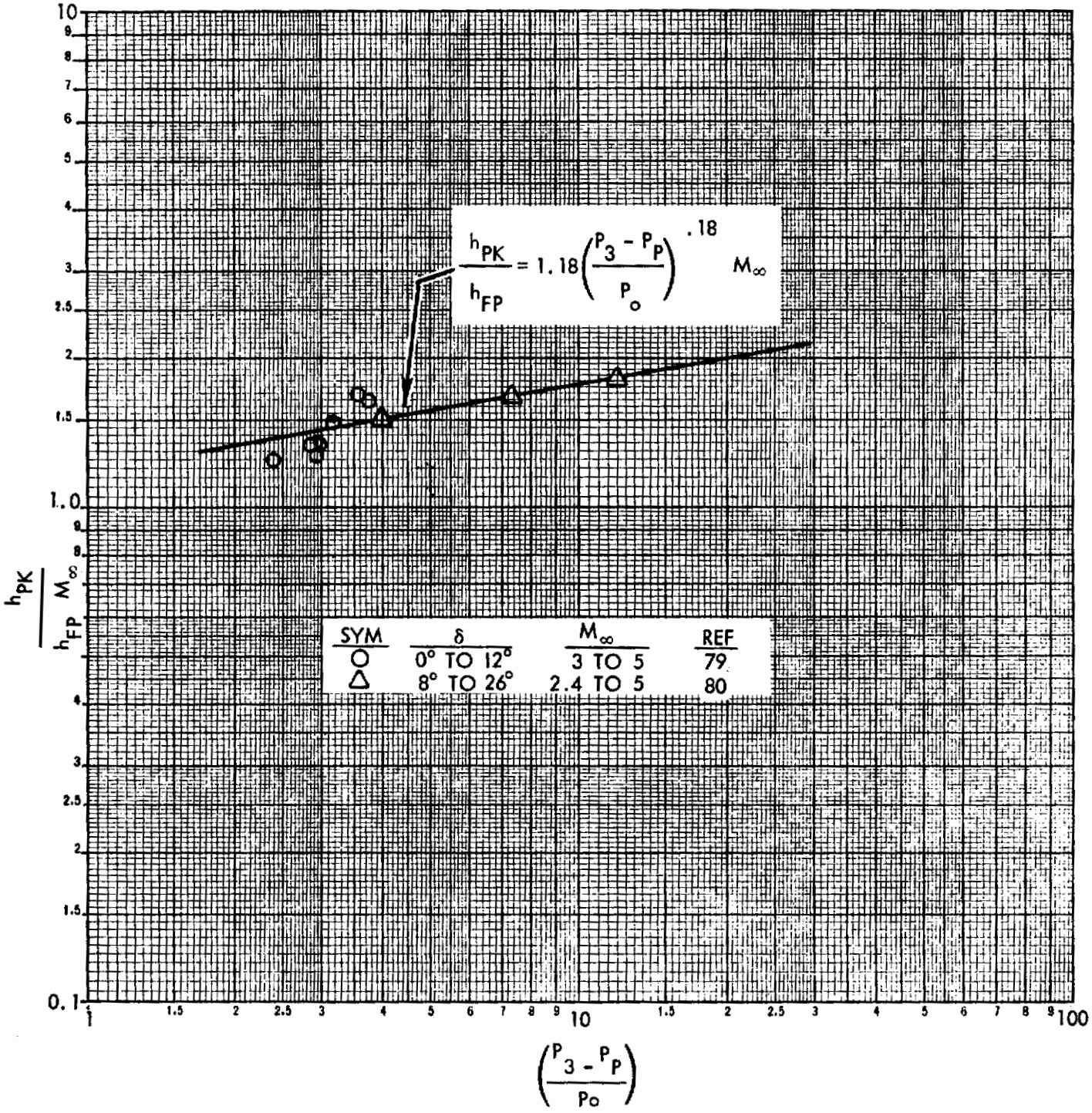

Figure 126. Peak Heat Transfer for Turbulent Flat Plate Flow with Extensive Separation

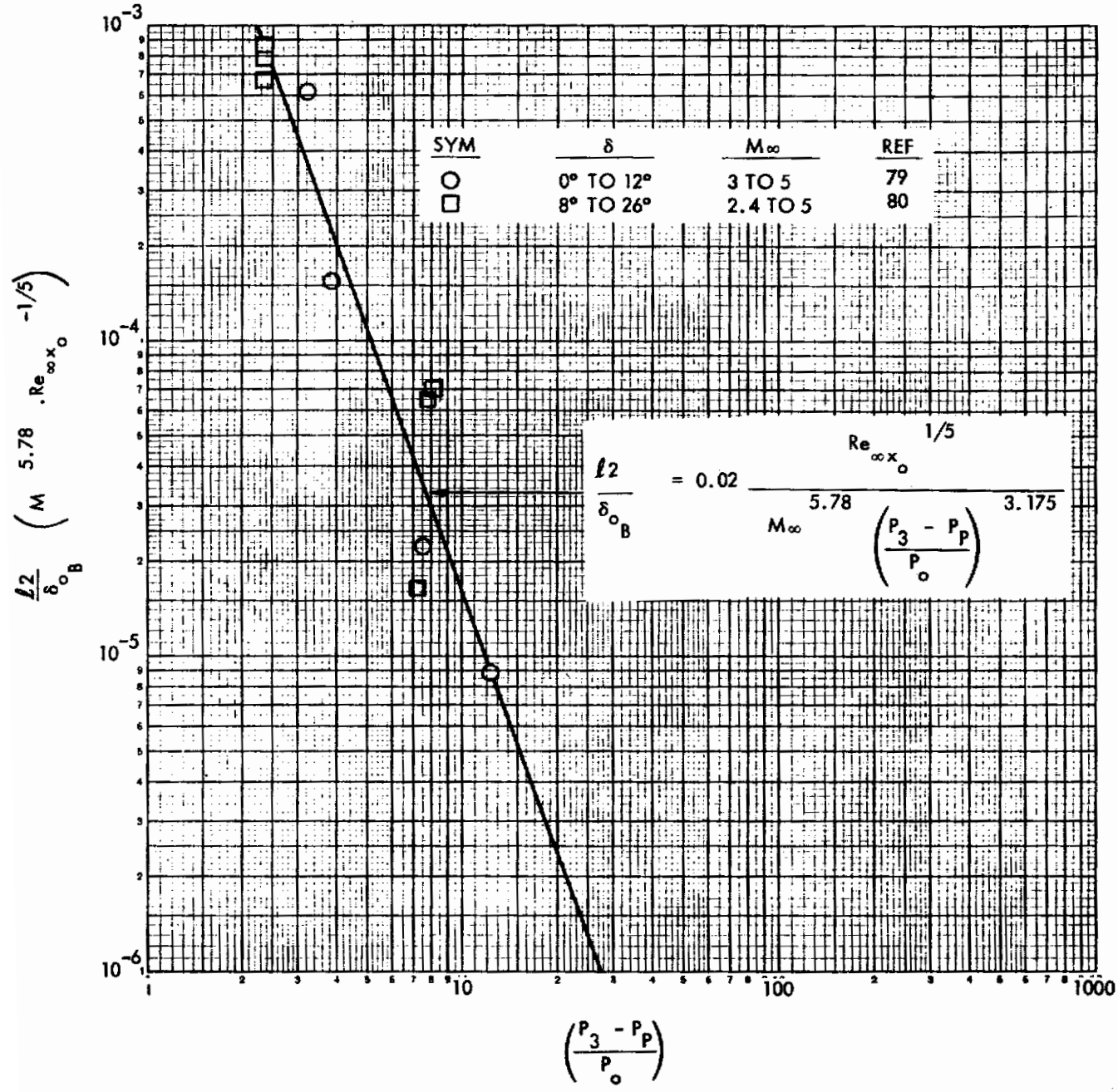

Figure 127. Downstream Heat Transfer Interaction Length for Turbulent Separated Flow

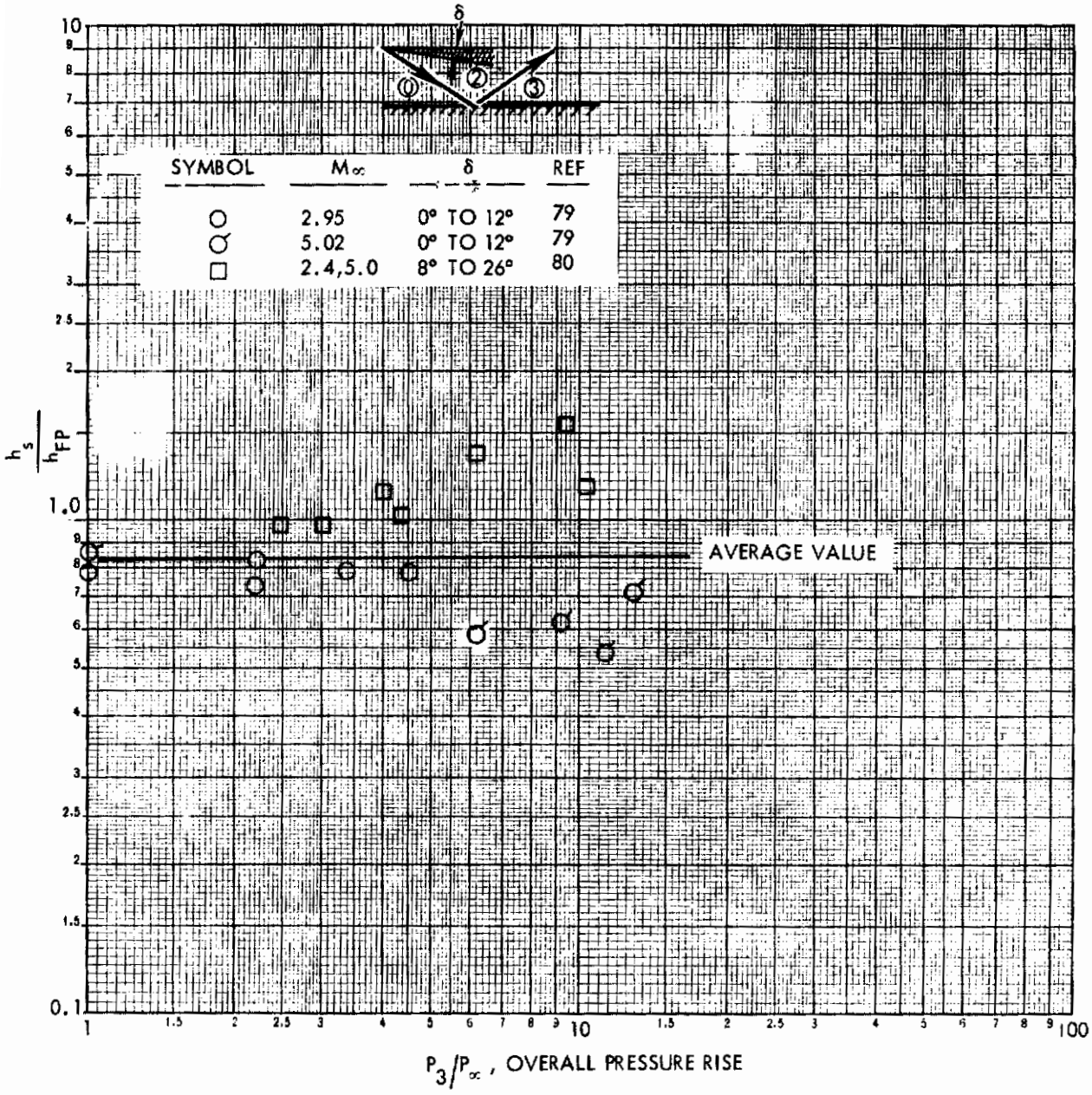

Figure 128. Heat Transfer Coefficient in the Separated Region for Turbulent Boundary Layer - Shock Wave Interaction

Heat Transfer in the Separated Region

The heat transfer coefficient in the turbulent separated region would be expected to be higher than for the laminar separated region. Figure 128 illustrates this for data covering a Mach number range from 2.4 to 5.02. The average value of heat transfer for a separated turbulent boundary layer as compared to an attached turbulent boundary layer is indicated in Figure 128 by the ratio $\frac{h_s}{h_{fp}} = 0.84$.

Section VIII

CRITICAL EVALUATION

CHARACTERISTICS OF EXPERIMENTAL DATA

Test Flow Properties

The experimental data from the several sources evaluated in this program does not completely cover the wide range of possible local flow conditions. In particular, higher local Mach number data for the turbulent cases would have been useful.

For the laminar interaction, Mach numbers varied generally from 3.1 through 8.4, with no sizable gaps. There was some data of limited usefulness around Mach 14. Local Reynolds numbers ranged from 1.2×10^5 to 1.4×10^6. This range is considered to be insufficient for accurately determining the effect of Reynolds number variation.

For turbulent interactions, Mach numbers varied generally from 1.8 through 3.8. There was some data of limited usefulness around Mach 6.2. Local Reynolds numbers ranged from 7×10^5 to 6×10^6. Neither the Mach number variation nor the Reynolds number range of the turbulent data is considered to be wide enough.

It would be desirable to have laminar separated flow data for a test section Mach number up to between 20 and 25 with local Mach number reduction to be achieved through pitching of the model. A wider variation of Reynolds number may be achieved through reservoir pressure variation and variation of model length.

Model Geometry

In order to simulate two-dimensional flow, high aspect ratio models are required. The visual evidence of the surface flow (Section 5.2) indicates that flow over a finite span body has three-dimensional features and is substantially influenced by the body tips. Thus the assumption of two-dimensionality seems questionable for all but very high aspect ratio models, as shown in Figures 61 to 69.

In some instances the streamwise spread of separated flow was of the order of the model size and no fully developed flow could be obtained. In order to

properly size the model, estimates of the extent of separated flow should be helpful. The length of the forward part of the model controls the boundary layer thickness, which is a prominent interaction parameter.

The addition of end plates fails to eliminate or reduce the three-dimensional effects and in fact introduces new complexities into the flow picture. In general the effects of end plates on the flow are not well understood and results are inconclusive.

All three major parameters of the flap geometry (deflection, chord dimension, and span dimension) and flow variation should be given detailed attention in any future test series. It is obvious that incipient separation can be pinpointed only if flap deflection is varied systematically in small increments. Downstream interaction length was found to be sensitive to flap chord length. Flap effectiveness can be substantially lowered by reducing flap aspect ratio.

Flow Visualization

Flow separation is a complex flow phenomenon, and for a thorough investigation some visual study is essential. Schlieren photography and oil flow surface patterns proved very useful and should not be overlooked. There is a need for other methods to indicate special flow details which are difficult to obtain otherwise (e.g. smoke method).

Instrumentation

A quantitative picture of the separated region is obtained by measurements of pressure and temperature. Two aspects concerning instrumentation are of paramount importance: instrumentation arrangement and density, and measurement accuracy. While availability of instrumentation may vary with the test facility used, judicious arrangement and density of instrumentation are the responsibility of the researcher. Consideration should be given to the spatial extent of the phenomena under study and especially to certain critical areas where more flow details may be desirable.

ACCURACY OF CORRELATIONS

Limitations of the data used in constructing the correlations contained in this report have been mentioned. The measurements have been taken from several sources. Each facility has its own characteristic peculiarities and generates its own systematic (as differentiated from random) errors. The combination of data from them all will therefore show more scatter about the best correlating line that can be drawn through the results, than is exhibited by the data from any single test series. However, the resulting correlation is more reliable from the inclusion of a large assortment of experimental data.

Some remarks concerning the characteristics of transitional cases will follow shortly. It is stated here that it is not always possible to predict the state of the separating boundary layer and a wrong judgement on this will always lead to failure of the correlation expression.

Some of the correlations were more difficult to construct than others. Particular difficulty was encountered in correlating the turbulent flow interaction distances. Therefore an idea of the maximum likely error associated with the use of the formulas contained herein can be obtained by noting the following. A survey of the data used in deriving the $d_1/\delta_o)_{turbulent}$ correlation showed that 75 percent of the data points had a deviation of less than $\pm$ 33% from the correlation line. Other quantities that have been correlated in this report exhibit much less scatter.

REAL VEHICLE CONFIGURATIONS

It seems certain that the data upon which the results of this report have been based do not cover all flight conditions of interest. The working charts which are given here have been constructed with this fact in mind, and indicate the range of test conditions. It is possible to select flight conditions that lead to unacceptable answers, such as $d_1 > X_{HL}$ or $d_1 < \ell_{fi}$, and the design engineer must be prepared to exercise some discretion in using these correlations (e.g. Sample Calculation Example 2, Appendix II).

Practical reentry vehicles will exhibit some geometrical features that were not reflected in the test models. For example, surfaces are likely to be highly swept as well as blunted, and sections normal to the stream direction may show a steady taper in thickness from the center to the edges. Such a shaping will tend to introduce a decisively three-dimensional character to the flow. Figure 84 shows such a configuration at an expansion angle of attack. It is seen that the flow is deflected in toward the centerline, away from the higher pressure edges. Also, streamlines are deflected about either side of the rather low aspect ratio flaps.

High speed vehicles are generally analyzed on a piecewise basis, and this viewpoint should be no less acceptable in interaction problems. Conditions upstream of the interaction region should be calculated as well as possible using standard methods. The correlations in this report may then be applied. Exact streamline direction is less important than static pressure and Mach number. There can be substantial reductions in flap effectiveness due to finite span, however.

SPECIAL PROBLEMS

Transition within the Interaction Region

In some problems, calculated transition distance will be such as to indicate that the boundary layer at the beginning of the interaction may be either laminar or turbulent. Transition may occur within the separated region. In such cases local pressure peaks may appear. The integrated pressure is what

is of interest, although it is not possible to say beforehand whether the laminar or the turbulent assumption is more conservative (that is, leading to a smaller integrated force increment). The turbulent assumption leads to higher local peak rates of heat transfer.

Real Gas Effects

An experimental facility which produces the desired Mach number and Reynolds number for a test model will generally fail to produce the ratio of real gas relaxation distance to characteristic body distance encountered by the real vehicle. Establishing of scaling laws accounting for these differences is beyond the scope of this program. The local outer flow properties should be obtained from ideal or real gas relations according to Section III.

Section IX

CONCLUSIONS

Semi-empirical correlations describing pressure distribution and heat transfer in laminar and turbulent corner flow have been developed. These correlations are based on presently available experimental results covering a limited range of test conditions. They are used for approximating the pressure distribution in the separated region and for calculating the effect of flow separation on aerodynamic coefficients. The developed prediction methods are applicable to regions were the assumption of two-dimensional flow is valid. In order to apply these methods to complex three-dimensional configurations, the degree of deviation from two-dimensional flow should be established and the proper method of determining the local flow properties selected. At some sector of the flight spectrum the vehicle will encounter real gas effects which were absent in the test flows. These effects, which undoubtedly will show up in the separated region, were not included in the available experimental data. It is suggested however to use real gas flow properties in regimes where the real gas effects become significant.

The primary emphasis during the development of these correlating expressions has been placed on providing the aerodynamic designer with a useful design tool for predicting the aerodynamic control characteristics of aircraft and reentry vehicles operating at hypersonic speeds. This method permits the designer to determine the presence, magnitude, and extent of flow separation and the pressure distributions induced by deflected control surfaces. A pressure distribution model, based on experimental observation, is employed for determining force and moment coefficients. Sample calculations are included for instructive purposes.

There is some error involved in the experimental measurements which were evaluated and additional error is introduced due to correlating procedure. Extrapolation of the prediction expressions outside the range of test conditions is feasible but should be accomplished with caution.

Appendix I

INCREMENTAL FORCE AND MOMENT EQUATIONS

The following is a derivation of the equations for the two-dimensional force and moment increments produced by separated compression corner flow. The idealized pressure distribution, coordinate axes system, and force and moment convention used in the derivation are defined in Figure 129.

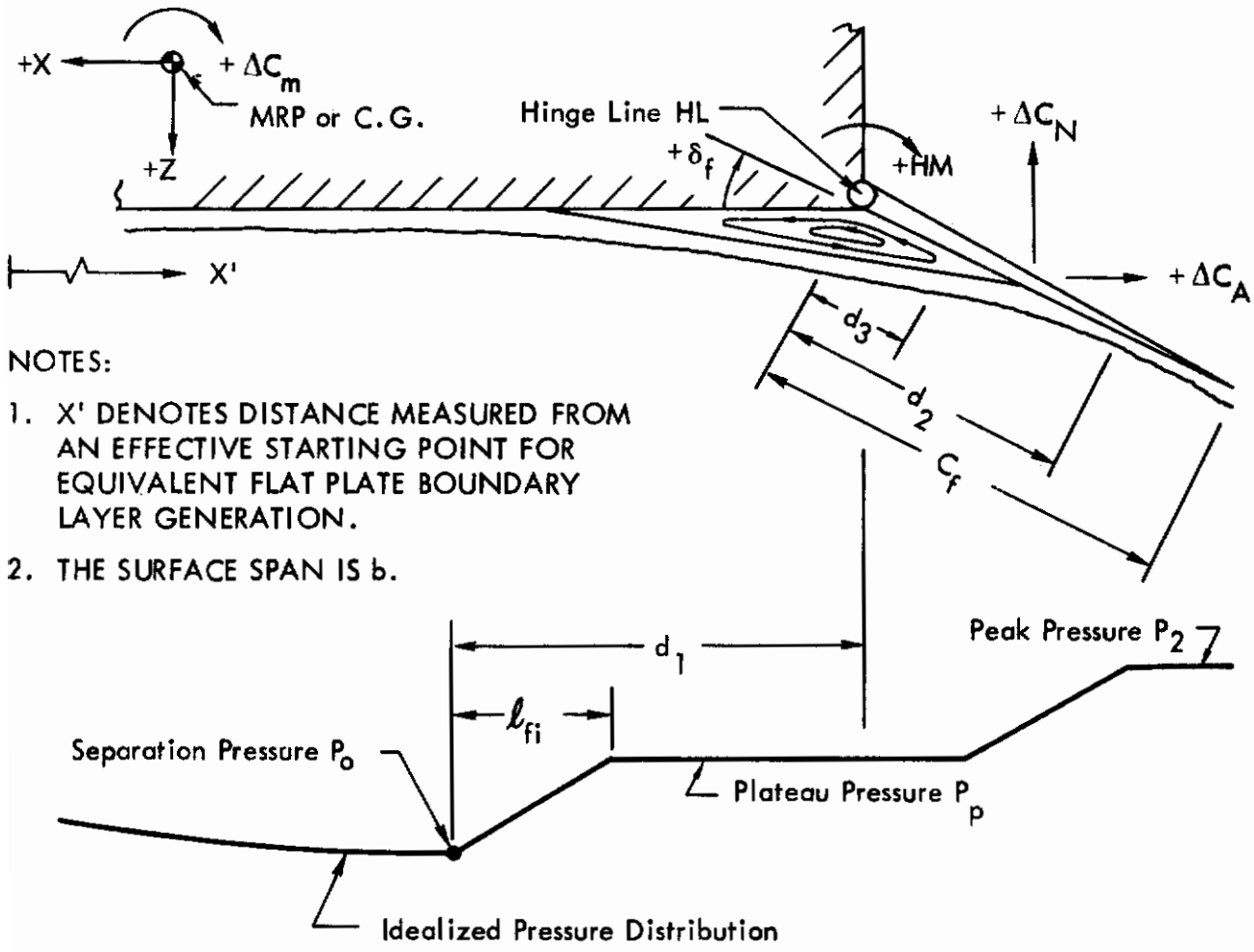

Figure 129. Two-Dimensional Flow Model and Body Axes System

1. Normal force increment:

$$\frac{\Delta N_w}{b} = (P_p - P_o)\frac{\ell_{fi}}{2} + (P_p - P_o)(d_1 - \ell_{fi})$$

$$+ (\cos \delta_f)\left[(P_p - P_o)C_f + (P_2 - P_p)\frac{d_2 - d_3}{2} + (P_2 - P_p)(C_f - d_2)\right]$$

$$\frac{\Delta N_w}{b} = (P_p - P_o)\left[d_1 - \frac{\ell_{fi}}{2} + (\cos \delta_f)\, C_f\right]$$

$$+ (P_2 - P_p)(\cos \delta_f)\left(C_f - \frac{d_2}{2} - \frac{d_3}{2}\right).$$

$$\Delta N \equiv \Delta C_N qS \text{ and } C_{p_\infty} \equiv \frac{P - P_\infty}{q_\infty}.$$

Therefore,

$$\left.\frac{\Delta C_N S}{b}\right]_w = \left[(C_{p\infty})_p - (C_{p\infty})_o\right]\left[d_1 - \frac{\ell_{fi}}{2} + (\cos \delta_f)\, C_f\right]$$

$$+ \left[(C_{p\infty})_2 - (C_{p\infty})_p\right](\cos \delta_f)\left[C_f - \frac{d_2}{2} - \frac{d_3}{2}\right]$$

2. Pitching moment increment about HL due to normal force increment:

$$\left.\frac{\Delta M_{HL}}{b}\right]_{\Delta N_w} = (P_p - P_o)\frac{\ell_{fi}}{2}\left(d_1 - \frac{2\ell_{fi}}{3}\right) + (P_p - P_o)(d_1 - \ell_{fi})\left(\frac{d_1 - \ell_{fi}}{2}\right)$$

$$- (P_p - P_o)C_f \cos \delta_f \frac{C_f}{2} \cos \delta_f - (P_2 - P_p)\left(\frac{d_2 - d_3}{2}\right) \cos \delta_f \left(\frac{d_3}{3} + \frac{2d_2}{3}\right) \cos \delta_f$$

$$- (P_2 - P_p)(C_f - d_2) \cos \delta_f \left(\frac{C_f}{2} + \frac{d_2}{2}\right) \cos \delta_f$$

$$\frac{\Delta M_{HL}\Big]_{\Delta N_w}}{b} = (P_p-P_o)\left(\frac{\ell_{fi}d_1}{2} - \frac{\ell_{fi}^2}{3}\right) + (P_p-P_o)\left(\frac{d_1^2}{2} - \ell_{fi}d_1 + \frac{\ell_{fi}^2}{2}\right)$$

$$- (\cos^2\delta_f)\left[(P_p-P_o)\frac{C_f}{2} + (P_2-P_p)\left(\frac{d_2^2}{3} - \frac{d_2d_3}{6} - \frac{d_3^2}{6}\right) + (P_2-P_p)\left(\frac{C_f^2}{2} - \frac{d_2^2}{2}\right)\right]$$

$$= (P_p-P_o)\left(\frac{\ell_{fi}^2}{6} - \frac{\ell_{fi}d_1}{2} + \frac{d_1^2}{2} - \frac{(\cos^2\delta_f)C_f^2}{2}\right)$$

$$- (P_2-P_p)(\cos^2\delta_f)\left(\frac{C_f^2}{2} - \frac{d_2^2}{6} - \frac{d_2d_3}{6} - \frac{d_3^2}{6}\right)$$

$$\Delta M \equiv \Delta C_m q\, SL$$

$$\frac{\Delta C_{m_{HL}} SL\Big]_{\Delta N_w}}{b} = \left[(C_{p_\infty})_p - (C_{p_\infty})_o\right]\left[\frac{\ell_{fi}^2}{6} - \frac{\ell_{fi}d_1}{2} + \frac{d_1^2}{2} - \frac{(\cos^2\delta_f)C_f^2}{2}\right]$$

$$\left[(C_{p_\infty})_2 - (C_{p_\infty})_p\right](\cos^2\delta_f)\left[\frac{C_f^2}{2} - \frac{d_2^2}{6} - \frac{d_2d_3}{6} - \frac{d_3^2}{6}\right]$$

3. Center of pressure of normal force increment:

$$\Delta C_{m_{HL}} L\Big]_{\Delta N_w} = \Delta C_{N_w}\left(X_{cp_{\Delta N_w}} - X_{HL}\right)$$

$$X_{cp\,\Delta N_w} = X_{HL} + \frac{\Delta C_{m_{HL}} L\Big]_{\Delta N_w}}{\Delta C_{N_w}}$$

4. Axial force increment:

$$\frac{\Delta A_w}{b} = (P_p-P_o)\,C_f \sin\delta_f + (P_2-P_p)\left(\frac{d_2-d_3}{2}\right)\sin\delta_f + (P_2-P_p)(C_f-d_2)\sin\delta_f$$

$$\frac{\Delta A_w}{b} = (\sin\delta_f)\left[(P_p-P_o)\,C_f + (P_2-P_p)\left(C_f - \frac{d_2}{2} - \frac{d_3}{2}\right)\right]$$

$$\frac{\Delta C_A\, S\big]_w}{b} = (\sin\delta_f)\left[\left[(C_{p_\infty})_p-(C_{p_\infty})_o\right]C_f + \left[(C_{p_\infty})_2-(C_{p_\infty})_p\right]\left(C_f - \frac{d_2}{2} - \frac{d_3}{2}\right)\right]$$

5. Pitching moment increment about HL due to axial force increment:

$$\frac{\Delta M_{HL}\big]_{\Delta A_w}}{b} = -(P_p-P_o)\,C_f\left(\sin\delta_f\right)\frac{C_f}{2}\sin\delta_f - (P_2-P_p)\left(\frac{d_2-d_3}{2}\right)\left(\sin\delta_f\right)$$

$$\left(\frac{2d_2}{3} + \frac{d_3}{3}\right)\left(\sin\delta_f\right) - (P_2-P_p)(C_f-d_2)\left(\sin\delta_f\right)\left(\frac{C_f}{2} + \frac{d_2}{2}\right)\sin\delta_f$$

$$= -(\sin^2\delta_f)\left[(P_p-P_o)\,\frac{C_f^2}{2} + (P_2-P_p)\left(\frac{d_2^2}{3} - \frac{d_2d_3}{6} - \frac{d_3^2}{6}\right)\right.$$

$$\left. + (P_2-P_p)\left(\frac{C_f^2}{2} - \frac{d_2^2}{2}\right)\right]$$

$$= -(\sin^2\delta_f)\left[(P_p-P_o)\,\frac{C_f^2}{2} + (P_2-P_p)\left(\frac{C_f^2}{2} - \frac{d_2^2}{6} - \frac{d_2d_3}{6} - \frac{d_3^2}{6}\right)\right]$$

$$\frac{\Delta C_{m_{HL}}\, SL\big]_{\Delta A_w}}{b} = -(\sin^2\delta_f)\left[\left[(C_{p_\infty})_p-(C_{p_\infty})_o\right]\frac{C_f^2}{2} + \left[(C_{p_\infty})_2-(C_{p_\infty})_p\right]\right.$$

$$\left.\left(\frac{C_f^2}{2} - \frac{d_2^2}{6} - \frac{d_2d_3}{6} - \frac{d_3^2}{6}\right)\right]$$

6. Center of pressure of axial force increment:

$$\Delta C_{m_{HL}} L\Big]_{\Delta A_w} = - \Delta C_{A_w} \left(Z_{cp_{\Delta A_w}} - Z_{HL} \right)$$

$$Z_{cp_{\Delta A_w}} = Z_{HL} - \frac{\Delta C_{m_{HL}} L\Big]_{\Delta A_w}}{\Delta C_{A_w}}$$

7. Total increment of pitching moment about MRP:

$$\Delta C_{m_{MRP}} L\Big]_w = \Delta C_{N_w} X_{cp_{\Delta N_w}} - \Delta C_{A_w} Z_{cp_{\Delta A_w}}$$

8. Windward component of elevon hinge moment:

$$HM_w = -P_p C_f \frac{C_f}{2} - (P_2 - P_p) \left(\frac{d_2 - d_3}{2} \right) \left(\frac{2d_2}{3} + \frac{d_3}{3} \right)$$

$$- (P_2 - P_p) (C_f - d_2) \left(\frac{C_f}{2} + \frac{d_2}{2} \right)$$

$$= - \left[P_p \frac{C_f^2}{2} + (P_2 - P_p) \left(\frac{d_2^2}{3} - \frac{d_2 d_3}{6} - \frac{d_3^2}{6} + \frac{C_f^2}{2} - \frac{d_2^2}{2} \right) \right]$$

$$= - \left[P_p \frac{C_f^2}{2} + P_2 \frac{C_f^2}{2} - P_p \frac{C_f^2}{2} - (P_2 - P_p) \left(\frac{d_2^2}{6} + \frac{d_2 d_3}{6} + \frac{d_3^2}{6} \right) \right]$$

$$\frac{HM_w}{qb} = - \left[(C_{p_\infty})_2 \frac{C_f^2}{2} - \frac{1}{6} \left[(C_{p_\infty})_2 - (C_{p_\infty})_p \right] (d_2^2 + d_2 d_3 + d_3^2) \right]$$

Appendix II

SAMPLE CALCULATIONS

The solutions to two sample problems are worked out in detail to illustrate the procedure for calculating control effectiveness which is developed in Section 6. A simple hinged, flat-plate configuration is analyzed for separate flight conditions. Example 1 is a straightforward problem for which the method is directly applicable. It is shown in Example 2 that for certain flight conditions the separated region extends forward to the leading edge of the configuration. For this case a modification of the method is suggested which provides a solution.

Example 1.

Given:

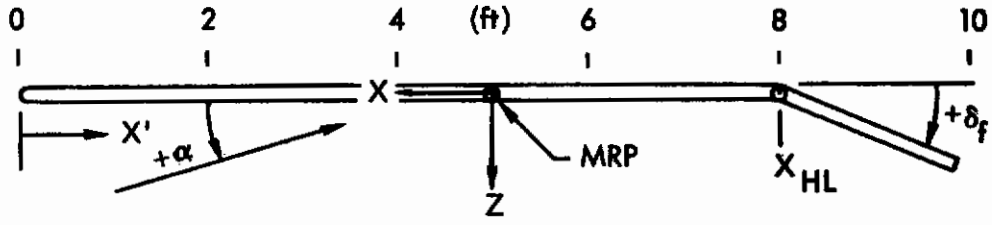

Configuration: Two-dimensional flat plate with negligible thickness. Span is b ft

M_∞ = 10

Altitude = 150,000 ft

$Re_\infty/_{ft}$ = 1.06×10^5

P_∞ = 2.84 psf

T_∞ = 479°R

α = 15 deg.

T_{wall} = 1500°R

Problem: Calculate the incremental normal force and pitching moment coefficients produced on the windward surface by a positive flap deflection of ten degrees. ($\delta_f = +10°$). Assume negligible viscous interaction.

Step 1. Determine the local flow conditions.

$$\frac{P_\alpha}{P_\infty} = 13.5 \qquad \text{(Figure 96c)}$$

$$(C_{p_\infty})_\alpha = \frac{P_\alpha / P_\infty - 1}{\frac{\gamma}{2} M_\infty^2} = 0.179$$

$$\frac{T_\alpha}{T_\infty} = 3.0 \qquad \text{(Figure 97c)}$$

$$T_\alpha = 1440\ °R$$

$$M_\alpha = 5.5 \qquad \text{(Figure 98c)}$$

$$\frac{Re_\alpha}{Re_\infty} = 1.94 \qquad \text{(Figure 99c)}$$

$$\frac{Re_\alpha}{ft} = 2.06 \times 10^5$$

Step 2. Verify the existence or non-existence of separated flow.

$$(C_{p_\alpha})_{2_{\text{inviscid}}} = 0.11 \text{ (Oblique shock compression)}$$

$$Re_{\alpha_{HL}} = 8\,(2.06 \times 10^5) = 1.65 \times 10^6$$

For simplicity, assume Re_α transition $= 2 \times 10^6$ (For a discussion of transition Reynolds number, see Section 4.1)

$$C_{p_{\alpha\ \text{incipient}}} = 0.020 \qquad \text{(Figure 104)}$$

Therefore, since $(C_{p_\alpha})_2 > C_{p_{\alpha\ \text{incipient}}}$, separation does exist.

Step 3. Determine where the flow separates.

For the 1st iteration, assume $X_o' = 7$ ft

$$R_{e_{\alpha_{X_o'_1}}} = 7\ (2.06 \times 10^5) = 1.44 \times 10^6$$

$$(C_{p_\alpha})_{p_1} = 0.0185 \qquad \text{(Figure 106)}$$

$$\left(\frac{d_1}{\delta_o}\right)_1 = 20 \qquad \text{(Figure 108)}$$

$$\frac{T_{wall}}{T_\alpha} \approx 1$$

$$\frac{Re^*_\alpha}{Re_\alpha} = 0.28 \qquad \text{(Figures 100 \& 101)}$$

$$\frac{Re^*_\alpha}{ft} = 5.77 \times 10^4$$

$$\frac{\delta}{\sqrt{X'}} = 0.0215 \qquad \text{(Figure 102)}$$

$$\delta_{o_1} = 0.057 \text{ ft}$$

$$(d_1)_1 = 1.14 \text{ ft}$$

$$X'_{o_1} + (d_1)_1 = 8.14 \text{ ft} > X'_{HL}$$

Assume $X'_o = 6.5$ ft for 2nd iteration.

$$Re_{\alpha_{X'_{o_2}}} = 1.34 \times 10^6$$

$$(C_{p_\alpha})_{p_2} = 0.019$$

$$\left(\frac{d_1}{\delta_o}\right)_2 = 21.5$$

$$\delta_{o_2} = 0.055 \text{ ft}$$

$$(d_1)_2 = 1.18 \text{ ft}$$

$$X'_{o_2} + (d_1)_2 = 7.68 \text{ ft} < X'_{HL}$$

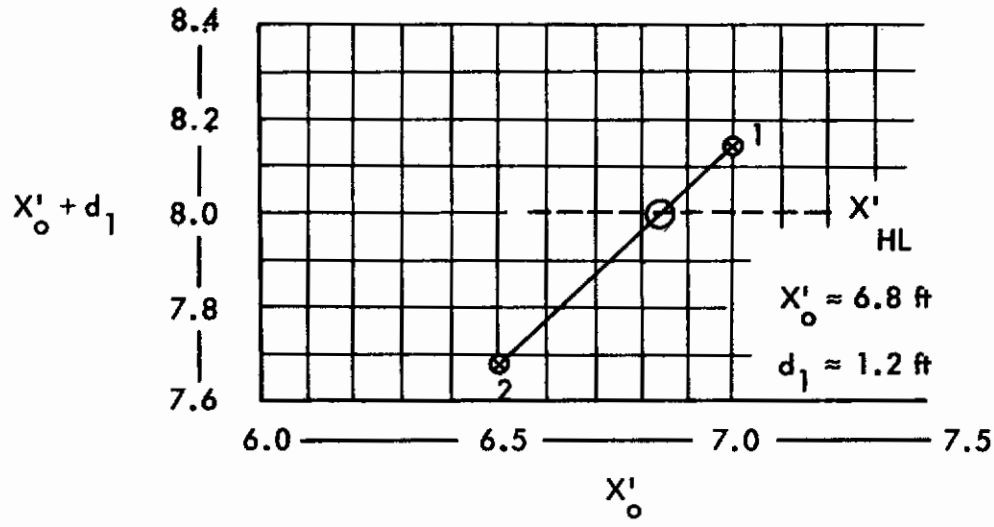

Step 4. Calculate the windward pressure distribution.

$Re_{\alpha_{X'_o}} = 1.4 \times 10^6$

$(C_{p_\alpha})_p \approx 0.019$

$$(C_{p_\infty})_p = (C_{p_\alpha})_p \left(\frac{M_\alpha}{M_\infty}\right)^2 \frac{P_\alpha}{P_\infty} + (C_{p_\infty})_\alpha$$

$= 0.257$

$\frac{\ell_{fi}}{\delta_o} = 8$ (Figure 110)

$\delta_o = 0.056$ ft

$\ell_{fi} = 0.45$ ft

$\frac{c_f}{d_1} = 1.67$

Since $\frac{c_f}{d_1} > 1$,

$\frac{d_2}{\sqrt{c_f d_1}} = \frac{d_2}{d_1} = 0.506$ (Figure 112)

$d_2 = 0.61$ ft

Equivalent flow deflection angle for $(C_{p\alpha})_p$ = 0.019:

ϕ = 2.6 deg (obtained from oblique shock relations)

$\frac{d_3}{d_1}$ = 0.35 (Figure 114)

d_3 = 0.42 ft

$(C_{p\alpha})_{2_{inviscid}}$ = 0.11 (oblique shock compression)

$(C_{p\alpha})_{2_{inviscid}}$ = 0.114 (compressing isentropically)

Since $\delta_f < 15°$, use the isentropic value. (See Section IV)

$$(C_{p\infty})_2 = (C_{p\alpha})_2 \left(\frac{M_\alpha}{M_\infty}\right)^2 \frac{P_\alpha}{P_\infty} + (C_{p\infty})_\alpha$$

$$= 0.644$$

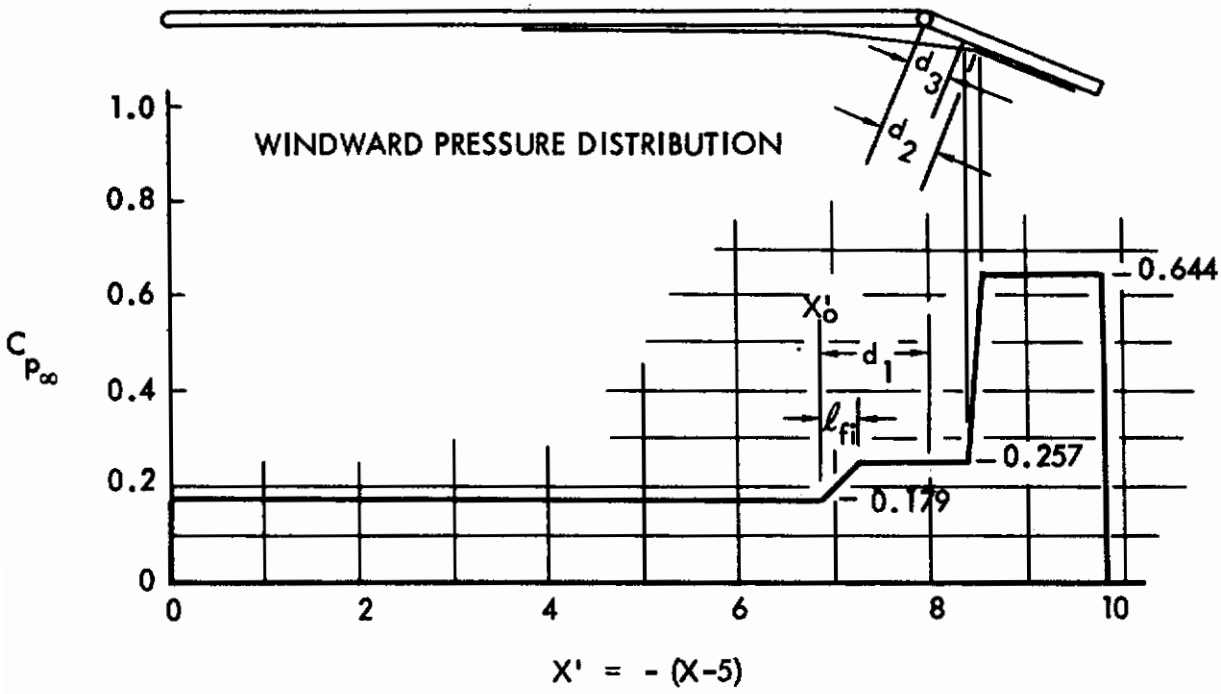

Step 5. Evaluate the incremental forces and moments.

1. Normal force increment:

$$\frac{\Delta C_N S}{b}\Big|_w = \left[(C_{p\infty})_p - (C_{p\infty})_\alpha\right]\left[d_1 - \frac{\ell_{fi}}{2} + \cos\delta_f\, C_f\right]$$

$$+ \left[(C_{p\infty})_2 - (C_{p\infty})_p\right](\cos\delta_f)\left[C_f - \frac{d_2}{2} - \frac{d_3}{2}\right]$$

$$\frac{\Delta C_N S\big]_w}{b} = \left[0.257 - 0.179\right]\left[1.2 - \frac{0.45}{2} + 0.985(2)\right]$$

$$+ \left[0.644 - 0.257\right](0.985)\left[2 - \frac{0.61}{2} - \frac{0.42}{2}\right]$$

$$= 0.796 \text{ ft}$$

2. Increment of pitching moment about HL due to normal force increment:

$$\frac{\Delta C_{m_{HL}} SL\big]_{\Delta N_w}}{b} = \left[(C_{p\infty})_p - (C_{p\infty})_\alpha\right]\left[\frac{\ell_{fi}^2}{6} - \frac{\ell_{fi} d_1}{2} + \frac{d_1^2}{2} - \frac{\cos^2\delta_f C_f^2}{2}\right]$$

$$- \left[(C_{p\infty})_2 - (C_{p\infty})_p\right](\cos^2\delta_f)\left[\frac{C_f^2}{2} - \frac{d_2^2}{6} - \frac{d_2 d_3}{6} - \frac{d_3^2}{6}\right]$$

$$= \left[0.257 - 0.179\right]\left[\frac{(0.45)^2}{6} - \frac{(0.45)(1.2)}{2} + \frac{(1.2)^2}{2} - \frac{(0.985)^2(2)^2}{2}\right]$$

$$- \left[0.644 - 0.257\right]\ (0.985)^2\left[\frac{(2)^2}{2} - \frac{(0.61)^2}{6} - \frac{(0.61)(0.42)}{6}\right.$$

$$\left. - \frac{(0.42)^2}{6}\right] = -0.813 \text{ ft}^2$$

3. Center of pressure of normal force increment:

$$X_{cp_{\Delta N_w}} = X_{HL} + \frac{\Delta C_{m_{HL}} L\big]_{\Delta N_w}}{\Delta C_{N_w}} = -3 + \frac{-0.813}{0.796}$$

$$= -4.02 \text{ ft}$$

4. Axial force increment:

$$\frac{\Delta C_A S\big]_w}{b} = (\sin\delta_f)\left\{\left[(C_{p_\infty})_p - (C_{p_\infty})_\alpha\right] C_f + \left[(C_{p_\infty})_2 - (C_{p_\infty})_p\right]\left[C_f - \frac{d_2}{2} - \frac{d_3}{2}\right]\right\}$$

$$= (0.174)\left\{\left[0.257 - 0.179\right] 2 + \left[0.644 - 0.257\right]\left[2 - \frac{0.61}{2} - \frac{0.42}{2}\right]\right\}$$

$$= 0.127 \text{ ft}$$

5. Increment of pitching moment about HL due to axial force increment:

$$\frac{\Delta C_{m_{HL}}^{SL}\Big]_{\Delta A_w}}{b} = -(\sin^2\delta_f)\left\{\left[(C_{p_\infty})_p-(C_{p_\infty})_\alpha\right]\frac{C_f^2}{2}+\left[(C_{p_\infty})_2-(C_{p_\infty})_p\right]\left[\frac{C_f^2}{2}-\frac{d_2^2}{6}-\frac{d_2d_3}{6}-\frac{d_3^2}{6}\right]\right\}$$

$$= -(0.174)^2\left\{\left[0.257-0.179\right]\frac{(2)^2}{2}+\left[0.644-0.257\right]\left[\frac{(2)^2}{2}-\frac{(0.61)^2}{6}-\frac{(0.61)(0.42)}{6}-\frac{(0.42)^2}{6}\right]\right\}$$

$$= -0.026 \text{ ft}^2$$

6. Center of pressure of axial force increment:

$$Z_{cp} = Z_{HL} - \frac{\Delta C_{m_{HL}}^{L}\Big]_{\Delta A_w}}{\Delta C_{A_w}} = 0 - \frac{-0.026}{0.127}$$

$$= 0.204 \text{ ft}$$

7. Increment of pitching moment about MRP:

$$\frac{\Delta C_{m_{MRP}}^{SL}\Big]_w}{b} = \frac{\Delta C_N S\Big]_w}{b} X_{cp_{\Delta N_w}} - \frac{\Delta C_A S\Big]_w}{b} Z_{cp_{\Delta A_w}} = 0.796\ (-4.02)$$

$$- 0.127\ (0.0204) = -3.23 \text{ ft}^2$$

8. Windward component of elevon hinge moment:

$$\frac{HM}{bq}\Big]_w = -\left\{(C_{p_\infty})_2\frac{C_f^2}{2}-\frac{1}{6}\left[(C_{p_\infty})_2-(C_{p_\infty})_p\right](d_2^2+d_2d_3+d_3^2)\right\}$$

$$= -\left\{0.644\frac{(2)^2}{2}-\frac{1}{6}\left[0.644-0.257\right]\left[(0.61)^2+(0.61)(0.42)+(0.42)^2\right]\right\}$$

$$= -1.24 \text{ ft}^2$$

Example 2.

Given:

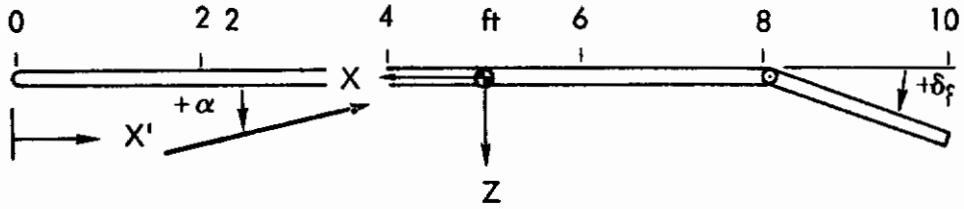

Configuration: Two-dimensional flat plate with negligible thickness.

$M_\infty = 20$

Altitude = 200,000 ft

$Re_{\infty/ft} = 3.27 \times 10^4$

$p_\infty = 4.13 \times 10^{-1}$ psf

$T_\infty = 457\ ^\circ R$

$\alpha = 10$ deg.

$T_{wall} = 2000\ ^\circ R$

Problem: Calculate the incremental force and pitching moment coefficients produced on the windward surface by a positive flap deflection of ten degrees ($\delta_f = +10^\circ$). Assume negligible viscous interaction.

Step 1. Determine the local flow conditions.

$$\frac{P_\alpha}{P_\infty} = 21 \qquad \text{(Figure 96d)}$$

$$(C_{p_\infty})_\alpha = \frac{\frac{P_\alpha}{P_\infty} - 1}{\frac{\gamma}{2} M_\infty^2} = 0.071$$

$$\frac{T_\alpha}{T_\infty} = 4.3 \qquad \text{(Figure 97d)}$$

$T_\alpha = 1970\ ^\circ R$

$M_\alpha = 9.8$ (Figure 98d)

$$\frac{Re_\alpha}{Re_\infty} = 1.87 \qquad \text{(Figure 99d)}$$

$$\frac{Re_\alpha}{ft} = 6.11 \times 10^4$$

Step 2. Verify the existence or non-existence of separated flow.

$$(C_{p_\alpha})_2 = 0.087 \text{ (Oblique shock compression)}$$

$$Re_{\alpha_{HL}} = 8\ (6.11 \times 10^4) = 4.9 \times 10^5$$

Therefore the flow is laminar. (See Figure 24)

$$C_{p_\alpha}{}_{\text{incipient}} = 0.019 \qquad \text{(Figure 104)}$$

Therefore, since $(C_{p\alpha})_2 > C_{p_{\alpha_{\text{incipient}}}}$, separation does exist.

Step 3. Determine where the flow separates.

For 1st iteration, assume $X'_o = 7$ ft

$$Re_{\alpha_{X'_{o_1}}} = 7\ (6.11 \times 10^4) = 4.28 \times 10^5$$

$$(C_{p_\alpha})_{p_1} \approx 0.020 \qquad \text{(Figure 106)}$$

$$\left(\frac{d_1}{\delta_o}\right)_1 = 140 \qquad \text{(Figure 108)}$$

$$\frac{T_{wall}}{T_\alpha} \approx 1$$

$$\frac{Re^*_\alpha}{Re_\alpha} = 0.079 \qquad \text{(Figures 100 and 101)}$$

$$\frac{Re^*_\alpha}{ft} = 4.83 \times 10^3$$

$$\frac{\delta}{\sqrt{X'}} = 0.075 \qquad \text{(Figure 103)}$$

$$\delta_{o_1} = 0.199 \text{ ft}$$

$$(d_1)_1 = 27.9 \text{ ft}$$

$$X'_{o_1} + (d_1)_1 = 34.9 > X_{HL}$$

Assume X'_o = 4 ft for 2nd iteration

$Re_{\alpha X'_{o_2}} = 4\ (6.11 \times 10^4) = 2.45 \times 10^5$

$(C_{p_\alpha})_{p_2} = 0.023$

$\left(\frac{d_1}{\delta_o}\right)_2 = 230$

$\delta_{o_2} = 0.15$

$(d_1)_2 = 34.5$

$X'_{o_2} + (d_1)_2 = 38.5 > X_{HL}$

Assume X'_o = 2 ft for 3rd iteration

$Re_{\alpha X'_{o_3}} = 2\ (6.11 \times 10^4) = 1.22 \times 10^5$

$(C_{p_\alpha})_{p_3} = 0.027$

$\left(\frac{d_1}{\delta_o}\right)_3 = 400$

$\delta_{o_3} = 0.106$

$(d_1)_3 = 42.4$

$X'_{o_3} + (d_1)_3 = 44.4 > X_{HL}$

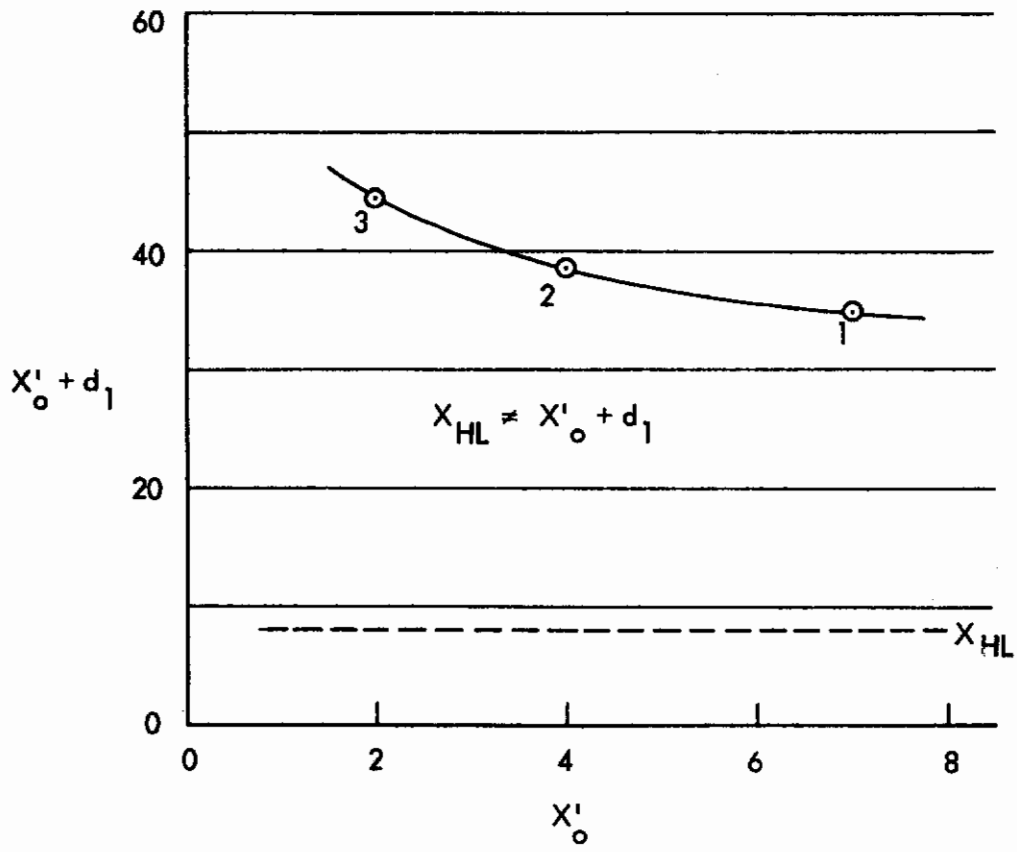

The magnitude of d_1 indicates that realistically the region of separation extends forward to the leading edge of the plate. For this case, an alternate approach can be used which is based on the assumption that the plateau pressure region extends forward to the leading edge; i.e., $d_1 = X'_{HL}$ and $\ell_{fi} = 0$.

Step 4. Alternate method for calculating pressure distribution.

Let $d_1 = X'_{HL} = 8$ ft

$$\frac{C_f}{d_1} = \frac{2}{8} = 0.25$$

For $\frac{C_f}{d_1} \leq 0.25$

$$2\ \frac{d_2}{d_1} = 0.475 \qquad \text{(Figure 112)}$$

$$d_2 = 1.9$$

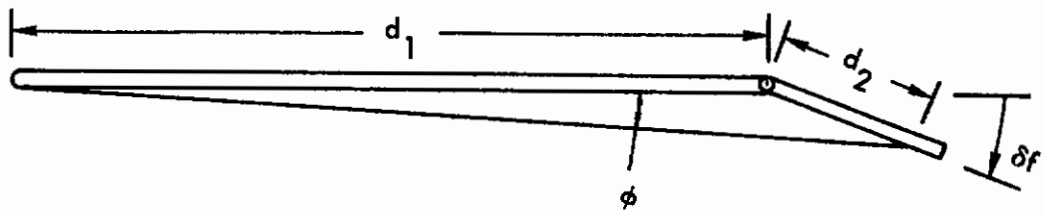

$$\phi = \tan^{-1} \frac{d_2 \sin \delta_f}{d_1 + d_2 \cos \delta_f}$$

$$= \tan^{-1} \frac{1.9 \sin 10^\circ}{8 + 1.9 \cos 10^\circ}$$

$$= \tan^{-1} 0.0335$$

$$\approx 2^\circ$$

Assuming the plateau pressure corresponds to wedge pressure for a local flow deflection angle of ϕ degrees,

$$(C_{p\alpha})_p = 0.0086 \text{ (Obtained from oblique shock relations)}$$

$$(C_{p\infty})_p = (C_{p\alpha})_p \left(\frac{M_\alpha}{M_\infty}\right)^2 \frac{P_\alpha}{P_\infty} + (C_{p\infty})_\alpha$$

$$= 0.0086 \left(\frac{9.8}{20}\right)^2 21 + 0.071$$

$$= 0.114$$

Let $\ell_{fi} = 0$

$$\frac{d_3}{d_1} = 0.25 \qquad \text{(Figure 114)}$$

$$d_3 = 2 \text{ ft}$$

However, since d_3 must be less than or equal to d_2, let

$$d_3 = d_2 = 1.9 \text{ ft}$$

$$(C_{p\alpha})_2 = 0.087 \text{ (Oblique shock compression)}$$

$$(C_{p\infty})_2 = (C_{p\alpha})_2 \left(\frac{M_\alpha}{M_\infty}\right)^2 \frac{P_\alpha}{P_\infty} + (C_{p\infty})_\alpha$$

$$= 0.087 \left(\frac{9.8}{20}\right)^2 21 + 0.071$$

$$= 0.51$$

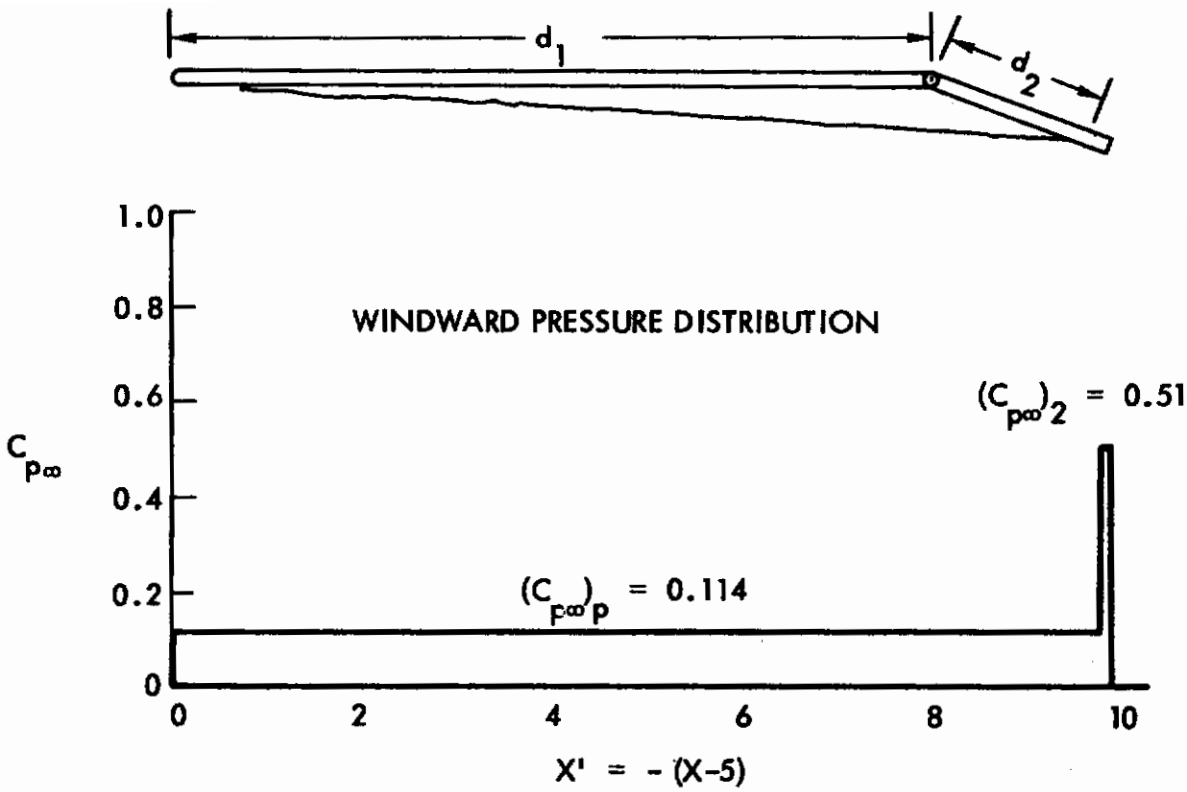

Step 5. Evaluate the incremental forces and moments.

1. Normal force increment:

$$\frac{\Delta C_N S}{b}\Big]_w = \left[(C_{p\infty})_p-(C_{p\infty})_\alpha\right]\left[d_1 - \frac{\ell_{fi}}{2} + \cos\delta_f\, C_f\right]$$

$$+ \left[(C_{p\infty})_2-(C_{p\infty})_p\right](\cos\delta_f)\left[C_f - \frac{d_2}{2} - \frac{d_3}{2}\right]$$

$$= \left[0.114 - 0.071\right]\left[8 + \cos 10^\circ\ (2)\right]$$

$$+ \left[0.510 - 0.114\right]\ (\cos 10^\circ)\left[2 - \frac{1.9}{2} - \frac{1.9}{2}\right]$$

$$= 0.468 \text{ ft}$$

2. Increment of pitching moment about HL due to normal force increment:

$$\frac{\Delta C_{m_{HL}}^{SL}\Big]_{\Delta N_w}}{b} = \left[(C_{p_\infty})_p-(C_{p_\infty})_\alpha\right]\left[\frac{\ell_{fi}^2}{6} - \frac{\ell_{fi}d_1}{2} + \frac{d_1^2}{2} - \frac{\cos^2\delta_f\, C_f^2}{2}\right]$$

$$- \left[(C_{p_\infty})_2-(C_{p_\infty})_p\right](\cos^2\delta_f)\left[\frac{C_f^2}{2} - \frac{d_2^2}{6} - \frac{d_2d_3}{6} - \frac{d_3^2}{6}\right]$$

$$= \left[0.114 - 0.071\right]\left[\frac{(8)^2}{2} - \frac{\cos^2 10^\circ\,(2)^2}{2}\right]$$

$$- \left[0.510 - 0.114\right](\cos^2 10^\circ)\left[\frac{(2)^2}{2} - \frac{(1.9)^2}{6} - \frac{(1.9)^2}{6} - \frac{(1.9)^2}{6}\right]$$

$$= 1.215 \text{ ft}^2$$

3. Center of pressure of normal force increment:

$$X_{cp_{\Delta N_w}} = X_{HL} + \frac{\Delta C_{m_{HL}}^{L}\Big]_{\Delta N_w}}{\Delta C_{N_w}}$$

$$= -3 + \frac{1.215}{0.468}$$

$$= -0.4 \text{ ft}$$

4. Axial force increment:

$$\frac{\Delta C_A^S\Big]_w}{b} = (\sin\delta_f)\left\{\left[(C_{p_\infty})_p-(C_{p_\infty})_\alpha\right]C_f + \left[(C_{p_\infty})_2-(C_{p_\infty})_p\right]\left[C_f - \frac{d_2}{2} - \frac{d_3}{2}\right]\right\}$$

$$= (0.174)\left\{\left|0.114 - 0.071\right|\,2 + \left|0.510 - 0.114\right|\left[2 - \frac{1.9}{2} - \frac{1.9}{2}\right]\right\}$$

$$= 0.022 \text{ ft}$$

5. Increment of pitching moment about HL due to axial force increment:

$$\frac{\Delta C_{m_{HL}}^{SL}\Big]\Delta A_w}{b} = -\left(\sin^2\delta_f\right)\left\{\left[(C_{p_\infty})_p-(C_{p_\infty})_\alpha\right]\frac{C_f^2}{2} + \left[(C_{p_\infty})_2-(C_{p_\infty})_p\right]\left[\frac{C_f^2}{2} - \frac{d_2^2}{6} - \frac{d_2d_3}{6} - \frac{d_3^2}{6}\right]\right\}$$

$$= -(0.174)^2\left\{\left[0.114-0.071\right]\frac{(2)^2}{2} + \left[0.510-0.114\right]\left[\frac{(2)^2}{2} - \frac{(1.9)^2}{6} - \frac{(1.9)^2}{6} - \frac{(1.9)^2}{6}\right]\right\}$$

$$= -0.005 \text{ ft}^2$$

6. Center of pressure of axial force increment:

$$Z_{cp_{\Delta A_w}} = Z_{HL} - \frac{\Delta C_{m_{HL}}^{L}\Big]_{\Delta A_w}}{\Delta C_{A_w}}$$

$$= 0 - \frac{-0.005}{0.022}$$

$$= 0.23 \text{ ft}$$

7. Increment of pitching moment about MRP:

$$\frac{\Delta C_{m_{MRP}}^{SL}\Big]_w}{b} = \frac{\Delta C_N S\Big]_w}{b} X_{cp_{\Delta N_w}} \quad \frac{\Delta C_A S\Big]_w}{b} Z_{cp_{\Delta A_w}}$$

$$= 0.468\ (-0.4) - 0.022\ (0.23)$$

$$= -0.192 \text{ ft}^2$$

8. Windward component of elevon hinge moment:

$$\frac{HM\Big]_w}{bq} = -\left\{(C_{p_\infty})_2\frac{C_f^2}{2} - \frac{1}{6}\left[(C_{p_\infty})_2-(C_{p_\infty})_p\right]\left[d_2^2 + d_2d_3 + d_3^2\right]\right\}$$

$$= -\left\{0.510\frac{(2)^2}{2} - \frac{1}{6}(0.510-0.114)\left\{(1.9)^2 + (1.9)^2 + (1.9)^2\right\}\right\}$$

$$= -0.306 \text{ ft}^2$$

REFERENCES

1. Pate, S. R., Investigation of Flow Separation on a Two-Dimensional Flat Plate Having a Variable-Span Trailing Edge Flap at M = 3 and 5, AEDC-TDR-64-14, March 1964.

2. Chapman, D. R., et al, Investigation of Separated Flows in Supersonic and Subsonic Streams with Emphasis on the Effect of Transition, NACA Report 1356, 1958.

3. Deitering, I. S., Investigation of Flow Separation on a Two-Dimensional Flat Plate Having a Variable-Span Trailing Edge Flap at M_∞ = 3 and 4.5 AEDC-TR-65-59, March 1965.

4. Chapman, D. R., Laminar Mixing of a Compressible Fluid, NACA Report 958, 1950.

5. Drougge, G., "An Experimental Investigation of the Influence of Strong Adverse Pressure Gradient on Turbulent Boundary Layers at Supersonic Speeds," FAA Report No. 46, The Aeronautical Research Institute of Sweden, Stockholm, 1953.

6. Popinski, Z., Shock Wave Boundary Layer Interaction, LR 18307, Lockheed-California Company, June 1965.

7. Nielsen, J. N., Goodwin, F. K., and Lynes, L. L., Calculation of Laminar Separation with Free Interaction by the Method of Integral Relations, Part II - Two-Dimensional Supersonic Non-Adiabatic Flow and Axi-Symmetric Supersonic Adiabatic and Non-Adiabatic Flows, AFFDL TR-65-107, Part II, October 1965.

8. Ferri, A., Experimental Results With Aerofoils in the High-Speed Tunnel at Guidonia Alti de Guidonia No. 17 (1939); translated as NACA TM 946.

9. Holder, D. W. and Gadd, G. E., "The Interaction Between Shock Waves and Boundary Layers and Its Relation to Base Pressure in Supersonic Flow," paper presented at the Boundary Layer Effects in Aerodynamics Symposium held at the National Physical Laboratory, London, 31 March and 1 April 1955.

10. Popinski, Z., Effects of Shock Impingement on Heat Transfer, LR 17299, Lockheed-California Company, 13 January 1964.

11. Wuerer, J. E., et al, Flow Separation in High Speed Flight, A Review of the State-of-the-Art, Douglas Report SM-46429, April 1965, Douglas Missile and Space Systems Division.

12. Ackeret, J., Feldman, F., and Rott, N., Investigation of Compression Shocks and Boundary Layers in Fast Moving Gases, Institute for Aerodynamic E.T.H., Zurich, Report No. 10 (1946). Translated as Aeronautical Research Council Report No. 10,044.

13. Fage, A. and Sargent, R. F., "Shock Waves and Boundary-Layer Phenomena Near a Flat Surface," Proc. Roy. Soc. A, Vol. 190, p. 1 (1947).

14. Barry, F. W.,Shapiro, A. H., and Neumann, E. P., "The Interaction of Shock Waves with Boundary Layers on a Flat Surface," Jour. Aero. Sci., Vol. 18. No. 4, p. 229, 1951

15. Howarth, L. "The Propagation of Steady Disturbances in a Supersonic Stream Bounded on One Side by a Parallel Subsonic Stream," Proc. Camb. Phil. Soc., Vol. 44, Part 3, 1947.

16. Tsien, H. S., et al, "Interaction Between Parallel Streams of Subsonic and Supersonic Velocities," Jour. Aero. Sci., Vol. 16, No. 9, p. 515, 1949.

17. Lighthill, M. J., "Reflection at a Laminar Boundary Layer of a Weak Steady Disturbance to a Supersonic Stream Neglecting Viscosity and Heat Conduction," Quart. Jour. Mech. and Appl. Math., Vol. 3, p. 203, 1950.

18. Oswatitsch, K. and Weighardt, K. Theoretical Analysis of Stationary Potential Flows and Boundary Layers at High Speed, German Wartime Report (1949), Transl. as NACA TM 1189.

19. Lighthill, M. J., "On Boundary Layers and Upstream Influence, Part II, Supersonic Flows Without Separation," Proc. Roy. Soc., Vol. 217, p. 478, 1953.

20. Lees, L., Interaction Between the Laminar Boundary Layer Over a Plane Surface and an Incident Oblique Shock Wave, Princeton University, Aero. Engrg. Lab., Report 143 (1949).

21. Crocco, L. and Lees, L., "A Mixing Theory for the Interaction Between Dissipative Flows and Nearly Isentropic Streams," Jour. Aero. Sci., Vol. 19, No. 10, 1952.

22. Gadd, G. E., "Interaction Between Wholly Laminar and Wholly Turbulent Boundary Layers and Shock Waves Strong Enough to Cause Separation," Jour. Aero. Sci., Vol. 20, No. 11, 1953.

23. Crocco, L., "Considerations on the Shock-Boundary Layer Interaction," Proc. Conference on High-Speed Aeronautics, Polytechnic Institute of Brooklyn, Jan. 20-22, 1955.

24. Glick, H. S., "Modified Crocco-Lees Mixing Theory for Separated Flows," Guggenheim Aero. Lab. Cal. Inst. of Tech. Hypersonic Research Project Memorandum 53, 2 May 1960; also Jour. Aero. Sci., Vol. 29, No. 10, p. 1238, 1962.

25. Bray, K. N. C., Gadd, G. E. and Woodger, M., Some Calculations by the Crocco-Lees and Other Methods of Interactions Between Shock Waves and Laminar Boundary Layers Including Effects of Heat Transfer and Suction, ARC 21, 834, FM 2937, AD No. 241 490, April 1960.

26. Martelluci, A., and Libby, P., "Heat Transfer Due to the Interaction of a Swept Planar Shock Wave With a Laminar Boundary Layer," Proc. USAF-ASD Symposium on Aeroelasticity, Dayton, Ohio, October 1960.

27. Makofski, R. A., "A Two-Parameter Method for Shock Wave-Laminar Boundary Layer Interaction and Flow Separation," Proc. 1963 Heat Transfer and Fluid Mechanics Institute, Pasadena, June 1963.

28. Abbott, D. E., Holt, M., and Nielson, N., "Studies of Separated Laminar Boundary Layers at Hypersonic Speed with Some Low Reynolds Number Data," AIAA Paper No. 63-172, presented at summer meeting, L. A., June 17-20, 1963.

29. Lees, Lester, and Reeves, Barry L., "Supersonic Separated and Reattaching Laminar Flows: I. General Theory and Application to Adiabatic Boundary Layer-Shock Wave Interactions," AIAA Paper No. 64-4, Aerospace Sciences Meeting, New York, January 1964.

30. Cohen, C. B., and Reshotka, E., Similar Solutions for the Compressible Laminar Boundary Layer With Heat Transfer and Pressure Gradient, NACA Report 1293, 1955.

31. Nielsen, Jack N., Goodwin, Frederick K. and Lynes, Larry L., Calculation of Laminar Separation with Free Interaction by the Method of Integral Relations, Part I - Two-Dimensional Supersonic Adiabatic Flow, AFFDL TR-65-107, May 1965.

32. Hayes, W. D., and Probstein, R. F., Hypersonic Flow Theory, Academic Press, New York and London, 1959.

33. Lees, Lester, "Hypersonic Flow," Fifth International Aeronautical Conference (Los Angeles, Calif., June 20-23, 1955), Institute of the Aeronautical Sciences, Inc., 1955, p. 241-276.

34. Creager, M. O., The Effect of Leading Edge Sweep and Surface Inclination on the Hypersonic Flow Field Over a Blunt Flat Plate, NASA Memo 12-26-58A, January 1959.

35. Lees, L., and Probstein, R. F., Hypersonic Viscous Flow Over a Flat Plate, Princeton University Aero. Engrg. Lab., Report 195 (1952).

36. Ames Research Staff, Equations, Tables, and Charts for Compressible Flow, NACA TR 1135, 1953.

37. Bertram, J. B., and Blackstock, T.A., Some Simple Solutions to the Problem of Predicting Boundary-Layer Self-Induced Pressures, NASA TN D-798, April 1961.

38. Randall, R. E., Bell, D. R., and Burk, J. L., Pressure Distribution Tests of Several Sharp Leading Edge Wings, Bodies, and Body-Wing Combinations at Mach 5 and 8, AEDC-TN-60-173, September 1960.

39. Shapiro, A. H., The Dynamics and Thermodynamics of Compressible Fluid Flow, Ronald Press Co., New York, 1954, Vol. II, p. 754-756.

40. Popinski, Z., Generalized Correlations of Aerodynamic Coefficients for a Lifting Body, LTM 50606, Lockheed-California Company, March 30, 1964.

41. Gregorek, F. M., Nark, T. C., and Lee, J. D., An Experimental Investigation of the Surface Pressure and the Laminar Boundary-Layer on a Blunt Flat Plate in Hypersonic Flow, ASD-TDR-62-792, Vol. I, March 1963.

42. Moeckel, W. E., Some Effects of Bluntness on Boundary Layer Transition and Heat Transfer at Supersonic Speeds, NACA Report 1312, 1957.

43. Bertram, M. H., and Feller, W. V., A Simple Method for Determining Heat Transfer, Skin Friction, and Boundary-Layer Thickness for Hypersonic Laminar Boundary-Layer Flows in a Pressure Gradient, NASA Memo 5-24-59L, June 1959.

44. Eckert, E. R. G., Survey of Boundary Layer Heat Transfer at High Velocities and High Temperatures, WADC TR 59-624, April 1960.

45. Gregorek, F. M., Nark, T. C., and Lee, J. D., An Experimental Investigation of the Surface Pressure and the Laminar Boundary-Layer on a Blunt Flat Plate in Hypersonic Flow, ASD-TDR-62-792, Vol. II, March 1963.

46. Creager, M. O., Effects of Leading-Edge Blunting on the Local Heat Transfer and Pressure Distributions Over Flat Plates in Supersonic Flow, NASA TN 4142, December 1957.

47. Hoerner, S. F., Fluid-Dynamic Drag, Second Edition, Midland Park, N.J., 1958, Section 2-3.

48. Deem, R. E., Erickson, C. R., and Murphy, J. S., Flat-Plate Boundary-Layer Transition at Hypersonic Speeds, FDL-TDR-64-129, October 1964.

49. Feldman, S., Hypersonic Gas Dynamic Charts for Equilibrium Air, Research Report 40, Avco Research Laboratory.

50. Popinski, Z., and Koehler, L. F., Hypersonic Flow and Real Gas Effects, LR 18443, Lockheed-California Company, July 1965.

51. Deem, R. E., and Murphy, J. S., "Flat Plate Boundary Layer Transition at Hypersonic Speeds," AIAA Paper No. 65-128, January 1965.

52. Sterrett, J. R., and Holloway, P. F., Effects of Controlled Surface Roughness on Boundary Layer Transition and Heat Transfer at Mach Numbers 4.8 and 6.0, NASA TN D-2054, April 1965.

53. Whitfield, J. D., and Potter, J. L., The Influence of Slight Leading Edge Bluntness on Boundary Layer Transition at a Mach Number of 8, AEDC-TDR-64-18, March 1964.

54. Bertram, M. H., Exploratory Investigation of Boundary Layer Transition on a Hollow Cylinder at a Mach Number of 6.9, NACA Report 1313, 1957.

55. Jack, J. R., Wisniewski, R. J., and Diaconis, N. S., Effects of Extreme Surface Cooling on Boundary Layer Transition, NACA TN 4094, October 1957.

56. Hakkinen, R. J., Greber, I., and Trilling, L., The Interaction of an Oblique Shock Wave With a Laminar Boundary Layer, NASA Memo 2-18-59W, March 1959.

57. Young, A. D., Boundary Layers, Modern Developments in Fluid Dynamics - High Speed Flow, Howarth, ed., Oxford, 1953.

58. Kaufman, L. G., Pressure Measurements for Mach 8 Flows Over Expansion Corners and Ramps on an Internally Cooled Model, RTD-TDR-63-4044 II, May 1964.

59. Kaufman, L. G., Pressure and Heat Transfer Measurements for Hypersonic Flows Over Expansion Corners and Ahead of Ramps, ASD-TDR-63-679 III, December 1963.

60. Kaufman, L. G., Pressure and Heat Transfer Measurements for Hypersonic Flows over Expansion Corners and Ahead of Ramps, ASD-TDR-63-679 II, September 1963.

61. Jones, R. A., Heat Transfer and Pressure Investigation of a Fin-Plate Interference Model at a Mach Number of 6, NASA TN D-2028, July 1964.

62. Stanbrook, A., and Squire, L. C., "Possible Types of Flow at Swept Leading Edges," Aeronautical Quarterly, Vol. XV, February 1964, Part I.

63. Fowell, L. R., "Exact and Approximate Solutions for the Supersonic Delta Wing," Journal of the Aeronautical Sciences, Vol. 23, August 1956, No. 8.

64. Pershing, B., Separated Flow Past Slender Delta Wings with Secondary Vortex Simulation, SSD-TDR-64-151, 24 August 1964.

65. Whitehead, Jr., A. H., and Dunavant, T. C., A Study of Pressure and Heat Transfer Over an 80° Sweep Slab Delta Wing in Hypersonic Flow, NASA TN D-2708, March 1965.

66. Collis, D. C., A Hypersonic Wind Tunnel Study of a Thick Delta Wing, Department of Supply, Australian Defense Scientific Service Aeronautical Research Laboratories, Aerodynamics Note 232, November 1964.

67. Kaufman, L.G., Pressure Measurements for Mach Five Flows Over a Blunt Pyramidal Configuration with Aerodynamic Controls, RTD-TDR-63-4239, January 1964.

68. Bertram, M. H., and Henderson, A., Jr., "Recent Hypersonic Studies of Wings and Bodies," American Rocket Society Journal, Vol. 31, August 1961.

69. Bertram, M. H., and Cook, B. S., The Correlation of Oblique Shock Parameters for Ratios of Specific Heats from 1 to 5/3 With Application to Real Gas Flows, NASA TR R-171, December 1963.

70. Huber, P. W., Hypersonic Shock-Heated Flow Parameters for Velocities to 46,000 Feet Per Second and Altitudes to 323,000 Feet, NASA TR R-163, Dec.1963.

71. Eckert, E. R. G., Survey of Heat Transfer at High Speeds, WADC TR 54-70, April 1954.

72. Kaufman, L. G., Weckler, L., Hartofilis, S. A., and Weiss, D., An Investigation of Hypersonic Flow Separation and Control Characteristics, AFFDL-TR-64-174, January 1965.

73. Nicoll, K. M., Mass Injection in a Hypersonic Cavity Flow, Report No. 714, Princeton University Department of Aerospace and Mechanical Sciences, December 1964.

74. Arnold Engineering Development Center, AFFDL Flapped Gap Study, VTO 611, September 1965.

75. Miller, D. S., and Higman, R., Mach 8 to 22 Studies of Flow Separation Due to Deflected Control Surfaces, AIAA Paper No. 63-173, June 1963.

76. Evans, W. J., and Kaufman, L. G., Pretest Report on Hypersonic Flow Separation and Control Models for AEDC Tunnels A, B, Hotshot 2, and Grumman Hypersonic Shock Tunnel, Grumman Memorandum RM-209, July 1962.

77. Grumman Aircraft Engineering Corporation, Tabulated Pressure and Heat Transfer Data at Mach 5 and 8 for Plate Ramp Model A, ASD-TDR 63-679 and ASD-TDR-63-4044, November 1962.

78. Holloway, P. F., An Investigation of Heat Transfer Within Regions of Separated Flow at Mach 6, NASA TN D-3074, November 1965.

79. Levin, V., and Fabish, T. J., Effects of Shockwave Turbulent Boundary Layer Interaction at M = 3 and 5, North American Aviation, November 1965.

80. Sayano, S., Bauch, H. P., and Donnelly, R. J., Aerodynamic Heating Due to Shock Impingement on a Flat Plate, Model IM-20, Douglas Report SM-41331, August 1962.

81. Popinski, Z., "Shock-Wave-Boundary Layer Interaction," Paper to be presented at the Third International Heat Transfer Conference, to be held in Chicago, August 1966.

82. Chapman, D. R., Theoretical Analysis of Heat Transfer in Regions of Separated Flow, NACA TN 3792, October 1956.

83. Kuehn, D. M., Experimental Investigation of the Pressure Rise Required for the Incipient Separation of Turbulent Boundary Layers in Two-Dimensional Supersonic Flow, NASA Memo 1-21-59A, 1959.

84. Sterrett, J. R., and Emery, J. C., Extension of Boundary Layer Separation Criteria to a Mach Number of 6.5 by Utilizing Flat Plates with Forward-Facing Steps, NASA TN-D-618, December, 1960.

85. Kaufman, L. G., Pressure Measurements for Mach 8 Flows Over Expansion Corners and Ramps on an Internally Cooled Model, RTD-TDR-63-4044 III, May 1964.

86. Levin, V. et. al., Thermal Effect of Shock Wave Turbulent Boundary Layer Interaction at Mach Numbers 3 and 5, NA 62H-795, North American Aviation, November 1962.

87. Grumman Aircraft Engineering Corporation, Tabulated Pressure and Heat Transfer Data at Mach 5 and 8 for Fin-Plate Model 'B', ASD-TDR-63-235, November 1962.

88. Melnikov, A. P., High Speed Aerodynamics, War Publishing of Department of Defense of U.S.S.R., Moscow, 1961 (in Russian).

89. Williams, J. C. III, AIAA Journal, Vol. 3, No. 12, 1965.

Unclassified
Security Classification

DOCUMENT CONTROL DATA - R&D

(Security classification of title, body of abstract and indexing annotation must be entered when the overall report is classified)

1. ORIGINATING ACTIVITY (Corporate author)
Lockheed-California Company
Burbank, California 91503

2a. REPORT SECURITY CLASSIFICATION
Unclassified

2b. GROUP
N/A

3. REPORT TITLE
DEVELOPMENT OF DESIGN METHODS FOR PREDICTING HYPERSONIC AERODYNAMIC CONTROL CHARACTERISTICS

4. DESCRIPTIVE NOTES (Type of report and inclusive dates)
Final Technical Report, June 1965 to April 1966

5. AUTHOR(S) (Last name, first name, initial)
Ehrlich, Carl F.
Popinski, Zenon

6. REPORT DATE	7a. TOTAL NO. OF PAGES	7b. NO. OF REFS
September 1966	279	89

8a. CONTRACT OR GRANT NO.	9a. ORIGINATOR'S REPORT NUMBER(S)
AF33(615)-2512	AFFDL-TR-66-85
b. PROJECT NO. 8219	
c.	9b. OTHER REPORT NO(S) (Any other numbers that may be assigned this report)
d. Task No. 821902	LR 19460

10. AVAILABILITY/LIMITATION NOTICES
Distribution of this document is unlimited

11. SUPPLEMENTARY NOTES	12. SPONSORING MILITARY ACTIVITY
None	AFFDL (FDCC) Wright-Patterson AFB, Ohio 45433

13. ABSTRACT Design methods are developed which predict arerodynamic control effectiveness of vehicles at hypersonic speeds. Pressure and heat transfer distribution in separated regions due to aerodynamic control deflection are described in terms of characteristic magnitudes and distance parameters by semi-empirical correlations. The forms of these correlations are inferred from theory and experimental data. General charts are developed which present separation and flow parameters over a range of flight conditions applicable to typical hypersonic vehicles. Using these charts, pressure distribution in the separated region over a deflected flap is approximated and expressions for for force and moment coefficients are determined.

Flow separation over a fin-plate configuration is presented using experimental measurements Also, deviations of the flow over a flat plate, flat delta wing, and delta with dihedral from that of two-dimensional flow are analyzed by visual flow records and pressure measurements. Applicability of the correlation expressions to separated flow on various configurations is discussed and calculated aerodynamic coefficients are compared with measured values. Accuracy of experimental data, and the resulting correlation expressions and prediction methods are reviewed critically to determine their range of applicability.

DD FORM 1 JAN 64 1473

Unclassified
Security Classification

14. KEY WORDS	LINK A		LINK B		LINK C	
	ROLE	WT	ROLE	WT	ROLE	WT
Aerodynamic control effectiveness						
Hypersonic flow						
Separated flow						
Boundary layer						
Aerodynamic heating						

INSTRUCTIONS

1. ORIGINATING ACTIVITY: Enter the name and address of the contractor, subcontractor, grantee, Department of Defense activity or other organization *(corporate author)* issuing the report.

2a. REPORT SECURITY CLASSIFICATION: Enter the overall security classification of the report. Indicate whether "Restricted Data" is included. Marking is to be in accordance with appropriate security regulations.

2b. GROUP: Automatic downgrading is specified in DoD Directive 5200.10 and Armed Forces Industrial Manual. Enter the group number. Also, when applicable, show that optional markings have been used for Group 3 and Group 4 as authorized.

3. REPORT TITLE: Enter the complete report title in all capital letters. Titles in all cases should be unclassified. If a meaningful title cannot be selected without classification, show title classification in all capitals in parenthesis immediately following the title.

4. DESCRIPTIVE NOTES: If appropriate, enter the type of report, e.g., interim, progress, summary, annual, or final. Give the inclusive dates when a specific reporting period is covered.

5. AUTHOR(S): Enter the name(s) of author(s) as shown on or in the report. Enter last name, first name, middle initial. If military, show rank and branch of service. The name of the principal author is an absolute minimum requirement.

6. REPORT DATE: Enter the date of the report as day, month, year, or month, year. If more than one date appears on the report, use date of publication.

7a. TOTAL NUMBER OF PAGES: The total page count should follow normal pagination procedures, i.e., enter the number of pages containing information.

7b. NUMBER OF REFERENCES: Enter the total number of references cited in the report.

8a. CONTRACT OR GRANT NUMBER: If appropriate, enter the applicable number of the contract or grant under which the report was written.

8b, 8c, & 8d. PROJECT NUMBER: Enter the appropriate military department identification, such as project number, subproject number, system numbers, task number, etc.

9a. ORIGINATOR'S REPORT NUMBER(S): Enter the official report number by which the document will be identified and controlled by the originating activity. This number must be unique to this report.

9b. OTHER REPORT NUMBER(S): If the report has been assigned any other report numbers *(either by the originator or by the sponsor)*, also enter this number(s).

10. AVAILABILITY/LIMITATION NOTICES: Enter any limitations on further dissemination of the report, other than those imposed by security classification, using standard statements such as:

(1) "Qualified requesters may obtain copies of this report from DDC."

(2) "Foreign announcement and dissemination of this report by DDC is not authorized."

(3) "U. S. Government agencies may obtain copies of this report directly from DDC. Other qualified DDC users shall request through _____."

(4) "U. S. military agencies may obtain copies of this report directly from DDC. Other qualified users shall request through _____."

(5) "All distribution of this report is controlled. Qualified DDC users shall request through _____."

If the report has been furnished to the Office of Technical Services, Department of Commerce, for sale to the public, indicate this fact and enter the price, if known.

11. SUPPLEMENTARY NOTES: Use for additional explanatory notes.

12. SPONSORING MILITARY ACTIVITY: Enter the name of the departmental project office or laboratory sponsoring *(paying for)* the research and development. Include address.

13. ABSTRACT: Enter an abstract giving a brief and factual summary of the document indicative of the report, even though it may also appear elsewhere in the body of the technical report. If additional space is required, a continuation sheet shall be attached.

It is highly desirable that the abstract of classified reports be unclassified. Each paragraph of the abstract shall end with an indication of the military security classification of the information in the paragraph, represented as *(TS)*, *(S)*, *(C)*, or *(U)*.

There is no limitation on the length of the abstract. However, the suggested length is from 150 to 225 words.

14. KEY WORDS: Key words are technically meaningful terms or short phrases that characterize a report and may be used as index entries for cataloging the report. Key words must be selected so that no security classification is required. Identifiers, such as equipment model designation, trade name, military project code name, geographic location, may be used as key words but will be followed by an indication of technical context. The assignment of links, rules, and weights is optional.